Some aspects of high frequency wave propagation in randomly perturbed media

Christophe Gomez

Aix*Marseille université
Socialement engagée

Habilitation à diriger des recherches

Spécialité : **Mathématiques Appliquées**

Christophe Gomez

Some aspects of high frequency wave propagation in randomly perturbed media

Soutenue publiquement le 12 Juin 2024

Rapporteurs:

Liliana Borcea, Professeure,
Univeristy of Michigan

Tomasz Komorowski, Professeur,
Polish Academy of Sciences,
Institute of Mathematics

George Papanicolaou, Professeur,
Stanford University

Composition du jury:

Liliana Borcea, Professeure,
Univeristy of Michigan

Sonia Fliss, Professeure,
ENSTA - Paris

Josselin Garnier, Professeur,
Ecole Polytechnique

Antoine Gloria, Professeur,
Sorbonne Université

Rémi Rhodes, Professeur,
Aix Marseille Université

Eric Savin, Professeur,
ONERA - CentraleSupelec

Abstract

This manuscript presents certain aspects of high-frequency wave propagation in randomly perturbed media. First, a particular attention is given to the role played by long-range correlations of the medium fluctuations. This property find applications in various areas of physics, engineering, and medical imaging for instance. The interactions between random fluctuations with long-range dependencies and oscillatory behaviors result in intriguing effects, leading to multiscale phenomena. Such multiscale properties contrast with scenarios involving random fluctuations with short-range correlations or mixing properties, where the stochastic effects are observed on a well-defined scale. These multiscale phenomena are investigated within the context of a stochastically forced nonlinear oscillator, the Schrödinger equation, the wave equation, and the radiative transfer equation. These properties are also investigated numerically, using a time-splitting scheme for the Schrödinger equation, and the design of a Monte-Carlo method in the context of radiative transfer.

Secondly, this manuscript describes the role played by boundaries or interfaces in the propagation domain. Radiative transfer models are discussed for propagation media with boundaries: a half-space, a slab, and a rectangle are considered. Each of these scenarios exhibits interference phenomena that affect the energy propagation at specific locations, and for which the geometry of the propagation media plays a critical role. The role played by rough boundaries and interfaces is discussed under two scenarios. First, a waveguide model inspired by underwater acoustics is considered, in which waves evolve along a randomly perturbed ocean surface and uneven bottom topography. Second, the standard problem of transmission and reflection at an interface is revisited. This time a wave impinges upon a random interface, and generalized Snell's laws for reflection and transmission are derived.

Finally, an aspect of mathematical biology is discussed, focusing on the stochastic and deterministic modeling of secondary metastatic emission. The relation between these two approaches allow the risk evaluation of a metastatic disease, even when unobservable at the time of cancer diagnosis.

Résumé

Ce manuscrit présente certains aspects de propagation d'ondes hautes fréquences dans des milieux aléatoires. Dans un premier temps, une attention particulière est accordée au rôle joué par les corrélations à longue portée des fluctuations du milieu de propagation. Cette propriété trouve des applications dans divers domaines en physique, ingénierie et en imagerie médicale par exemple. Les interactions entre des fluctuations aléatoires ayant des dépendances à longue portée et des comportements oscillatoires produisent des effets surprenants, conduisant à des phénomènes multi-échelles. Ces propriétés multi-échelles contrastent avec les comportements effectifs observés pour des fluctuations aléatoires avec des propriétés de mélange ou de corrélations à courte portée. Dans ce dernier cas les effets stochastiques sont observés sur une échelle bien définie. Ces phénomènes multi-échelles sont étudiés dans le contexte d'un oscillateur non linéaire avec un terme source aléatoire, de l'équation de Schrödinger, de l'équation des ondes et de l'équation de transfert radiatif. Ces propriétés sont étudiées numériquement à l'aide un schéma *time-splitting* pour l'équation de Schrödinger et la mise en place d'une méthode de Monte-Carlo appropriée pour le transfert radiatif.

Dans un deuxième temps, ce manuscrit décrit le rôle joué par les frontières, ou interfaces, du domaine de la propagation. Les modèles de transfert radiatif sont abordés pour des milieux de propagation avec des frontières : un demi-espace, une couche et un rectangle. Chacun de ces cas présente des phénomènes d'interférence qui affectent la propagation de l'énergie à des endroits spécifiques, et pour lesquels la géométrie du milieu de propagation joue un rôle essentiel. Le rôle joué par des frontières, ou interfaces, rugueuses est présenté dans deux contextes différents. Tout d'abord, nous présentons un modèle de guide d'ondes inspiré de l'acoustique sous-marine, dans lequel les ondes évoluent le long de la surface de l'océan et d'un fond marin irrégulier. Ensuite, nous revisitons le problème classique de transmission et réflexion d'une onde incidente par une interface aléatoire. Des généralisations des lois de Snell-Descarte pour la réflection et la transmission sont proposées.

Enfin, un aspect de *mathbio*, concernant la modélisation stochastique et déterministe de l'émission secondaire de métastases, est présenté. La relation entre ces deux approches permet d'évaluer le risque métastatique, même lorsque celles-ci ne sont pas observables au moment du diagnostic du cancer.

Acknowledgments

First and foremost, I would like to express my gratitude to the referees of my habilitation thesis, Liliana Borcea, Tomasz Komorowski, and George Papanicolaou. It is a great honor that they took the time to evaluate my work, and I am especially thankful to Liliana for participating in the defense committee in person.

I am equally honored to have Sonia Fliss, Antoine Gloria, Rémi Rhodes, and Eric Savin on the defense committee. Special thanks go to Rémi for accepting the role of local mentor for the habilitation process and handling the associated administrative duties. I also thank Guillaume Bal for his administrative report recognizing the eligibility of my habilitation application.

I sincerely thanks Josselin Garnier, not only for being part of the defense committee but also for having been a very nice Ph.D. advisor. I am also deeply grateful to Lenya Ryzhik for hiring me as a postdoc at Stanford, where I spent two unforgettable years in California. I realize how lucky I was to begin my research career under such excellent conditions with wonderful advisors, both in terms of their human and scientific qualities.

I extend my gratitude to all my collaborators for the stimulating discussions and exciting projects we are working on. Thanks also to my colleagues at I2M, LMA, and the Qarma team for the enjoyable moments during coffee breaks, lunches, scientific-social events, informal or teaching-related discussions,... and even doing some maths sometimes. Special thanks to Caroline Bauzet, for providing me materials to go through all the administrative processes of the habilitation more easily, as well as Joelle Pieret, at the habilitation office, for her administrative flexibility, which allowed me to defend this habilitation on time.

Finally, a special thanks to my wife and kids for their support and our nice everyday life moments.

Contents

List of publications

[1] C. Gomez, *Time-reversal superresolution in random waveguides*, SIAM Multiscale Model. Simul., 7 (2009), pp. 1348–1386

[2] C. Gomez, *Wave propagation in shallow-water acoustic random waveguides*, Commun. Math. Sci., 9 (2011), pp. 81–125

[3] C. Gomez, *Radiative transport limit for the random Schroödinger equation with long-range correlations*, J. Math. Pures Appl., 98 (2012), pp. 295–327

[4] C. Gomez, *Wave decoherence for the random Schroödinger equation with long-range correlations*, Commun. Math. Phys., 320 (2013), pp 37–71

[5] C. Gomez, *Loss of resolution for the time reversal of wave in underwater acoustic random channels*, Math. Mod. Meth. App. Sci., 23 (2013), pp. 2065–2110

[6] C. Gomez and O. Pinaud, *Asymptotics of a time-splitting scheme for the random Schrödinger equation with long-range correlations*, Math. Model. Numer. Anal., 48 (2014), pp. 411–431

[7] C. Gomez, *Wave propagation in underwater acoustic waveguides with rough boundaries*, Commun. Math. Sci., 13 (2015), pp. 2005–2052

[8] C. Gomez, O. Pinaud, and L. Ryzhik, *Hypoelliptic estimates in radiative transfer*, Commun. Part. Diff. Eq., 41 (2015), pp. 150–184

[9] C. Gomez, O. Pinaud, and L. Ryzhik, *Radiative transfer with long-range interactions: regularity and asymptotics*, SIAM Multiscale Model. Simul., 15 (2017), pp. 1048–1072

[10] C. Gomez and O. Pinaud, *Fractional white-noise limit and paraxial approximation for waves in random media*, Arch. Rat. Mech. Anal., 226 (2017), pp. 1061–1138

[11] C. Gomez and N. Hartung, *Stochastic and deterministic models for the metastatic emission process: formalisms and crosslinks*, Cancer Systems Biology : Methods and Protocols, Springer 2018

[12] C. Gomez and K. Sølna, *Wave propagation in random waveguide with long-range correlations*, Commun. Math. Sci., 16 (2018), pp. 1557–1596

[13] C. Gomez and O. Pinaud, *Monte Carlo methods for radiative transfer with singular kernels*, SIAM J. Sci. Comput., 40 (2018), pp. A1714–A1741

[14] C. Gomez, G.Iyer, H. Le, and A. Novikov, *An oscillator driven by algebraically decorrelating noise*, Commun. Math. Phys., 402 (2023), pp. 231–284

[15] C. Gomez and O. Pinaud, *A Monte Carlo method for 3D radiative transfer equations with multifractional singular kernels*, J. Comput. Phys., 489 (2023), 112279

[16] A. Messaoudi, R. Cottereau and C. Gomez, *Boundary effects in radiative transfer of acoustic waves in a randomly fluctuating half-space*, SIAM Multiscale Model. Simul., 21 (2023), pp. 1299–1321

[17] C. Gomez, *An effective fractional paraxial wave equation for wave-fronts in randomly layered media with long-range correlations*, SIAM Multiscale Model. Simul., 21 (2023), pp. 1410–1456

[18] A. Messaoudi, R. Cottereau and C. Gomez, *Weak localization in radiative transfer of acoustic waves in a randomly-fluctuating slab*, submitted (hal-04174463).

[19] C. Gomez and K. Sølna, *Reflection and transmission problems for high-frequency waves at a randomly perturbed interface: generalized Snell's laws*, submitted (hal-04317227).

Introduction

The present manuscript gathers all my scientific contributions dating back to my Ph.D. defense. The main topic revolves around the propagation of high-frequency waves in randomly perturbed media under various angles encompassing theoretical and numerical aspects. These researches cover scalar wave propagation, governs by the standard wave equation, as well as the random Schrödinger equation. Although the Schrödinger equation is known as the fundamental equation of quantum mechanics, describing the motion of wave functions at the atomic level, it can also be derived from the standard wave equation to elucidate wave-front propagation for high-frequency collimated waves at the macroscopic level. This latter approximation, known as paraxial (or parabolic) approximation, is widely used in practice as it strongly simplifies the description of physical phenomena at the macroscopic scale, along with the corresponding numerical simulations. In practical aspects the fine scales of variation occurring within the propagation media cannot be described exactly. These fluctuations can have various origins: *impurities* within the propagation medium, salinity or temperature variations, or even geometric perturbations of the medium itself for instance. Therefore, it is natural to treat some propagation media as inherently random. For a given situation, the fluctuations occurring in the propagation medium are deterministic, but they can be considered as a realization of a random process. This manuscript specifically focuses on *weak scattering* type regimes. Roughly speaking, for high-frequency waves, this regime corresponds to propagation media characterized by fast fluctuations occurring at the same rate as the wave frequency, while having low amplitudes. Despite the relatively small amplitudes of these fluctuations, the high-frequency waves and fast variations of the propagation media lead to strong interactions, resulting to significant cumulative stochastic effects on the propagating waves. The *microscopic* description provided by the wave equation at the wavelength scale (which is small for high-frequency waves), or by the Schrödinger equation, is in many cases too rich or too complex to be effectively exploited theoretically or numerically at large macroscopic scales. The derivation of macroscopic models from the microscopic dynamics aims to capture effective features or behaviors that prove useful for applications or theoretical studies on macroscopic scales. By mean of considerations on characteristic scales of the problem at hand, interesting macroscopic models that highlight the main characteristics can be identified. These models offer an effective statistical description of the effects on the propagating waves and can serve as the foundation for imaging techniques among other applications. Importantly, these derived macroscopic models do not depend on specific (unknown in practice) realizations of the medium fluctuations, but rather on their statistical properties through power spectral densities. Various models of power spectra can be found in the physical literature. Well known examples include the Kolmogorov power spectrum for standard atmospheric turbulence, the Pierson-Neuman or Pierson-Moscvitz spectra for the modeling of the swell in underwater acoustics, Gegenbauer scattering kernel in neutronics, and Henyey-Greenstein scattering kernel for imaging through biological tissues, among others.

It is worth mentioning that both the wave equation and the Schrödinger equation can be related to radiative transfer models that describe scattering properties and energy propagation through random media at the macroscopic scale. The concept of radiative transfer is one of the main aspect of this manuscript. The origin of this theory trace back to 1871, when the physicist John William Strutt (lord Rayleigh) conducted pioneering researches on the scattering of light by the atmosphere, shedding light on the explanation for the color of the sky. The theory of radiative transfer as a well-defined mathematical framework took shape in the early 20th century mainly due to the efforts of

Eugen von Lommel (1887), Orest Khvolson (1890), and Arthur Schuster (1905). A. Schuster plays a pivotal role in this theory when, in 1905, he formulated a radiative transfer problem to elucidate the origins of absorption and emission lines observed in stellar spectra [185]. In the 1930s, Subrahmanyan Chandrasekhar made remarkable contributions to the field of radiative transfer by developing a more comprehensive version of the radiative transfer equation that could be applied to a wide range of astrophysical problems [48]. Chandrasekhar's equation incorporates the intricate interplay of scattering, absorption, and emission of radiation within stellar atmospheres. Consequently, radiative transfer theory experienced a surge in prominence among the astrophysics community during the first half of the 20th century. Today, radiative transfer models find applications in many other areas such as neutronics, optics, geophysics, weather forecasting, and even the illumination of scenes in animated movies. Despite the stochastic nature of wave propagation problems, the associated radiative transfer models are deterministic, exhibiting therefore a property called *self-averaging*. When looking a the wave energy, this property results from highly-oscillating random phases that average out, leading to deterministic quantities. Rigorous derivations of the radiative transfer equation from the Schrödinger equation can be found in [18, 66, 92] and for the wave equation in [45, 180].

A significant part of the results in this manuscript is based on approximation-diffusion theorems for random ordinary differential equations or partial differential equations. Stochastic diffusion processes, defined as solutions to stochastic (partial) differential equations, can serve as a macroscopic model to describe effective wave scattering properties. The first results related to approximation-diffusion date back to 1966 with the pioneer works of Rafail Khasminskii [128,129]. These asymptotic results were further extended to the general context of random fluctuations with mixing properties by George C. Papanicolaou and Werner Kohler in 1974 [171]. Additionally, martingale techniques were employed in this context by George C. Papanicolaou, Daniel W. Stroock and S. R. S Varadhan [173], as martingales and diffusion processes exhibit close connections [197]. This approach has found a wide range of applications in the field of wave scattering as discussed in [70]. The main applications of these models are to devised imaging and inverse problem techniques involving waves in complex media [35–38, 80, 88]. For instance, imaging functionals characterizing object localizations buried in strongly scattering propagation media can be designed by incorporating explicit quantities from macroscopic models accounting for wave scattering. Imaging methodologies have also been proposed by leveraging radiative transfer models [20, 21]. The use of macroscopic models to design these imaging functionals results in efficient inversion methodologies as they accurately represent scattering phenomena responsible for the degradation of the recorded signals at sensors.

There is an extensive literature describing physical systems perturbed through white-noises, Markov processes, or processes with mixing properties. These choices are related to the notion of memoryless perturbations, and under proper assumptions give rise to diffusion phenomena. Despite earlier findings, the notion of long-range dependence, as a distinct phenomena, started gaining recognition in the early 1960's thanks to a series of paper by Benoit Mandelbrot and James Wallis [146, 147]. These works were spurred by empirical observations from Harold E. Hurst [118, 119] in the 1950's regarding the water flow in the Nile river. Random fluctuations with long-range dependencies exhibit memory properties and can lead to *anomalous* diffusion phenomena as well as interesting macroscopic phenomena in physical systems such as for the Schrödinger equation [13, 15, 51, 106], the heat equation [131], turbulent transport [67, 132–135], or the wave equation [153, 154, 191]. This notion of long-range correlations plays also a central role in this manuscript, from Chap. 1 to 4, through the study of nonlinear oscillators, the Schrödinger equation, the wave equation, or radiative transfer models. It unveils interesting properties when studied at various propagation scales, and even whithin numerical schemes for the random Schrödinger equation. Analyzing the asymptotic behavior of random ordinary differential equations or partial differential equations involving long-range correlations presents inherent technical challenges. The standard martingale approach, typically applied for mixing random fluctuations, may not be suitable for situations involving long-range correlations. In such cases one often resorts to the rough path theory [74, 152] or a moment technique [15, 67] as an alternative approach. Monte-Carlo methods for radiative transfer models, related to randomly perturbed propagation media with long-range correlations, are also presented. The fundamental idea behind this method is to express the solution of the radiative transfer equation as an expectation of an appropriate Markov process, whose infinitesimal generator corresponds to the scattering properties (scattering kernel) of this equation. In the context of long-range correlations, the scattering properties exhibit a singular behavior giving rise to technical challenges. Although energy is scattered in every

directions, the singularity allocates an infinite weight on *infinitely small* changes of directions of the underlying Markov process [96], rendering the standard notion of mean-free path/time invalid.

Scattering of waves by rough surfaces is a fundamental phenomenon with profound implications across various fields of physics and engineering. Problems related to the role played by boundaries or interfaces are discussed in Chap. 5 and 6. The understanding of these phenomena is of significant importance across a wide spectrum of disciplines including optics, solid state physics, remote sensing, radar technology, environmental monitoring, communications, and non-destructive testing among others [29, 57, 120, 169]. The interplay between waves and rough surfaces results in complex phenomena of reflection, transmission, and diffraction, that necessitates the generalization of the standard Snell's laws of refraction and transmission. The influence of random boundaries has also been studied in various physical contexts. For instance, in fluid flows within a medium with random boundaries [30], water wave propagation with a free surface or a random depth [63, 81], and also in wave propagation in underwater acoustics with a perturbed sea surface [61,137]. While not randomly perturbed, boundaries can also lead to technical difficulties in radiative transfer and interesting interference effects, such as intensity enhancement at boundaries and *weak localization effects* as described in [47, 76], for instance. The derivation of radiative transfer models usually takes place in the full physical space $\mathbb{R}^3$ [12, 45, 180], and some adjustments are required to deal with propagation media involving boundaries. In particular, the main tool to derive radiative transfer equations is the Wigner transform, which is not directly well-suited to address the presence of boundaries. This is a reason why such situations have been less studied in the literature [2, 22, 150, 161, 181]. For instance, in the case of a half-space, the standard radiative transfer equation is equipped with boundary conditions corresponding to a geometric optic type reflection of the energy. This condition is valid for both Dirichlet and Neumann boundary conditions. To account for interference effects at boundaries, the Wigner transform needs to be considered carefully.

One aspect of mathematical biology is also discussed (Chap. 7) while not being entirely disconnected from the ideas discussed for wave propagation. Mathematical models are valuable tools to gain insights into complex biological processes, such as population dynamics, disease dissemination, ecological interactions, and cellular behavior. These models enable quantitative analyses and predictions for biological systems, thus yielding a deeper understanding of these intricate phenomena. Metastasis are responsible for most cancer-related deaths and constitutes a pivotal point in course of the cancer disease [209]. However, knowing that metastases smaller than approximately 10^7 cells remain undetectable by medical imaging and other diagnostic tools, the clinical absence of visible metastases may not accurately represent a patient's true metastatic status. Consequently, the estimation of metastatic risk in cancer patients without observable metastases holds significant clinical importance [170]. In this context, probabilistic techniques have the potential to derive risk scores from clinical data. For instance, probabilistic representation and Monte-Carlo methods can serve as valuable tools to handle *complex* PDE models, such as the Iwata model for metastatic emission [122]. After model inference from clinical data, the Monte-Carlo approach can be used in assessing forecast uncertainty and for diagnosis purposes.

The remaining of this section is dedicated to providing a chapter by chapter overview of the contents of this manuscript, along with the corresponding main results.

Chapter 1

The notion of random fluctuations exhibiting long-range correlations plays a central role in this manuscript (from Chap. 1 to 4). A stationary process v is said to have *long-range correlations or dependencies* if its two-point correlation function

$$R(t) := \mathbb{E}[V(t+s)V(s)],$$

for $(t, s) \in \mathbb{R} \times \mathbb{R}$, decays slowly enough at infinity,

$$R(t) \underset{|t|\to\infty}{\sim} \frac{R_0}{|t|^\gamma} \qquad \gamma \in (0, 1],$$

to not be integrable:

$$\int_0^\infty |R(t)|\, dt = \infty.$$

This is in contrast with the notion of *short-range correlations* for which the correlation function is integrable at infinity. As outlined in this manuscript, the mere distinction between long-range and short-range correlations can result in drastically different behaviors in noisy physical systems. Some examples of stochastic processes or random fields are provided in this chapter, and one of them provides a construction that will be used in the following chapters.

The remaining of this chapter describes the long-time behavior of a stochastically forced nonlinear oscillator with 1 degree of freedom

$$\ddot{x}(t) + f(x(t)) = \varepsilon V(t) \qquad t \geq 0.$$

Here $f\colon \mathbb{R} \to \mathbb{R}$ is a given smooth function, and V is a stochastic process with long-range correlations representing the noise. This situation provides a simple framework highlighting the interactions between random fluctuations with long-range correlations and oscillatory behaviors. The parameter $\varepsilon \ll 1$ represents the amplitude of these random fluctuations. It turns out that the noise itself has a nontrivial behavior over a time scale of order

$$\frac{1}{\varepsilon^{1/\mathfrak{H}}} \qquad \text{with} \qquad \mathfrak{H} = 1 - \frac{\gamma}{2} \in (1/2, 1).$$

More precisely, the process defined by

$$v^\varepsilon(t) = \varepsilon \int_0^{t/\varepsilon^{1/\mathfrak{H}}} V(s) ds \qquad t \geq 0,$$

converges in law, in the space of continuous functions, to a fractional Brownian motion with Hurst index $\mathfrak{H}$ depending on the decay rate of the correlation function γ. This result is known as *non-central* limit theorem [152, 202, 203]. A one dimensional standard fractional Brownian motion $W_{\mathfrak{H}}$ with Hurst index $\mathfrak{H}$, on a probability space $(\Omega, \mathcal{T}, \mathbb{P})$, is a centered Gaussian process with covariance function

$$\mathbb{E}[W_{\mathfrak{H}}(t) W_{\mathfrak{H}}(s)] = \frac{1}{2}(t^{2\mathfrak{H}} + s^{2\mathfrak{H}} - |t-s|^{2\mathfrak{H}}),$$

for any $t, s \geq 0$. The case $\mathfrak{H} = 1/2$ corresponds to a standard Brownian motion.

The *non-central* limit theorem is in contrast with the standard invariance principle, which relies on the standard central limit theorem for processes with short-range correlations or mixing properties [139, 152]. For the latter the appropriate time scale to observe nontrivial stochastic effects is $1/\varepsilon^2$. Long-range correlations provide nontrivial stochastic effects that become apparent at shorter time scale compared to situations involving short-range correlations or mixing properties:

$$\frac{1}{\varepsilon^{1/\mathfrak{H}}} \ll \frac{1}{\varepsilon^2} \qquad \text{for} \qquad \mathfrak{H} \in (1/2, 1).$$

A more general *non-central* limit theorem is discussed in this chapter. One can naturally wonder how such statistical behavior affects the one of the nonlinear oscillator. It turns out that the energy of the system exhibits nontrivial diffusive effects only at time scales of order $1/\varepsilon^2$ despite fluctuations with long-range correlations, and not at shorter time scales. This scale aligns with the one at which diffusive effects become apparent when considering fluctuations with short-range correlations or mixing properties within the oscillator system. As a result, even though the random perturbations exhibit a degenerate behavior at the time scale $1/\varepsilon^2$, the oscillatory behavior of the system prevents the emergence of pathological behaviors. In the limit $\varepsilon \to 0$, the energy of the system can be described through a standard diffusion process similar (though not identical) to the one of the classical result [71] for a white-noise perturbation. More precisely, considering a smooth Hamiltonian

$$H(x, y) = \frac{y^2}{2} + \int_0^x f(s) ds \qquad x, y \in \mathbb{R},$$

with exactly one non-degenerate critical point at $(0, 0)$, which is also the global minimum, and V be a stationary Gaussian noise with long-range correlations, we observe the following convergence in law in $\mathcal{C}(0, \infty)$,

$$H(X^\varepsilon) \underset{\varepsilon \to 0}{\Longrightarrow} \mathcal{X}.$$

Here, $X^\varepsilon(t) = (x(t/\varepsilon^2), \dot{x}(t/\varepsilon^2))^T$ and $\mathcal{X}$ is a diffusion process driven by a standard Brownian motion (and not a fractional Brownian motion), with infinitesimal generator similar to the one of the standard Freidlin and Wentzell theory with white-noise perturbations of the oscillator [71–73].

This chapter covers the results obtained in [14] of the publication list on page 6, and was conducted during Hai Le's Ph.D. program under the supervision of A. Novikov at Penn State University.

Chapter 2

The first situation we present to describe the influence of long-range correlations on a wave propagation problem concerns the Schrödinger equation with a time-dependent random potential. More precisely, we consider the wave function ϕ which satisfies

$$i\partial_t\phi + \frac{1}{2}\Delta_{\mathbf{x}}\phi - V(t,\mathbf{x})\phi = 0 \qquad t \geq 0, \quad \mathbf{x} \in \mathbb{R}^d,$$

where V exhibits long-range correlations w.r.t. the time variable. The long-time behavior of ϕ is studied under the weak scattering regime that consists of small random fluctuations, of order $\sqrt{\varepsilon}$, with $\varepsilon \ll 1$, as well as the time and space scaling

$$\phi_\varepsilon(t,\mathbf{x}) = \phi\Big(\frac{t}{\varepsilon^s}, \frac{\mathbf{x}}{\varepsilon^s}\Big).$$

The parameter $s > 0$ represents how long and how far the wave function propagates. Under this scaling the Schrödinger equation now reads

$$i\varepsilon^s\partial_t\phi_\varepsilon + \frac{\varepsilon^{2s}}{2}\Delta_{\mathbf{x}}\phi_\varepsilon - \sqrt{\varepsilon}\,V\Big(\frac{t}{\varepsilon^s}, \frac{\mathbf{x}}{\varepsilon^s}\Big)\phi_\varepsilon = 0. \tag{1}$$

To observe non-trivial cumulative stochastic effects on the wave function ϕ_ε in the limit $\varepsilon \to 0$, an appropriate choice of s needs to be made. Considering short-range correlations or mixing properties for the potential V leads to the unique choice $s = 1$ [15]. In case of long-range correlations the situation is much richer. Equipped with appropriate initial conditions, the latter scaled Schrödinger equation exhibits effective multiscale effects w.r.t. the propagation parameter s. In [15] the authors show that for an appropriate choice of $s = s_0$, corresponding to the non-central limit theorem scaling, the wave function exhibits a random phase modulation driven by a unique fractional Brownian motion for all the wavevectors supported by the wave function.

This chapter describes how the wave function is affected when it propagates over longer scales, that is when $s > s_0$. Over such scalings the wave function experiences a highly oscillating random phase modulation that is expected to break the wave function coherence. In this context the main tool to analyze this loss of coherence is based on a properly scaled Wigner transform of the wave function. This Wigner transform relates to the Fourier transform of the correlation function of the wave function at two nearby points. The resulting diffusive behaviors w.r.t. the momentum variable (the Fourier variable of the Wigner transform) quantifies the effective loss of coherence of the wave function. Three different regimes can be exhibited as the propagation parameter s increases. As already mentioned, for $s > s_0$, the wave function produces fast phase modulations that affects significantly the structure of the wave function. One can show that for some $s = s_1 > s_0$ a loss of coherence of the wave field can be quantified through a stochastic fractional heat equation (SFHE) for the Wigner transform. At this stage the Wigner transform analyses the correlations of points that are far apart from each other. In other words, the loss of coherent impacts the large structures of the wave function in a first place. While the SFHE describes how the Wigner transform is impacted, its energy is conserved. Then, as the propagation scale increases $s > s_1$, the finer structures of the wave function are increasingly affected. This time, the random behavior of the SFHE averages out, homogenization phenomena take place, and the resulting equation governing the loss of coherence is a deterministic fractional heat equation. Once $s = 1$ is reached, the loss of coherence is described by a semi-classical limit and a radiative transfer equation. At this scale, the loss of coherence mechanisms are identical whether the random fluctuations exhibit long-range correlations or shot-range correlations.

At the numerical point of view, a time-splitting scheme for the scaled Schrödinger equation (1) can be considered. This numerical scheme provides a discretized solution in time (the spatial variable being handle through a Fourier transformation), which is able to capture, in the statistical sense,

all the mentioned asymptotic regimes. Surprisingly, in addition to all these regimes, the long-range correlations allow a time stepsize independent of ε for most of the configurations.

This chapter covers the results obtained in [3, 4, 6] of the publication list on page 6.

Chapter 3

The analysis of the impact of random fluctuations with long-range correlations is extended in this chapter to the scalar wave equation for 2D and 3D propagation media. In this context the random fluctuations of the propagation media translate through random fluctuations of the wave-speed profile. This chapter presents some results that extend the ones obtained for 1D propagation media [84,85,154].

Three scenarios are considered in this chapter. The first situation concerns wave propagation in a planar waveguide, which constitutes an intermediate situation between 1D propagation media and propagation in a full space. The type of waveguide considered in this chapter supports a discrete number of modes, which simplifies in some sense the mathematical analysis. The regime under consideration corresponds to the one of a non-central limit theorem and a result similar to [153] is obtained. In this situations the effective stochastic effects lead to phase modulations for each of the propagating modes, but without any coupling between the modes. However, as for the Schrödinger equation, these modulations are driven by the same fractional Brownian motion. This latter characteristic is in contrast to what is observed in [70, Chap. 20] under medium fluctuations with short-range correlations, where the phase modulations are driven by correlated Brownian motions.

The second scenario considers again a regime similar to the non-central limit theorem but for the wave equation over the full ambient space $\mathbb{R}^3$. More precisely, two asymptotic regimes are simultaneously investigated under the same high-frequency limit: the paraxial approximation, where the wave is collimated and propagates along a privileged direction of propagation, and the fractional white-noise limit. It results that the frequency content of the asymptotic pulse front can be described through the fractional Itô-Schrödinger equation

$$d\Psi_\omega(z,\mathbf{x}) = \frac{i}{2k_\omega}\Delta_{\mathbf{x}}\Psi_\omega(z,\mathbf{x}) + ik_\omega\Psi_\omega(z,\mathbf{x})dW_{\mathfrak{H}}(z,\mathbf{x}) = 0,$$

where ω is a given frequency, z corresponds to the variable of the main propagation axis, and $W_{\mathfrak{H}}$ to a fractional random field w.r.t. z. The variable $\mathbf{x}$ represents the transverse section w.r.t. the main propagation axis. The stochastic integral corresponds here to the fractional equivalent of the Itô-Stratonovich integral. Under short-range correlations a similar result has been obtained in [83] involving a standard Brownian random field and Itô-Stratonovich integral.

The last scenario corresponds this time to a regime similar to a central limit theorem, but involving a randomly layered propagation medium with long-range correlations. This scenario extends the result of [84, 85] for 1D propagation media. In this situation, we observe first a random travel time for the pulse characterized by a fractional Brownian motion that appears to have a standard deviation larger than the pulse width. This is in contrast with the standard O'Doherty-Anstey theory for random propagation media with short-range correlations for which both the standard deviation of the random travel time and the pulse width are of the same order [70, Chapter 8]. This *unstable* behavior of the travel time under long-range correlations may have a dramatic effect for applications in inverse problems based on travel time estimations, and a deeper understanding of the propagating waves is required. Second, in the present context, the pulse deformation can be characterized by a deterministic paraxial wave equation of the form

$$\partial^2_{tz}\psi - \frac{c_0}{2}\Delta_{\mathbf{x}}\psi - a_0 D_t^{2+\gamma}\psi = 0 \qquad \gamma \in (0,1),$$

where the z-variable corresponds again to the main propagation axis, the $\mathbf{x}$-variable to the transverse section, t to the time variable, c_0 to the background wave speed, and $a_0 > 0$ is a constant. Here, $D_t^{2+\gamma}$ stands for the Weyl fractional derivative with respect to time, and whose order depends explicitly on the power decay rate $\gamma \in (0,1)$ of the correlation function of the medium fluctuations. In the Fourier domain, this equation can be recast as a Schrödinger equation of the form

$$i\frac{\omega}{c_0}\partial_z\check{\psi} + \frac{1}{2}\Delta_{\mathbf{x}}\check{\psi} + \tilde{a}_0\omega|\omega|^{1+\gamma}\check{\psi} = 0,$$

where $\tilde{a}_0$ is a constant with positive imaginary part. This equation provides a frequency-dependent power-law attenuation of the form

$$|\omega|^\lambda \qquad \text{with} \qquad \lambda = 1 + \gamma \in (1, 2].$$

Such power law attenuations can be observed in various contexts such as geophysics, laser beam propagation through the atmosphere, or medical imaging for instance. Values for λ ranging from 2 to 3 are typical of attenuations in biological tissues [117].

This chapter covers the results obtained in [10, 12, 17] of the publication list on page 6

Chapter 4

Radiative transfer models have been used for more than a century to describe the propagation of the energy density through random media. When the momentum variable is restricted over the unit sphere $\mathbb{S}^{d-1}$, the radiative transfer equation can be written as

$$\partial_t u + \widehat{\mathbf{k}} \cdot \nabla_{\mathbf{x}} u = \int_{\mathbb{S}^{d-1}} \Phi(|\widehat{\mathbf{p}} - \widehat{\mathbf{k}}|)(u(\widehat{\mathbf{p}}) - u(\widehat{\mathbf{k}}))\sigma(d\widehat{\mathbf{p}}) \qquad (t, \mathbf{x}, \widehat{\mathbf{k}}) \in (0, \infty) \times \mathbb{R}^d \times \mathbb{S}^{d-1},$$

where $\sigma(d\widehat{\mathbf{p}})$ stands for the surface measure on $\mathbb{S}^{d-1}$, and Φ for the scattering kernel. Under fluctuations with long-range correlations this model can be derived from the Schrödinger equation under a semi-classical limit [66]. For the full wave equation such a rigorous derivation has been obtained in [45] for short-range correlations, but it remains an open problem for long-range correlations. Radiative transfer models can be though considered in this situation by just considering scattering kernels with appropriate shapes. The scattering kernel being directly related to the power spectral density of the medium fluctuations, under long-range correlations the associated scattering kernel presents a nonintegrable singularity $\Phi(r) \propto r^{-(d-1+\alpha)}$ with $\alpha \in (0, 2)$. Despite this singularity the radiative transfer equation remains well-defined.

The first part of this chapter consists in presenting qualitative properties of the radiative transfer equation with a nonintegrable singular kernel. We present regularizing effects of such equation through the hypoellipticity property of the transport operator, which implies in particular that the solutions are infinitely differentiable in all variables. This property is obtained through hypoelliptic estimates for a kinetic equation of the form

$$\partial_t u + \widehat{\mathbf{k}} \cdot \nabla_{\mathbf{x}} u = (-\Delta_{\mathbb{S}^{d-1}})^\beta h \qquad (t, \mathbf{x}, \widehat{\mathbf{k}}) \in \mathbb{R} \times \mathbb{R}^d \times \mathbb{S}^{d-1},$$

where $d \geq 2$, $\beta \geq 0$, $\mathbb{S}^{d-1}$ denotes the unit sphere of $\mathbb{R}^d$ and $\Delta_{\mathbb{S}^{d-1}}$ the Laplace-Beltrami operator on $\mathbb{S}^{d-1}$. Assuming some fractional Sobolev regularity in the momentum variable $\widehat{\mathbf{k}} \in \mathbb{S}^{d-1}$, we obtain estimates for fractional derivatives of u w.r.t the $(t, \mathbf{x})$-variables whose order depends on β and the assumed regularity. The smoothness of u is then obtained using a bootstrap argument. The diffusion limit is proved using probabilistic techniques as in the case of a regular scattering operator. The diffusion coefficient is therefore non-zero and finite.

The second part of this chapter is devoted to Monte-Carlo methods for radiative transfer equations with non-integrable singular scattering kernels. As opposed to the case where the scattering cross section is integrable and leads to a non-zero mean free time, the cross section is no longer integrable in the long-range situation and yields a vanishing mean free time. This gives rise to numerical difficulties as standard Monte-Carlo methods based on a naive regularization, by just introducing a cutoff around the singularity, exhibit large jump intensities and an increased computational cost to reach a proper accuracy. A particular care is then required when constructing the stochastic processes used in the Monte-Carlo methods. We propose a method inspired by the finance literature, and introduced by Asmussen-Rosiński [9] and Cohen-Rosiński [53]. This method is based on a small jumps - large jumps decomposition allowing us to treat the small jumps efficiently and reduce the computational burden.

This chapter covers the results obtained in [8, 9, 13, 15] of the publication list on page 6.

Chapter 5

This chapter concerns as well some aspects of radiative transfer arising from acoustic wave propagation, but from a different perspective as the one discussed in the previous chapter. Rather than

investigating the effects produced by a singular scattering kernel, we discuss the role played by boundaries of the propagation medium. We present three scenarios: a half-space, a slab, and a rectangle. This chapter covers the results in [16,18] of the publication list on page 6, which are parts of Adel Messaoudi's Ph.D thesis conducted under the supervision of Régis Cottereau (Laboratory of Mechanics and Acoustics in Marseille) and myself.

For each scenarios two distinct aspects are discussed. While the standard derivations of radiative transfer models from the wave equation usually take place in the full physical space $\mathbb{R}^3$ [12, 45, 180], some adjustments are required to deal with medium involving boundaries. In particular, the main tool to derive radiative transfer equations is the Wigner transform. This tool is not directly well-suited to address the presence of boundaries. In this chapter, for each scenario, the wave propagation problem is extended to the full space thanks to the method of images together with a proper periodization of the medium parameters and the source. Such an extension allows the use of the standard Wigner transform and enable a standard asymptotic analysis [12, 180].

The other aspect discussed in this chapter concerns interference effects resulting front reverberations at the boundaries. In a first time, we discuss the case of the half-space where boundary effects can be observed within one wavelength along the boundary. This results in a doubling of the intensity for Neumann boundary conditions, and a canceling of intensity for Dirichlet boundary conditions. In a second time, the situation of a slab is discussed. As for the half-space, interference effects are obtained within one wavelength of the two slab boundaries. However, additional interference effects are observed within one wavelength along two parallel plans w.r.t to the boundaries, and passing through the source location and one symmetric point. These extra effects are referred to as *weak localization* phenomena in the sens of [47, 76]. These effects result in intensity enhancement or canceling (depending on the boundary conditions) of the coherent energy only, not the one carried by the coda (the multiply scattered signal). The underlying idea of *weak localization* is the following. When coherent waves propagate through a medium delimited by boundaries, they follow different paths and bounce on these boundaries. However, some of these paths are the reciprocal versions of others, meaning that the waves can traverse a similar path in opposite directions. This symmetry between paths results in constructive interference effects within the considered structure. Finally, the case of a rectangle is discussed where radiative transfer models are related to non destructive testing applications [47, 76]. As for the slab, both types of interference effects can be observed within one wavelength of the boundaries, and along lines parallel to the rectangle boundaries passing through the source location and three symmetric points. These lines are fixed over time. In this context, additional interference effects can be observed. Constructive interferences affecting the whole energy (coherent and coda) can be observed along lines passing through the corners, and interference effects, affecting only the coherent part of the energy, appear along oblique lines passing through the source location and eleven symmetric points inside the rectangle. In both cases, these lines support interference effects only once over time.

Chapter 6

This chapter discusses two distinct scenarios. First, we discuss the situation where the waves propagate along a waveguide with rough-boundaries, and second, the case where waves impinge upon a rough surface. In both scenarios, the waves interact with the interface in different manners, leading to distinct mathematical approaches.

In underwater acoustic the role of ocean swell or variations of the seabed topography can have a significant impact on acoustic signals. Wave propagation in waveguides with rough boundaries has been studied for a long time due to its wide range of applications, but mainly motivated by submarine detection and telecommunication [126, 138]. In this context, a pressure field can be decomposed over three kinds of mode: the propagating modes, which travel over long distances along the waveguide; the radiating modes, able to propagate deeply into the ocean bottom; and the evanescent modes, which decay exponentially w.r.t to the propagation distance along the waveguide. We describe in the first part of this chapter the effects produced by a randomly perturbed free surface and an uneven bottom topography on the propagating modes. Using an asymptotic analysis based on a separation of scales technique and an approximation-diffusion theorem, an asymptotic form of the distribution for the forward mode amplitudes can be obtained. This distribution allows to characterize effective attenuations on the propagating-mode amplitudes induced by the surface and bottom fluctuations.

It appears that both the surface and bottom fluctuations affect the propagating-mode amplitudes mainly in similar manners. However, this attenuation is stronger for the highest propagating modes, with losses into the ocean bottom, due to a strong coupling with the radiating modes.

The second scenario discussed in this chapter corresponds to the standard problem of reflexion and transmission of a high-frequency pulse at a rapidly oscillating rough interface with general mixing properties. Under the paraxial (parabolic) scaling, the specular and speckle (diffusive) components of the reflected and transmitted signals are precisely characterized. The specular components correspond to the reflected and transmitted components resulting from the standard laws of reflexion and transmission for a flat (unperturbed) interface, and producing what we refer to as specular cones. The speckles correspond to incoherent (random) wave fluctuations resulting from diffraction and mainly observed away from the specular cones. A *critically scaled* interface is considered, in the sense that the amplitudes of the interface fluctuations and the central wavelength are of the same order. In this context, if the correlation length of the interface fluctuations and the beam width are of the same order, random specular components are observed, but no speckle component. The reflected and transmitted fields are confined to the specular cones. The situation with a correlation length smaller than the beam width leads to homogenization effects providing deterministic specular components similar to the case of a flat interface, but with effective initial conditions accounting for the scattering effects. However, in this situation, there are also relatively broad cones (containing the specular cones) where the wavefields form speckle patterns. The width of these cones is characterized by the ratio λ/l_c, where λ is the central wavelength and l_c the correlation length of the interface fluctuations. The two-point correlation functions for these speckle patterns are presented and exhibit self-averaging properties. Furthermore, we present a central limit theorem type result for the speckle patterns, showing that they can be modeled as Gaussian random fields. These descriptions allow the derivation of generalized Snell's laws of refraction and transmission depending on an effective scattering operator at the interface.

This chapter covers the results obtained in [7, 19] of the publication list on page 6.

Chapter 7

This chapter presents an aspect of mathematical biology related to metastatic spreading. This work has been conducted in collaboration with Niklas Hartung during his Ph.D. program, at the Institut of Mathematics of Marseille, under the supervision of Guillemette Chapuisat and Florence Hubert (see [11] in the publication list on page 6).

Although the detection of metastases radically influences the prognosis and treatment decisions for cancer patients, the presence of clinically undetectable micrometastases hampers the consistent classification of the disease as localized or metastatic. This chapter discusses mathematical modeling efforts that could help to estimate the metastatic risk in such a scenario. We focus on two approaches both accounting for secondary metastatic emissions, that is the ability for metastases to emit some metastases themselves. The first one relies on a deterministic framework to describe the micrometastatic state using a size-structured density function in a partial differential equation model. The second approach is based on a stochastic framework to describe metastatic emission events occurring at random times formalized through a cascade of Poisson processes. We highlight an inherent crosslink between the stochastic and deterministic frameworks and discuss its implication for assessing metastatic risk post-surgery.

The remaining of the manuscript consists in providing more detail presentations of the results outlined in this introduction.

Chapter 1

Random perturbations with long-range correlations and nonlinear oscillators

It is well known that a properly scaled stochastic process with long-range correlations (or dependencies) converges to a fractional Brownian motion (fBm), whose Hurst index is determined by the rate at which the correlation function decays [152, 202, 203]. This result is known as *non-central* limit theorem. When the Hurst parameter is not $1/2$, the normalized limit of the noise has memory properties and is a non-Markovian process. An interesting example to illustrate how oscillatory behaviors effectively erase memory effects of random fluctuations is a stochastically forced nonlinear oscillator with 1 degree of freedom:

$$\ddot{x}(t) + f(x(t)) = \varepsilon V(t), \quad x_0 \in \mathbb{R}, \quad \dot{x}_0 = y_0 \in \mathbb{R}\,. \tag{1.1}$$

Here, $f\colon \mathbb{R} \to \mathbb{R}$ is a given smooth function, and V is a stochastic process with long-range correlations as defined precisely below. Our interest is here to study the asymptotic long-time behavior of x. This chapter is based on the results obtained in [14] of the publication list on page 6.

Although the rescaled noise converges to a fBm, a process that exhibits memory properties, the oscillatory behavior of the system has the ability to affect the memory properties of the random fluctuations, resulting in an effective diffusive behavior with no memory. The aim of this chapter is to provide a precise description of how the oscillatory behavior is able to erase all the memory of the random fluctuations. A similar question was investigated in [133] for a passive tracer advected by a periodic shear flow. In this case, it appears that there exists a parameter regime where the time-rescaled dynamics is Markovian, and the memory effect of the noise is erased. However, there is also a regime (namely the *very long-time* behavior when the Hurst index of the driving noise is larger than $1/2$) where the memory effect persists. In contrast, for the oscillator (1.1), the memory effect *never* persists, and the effective long-time statistical behavior is always Markovian. The main reason is that the oscillatory nature of the deterministic dynamics counterbalances the slowly decaying correlations, and kills the memory effects. To study (1.1) we cannot use directly the limit theorem for additive functionals of fBm's used by [133]. Instead, we recast (1.1) as a fast-slow system and use an approximation-diffusion framework.

To recast (1.1) as a stochastically perturbed Hamiltonian system, we first introduce the Hamiltonian

$$H(x, y) := \frac{1}{2}y^2 + \int_0^x f(s)\, ds\,, \tag{1.2}$$

so that, setting $X(t) := (x(t), y(t))^T = (x(t), \dot{x}(t))^T$, we have

$$\dot{X}(t) = \nabla^\perp H(X(t)) + \varepsilon\, V(t)\mathbf{e}_2, \qquad X(0) = \begin{pmatrix} x_0 \\ y_0 \end{pmatrix} \in \mathbb{R}^2, \tag{1.3}$$

with

$$\nabla^\perp := \begin{pmatrix} \partial_y \\ -\partial_x \end{pmatrix}, \qquad \text{and} \qquad \mathbf{e}_2 := \begin{pmatrix} 0 \\ 1 \end{pmatrix}.$$

Here, the Hamiltonian H is assumed to have exactly one non-degenerate critical point. To study the long-time behavior of this system, we consider the time rescaled process

$$X^\varepsilon(t) := X(t/\varepsilon^2),$$

satisfying

$$\dot{X}^\varepsilon(t) = \frac{1}{\varepsilon^2}\nabla^\perp H(X^\varepsilon(t)) + \frac{1}{\varepsilon}V\left(\frac{t}{\varepsilon^2}\right)\mathbf{e}_2\,, \qquad X_0^\varepsilon = X(0) = \begin{pmatrix} x_0 \\ y_0 \end{pmatrix} \in \mathbb{R}^2. \tag{1.4}$$

In the absence of noise (meaning that $V \equiv 0$), the process X^ε travels very fast along the level sets of the Hamiltonian. When V is a white-noise, the asymptotic behavior of X^ε is described through the averaging principle of Freidlin and Wentzell [71–73] by a diffusion process across these level sets. To capture this limiting behavior, the fast motion is filtered out by projecting X^ε onto the *Reeb graph* of the Hamiltonian. This has the effect of identifying all closed trajectories of the Hamiltonian system, where the fast motions take place, into single points. In this context it is convenient to describe X^ε through action-angle coordinates. The angular coordinate of X^ε evolves very fast providing no meaningful limit as $\varepsilon \to 0$. On the other hand, the action coordinate of X^ε exhibits a non-trivial limit as $\varepsilon \to 0$, which results from the interaction between the noise and the averaged angular coordinate. To study this behavior, the Hamiltonian itself is used as a proxy for the action coordinate and the convergence is obtained for $(H(X^\varepsilon))_\varepsilon$.

This chapter is organized as follows. Some examples of stochastic processes with long-range correlations are provided in Sect. 1.1. One them is used in several chapters of this manuscript. Sect. 1.2 describes how long-range dependencies are related to memory effects through fBm's and a *non-central* limit theorem. Finally, Sect. 1.3 describes how the memory properties of the noise are erased by the oscillatory behavior of the Hamiltonian system. The case of the quadratic Hamiltonian ($f(x) = x$) is presented as it provides explicit formulations and a simple understanding of the phenomena. For general Hamiltonian (1.2), action-angle coordinates are introduced as well as their corresponding approximation-diffusion theorem. From this result, the asymptotic diffusive behavior of $(H(X^\varepsilon))_\varepsilon$ is derived.

1.1 Random fluctuations with long-range correlations

A stationary random process V is said to have long-correlations if its two-point correlation function

$$R(t) := \mathbb{E}[V(t+t')V(t)] \qquad (t,t') \in \mathbb{R}\times\mathbb{R}$$

decays slowly enough at infinity, for instance

$$R(t) \underset{|t|\to\infty}{\sim} \frac{R_0}{|t|^\gamma} \qquad \text{with} \qquad \gamma \in (0,1], \tag{1.5}$$

to not be integrable, in the sense that

$$\int_0^\infty |R(t)|\,dt = \infty.$$

There exists several basic examples of continuous-time processes with long-range correlations that can be found in the literature (see [84,154] for instance). Two simple examples are the following: the fractional white-noise model corresponding to

$$V(t) = W_{\mathfrak{H}}(t) - W_{\mathfrak{H}}(t+l_c),$$

and the fractional Ornstein-Uhlenbeck model for which

$$V(t) = W_{\mathfrak{H}}(t) - \frac{1}{l_c}\int_{-\infty}^{z} e^{(y-t)/l_c} W_{\mathfrak{H}}(y)dy.$$

In these two examples, $W_{\mathfrak{H}}$ is a fBm with Hurst index $\mathfrak{H} \in (1/2,1)$, and the asymptotic behavior at infinity of their correlation functions is given by (1.5) with

$$\gamma = 2-2\mathfrak{H}, \qquad \text{and} \qquad R_0 = \mathfrak{H}(2\mathfrak{H}-1)l_c^2.$$

More sophisticated models can also be found in [154]. These two Gaussian models are convenient for an analysis based on moment techniques [15,66,99] or the rough-path theory [152,154]. When studying the asymptotic behaviors of certain randomly perturbed physical systems arising from the Schrödinger equation or the wave equation for instance, it is not always clear how these two approaches can be effectively applied. While the application of the moment technique may rely on purely technical aspects, the rough-path approach has to face the inherent infinite-dimensional nature of the functional spaces to which the solutions belong. Additionally the absence of a Hilbert-Schmidt structure in the PDE's further complicates the process of reducing the original problem to a finite-dimensional one. This latter aspect needs further investigations. Even for the simple oscillator presented in this chapter, a nonlinear Hamiltonian gives rise to an oscillatory behavior that needs to be expended over the infinite basis of Fourier modes. The resulting structure of the system involves a nonlinear relationship between the noise V with a degenerate term. This nonlinear relationship brings technical difficulties to apply both the moment technique or the rough-path approach. To address these technical difficulties, a specific definition of the random fluctuations is considered, exhibiting long-range correlations, but allowing the use of the perturbed-test-function method and the martingale approach [139]. These approaches can be applied together to handle non-necessarily Markovian noise, such as *mixing processes*. The noise we consider to apply this approach is obtained, as in [15], by super-imposing Ornstein-Uhlenbeck type processes written in the form

$$V(t) = \int_{-\infty}^{t} \int_{S} e^{-\mu|p|^{2\beta}(t-u)} \mathcal{B}(du, dp). \tag{1.6}$$

Here, $S \subseteq \mathbb{R}$ is a bounded symmetric open interval containing 0. Also, μ and β are positive constants, and $\mathcal{B}$ is a Gaussian random measure that is white in time and colored in space:

$$\mathcal{B}(du, dp) = \sqrt{2\mu\, r(p)}\, |p|^{\beta} \mathbf{1}_S(p)\, \xi(du, dp),$$

where ξ is a 2D Gaussian white noise, and $r\colon S \setminus \{0\} \to [0, \infty)$ is defined by

$$r(p) = \frac{\lambda(p)}{|p|^{2\alpha}}.$$

Here, $\lambda\colon S \to \mathbb{R}_+$ is a smooth bounded even function such that $\lambda(0) \neq 0$. The correlation function of V is therefore given by

$$R(t) = \int_S r(p) e^{-\mu|p|^{2\beta}|t|}\, dp, \tag{1.7}$$

so that the condition

$$\int_S r(p)\, dp \in (0, \infty),$$

that is

$$\alpha < \frac{1}{2},$$

is required for this correlation function to be well defined. This construction gives rise to the limit

$$\lim_{t\to\infty} t^{\gamma} R(t) = R_0,$$

where R_0 and γ are defined by

$$\gamma = \frac{1 - 2\alpha}{2\beta} \qquad \text{and} \qquad R_0 = \lambda(0) \int \frac{e^{-\mu|p|^{2\beta}}}{|p|^{2\alpha}}\, dp.$$

Long-range correlations for V are therefore obtained by assuming

$$2(\alpha + \beta) \geq 1.$$

In Fig. 1.1, we illustrate the difference of statistical behavior between long-range correlations and short-range correlations, the latter having an integrable two-point correlation function. From these pictures, one can observe that slowly decaying correlations produce longer excursions of the random trajectories, due to the persistence of the correlations, than for rapidly decaying correlations. In this latter case, the trajectories cannot really produce correlation patterns and look almost like the ones of a white-noise.

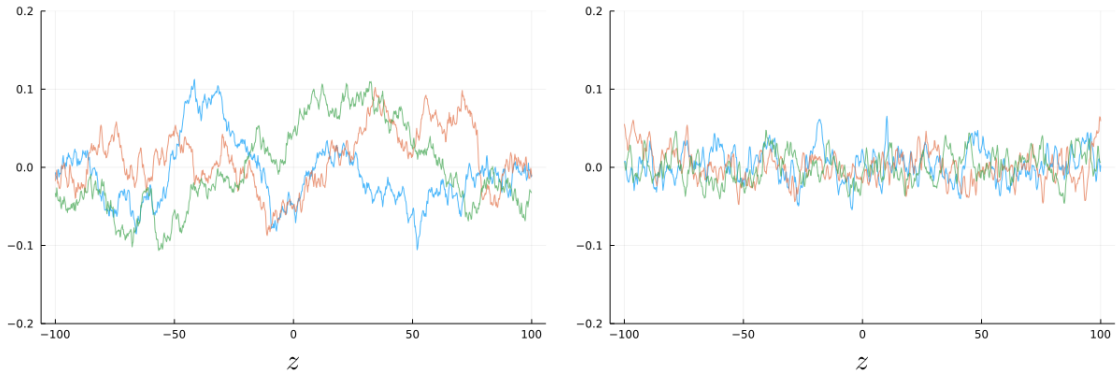

Fig. 1.1: Illustration of three realizations of the random process defined by (1.6) with long-range correlations for the left-picture, and short-range correlations for the right-picture. Here, $\mu = 1$, $\alpha = 1/4$, $a(p) = \mathbf{1}_{(-10,10)}(p)$, $\beta = 1/2$ (that is $\gamma = 1/2$) for the left-picture illustrating the long-range correlations, and $\beta = 1/6$ (that is $\gamma = 3/2$) for the right-picture illustrating short-range correlations.

1.2 A non-central limit theorem

It is known for quite some time that under long-range correlations the normalized integrated noise converges to a fBm [152, 202, 203]. A version of this result, known as non-central limit theorem, is the following.

Proposition 1.2.1 *Let V be a stationary Gaussian process with covariance function R given by*

$$R(t) = \frac{L(t)}{t^\gamma} \tag{1.8}$$

for some $\gamma \in (0,2)$, and a slowly varying function L at infinity[1]*. If $\gamma \in (1,2)$, we additionally suppose*

$$\int_0^\infty R(t)\, dt = 0\,. \tag{1.9}$$

Let

$$\sigma(\varepsilon) := \begin{cases} L(\varepsilon^{-2})^{1/2}\varepsilon^\gamma & \text{if} \quad \gamma \neq 1\,, \\ L(\varepsilon^{-2})^{1/2}\varepsilon|\ln(\varepsilon)|^{1/2} & \text{if} \quad \gamma = 1\,, \end{cases} \qquad \text{and} \qquad u^\varepsilon(t) := \frac{1}{\sigma(\varepsilon)} \int_0^t V\left(\frac{s}{\varepsilon^2}\right) ds\,.$$

Then, as $\varepsilon \to 0$, the family of processes $(u^\varepsilon)_\varepsilon$ converges in law in $\mathcal{C}(0,\infty)$ to $\sigma_{\mathfrak{H}} W_{\mathfrak{H}}$, where $W_{\mathfrak{H}}$ is a fractional Brownian motion with Hurst index $\mathfrak{H} = 1 - \gamma/2$, and

$$\sigma_{\mathfrak{H}}^2 := \begin{cases} \dfrac{1}{\mathfrak{H}|2\mathfrak{H}-1|} & \text{if} \quad \mathfrak{H} \neq \frac{1}{2}\,, \\ 1 & \text{if} \quad \mathfrak{H} = \frac{1}{2}\,. \end{cases}$$

Note that despite short-range correlations, the additional assumption (1.9) leads to a negatively correlated fBm with Hurst index $H < 1/2$. Note also that (1.9) is not compatible with the definition (1.6) in view of (1.7). Without this additional assumption, a standard invariance principle would applied with the scaling $\sigma(\varepsilon) = L(\varepsilon^{-2})^{1/2}\varepsilon$, and a standard Brownian motion as limiting process.

A more refined version of this result can be found in [154]. Under additional assumptions the limiting process can be a general Hermite process, in particular with non-Gaussian statistics. This is in contrast to processes with short-range correlations (or mixing properties) and the standard invariance principle where the limits inherently exhibit Gaussian statistics. As described below, when introducing oscillatory behaviors, the memory effects of the random fluctuations are lost and standard diffusion phenomena (memoryless Markov processes) emerge despite the memory effects of the system perturbations.

Note that the above result, is not exactly what is stated in the introduction. However, both are connected through the change of variable $\varepsilon \to \varepsilon^{1/(2-\gamma)}$.

[1] A function L is said to be slowly varying at infinity if for every $s > 0$ we have $L(st)/t \to 1$ as $t \to \infty$.

1.3 A randomly perturbed nonlinear oscillator

The remaining of this chapter discusses two results showing that even though the driving noise has memory properties, the time correlations are erased by the oscillatory dynamics of (1.4), and $(H(X^\varepsilon))_\varepsilon$ converges to a diffusion driven by standard Brownian motion (without memory). Two scenarios are discussed below. The first one concerns a quadratic Hamiltonian, for which explicit formulations can be carried out, highlighting explicitly the role of the oscillations in the loss of memory properties. In this particular case, the limiting diffusion is a scaled version of a 2D square Bessel process. The second scenario extends this result to more general smooth Hamiltonian with exactly one non-degenerate critical point.

1.3.1 Diffusive limit for a quadratic Hamiltonian

For a quadratic Hamiltonian the level sets are simply circles centered at 0 and whose radii depend on the associated energy. This simple characterization of the level sets provides a simple description of the role played by the oscillations of the oscillator. The first result is as follows.

Proposition 1.3.1 *Let H be the quadratic Hamiltonian,*

$$H(X) = \frac{|X|^2}{2}, \tag{1.10}$$

for $X = (x, y) \in \mathbb{R}^2$, and suppose that the noise V is a stationary Gaussian process whose covariance function is of the form (1.8)*. For $\gamma \in (0, 1]$, we further assume that L has the slow increase property*

$$\lim_{t\to\infty} \frac{L'(t)}{L(t)/t} = 0\,.$$

Then, the family $(H(X^\varepsilon))_\varepsilon$ converges in law to $H(W)$, as $\varepsilon \to 0$, where W is a 2D Brownian motion with $W_0 = X_0$ and 2×2 covariance matrix

$$D := \begin{pmatrix} \Gamma_c & 0 \\ 0 & \Gamma_c \end{pmatrix}, \qquad \textit{with} \qquad \Gamma_c := \int_0^\infty R(t)\cos(t)\,dt. \tag{1.11}$$

It is worth noticing that, even for $\gamma \in (0, 1]$, the coefficient Γ_c in (1.11) is well-defined since the cos function is periodic and mean zero. This resulting cos function is due to the quadratic shape of the Hamiltonian (1.10) and the resulting circular level sets. As a result, despite the nonintegrability of the correlation function and the memory effects, the diffusive (memoryless) limit is valid thanks to the oscillatory behavior of the system.

The Hamiltonian H being here rotationally invariant, Prop. 1.3.1 is based on a time-dependent rotation in space that prove convergence of $(H(X^\varepsilon))_\varepsilon$ by studying integrals of the form

$$\frac{1}{\varepsilon}\int_0^t V\Big(\frac{s}{\varepsilon^2}\Big)\cos\Big(\frac{s}{\varepsilon^2}\Big)ds \qquad \text{and} \qquad \frac{1}{\varepsilon}\int_0^t V\Big(\frac{s}{\varepsilon^2}\Big)\sin\Big(\frac{s}{\varepsilon^2}\Big)ds.$$

At the limit these processes provide a $2D$ standard Brownian motion with diagonal covariance matrix D. This result has also been obtained in [152] under slightly different assumptions, and generalized in [155].

To reiterate our main point, note that Prop. 1.3.1 corresponds to

$$H\left(X_0 + \frac{1}{\varepsilon^2}\int_0^t \nabla^\perp H(X^\varepsilon(s))\,ds + \frac{1}{\varepsilon}\int_0^t V\Big(\frac{s}{\varepsilon^2}\Big)\mathbf{e}_2\,ds\right) \underset{\varepsilon\to 0}{\Longrightarrow} H(W(t)), \tag{1.12}$$

in law in $\mathcal{C}(0, \infty)$. However, from Prop. 1.2.1, the noise term satisfies

$$\frac{1}{\sigma(\varepsilon)}\int_0^t V\Big(\frac{s}{\varepsilon^2}\Big)\,ds \underset{\varepsilon\to 0}{\Longrightarrow} \sigma_{\mathfrak{H}} W_{\mathfrak{H}}(t)\,,$$

for a fBm $W_{\mathfrak{H}}$ with Hurst index $\mathfrak{H}$. Interestingly, while $H(W)$ is a Markov process with no memory, $W_{\mathfrak{H}}$ is a non-Markovian process with memory. Note further that:

- When $\gamma \in (0,1]$, we have $\varepsilon \ll \sigma(\varepsilon)$ and so the term $\frac{1}{\varepsilon}\int_0^t V(s/\varepsilon^2)\,ds$ appearing in (1.12) diverges as $\varepsilon \to 0$.
- On the other hand, when $\gamma \in (1,2)$, together with (1.9), we have this time $\sigma(\varepsilon) \ll \varepsilon$, and so the term $\frac{1}{\varepsilon}\int_0^t V(s/\varepsilon^2)\,ds$ vanishes.

In both cases, the oscillatory behavior of the Hamiltonian system contributes non-trivially by preventing from a blow up of the fluctuations when $\gamma \in (0,1]$, or enhancing the effects of the fluctuations for $\gamma \in (1,2)$.

1.3.2 Diffusive limit for the general Hamiltonian with one non-degenerate critical point

The case where the Hamiltonian (1.2) has exactly one non-degenerate critical point, but is not necessarily quadratic, is now discussed. As the orbits of the Hamiltonian are more complex, a more involved analysis is required. Using the action-angle coordinates, the role of the oscillatory behavior can still be highlighted though the angle variable, but in a more complex framework. In this case, for technical reasons discussed in Sect. 1.1, we need to work with the stationary Gaussian noise given by (1.6). The asymptotic behavior of $(H(X^\varepsilon))_\varepsilon$ can be described as follows.

Theorem 1.3.1 *Let $H\colon \mathbb{R}^2 \to \mathbb{R}$ be a smooth Hamiltonian with exactly one non-degenerate critical point at $(0,0)$, which satisfies (1.19) and (1.20) under the action-angle coordinates introduced below, and let V be the stationary Gaussian noise given by (1.6). Then*

$$H(X^\varepsilon) \underset{\varepsilon\to 0}{\Longrightarrow} \mathcal{X}, \tag{1.13}$$

in law in $\mathcal{C}(0,\infty)$, where $\mathcal{X}$ is a diffusion process driven by a standard Brownian motion, and infinitesimal generator

$$L := \frac{1}{2\Lambda(\mathcal{X})}\partial_{\mathcal{X}}(\Sigma(\mathcal{X})\partial_{\mathcal{X}})\,. \tag{1.14}$$

Here, the coefficients Λ and Σ are defined by

$$\Lambda(\mathcal{X}) := \oint_{\{H=\mathcal{X}\}} \frac{dl}{|\nabla H|}\,,$$

and

$$\Sigma(\mathcal{X}) := 2\int_0^\infty ds\, R(s) \oint_{\{H=\mathcal{X}\}} \partial_y H(\check{X}^{x,y}(s))\partial_y H(x,y)\frac{dl(x,y)}{|\nabla H(x,y)|}\,,$$

where $\check{X}^{x,y}$ is the solution to the unperturbed Hamiltonian system:

$$\partial_t \check{X}^{x,y}(t) = \nabla^\perp H(\check{X}^{x,y}(t)), \qquad \text{with} \qquad \check{X}^{x,y}(t=0) = (x,y)\,.$$

Thm. 1.3.1 follows immediately from the more general Thm. 1.3.2 below concerning a fast-slow system.

Let us make some comments on this result before diving into the ideas behind the proof. First of all, the main difference between Thm. 1.3.1, and the standard Freidlin-Wentzell theory [71] is in the coefficient Σ. In the present context, Σ involves an average of the term $\partial_y H(\check{X}^{x,y}(s))\partial_y H(x,y)$ along the level sets, with a shift of one factor to the point $\check{X}^{x,y}(s)$, while in [71] the coefficient Σ depends only on $(\partial_y H(x,y))^2$. This shifted average term plays the role of the cos function in (1.11) for the quadratic Hamiltonian, so that the diffusion coefficient is still well defined despite long-range correlations of the noise term. The reason for this modification, compared to [71], lies in the fact that the oscillations of the Hamiltonian system and the random fluctuations in (1.4) are strongly coupled in our case, they are both evolving on the scale $1/\varepsilon^2$, and fully interact with each. This strong interaction produces an effective diffusion coefficient involving the correlation of pairs of points belonging to the same orbit: $\partial_y H(\check{X}^{x,y}(s))$ and $\partial_y H(x,y)$. If the oscillatory behavior of the Hamiltonian system is slower than the random fluctuations, then their coupling is weak and the same generator as in [71] would be obtained. This dichotomy of limiting behaviors between strongly and weakly coupled setups is well-known in other approximation-diffusion limits of random differential equations with periodic components, (for

instance Thm. 6.4 and 6.5 in [70] can be compared). However, in the present chapter, the oscillations of the Hamiltonian system need to behave at the same scale as the random fluctuations, in other words the oscillations need to be strong enough, for the coefficient Σ to be well-defined.

When H is not quadratic, the convergence of $H(X^\varepsilon)$ cannot be reduced to Gaussian integrals as in Prop. 1.3.1, and so the proof of Thm. 1.3.1 is more involved. One way to analyze integrable Hamiltonian systems is to use a set of *action-angle coordinates*. These coordinates separate the slow and fast motion, and preserve the Hamiltonian structure. The Liouville-Arnold theorem [8, Sect. 50 pp. 279] asserts that there exists a symplectic canonical transformation $\varphi\colon X = (x, y) \mapsto (I, \theta) \in \mathbb{R}\times\mathbb{T}$, where the action variable I and the angle variable θ satisfy

$$K(I) = H(x, y) \qquad \text{and} \qquad \{I, \theta\} = 1\,,$$

where K is a smooth enough one variable increasing function such that $K(0) = 0$, $\{\cdot, \cdot\}$ stands for the standard Poisson bracket and is defined by

$$\{g, h\} := \partial_x g \partial_y h - \partial_y g \partial_x h$$

for our Hamiltonian system with one degree of freedom. In the action-angle coordinates the Hamiltonian is a function of the action coordinate alone. Writing $\varphi = (\varphi_1, \varphi_2)$ the action-angle coordinates are defined as

$$I(t) := I(X(t)) = \varphi_1(X(t))\,, \qquad \text{and} \qquad \theta(t) := \theta(X(t)) = \varphi_2(X(t))\,.$$

In the absence of random fluctuations (that is when $V \equiv 0$), the Hamiltonian system $\dot{X}(t) = \nabla^\perp H(X(t))$ becomes

$$\dot{I}(t) = 0 \qquad \text{and} \qquad \dot{\theta(t)} = \omega(I(t))\,, \qquad \text{with} \qquad \omega(I) = K'(I)\,.$$

In the presence of random fluctuations, the Hamiltonian system (1.3) now becomes

$$\dot{I}(t) = \varepsilon V(t) a(I(t), \theta(t)) \qquad \text{and} \qquad \dot{\theta}(t) = \omega(I(t)) + \varepsilon V(t) b(I(t), \theta(t))\,, \tag{1.15}$$

where

$$a = \mathbf{e}_2 \cdot \nabla\varphi_1 \circ \varphi^{-1} \qquad \text{and} \qquad b = \mathbf{e}_2 \cdot \nabla\varphi_2 \circ \varphi^{-1}.$$

As an example, when the Hamiltonian is quadratic the action-angle coordinates read

$$x = \sqrt{\frac{I}{\pi}} \cos\Big(2\pi\theta - \frac{\pi}{2}\Big) \qquad \text{and} \qquad y = \sqrt{\frac{I}{\pi}} \sin\Big(2\pi\theta - \frac{\pi}{2}\Big).$$

One can then see that the action variable is a multiple of the Hamiltonian,

$$K(I) = \frac{I}{2\pi} \qquad \text{and} \qquad \omega(I) = \frac{1}{2\pi},$$

while the angle variable corresponds to the angle of a trajectory describing a circle with period 1 in this case. One can show that the functions a and b are in this case of the form

$$a(I, \theta) = 2\sqrt{\pi I} \sin\Big(2\pi\theta - \frac{\pi}{2}\Big) \qquad \text{and} \qquad b(I, \theta) = \frac{1}{2\sqrt{\pi I}} \cos\Big(2\pi\theta - \frac{\pi}{2}\Big)\,.$$

In the general case, to study the long-time behavior of (1.15), we consider

$$I^\varepsilon(t) = I(t/\varepsilon^2) \qquad \text{and} \qquad \theta^\varepsilon(t) = \theta(t/\varepsilon^2),$$

satisfying

$$\dot{I}^\varepsilon(t) = \frac{1}{\varepsilon} V\Big(\frac{t}{\varepsilon^2}\Big) a(I^\varepsilon(t), \theta^\varepsilon(t)) \qquad \text{and} \qquad \dot{\theta}^\varepsilon(t) = \frac{\omega(I^\varepsilon(t))}{\varepsilon^2} + \frac{1}{\varepsilon} V\Big(\frac{t}{\varepsilon^2}\Big) b(I^\varepsilon(t), \theta^\varepsilon(t))\,, \tag{1.16}$$

with $I^\varepsilon(0) = I_0$ and $\theta^\varepsilon(0) = \theta_0$. As illustrated in Prop. 1.3.1 with the cos function in Γ_c, a key feature to handle the long-range correlations in the asymptotic analysis is the mean-zero property in θ for a and b. In fact, if the system possesses a Fourier mode of order zero, that is with no oscillatory

behavior, a noise with long-range correlations will charge this component and cause the system to blow up as $\epsilon \to 0$. Due to the symplectic property of the transformation φ,

$$a(I,\theta) = -\partial_\theta \varphi_1^{-1}(I,\theta)$$

is clearly mean-zero with respect to θ as being the derivative of a periodic function, but regarding b it is not as clear. Following the approach of [78], the fast and slow component of the angular variable are separated, and θ^ε is split into two parts,

$$\theta^\varepsilon = \psi^\varepsilon + \tau^\varepsilon.$$

Here, we set

$$\dot\tau^\varepsilon(t) = \frac{\omega(I^\varepsilon(t))}{\varepsilon^2} + \frac{1}{\varepsilon} V\Big(\frac{t}{\varepsilon^2}\Big)\big\langle b(I^\varepsilon(t),\cdot)\big\rangle \tag{1.17}$$

with initial condition $\tau^\varepsilon(0) = 0$, and

$$\langle g\rangle := \int_0^1 g(\theta)\, d\theta\,.$$

Regarding the slow motion variables $(I^\varepsilon, \psi^\varepsilon)$, the system (1.16) becomes

$$\dot I^\varepsilon(t) = \frac{1}{\varepsilon} v\Big(\frac{t}{\varepsilon^2}\Big) A(I^\varepsilon(t),\psi^\varepsilon(t),\tau^\varepsilon(t)) \qquad \text{and} \qquad \dot\psi^\varepsilon(t) = \frac{1}{\varepsilon} V\Big(\frac{t}{\varepsilon^2}\Big) B(I^\varepsilon(t),\psi^\varepsilon(t),\tau^\varepsilon(t)) \tag{1.18}$$

with

$$A(I,\psi,\tau) := a(I,\psi+\tau) \qquad \text{and} \qquad B(I,\psi,\tau) := b(I,\psi+\tau) - \big\langle b(I,\cdot)\big\rangle\,,$$

which are both mean-zero with respect to τ. The above equations are coupled with the initial conditions $I^\varepsilon(0) = I_0$, and $\psi^\varepsilon(0) = \theta_0$.

Thm. 1.3.2 below obtains the limiting behavior of (1.18) as $\epsilon \to 0$ under the following assumptions on K:

- The function K is smooth, and

$$\inf_{I\geq 0} K'(I) = \inf_{I\geq 0} \omega(I) > \omega_0 > 0, \tag{1.19}$$

  for some strictly positive number ω_0;

- There exists $r > 0$, and positive constants $c_{1,r}$, $c_{2,r} > 0$, such that for any $I \in (0,r)$

$$c_{1,r} I \leq K(I) \leq c_{2,r} I \qquad \text{and} \qquad |\omega'(I)| \leq \frac{c_{2,r}}{I}\,. \tag{1.20}$$

These conditions imply that $K(0) = 0$ and that K is an increasing function in I. These requirements are not too restrictive as any Hamiltonian satisfies (1.19) and (1.20) near non-degenerate critical points.

Theorem 1.3.2 *Assuming* (1.19) *and* (1.20)*, the family* $(I^\varepsilon, \psi^\varepsilon)_\varepsilon$*, defined by* (1.17)–(1.18)*, converges in law in* $\mathcal{C}([0,\infty),\mathbb{R}^2)$*, as* $\varepsilon \to 0$*, to a diffusion process* $(I(t),\psi(t))_{t\geq 0}$ *where* $(I_t)_{t\geq 0}$ *is the unique weak solution to the SDE*

$$\begin{aligned} dI(t) = &\int_0^1 a(I(t),\tau)\, dW(t,I(t),\tau)\, d\tau \\ &+ \Big[\int_0^\infty R(s) \int_0^1 \partial_I\big(a(I,\tau+\omega(I)s)\big)_{|I=I(t)} a(I(t),\tau) \\ &\qquad + a(I(t),\tau+\omega(I(t))s)\partial_I a(I(t),\tau)\, d\tau\, ds\Big]\, dt\,, \end{aligned}$$

with initial condition $I(0) = I_0$*. Here,* W *is a real valued Brownian field with covariance function*

$$\begin{aligned} \mathbb{E}[W(t_1,y,\phi_1)W(t_2,y,\phi_2)] = t_1 \wedge t_2 &\int_0^\infty R(s) \\ &\times \int_0^1 \phi_1(\tau+\omega(y)s)\phi_2(\tau) + \phi_1(\tau)\phi_2(\tau+\omega(y)s)\, d\tau\, ds\,, \end{aligned}$$

for any $\phi_1, \phi_2 \in L^2_0(\mathbb{T})$ *where*

$$L^2_0(\mathbb{T}) := \left\{ \phi \in L^2(\mathbb{T}) : \langle \phi \rangle = 0 \right\}.$$

Also, we have

$$\begin{aligned} d\psi(t) = \int_0^1 b(I(t),\tau)\, dW(t, I(t), \tau)\, d\tau \\ + \Big[\int_0^\infty R(s) \int_0^1 \partial_I \big(b(I, \tau + \omega(I)s) \big)_{|I=I(t)} a(I(t), \tau) \\ + b(I(t), \tau + \omega(I(t))s) \partial_I a(I(t), \tau)\, d\tau\, ds \Big] dt\,, \end{aligned}$$

with $\psi(0) = \theta_0$.

Note that the action variable I does not depend on the slow angular motion ψ. However, the distribution of ψ is completely determined by the motion of the action variable I and the Brownian field.

The proof of Thm. 1.3.1 follows from a direct application of the Itô formula applied to the limiting diffusion process I.

For the quadratic Hamiltonian, stochastic differential equations for $(I(t))_{t\geq 0}$ and $(\psi(t))_{t\geq 0}$ can be directly derived leading to

$$dI_t = 2\sqrt{mI_t} dB^1_t + 2m\, dt \qquad \text{and} \qquad d\psi_t = \frac{m}{2\pi\sqrt{I_t}}\, dB^2_t,$$

with

$$m = \pi \int_0^\infty R(u) \cos(u)\, du\,,$$

and where B^1 and B^2 are two independent standard Brownian motions. One can easily remark that $(I_t/m)_{t\geq 0}$ is a 2D squared Bessel process, so that $(I_t/2\pi)_{t\geq 0}$ has the same law as $(|W_t|^2/2)_{t\geq 0}$, for W being a 2D Brownian motion with covariance matrix (1.11). Then, we recover the result of Prop. 1.3.1, but we also access to the effective behavior of the slow component of the angle variable.

1.4 Perspectives

The present analysis, which leads to diffusion behaviors, relies on the perturbed-test-function technique together with a martingale approach, limiting the class of noises that can be considered. It can be expected to extend the class of noise by the use of the more general, but more involved, rough path framework [74,144]. Further investigations are required in this direction in order to overcome the technical difficulty of the dimensionality as well as dealing with nonlinear relations involving the noise. In the present context, these mentioned nonlinear relations can be seen in (1.18) together with (1.17) where the blowing term $V(t/\varepsilon^2)/\varepsilon$ is involved. The exact same difficulty is observed for the wave propagation problem discussed in Sect. 3.3 of Chap. 3. At present, we are only able to analyze the scenario where the Hamiltonian is smooth with exactly one non-degenerate critical point. The Reeb graph of such Hamiltonian is simply the half line, and the limiting process in Thm. 1.3.1 is a diffusion on the half line. For general Hamiltonians, Reeb graph may have multiple vertices, and the limiting process should be a diffusion on this Reeb graph. When the driving noise is a standard Brownian motion (as in the Freidlin-Wentzell theory), this diffusion is characterized through its generator on each edge of the Reeb graph, and certain gluing conditions on the vertices. While the proofs in the Freidlin-Wentzell theory rely heavily on the Markov property, and do not apply to our situation, the form of the infinitesimal generator (1.14) is similar to that in [71, Eq. (1.8)]. As a result, similar gluing conditions are expected in our context. Explicitly, for a sufficiently general class of Hamiltonians, we expect that the process $(H(X^\varepsilon))_\varepsilon$ converges in law to a diffusion process on the Reeb graph. The generator of this diffusion should be

$$L_j h_j(\mathcal{X}) = \frac{1}{2\Lambda_j(\mathcal{X})} \partial_{\mathcal{X}} (\Sigma_j(\mathcal{X}) \partial_{\mathcal{X}} h_j)$$

on each edge I_j. Considering $\mathcal{C}_j(\mathcal{X})$ the connected components of the level set $\{H = \mathcal{X}\}$ corresponding to a point $\mathcal{X} \in I_j$, Σ_j and Λ_j should be

$$\Sigma_j(\mathcal{X}) = 2 \int_{u=0}^{\infty} du\, R(u) \oint_{C_j(\mathcal{X})} \partial_y H(\check{X}_u^{x,y}) \partial_y H(x,y)\, \frac{dl(x,y)}{|\nabla H(x,y)|},$$

and

$$\Lambda_j(\mathcal{X}) = \oint_{C_j(\mathcal{X})} \frac{dl(x,y)}{|\nabla H(x,y)|}\,.$$

To describe the gluing conditions on the vertices, consider an interior vertex O_k corresponding to the saddle point $(\mathbf{x}_k, \mathbf{y}_k)$ and the level set $\{H = \mathcal{X}_k\}$, at which the collection of edges $\{I_j\}$ meet. Now define

$$\beta_{kj} = \lim_{\mathcal{X} \to \mathcal{X}_k} C_j(\mathcal{X})\,,$$

where the limit is taken along the edge I_j. The gluing condition at the vertex O_k can then be written as

$$\sum_{j:\, I_j \sim O_k} \pm \beta_{kj}\, h_j'(H(\mathbf{x}_k, \mathbf{y}_k)) = 0\,,$$

where the sign before β_{kj} is positive if $\mathcal{X} > \mathcal{X}_k$ along the edge I_j, and negative if $\mathcal{X} < \mathcal{X}_k$ along the edge I_j.

Chapter 2

Random Schrödinger equation with long-range correlations

The Schrödinger equation with a time-dependent random potential has been studied for a long time [17, 64–66, 115, 193], with a particular interest for applications in wave propagation in random media under the so-called paraxial (or parabolic) approximation [11, 18, 34, 52, 80, 87, 151, 196, 201]. The paraxial approximation allows a simplified treatment of wave propagation phenomena at both the theoretical and numerical point of views. The main idea is to provide an approximation of a solution u to the scalar wave equation

$$\Delta u - \frac{1}{c^2(z,\mathbf{x})}\partial_{tt}^2 u = 0 \qquad (t,z,\mathbf{x}) \in \mathbb{R}\times\mathbb{R}\times\mathbb{R}^2,$$

with

$$\frac{1}{c^2(z,\mathbf{x})} = \frac{1}{c_0^2}(1+V(z,\mathbf{x})),$$

where $\Delta = \partial_{zz}^2 + \Delta_{\mathbf{x}}$ is the Laplacian operator, and V is a mean-zero random field describing fluctuations of the wave-speed profile around its background value c_0.

Considering the z-axis as the main propagation axis, that is along which the wave is mainly propagating, the paraxial approximation consists in approximating u by

$$u(t,z,\mathbf{x}) \simeq \int \phi_\omega(z,\mathbf{x}) e^{i\omega(z/c_0-t)} d\omega.$$

From this representation, the wave is assumed to propagate in only one direction along the z-axis, neglecting the backscattering phenomena. This latter aspect is the key point that simplifies theoretical and numerical treatments of wave propagation in random media. The envelop ϕ_ω therefore satisfies the following random Schrödinger equation

$$ik_\omega \partial_z \phi_\omega + \frac{1}{2}\Delta_{\mathbf{x}}\phi_\omega + k_\omega^2 V(z,\mathbf{x})\phi_\omega = 0, \tag{2.1}$$

with wavenumber $k_\omega = \omega/c_0$. In this Schrödinger equation, the time variable is played by the z-variable of the main propagation axis on which the random fluctuation V depends. A rigorous treatment of this approximation will be discussed in Sect. 3.2 of Chap. 3.

The random Schrödinger equation involving a time-dependent potential,

$$i\partial_t\phi + \frac{1}{2}\Delta_{\mathbf{x}}\phi - \sqrt{\varepsilon}V(t,\mathbf{x})\phi = 0 \qquad (t,\mathbf{x}) \in (0,\infty)\times\mathbb{R}^d, \tag{2.2}$$

have been considered in [14, 17] to derive a radiative transfer model under short-range correlations, but also in [15] under both short-range and long-range correlations. In this latter work the asymptotic behavior of the wave function itself is explored. Under long-range correlations the authors prove a non-central limit theorem type result (described below) using a moment technique. This chapter

presents other scaling regimes exhibiting non-trivial effects under long-range correlations. In contrast with Chap. 1, where no spatial effect can take place, the multiscale properties of the potential w.r.t. the variable $\mathbf{x}$ enable intermediate non-trivial regimes from the non-central type result up to the radiative transfer regime under the so-called semi-classical limit. This chapter is based on the results obtained in [3, 4, 6] of the publication list on page 6.

To highlight the effective phenomena produced by long-range correlations over a range of scaling regimes, we introduce the time and space scaling:

$$t \to t/\varepsilon^s \qquad \text{and} \qquad \mathbf{x} \to \mathbf{x}/\varepsilon^s, \qquad s \in (0,1],$$

where s represents the propagation scale parameter. The wave function associated to this scaling is

$$\phi_\varepsilon(t,\mathbf{x}) := \phi\Big(\frac{t}{\varepsilon^s}, \frac{\mathbf{x}}{\varepsilon^s}\Big),$$

with corresponding Schrödinger equation

$$i\varepsilon^s \partial_t \phi_\varepsilon + \frac{\varepsilon^{2s}}{2}\Delta_{\mathbf{x}}\phi_\varepsilon - \sqrt{\varepsilon} V\Big(\frac{t}{\varepsilon^s}, \frac{\mathbf{x}}{\varepsilon^s}\Big)\phi_\varepsilon = 0, \qquad \text{and} \qquad \phi_\varepsilon(0,\mathbf{x}) = \phi_0(\mathbf{x}/\varepsilon^{s-s_c}). \tag{2.3}$$

The parameter s_c accounts for low frequency oscillations of the wave function. Such low frequencies are the key points when describing how the loss of coherence affects the wave function over the different propagation scales. Note that the standard semi-classical limit holds for $s = 1$ and $s_c = 0$. An anisotropy parameter $\varrho \in [0, 1)$ can also be added into the fluctuation model,

$$\varepsilon^{\frac{1-\varrho}{2}} V\Big(\frac{t}{\varepsilon^{s+\varrho}}, \frac{\mathbf{x}}{\varepsilon^s}\Big).$$

Recalling that for the paraxial approximation the time variable t plays the role of the main propagation axis (see (2.1)), $\varrho > 0$ corresponds to faster fluctuations along this axis than in the transverse direction. In other words, this condition corresponds to a statistical anisotropy of the medium fluctuations.

The organization of this chapter is as follows. After a brief description of the random potential under consideration in Sect. 2.1, the different non-trivial regimes describing the loss of coherence are presented. Sect. 2.2 reviews the result obtained in [15] regarding the onset of the random phase modulation. In Sect. 2.3 a scaled Wigner transform is introduced. Its scaling enables the description of the loss of coherence, in Sect. 2.4 and 2.5, over different scaling regimes and how this loss of coherence propagates from the large scales supported by the wave function to the finer ones. Finally, Sect. 2.6 introduces a time-splitting scheme that are able to capture statistically all the scaling regimes we describe under long-range correlations.

2.1 The random potential

Throughout this chapter the random potential is defined following the lines of Chap. 1 (see also [15]) by

$$V(t,\mathbf{x}) := \int_{-\infty}^{t}\int_S e^{i\mathbf{p}\cdot\mathbf{x}} e^{-\mu|\mathbf{p}|^{2\beta}(t-u)} \mathcal{B}(du, d\mathbf{p}),$$

where $S \subseteq \mathbb{R}^d$ is a bounded symmetric open set containing 0. Here, μ and β are constants, and $\mathcal{B}$ is a Gaussian random measure which is white in time and colored in space:

$$\mathcal{B}(du, d\mathbf{p}) := \sqrt{2\mu\, r(\mathbf{p})}\, |\mathbf{p}|^\beta \mathbf{1}_S(\mathbf{p})\, \xi(du, d\mathbf{p}),$$

where ξ is a $\mathbb{R}^{d+1}$ Gaussian white noise, and $r\colon S \setminus \{0\} \to [0,\infty)$ is defined again by

$$r(\mathbf{p}) := \frac{\lambda(\mathbf{p})}{|\mathbf{p}|^{d-1+2\alpha}}. \tag{2.4}$$

Here, $\lambda\colon S \to \mathbb{R}_+$ is a smooth bounded even function such that $\lambda(0) \neq 0$. The correlation function of V is this time given by

$$R(t,\mathbf{x}) := \mathbb{E}[V(t+s,\mathbf{x}+\mathbf{y})V(s,\mathbf{y})] = \int_S e^{i\mathbf{p}\cdot\mathbf{x}} r(\mathbf{p}) e^{-\mu|\mathbf{p}|^{2\beta}|t|}\, d\mathbf{p}.$$

Again, the condition

$$\alpha < \frac{1}{2}$$

is required for the process and correlation function to be well defined. In this chapter the condition $\beta \in (0, 1/2]$ is also required for technical reasons.

One can observe from (2.4) that the random field $V(t)$, for any fixed time t, exhibits long-range correlations in space. In fact, the function r is singular at $\mathbf{p} = 0$ (therefore unbounded), so that its inverse Fourier transform is not integrable. However, for any fixed $\mathbf{x} \in \mathbb{R}^d$,

$$\lim_{t\to\infty} t^\gamma R(t, \mathbf{x}) = R_0,$$

where

$$\gamma = \frac{1-2\alpha}{2\beta} \qquad \text{and} \qquad R_0 = \lambda(0) \int \frac{e^{-\mu|\mathbf{p}|^{2\beta}}}{|\mathbf{p}|^{d-1+2\alpha}}\, d\mathbf{p}.$$

Long-range correlations (in time) are therefore considered here by assuming

$$2(\alpha + \beta) > 1,$$

but short-range correlations (still in time) can also be obtained by assuming $2(\alpha + \beta) < 1$.

Note that Eq. (2.2) is a time evolution problem, so we have to take care about the statistical properties of the random potential V w.r.t. the temporal variable. It is worth mentioning that if V is assumed to have rapidly decaying correlations in time, $(V(t_1), V(t_2))$ exhibits now rapidly decaying cross-spatial correlations, and the evolution problem (2.2) behaves like in the short-range case addressed in [15]. As a result, even if at each fixed time the spatial correlations are slowly decaying, the resulting time evolution problem behaves as if the random potential has rapidly decaying correlations in all variables.

As in Sect. 1.3.2 of Chap. 1, this specific form for V is considered to carry out the asymptotic analysis.

2.2 Phase modulation

As in Chap. 1, a nontrivial scaling regime, corresponding to the non-central limit theorem, can be exhibited. In the context of this chapter, it is given by the following result (provided by [15, 93]) that can be proved through a moment technique.

Theorem 2.2.1 *Denoting*

$$\mathfrak{H} := 1 - \gamma/2 \in (1/2, 1) \qquad \text{and} \qquad \mathfrak{H}_\varrho := \frac{\mathfrak{H}}{1 - \varrho\Big(\frac{\alpha+\beta-1/2}{\beta}\Big)}, \tag{2.5}$$

for $\varrho \in [0, 1)$, the process $\widehat{\xi}_{\mathfrak{H}_\varrho,\varepsilon}(t, \mathbf{k})$ defined by

$$\widehat{\xi}_{\mathfrak{H}_\varrho,\varepsilon}(t, \mathbf{k}) := \frac{1}{\varepsilon^{d\,s}} \widehat{\phi}_\varepsilon\Big(t, \frac{\mathbf{k}}{\varepsilon^{s-s_c}}\Big) e^{i|\mathbf{k}|^2 t/(2\varepsilon^{s-2s_c})}, \quad \text{with} \quad s = 1/(2\mathfrak{H}_\varrho), \tag{2.6}$$

converges in law to

$$\widehat{\xi}(t, \mathbf{k}) = \widehat{\phi}_0(\mathbf{k}) \exp\Big(i\sqrt{D(\alpha, \beta, \mathbf{k})} W_{\mathfrak{H}}(t)\Big),$$

for each $t \geq 0$ and $\mathbf{k} \in \mathbb{R}^d$. Here, $W_{\mathfrak{H}}$ is a standard fractional Brownian motion with Hurst index $\mathfrak{H}$,

$$D(\alpha, \beta, \mathbf{k}) := \frac{a(0)}{(2\pi)^d \mathfrak{H}(2\mathfrak{H}-1)} \int_0^\infty d\rho \frac{e^{-\mu\rho}}{\rho^{2\alpha-1}} \int_{\mathbb{S}^{d-1}} dS(u) e^{i|\mathbf{k}|\rho u\cdot \mathbf{e}_1}, \tag{2.7}$$

if $\beta = 1/2$, $\varrho = 0$, $s_c = 0$, and

$$D(\alpha, \beta, \mathbf{k}) := D(\alpha, \beta) = \frac{a(0)\Omega_d}{(2\pi)^d \mathfrak{H}(2\mathfrak{H}-1)} \int_0^\infty d\rho \frac{e^{-\mu\rho^{2\beta}}}{\rho^{2\alpha-1}}, \tag{2.8}$$

otherwise, where Ω_d stands for the surface area of the unit sphere in $\mathbb{R}^d$, and $\mathbf{e}_1 \in \mathbb{S}^{d-1}$.

In this result, the term $\widehat{\xi}_{\mathfrak{H}_\varrho,\varepsilon}$ is scaled according to the initial condition $\phi_\varepsilon(t=0,\mathbf{x}) = \phi_0(\mathbf{x}/\varepsilon^{s-s_c})$. The resulting highly-oscillating behavior of the solution ϕ_ε is filtered out through the term $e^{i|\mathbf{k}|^2 t/(2\varepsilon^{s-2s_c})}$. As a result, $\widehat{\xi}_{\mathfrak{H}_\varrho,\varepsilon}$ exhibits mainly an effective random behavior through the term $\exp(i\sqrt{D(\alpha,\beta,\mathbf{k})}W_{\mathfrak{H}}(t))$, corresponding to a random phase modulation.

As described in Chap. 1, when the system propagates over longer time scales, other effective phenomena can be observed. Over longer propagation scales $s > 1/(2\mathfrak{H}_\varrho)$ such phase modulations oscillate fast enough to affect the coherence of the wave function. To understand how these phenomena take place a properly scaled Wigner transform and initial conditions are considered.

2.3 The Wigner transform

To highlight the loss of coherence effects on the wave function ϕ_ε, we can consider an initial conditions $\phi_{0,\varepsilon}$, for (2.3), of the form:

$$\phi_{0,\varepsilon}(\mathbf{x}) = \phi_0(\mathbf{x})\exp(i\zeta\cdot\mathbf{x}/\varepsilon^{s-s_c}). \tag{2.9}$$

This initial condition represents a quasi-plane wave with direction ζ, and slowly varying envelop ϕ_0. The plane wave is slowly varying for $s_c = s$, and highly oscillating when $s_c < s$. In this latter case self-averaging effects take place and the loss of coherence mechanism will be deterministic. It is worth mentioning that the spatial frequency of the initial condition ($\sim \varepsilon^{-(s-s_c)}$) is low compared to the one of the random fluctuations ($\sim \varepsilon^{-s}$). For random media with rapidly decaying correlations, such low spatial frequency sources do not interact with the random medium, and provide trivial limits. However, they do interact with slowly decorrelating random media and provide nontrivial limits. Due to technical difficulties in the asymptotic analysis, it is convenient to consider the direction ζ as being randomly distributed, according to some probability law $\nu(d\zeta)$ over some space $U \subset \mathbb{R}^d$, in order to provide a rigorous derivation of the self-averaging effects.

The loss of coherence phenomena are analyzed through the following scaled Wigner transform

$$\begin{aligned} W_\varepsilon(t,\mathbf{x},\mathbf{k}) &:= \frac{1}{(2\pi)^d}\int_{\mathbb{R}^d\times U} d\mathbf{y}\nu(d\zeta)e^{i\mathbf{k}\cdot\mathbf{y}}\phi_\varepsilon\Big(t,\mathbf{x}-\varepsilon^{s-s_c}\frac{\mathbf{y}}{2},\zeta\Big)\overline{\phi_\varepsilon\Big(t,\mathbf{x}+\varepsilon^{s-s_c}\frac{\mathbf{y}}{2},\zeta\Big)} \\ &= \frac{1}{(2\pi)^d}\int_{\mathbb{R}^d\times U} d\mathbf{y}\nu(d\zeta)e^{i\mathbf{k}\cdot\mathbf{y}}\phi\Big(\frac{t}{\varepsilon^s},\frac{\mathbf{x}}{\varepsilon^s}-\frac{\mathbf{y}}{2\varepsilon^{s_c}},\zeta\Big)\overline{\phi\Big(\frac{t}{\varepsilon^s},\frac{\mathbf{x}}{\varepsilon^s}+\frac{\mathbf{y}}{2\varepsilon^{s_c}},\zeta\Big)}, \end{aligned}$$

The terminology *loss of coherence* refers to diffusion phenomena through the momentum variable $\mathbf{k}$. The Wigner transform can be seen as the Fourier transform of the two-point correlation function of the wave function, and where $s_c \in [0,s]$ corresponds to a spatial correlation parameter. This parameter captures the evolution of the degree of correlation of the wave function. We refer to Fig. 2.1 for some illustrations. Let us note that the cases $s_c < s$ study the local loss of coherence, while the case $s = s_c$ study the nonlocal loss of coherence. As we will see, for a given propagation scale parameter s the loss of coherence of the wave field ϕ_ε can be observed at a particular spatial correlation parameter s_c. The larger the propagation scale parameter is the shorter the correlation scale parameter s_c is. In other words, depending on the propagation time and distance we adjust the spacial correlation scale to exhibit the loss of coherence. It appears that as the wave function propagates over longer scales, the correlation scales affected by the random fluctuations become smaller.

The developments of this chapter are based on the following equation satisfied by the Wigner transform,

$$\begin{aligned} &\partial_t W_\varepsilon(t,\mathbf{x},\mathbf{k}) + \varepsilon^{s_c}\mathbf{k}\cdot\nabla_{\mathbf{x}}W_\varepsilon(t,\mathbf{x},\mathbf{k}) = \\ &\qquad \frac{\varepsilon^{(1-\varrho)/2-s}}{(2\pi)^d i}\int_{\mathbb{R}^d}\widehat{V}\Big(\frac{t}{\varepsilon^{s+\varrho}},d\mathbf{p}\Big)e^{i\mathbf{p}\cdot\mathbf{x}/\varepsilon^s}\Big(W_\varepsilon\Big(t,\mathbf{x},\mathbf{k}-\frac{\mathbf{p}}{2\varepsilon^{s_c}}\Big)-W_\varepsilon\Big(t,\mathbf{x},\mathbf{k}+\frac{\mathbf{p}}{2\varepsilon^{s_c}}\Big)\Big). \end{aligned} \tag{2.10}$$

If $V \equiv 0$, the Wigner transform is simply given by $W_\varepsilon(t,\mathbf{x},\mathbf{k}) = W_\varepsilon(t=0,\mathbf{x}-\varepsilon^{s_c}t\mathbf{k},\mathbf{k})$, the momentum of W_ε is preserved during the propagation, that is there is no loss of coherence. For nonnull random fluctuations, the radiative transfer equation (2.10) describes the loss of coherence of the function ϕ_ε through the random integral operator. However, depending on the scaling under consideration, this operator can be of negligible effect, and no loss of coherence can be observed. For example, when considering the correlation scale $s_c = 0$, no loss of coherence can be observed before $s = 1$ (semi-classical limit). Also, the dispersion term $\mathbf{k}\cdot\nabla_{\mathbf{x}}$ is of order ε^{s_c}, so that dispersion is only capture for $s_c = 0$.

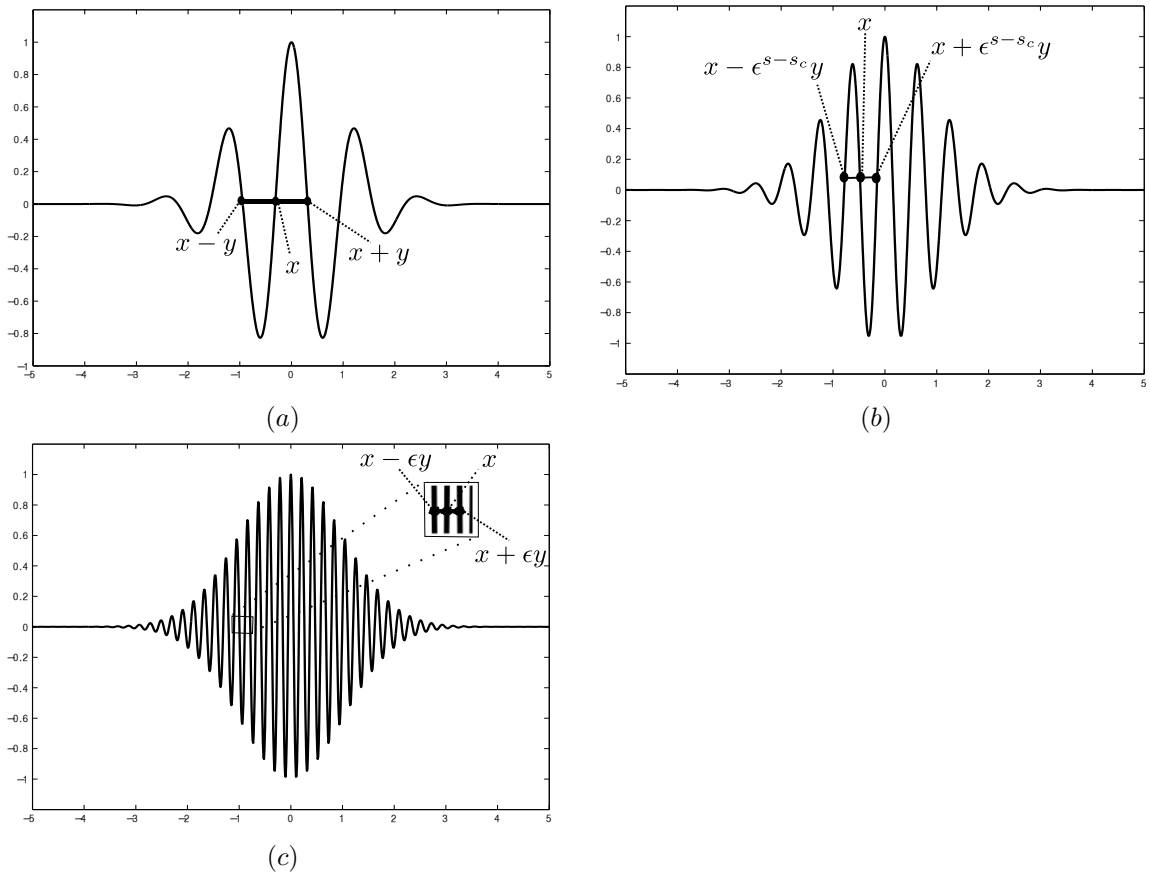

Fig. 2.1: Illustration of the initial condition (2.9). (a) and (b) represent low spatial frequency initial conditions. (a) represents the case $s_c = s$, and (b) represents the case $s_c < s$. (c) represents the case $s_c = 0$ and $s = 1$ corresponding to the radiative transfer regime.

2.4 Loss of coherence

As described in Thm. 2.4.2, Thm. 2.4.1, and Thm. 2.5.1 below, at a given propagation scale s, the corresponding spatial correlation parameter is given by

$$s_c = \frac{1-s}{\theta}, \tag{2.11}$$

with

$$\theta = 2(\alpha+\beta) - 1 \in (0,1), \tag{2.12}$$

so that for $s_c \leq s$ we have

$$\frac{1}{2\mathfrak{H}_\varrho} \leq \frac{1}{1+\theta} \leq s.$$

As a result, no loss of coherence can be observed before the propagation scale $s = 1/(1+\theta)$, which is larger than the propagation scale to observe the onset of the phase modulation. This relation holds true for any spatial correlation parameter $s_c \leq s$. Furthermore, Eq. (2.11) expresses how the spatial correlation scale decreases as the propagation scale increases.

The case $s = s_c = 1/(1+\theta)$ corresponds to the first effects happening after the onset of the random phase modulation, and they hold on the envelop ϕ_0 itself and not at a local level. These effects can be described as follows.

Theorem 2.4.1 *For either $\varrho > 0$ or $\beta < 1/2$, and*

$$s_c = s = \frac{1}{1+\theta},$$

the family $(W_\varepsilon)_\varepsilon$ converges in law in $\mathcal{C}([0,\infty), L^2(\mathbb{R}^{2d}))$, as $\varepsilon \to 0$, to a limit W defined by

$$W(t,\mathbf{x},\mathbf{k}) = \frac{1}{(2\pi)^d}\int d\mathbf{q}\widehat{W}_0^{\mathbf{k}}(\mathbf{x},\mathbf{q}) \exp\Big(i\mathbf{k}\cdot\mathbf{q} + i\int \mathcal{B}(t,d\mathbf{p})e^{i\mathbf{p}\cdot\mathbf{x}}(e^{-i\mathbf{q}\cdot\mathbf{p}/2} - e^{i\mathbf{q}\cdot\mathbf{p}/2})\Big), \tag{2.13}$$

where $\widehat{W}_0^{\mathbf{k}}$ stands for the Fourier transform of

$$W_0(\mathbf{x},\mathbf{k}) := W(t=0,\mathbf{x},\mathbf{k}) = \frac{1}{(2\pi)^d}\int_{\mathbb{R}^{2d}} d\mathbf{y}\nu(d\zeta)e^{i(\mathbf{k}-\zeta)\cdot\mathbf{y}}\phi_0(\mathbf{x}-\mathbf{y}/2)\overline{\phi_0(\mathbf{x}+\mathbf{y}/2)}$$

with respect to the $\mathbf{k}$-variable. Here, $(\mathcal{B}_t)_t$ is a Wiener process on the dual of the Hilbert space

$$\mathcal{H}_\theta := \Big\{\varphi : \quad \varphi(\mathbf{p}) = \overline{\varphi(-\mathbf{p})} \quad \text{and} \quad \int \frac{d\mathbf{p}}{|\mathbf{p}|^{d+\theta}}|\varphi(\mathbf{p})|^2 < \infty\Big\},$$

such that $\mathcal{B}^*(t,d\mathbf{p}) = \mathcal{B}(t,-d\mathbf{p})$, and with covariance function

$$\mathbb{E}[\mathcal{B}_t(\varphi)\mathcal{B}_s(\psi)] = t\wedge s\int \frac{d\mathbf{p}}{|\mathbf{p}|^{d+\theta}}\varphi(\mathbf{p})\overline{\psi(\mathbf{p})} \qquad \varphi,\psi\in\mathcal{H}_\theta.$$

Moreover, W is the unique weak solution of the stochastic partial differential equation

$$\begin{aligned} dW(t,\mathbf{x},\mathbf{k}) = &-\sigma(\theta)(-\Delta_{\mathbf{k}})^{\theta/2}W(t,\mathbf{x},\mathbf{k}) \\ &+ \frac{2ia(0)}{(2\pi)^d}\int d\mathcal{B}(t,d\mathbf{p})e^{i\mathbf{x}\cdot\mathbf{p}}\Big(W\big(t,\mathbf{x},\mathbf{k}-\frac{\mathbf{p}}{2}\big) - W\big(t,\mathbf{x},\mathbf{k}+\frac{\mathbf{p}}{2}\big)\Big), \end{aligned} \tag{2.14}$$

where

$$\sigma(\theta) = \frac{2a(0)\theta\Gamma(1-\theta)}{(2\pi)^d}\int_{\mathbb{S}^{d-1}} dS(\mathbf{u})|\mathbf{e}_1\cdot\mathbf{u}|^\theta, \tag{2.15}$$

with $\mathbf{e}_1 \in \mathbb{S}^{d-1}$, and Γ the standard Gamma function.

The representation (2.13) is still random as it exhibits, in the Fourier domain, a random phase modulation. In this case the wave does not propagate enough to produce self-averaging phenomena as for the standard semi-classical limit $s = 1$ [11, 17, 18]. The case $\varrho = 0$, $\beta = 1/2$, and $s = s_c$ is addressed by Thm. 2.2.1, since in this particular case $1/(1+\theta) = 1/(2\mathfrak{H})$, and no loss of coherence takes place.

As described in the following result, for a longer propagation scale $s > 1/(1+\theta)$ the random phase modulation in the Wigner transform starts to oscillate fast enough to average out and produces a homogenization phenomenon. It turns out that the deterministic limit corresponds to the expectation of the limiting Wigner transform obtained for $s_c = s = 1/(1+\theta)$. Both Thm. 2.4.1 and the following result are proved through approximation-diffusion theorems based on a perturbed-test-function approach [139].

Theorem 2.4.2 *For any $s \in (1/(1+\theta), 1)$, and*

$$s_c = \frac{1-s}{\theta} < s, \tag{2.16}$$

the family $(W_\varepsilon)_\varepsilon$ converges in probability in $\mathcal{C}([0,+\infty), L^2_w(\mathbb{R}^{2d}))$, as $\varepsilon \to 0$, to the unique solution of the fractional diffusion equation

$$\partial_t W = -\sigma(\theta)(-\Delta_{\mathbf{k}})^{\theta/2} W, \tag{2.17}$$

with

$$W_0(\mathbf{x},\mathbf{k}) := W(t=0,\mathbf{x},\mathbf{k}) = |\phi_0(\mathbf{x})|^2 \nu(\mathbf{k}), \tag{2.18}$$

and $\sigma(\theta)$ defined by (2.15). Here, $L^2_w(\mathbb{R}^{2d})$ stands for $L^2(\mathbb{R}^{2d})$ equipped with the weak topology, $(-\Delta_{\mathbf{k}})^{\theta/2}$ is the fractional Laplacian with Hurst index $\theta \in (0,1)$. Moreover, W is given by

$$W(t,\mathbf{x},\mathbf{k}) = \frac{1}{(2\pi)^d} \int d\mathbf{q} \exp(i\mathbf{k}\cdot\mathbf{q} - \sigma(\theta)|\mathbf{q}|^\theta t) \widehat{W_0^{\mathbf{k}}}(\mathbf{x},\mathbf{q}),$$

where $\widehat{W_0^{\mathbf{k}}}$ stands for the Fourier transform of W_0 with respect to the $\mathbf{k}$-variable.

The observed fractional diffusion exhibits a damping term that obeys to a power law with exponent $\theta \in (0,1)$. This term characterizes how fast the wave function ϕ_ε loses its coherence.

We conclude this section by providing a heuristic explanation for why such loss of coherence phenomena are observable under long-range correlations but not under short-range correlations. After homogenization of the stochastic dynamic, the diffusion operator w.r.t. the momentum variable is approximately given by

$$\varepsilon^{1-s} \int d\mathbf{p} \sigma(\mathbf{p}) \Big(\varphi\big(\mathbf{k} + \frac{\mathbf{p}}{\varepsilon^{s_c}}\big) - \varphi(\mathbf{k}) \Big).$$

In case of rapidly decaying correlations $\sigma(\mathbf{p}) \in L^1(\mathbb{R})$, unless $s = 1$, the term ε^{1-s} cannot be compensated, and we cannot observe any significant interaction between the wave function and the random fluctuations. However, random fluctuations with long-range correlations allow the following asymptotic

$$\varepsilon^{1-s} \int d\mathbf{p} \frac{a(\mathbf{p})}{|\mathbf{p}|^{d+\theta}} \Big(\varphi\big(\mathbf{k} + \frac{\mathbf{p}}{\varepsilon^{s_c}}\big) - \varphi(\mathbf{k}) \Big) \underset{\varepsilon\to 0}{\sim} \varepsilon^{1-s-\theta s_c} a(0) \int \frac{d\mathbf{p}}{|\mathbf{p}|^{d+\theta}} \Big(\varphi(\mathbf{k}+\mathbf{p}) - \varphi(\mathbf{k}) \Big),$$

and therefore significant momentum diffusion as soon as $s_c = (1-s)/\theta$. In other words, the asymptotic autosimilarity property of the correlation function enables significant interactions between the low-frequency structures of the wave function, characterized by s_c, with the random fluctuations.

2.5 Radiative transfer regime

The scaling $s = 1$ and $s_c = 0$ corresponds to the standard semi-classical limit for which the loss of coherence is described by a radiative transfer equation (RTE). This limiting RTE holds for both slowly- and rapidly- decaying correlations.

Theorem 2.5.1 *The family $(W_\varepsilon)_\varepsilon$ converges in probability in $\mathcal{C}([0,+\infty), L^2_w(\mathbb{R}^{2d}))$, as $\varepsilon \to 0$, to a limit denoted by W, which is the unique, uniformly bounded in $L^2(\mathbb{R}^{2d})$, classical solution of the RTE*

$$\partial_t W + \mathbf{k}\cdot\nabla_{\mathbf{x}} W = \mathcal{L}W, \tag{2.19}$$

with $W(t=0) = W_0 \in L^2(\mathbb{R}^{2d})$ defined by (2.18). Here, $\mathcal{L}$ is defined by

$$\mathcal{L}\varphi(\mathbf{k}) := \int d\mathbf{p}\,\sigma\Big(\mathbf{p}-\mathbf{k}, \frac{|\mathbf{k}|^2-|\mathbf{p}|^2}{2}\Big)\big(\varphi(\mathbf{p})-\varphi(\mathbf{k})\big),$$

for $\varphi \in \mathcal{C}^\infty(\mathbb{R}^d)$, where

$$\sigma(\mathbf{p},\omega) = \sigma(\mathbf{p}) := \frac{2a(\mathbf{p})}{(2\pi)^d|\mathbf{p}|^{d+\theta}} \qquad \textit{for} \qquad \varrho > 0, \tag{2.20}$$

and

$$\sigma(\mathbf{p},\omega) := \frac{2\mu\, a(\mathbf{p})}{(2\pi)^d|\mathbf{p}|^{d+2\alpha-2\beta-1}(\mu^2\,|\mathbf{p}|^{4\beta}+\omega^2)} \qquad \textit{for} \qquad \varrho = 0. \tag{2.21}$$

Moreover, $W \in \mathcal{C}^\infty((0,\infty)\times\mathbb{R}^d\times\mathbb{R}^d)$ for any initial condition $W_0 \in L^2(\mathbb{R}^{2d})$.

Originally, the case $\varrho = 0$ was not covered in [92]. In this case the difficulty comes from the identification of the accumulation points once the tightness of the family $(W_\varepsilon)_\varepsilon$ is obtained. Due to the singular kernel in $\mathcal{L}$, this can be achieved by proving the weak uniqueness of the limiting radiative transfer equation. To obtain this weak uniqueness, it is enough to prove the smoothness of classical solutions for this equation. While the regularity can be obtained with relatively straightforward algebra for $\varrho > 0$, the case $\varrho = 0$ requires more efforts as described in Sect. 4.1 of Chap. 4 [97, 98].

Interestingly, the radiative transfer model remains well-defined regardless of whether the integral $\int d\mathbf{p}\,\sigma(\mathbf{p},\omega)$ is finite or not. In other words, the RTE (2.19) is valid under both slowly and rapidly decaying correlations in time. However, although long-range correlations lead to regularizing effects, short-range correlations do not yield similar properties. This regularizing properties highlight an important qualitative distinction between short-range and long-range correlations.

For long-range correlations, although the behavior of the momentum in (2.19) does not exactly align with the diffusion mechanism obtained in Thm. 2.4.2, they are very closed to each other. The momentum diffusion provided in Thm. 2.4.2 is characterized by a fractional Laplacian, whereas in the radiative transfer regime the momentum diffusion is described using a nonlocal operator that is almost a fractional Laplacian. Nevertheless, both of these diffusion mechanisms fall under the category of anomalous diffusion, as they result in damping terms obeying to a power law with exponent $\theta \in (0,1)$. From the radiative transfer model, one needs to consider a proper scaling regime to once again observe a momentum diffusion given by a fractional Laplacian [92].

2.6 Asymptotic preserving time-splitting schemes

Time-splitting schemes for the Schrödinger equation have been widely used for applications that range from quantum transport to wave propagation in random media [26, 125, 151]. In this section, we discuss how the aforementioned asymptotic regimes (random phase modulation, loss of coherence, and radiative transfer regime) can be captured by a time-splitting scheme. It is a natural question to wonder how can we select sufficiently large stepsizes to reduce computational expenses while still accurately recovering the desired limiting regimes.

In order to define the splitting scheme for (2.3), consider a fixed stepsize $h > 0$, $n \in \mathbb{N}^*$, and let

$$\mathcal{A}_\varepsilon = \frac{i\varepsilon^s}{2}\Delta_{\mathbf{x}}, \qquad \text{and} \qquad \mathcal{B}^\varepsilon_{n,h}(\mathbf{x}) = \frac{1}{\varepsilon^{s-(1-\varrho)/2}}\int_{(n-1)h}^{nh} V\left(\frac{s}{\varepsilon^{s+\varrho}}, \frac{\mathbf{x}}{\varepsilon^s}\right) ds.$$

The standard first-order semi-discrete split-step scheme then reads

$$\Psi^\varepsilon_n = e^{h\mathcal{A}_\varepsilon} e^{-i\mathcal{B}^\varepsilon_{n,h}}\Psi^\varepsilon_{n-1}, \qquad \text{for } n = 1,2,\ldots, \qquad \text{with} \quad \Psi_{0,\varepsilon}(\mathbf{x}) = \phi_{0,\varepsilon}(\mathbf{x}). \tag{2.22}$$

Following the approach of [157, 194] for instance, the order in time of this scheme can be improved by taking other combinations of exponentials of operators. Note that the spatial variable $\mathbf{x}$ is not

discretized as the semi-group $e^{h\mathcal{A}_\varepsilon}$ can be evaluated at low cost with high accuracy using spectral methods, such as Fast Fourier Transforms (FFT), provided the spatial stepsize $\Delta\mathbf{x}$ satisfies $\Delta\mathbf{x} \ll \varepsilon^s$. Absorbing boundary conditions are necessary since the wave function solves the Schrödinger equation in the entire space, and boundary conditions compatible with FFT can be found in [100].

Splitting techniques are efficient numerical methods for solving Schrödinger equations under the semi-classical limit. This scheme is always stable since it preserves the L^2 norm w.r.t. the variable $\mathbf{x}$. For short-range correlations, and under the transport scaling ($s = 1$ and $\varrho = 0$), it has been shown in [23] that the scheme accurately captures (in the sense of a convergence in probability) the radiative transfer regime if the stepsize h is of the form $\varepsilon h'$, where $h' \ll 1$ is small but independent of ε. It worth mentioning that a larger stepsize would still lead to a radiative transfer regime, but with an incorrect scattering cross-section (the one given by (2.20) for $\varrho > 0$ in Thm. 2.5.1 instead of (2.21)). The constraint $h = \varepsilon h'$ is already a great improvement on the consistency constraint to capture the statistical behavior of the wave function. In fact, for a given realization of the random fluctuation V, the local error estimate between the exact solution and its approximation after one single step is readily shown to be

$$\|\phi_\varepsilon(h) - \Psi_1^\varepsilon\|_{L^2(\mathbb{R}^d)} \leq \frac{h^2}{\varepsilon}\|[\varepsilon\Delta_{\mathbf{x}}, \sqrt{\varepsilon}V]e^{-\frac{i\varepsilon}{2}\Delta_{\mathbf{x}}}\phi_{0,\varepsilon}\|_{L^2(\mathbb{R}^d)} + \frac{h^2}{\varepsilon}\|\phi_{0,\varepsilon}\|_{L^2(\mathbb{R}^d)}\sup_{t,\mathbf{x}}|V(t,\mathbf{x})|^2,$$

where $[\cdot,\cdot]$ denotes the commutator between two operators. Assuming $\phi_{0,\varepsilon}$ and V smooth enough, the local error is then controlled by $Ch^2\varepsilon^{-3/2}$, and the global error by $h\varepsilon^{-3/2}$, requiring $h \ll \varepsilon^{3/2}$ for the scheme to be consistent in the pathwise sense. This condition is considerably more restrictive than $h = \varepsilon h'$ required to capture the transport regime in probability (in a statistical sense).

In what follows, we discuss the constraints on the stepsize h to capture the three asymptotic regimes described above. For most of our parameter configurations, all three regimes are captured for any $h > 0$, independently of ε. Such a result is a consequence of several factors. First, we only need to approximate the behavior of the wave function in the statistical sense, not in the pathwise sense, as the above asymptotic regimes are derived in a statistical sense and not w.r.t a particular realization of the fluctuations. Second, the random medium fluctuations exhibit multiscale properties allowing an accurate description of the dynamics at larger scales in the statistical sense.

2.6.1 The phase modulation

To capture the behavior of (2.6), a discretized version of the wave function is considered:

$$\zeta_n^\varepsilon(\mathbf{k}) = \frac{1}{\varepsilon^{d(s-s_c)}}\widehat{\Psi}_n^\varepsilon\Big(\frac{\mathbf{k}}{\varepsilon^{s-s_c}}\Big)e^{inh\frac{|\mathbf{k}|^2}{2\varepsilon^{s-2s_c}}},$$

where $\widehat{\Psi}_n^\varepsilon(\mathbf{k})$ stands for the Fourier transform of $\Psi_n^\varepsilon(\mathbf{x})$ defined by (2.22). We have the following result for

$$s = 1/(2\mathfrak{H}_\varrho),$$

with $\mathfrak{H}_\varrho$ given by (2.5).

Theorem 2.6.1 *For any $\mathbf{k} \in \mathbb{R}^d$, $h > 0$, $n > 0$, and $s_c \in [0, s]$, the family $(\zeta_n^\varepsilon(\mathbf{k}))_\varepsilon$ converges in law, as $\varepsilon \to 0$, to*

$$\zeta(nh, \mathbf{k}) = \widehat{\phi}_0(\mathbf{k})\exp\Big(i\sqrt{D_{n,h}(\mathbf{k})}W_{\mathfrak{H}}(nh)\Big).$$

Here, $W_{\mathfrak{H}}$ is a standard fractional Brownian motion with Hurst index $\mathfrak{H}$, and $D_{n,h}$ satisfies

$$\lim_{h\to 0} D_{[T/h],h}(\mathbf{k}) = D(\alpha, \beta, \mathbf{k}), \tag{2.23}$$

given by (2.7) in the case $\beta = 1/2$, $\varrho = 0$, and $s_c = s$, and $D_{n,h}$ is given by (2.8) otherwise.

This result shows that the proposed time-splitting scheme captures the correct behavior as $\varepsilon \to 0$ for any stepsize $h > 0$, *independently* of ε, when at least one of the three following conditions hold: $\beta < 1/2$, $\varrho > 0$, $s_c < s$. When $\beta = 1/2$, $\varrho = 0$, and $s_c = s$, the condition $h \ll 1$ is required but independently of ε. As already mentioned, such a result holds only because the statistical behavior of the wave function is of interest.

2.6.2 Loss of coherence

Let us recall that after the onset the random phase modulation the loss of coherence phenomena are described through two different behaviors. When $s = s_c = 1/(\theta+1)$ (for $\beta < 1/2$, or $\varrho > 0$) the Wigner transform converges in law to the solution of a stochastic fractional heat equation (see Thm. 2.4.1). When $0 < s_c < s$, with s_c given by (2.16), homogenization takes place and the Wigner transform converges in probability to the solution of a fractional heat equation (see Thm. 2.4.2).

These two behaviors are captured using the following discretized version of the Wigner transform:

$$W^\varepsilon_{n,h}(\mathbf{x},\mathbf{k}) = \frac{1}{(2\pi)^d}\int_{\mathbb{R}^d\times S} d\mathbf{y}\nu(d\zeta)\, e^{i\mathbf{k}\cdot\mathbf{y}}\Psi^\varepsilon_n\big(\mathbf{x}-\varepsilon^{s-s_c}\frac{\mathbf{y}}{2},\zeta\big)\overline{\Psi^\varepsilon_n\big(\mathbf{x}+\varepsilon^{s-s_c}\frac{\mathbf{y}}{2},\zeta\big)},$$

where $\Psi^\varepsilon_n(\mathbf{x})$ is defined by (2.22), with initial condition (2.9).

Theorem 2.6.2 *For either $\varrho > 0$ or $\beta < 1/2$, and $s_c = s = 1/(1+\theta)$, where $\theta \in (0,1)$ is defined by (2.12), and for all $n > 0$ and $h > 0$, $(W^\varepsilon_{n,h})_\varepsilon$ converges in law on $L^2(\mathbb{R}^{2d})$, as $\varepsilon \to 0$, to a limit $W(nh,\mathbf{x},\mathbf{k})$ defined by*

$$W(t,\mathbf{x},\mathbf{k}) = \frac{1}{(2\pi)^d}\int_{\mathbb{R}^d} d\mathbf{q}\widehat{W}^{\mathbf{k}}_0(\mathbf{x},\mathbf{q})\exp\Big(i\mathbf{k}\cdot\mathbf{q} + i\int_{\mathbb{R}^d}\mathcal{B}(t,d\mathbf{p})e^{i\mathbf{p}\cdot\mathbf{x}}(e^{-i\mathbf{q}\cdot\mathbf{p}/2}-e^{i\mathbf{q}\cdot\mathbf{p}/2})\Big), \qquad (2.24)$$

which is the unique solution of the stochastic fractional heat equation (2.14). In (2.24), $\widehat{W}^{\mathbf{k}}_0$ stands for the Fourier transform of W_0 defined by (2.18) with respect to the $\mathbf{k}$-variable .

As already explained, the remaining case $s = s_c$, $\varrho = 0$ and $\beta = 1/2$ is included in Thm. 2.6.1. The splitting scheme captures again the correct asymptotics for any $h > 0$. In this critical case, the limiting Wigner transform is random because the wave function does not propagate enough to average out the stochastic effects. This self-averaging effect is observed for longer propagation scale s and the splitting scheme is again able to capture this effect.

Theorem 2.6.3 *Let $s_c = (1-s)/\theta < s$, where θ is defined by (2.12). Then, for all $n > 0$, $h > 0$, $(W^\varepsilon_{n,h})_\varepsilon$ converges in probability in $L^2_w(\mathbb{R}^{2d})$, as $\varepsilon \to 0$, to a limit $W(nh,\mathbf{x},\mathbf{k})$ defined by*

$$W(t,\mathbf{x},\mathbf{k}) = \frac{1}{(2\pi)^d}\int_{\mathbb{R}^d} dq e^{i\mathbf{k}\cdot\mathbf{q}-\sigma(\theta)|\mathbf{q}|^\theta t}\widehat{W}^{\mathbf{k}}_0(\mathbf{x},\mathbf{q}),$$

which is the unique solution of (2.17) uniformly bounded in $L^2(\mathbb{R}^{2d})$.

In this regime as well, the splitting scheme captures the correct asymptotic behavior for any $h > 0$.

2.6.3 Radiative transfer regime

In this regime ($s = 1$ and $s_c = 0$), there is some requirements on the stepsize h. The following result guarantees that the time-splitting scheme (2.22), for a stepsize $h \ll 1$ *independent* of ε, leads to the correct limit for $\varrho > 0$.

Theorem 2.6.4 *For any $\varrho > 0$, $n > 0$, $h > 0$, the family $(W^\varepsilon_{n,h})_\varepsilon$ converges in probability on $L^2_w(\mathbb{R}^{2d})$, as $\varepsilon \to 0$, to a limit defined by*

$$W_{n,h}(\mathbf{x},\mathbf{k}) = \frac{1}{(2\pi)^{2d}}\int_{\mathbb{R}^d} d\mathbf{y}d\mathbf{q}e^{i(\mathbf{x}\cdot\mathbf{y}+\mathbf{k}\cdot\mathbf{q})+\psi_{n,h,\theta}(\mathbf{y},\mathbf{q})}\widehat{W}_0(\mathbf{y},\mathbf{y}+t\mathbf{q}).$$

Here,

$$\psi_{n,h,\theta}(\mathbf{y},\mathbf{q}) = h\sum_{j=1}^n \psi(\mathbf{y}+nh(1-j/n+1/n)\mathbf{q}),$$

with

$$\psi(\mathbf{q}) = \frac{2}{\mu(2\pi)^d}\int_{\mathbb{R}^d} d\mathbf{p}\,\frac{a(\mathbf{p})}{|\mathbf{p}|^{d+\theta}}(e^{i\mathbf{p}\cdot\mathbf{q}}-1),$$

so that

$$\lim_{h\to 0} W_{[T/h],h}(\mathbf{x},\mathbf{k}) = W(T,\mathbf{x},\mathbf{k}),$$

which is the unique solution to (2.19) uniformly bounded in $L^2(\mathbb{R}^{2d})$.

When $\varrho = 0$ the situation is different. The transport term and momentum variables interact, which leads to another expression of the collision operator (see (2.20) versus (2.21)). This situation corresponds to the one considered in [23] under random media with short-range correlations, and for which one needs $h = \varepsilon h'$, with $h' \ll 1$ independent of ε to recover the correct scattering operator. Without this restriction the scattering kernel (2.20) is obtained instead of (2.21).

2.7 Perspectives

The Schrödinger equation exhibits intriguing effective multiscale properties when coupled with a slowly decorrelating random potential. Capturing numerically these effects is also an interesting question as these properties seem to influence the performance of the numerical schemes. The perspectives in these directions are twofolds. First, these time-splitting schemes have not been implemented so far. It would be interesting to investigate if all the scaling regimes, described theoretically in this chapter, can effectively be captured numerically, and evaluate how these schemes are sensitive to the time stepsize.

In [15] under short-range correlations, or [105] where the authors start directly from a white-noise model for the random fluctuations, the long-time behavior of the wave function itself, and not the Wigner transform, is investigated. The asymptotic wavefield can be described through a Gaussian random field with a correlation function related to the radiative transfer model (2.19). A full description of the correlation function holds significant importance in the context of wave propagation, particularly for imaging problems through strongly scattering media relying on incoherent recorded signals. While the quadratic nature of the Wigner transform does not capture the slow phase of the wavefield (as it corresponds to the energy density) the direct analysis of the wavefield enables to extract information about the phase itself, as illustrated in Chap. 1 through the slow angle variable. It is well known in the imaging community that information carried by the phase is highly relevant for inversion algorithms. The second perspective consists in describing the loss of coherence phenomena on the wavefield itself and investigate whether it exhibits Gaussian statistics or not.

Chapter 3

Wave propagation in random media with long-range correlations

Analysis of physical measurements reveals that propagation media may exhibit perturbations with long-range dependencies [49,60,117,172,188]. This has sparked interest in a mathematical understanding of how waves propagate through multiscale media. Multiscale random media with long-range correlations find applications in modeling the heterogenous earth crust, the turbulent atmosphere, and also biological tissues for instance. While there exists a large literature on wave propagation in heterogeneous media which vary on a well-defined microscale [70], the study of wave behavior in multiscale random media remains an area with many open questions. In order to be efficient, imaging and communication algorithms necessitate a deep understanding on how waves are affected by the rough medium fluctuations. In view of its potential for applications, mathematical descriptions of wave propagation in multiscale random media with long-range correlations has attracted a lot of interest over the last decade [15, 84, 153, 154, 191].

The full scalar wave equation is considered in this chapter with a continuous multiscale medium characterized by a stochastic process with long-range correlations:

$$\Delta p - \frac{1}{c^2(z,\mathbf{x})}\partial_{tt}^2 p = \nabla \cdot F(t,\mathbf{x},z) \qquad (t,\mathbf{x},z) \in \mathbb{R}\times\mathcal{D}\times\mathbb{R}, \tag{3.1}$$

with null initial conditions, $p(t=0) = \partial_t p(t=0) = 0$, so that the system is supposed to be initially at rest. Here, p represents the acoustic pressure, and c the wave-speed profile. The coordinate z represents the main propagation axis, and the coordinate $\mathbf{x} \in \mathcal{D}$ represents the transverse variable (see Fig. 3.1). In this chapter, $\mathcal{D} = (0,d)$ is considered in Sect. 3.1 to define a planar waveguide with

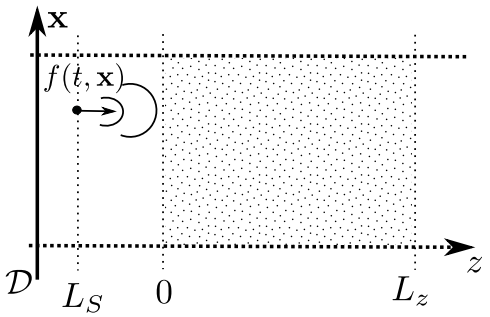

Fig. 3.1: Illustration of the wave propagation model. The source F generates a wave with profile f, which propagates along the z-axis. The section $z \in [0, L_z]$ is randomly heterogeneous with long-range correlations. Our objective is to characterize the pulse as it emerges at the end of the random section ($z = L_z$).

a bounded cross-section, and $\mathcal{D} = \mathbb{R}^2$ in Sect. 3.2 and 3.3 to model open propagation media. The forcing term $\mathbf{F}(t, z, \mathbf{x})$ is given by

$$F(t, z, \mathbf{x}) = f(t, \mathbf{x})\delta(z - L_S)\mathbf{e}_z,$$

where $\mathbf{e}_z$ is the unit vector pointing in the z-direction. This term models a source located in the plan $z = L_S$, emitting a wave of the form $f(t, \mathbf{x})$. The wave-speed profile is assumed to be of the form

$$\frac{1}{c^2(z, \mathbf{x})} := \frac{1}{c_0^2}\Big(1 + \nu(z, \mathbf{x})\mathbf{1}_{(0,L_z)}(z)\Big),$$

where ν models the fluctuations of the propagation medium. The aim of this chapter is to present mathematical descriptions of the wavefield as it exits the random section at $z = L_z$ in three different scenarios, emphasizing the crucial role of the fluctuations with long-range correlations.

As described in Chap. 2 for the Schrödinger equation, random media with long-range correlations affect the wave propagation in a way that differs greatly from the corruption caused by media fluctuating on a well-defined microscale (short-range correlations) [70]. Wave propagation in random media with long-range correlations has already been considered in one-dimensional propagation media [84,153], or open media under the paraxial approximation [15,68,69]. These works have demonstrated that wave propagating in such random media exhibits stochastic effects at various propagation scales. Unlike for propagation media with short-range correlations, all the stochastic effects do not appear on the same propagation scale. Perturbations with long-range correlations first induce a random phase modulation on the waves driven by a single standard fractional Brownian motion, which does not depend on the frequency band [15, 152]. For larger propagation distances, the random phase modulation starts to oscillate very fast up to produce diffusion phenomena and affects the energy propagation [84]. This picture follows the ones presented in Chap. 1 and 2, where the phase modulation is exhibited by a non-central limit theorem, and the diffusion phenomena by approximation-diffusion theorems.

This chapter is organized as follows. First, we consider in Sect. 3.1 the context of a waveguide supporting a discrete number of modes. This section considers $\mathcal{D} = (0, d)$ as transverse section and constitutes an intermediate situation between a one-dimensional propagation medium and the full ambient physical space (obtained for $\mathcal{D} = \mathbb{R}^2$). In this section, an analysis similar to the non-central limit theorem is developed to exhibit phase modulations driven by a unique fractional Brownian motion for each propagating modes in a high-frequency limit. In Sect. 3.2 a similar approach is developed for $\mathcal{D} = \mathbb{R}^2$, but this time two phenomena are captured at once in a single high-frequency limit: a non-central limit type result, as well as the paraxial approximation. This approximation consists in describing the wave propagation along a privileged axis, and has been extensively studied and used in applications (see [10, 24, 54, 201] for instance). Under suitable assumptions on physical parameters, this approximation can greatly simplify the description of propagation phenomena as well as their numerical simulations [151]. The paraxial approximation together with the fractional white-noise approximation lead to a model of fractional Itô-Schrödinger equation driven by a fractional noise, not necessarily Gaussian, to describe the impact of the medium fluctuations on the propagating waves. The evolution variable of this fractional Itô-Schrödinger equation corresponds to the one of the main propagation axis. Under the setting of this section, the backscattering effects are shown to be negligible, and the energy carried by the propagating wave is conserved. Finally, in Sect. 3.3, under the simpler setting of a randomly layered medium (that is $\nu(z, \mathbf{x}) = \nu(z)$), but still with $\mathcal{D} = \mathbb{R}^2$, the waves are allowed to propagate on a larger propagation distance than the one of the non-central limit theorem exhibiting the phase modulation. Typically, despite considering long-range correlations, we let the waves propagate over distances leading to diffusion effects under short-range correlations. At this scale, the random phase modulation oscillates very fast up to produce effective diffusion phenomena. The backscattering effects become now nonnegligible and the energy is now affected by the medium fluctuations. In this section as well, the diffusion phenomena and paraxial approximation are obtained under a single high-frequency limit. These phenomena can be described through a deterministic fractional paraxial equation, wherein the order of the fractional time derivative is directly determined by the decay rate of the correlation function of the random fluctuations.

This chapter covers the results obtained in [10, 12, 17] of the bibliography list on page 6.

3.1 Random waveguides

Considering $\mathcal{D} = (0, d)$, Eq. (3.1) describes scalar wave propagation in a planar waveguide with propagation axis given by the z-direction (see Fig. 3.1). To simplify the presentation, only Dirichlet boundary conditions are here considered to complete the system on $\partial\mathcal{D}$. A similar analysis can be applied to other boundary conditions. The wave equation (3.1) being linear in p, its solution can be expressed as a superposition of monochromatic waves through the Fourier transform:

$$\widehat{p}(\omega, \mathbf{x}, z) = \int p(t, \mathbf{x}, z) e^{i\omega t} dt \qquad \text{and} \qquad p(t, \mathbf{x}, z) = \frac{1}{2\pi} \int \widehat{p}(\omega, \mathbf{x}, z) e^{-i\omega t} d\omega.$$

The wavefield $\widehat{p}(\omega, \mathbf{x}, z)$ satisfies, in the randomly perturbed section $z \in (0, L_z)$, the following Helmholtz equation (time-harmonic wave equation)

$$\partial^2_{zz}\widehat{p}(\omega, \mathbf{x}, z) + \partial^2_{\mathbf{xx}}\widehat{p}(\omega, \mathbf{x}, z) + k_\omega^2(1 + \varepsilon\,\nu(z, \mathbf{x}))\widehat{p}(\omega, \mathbf{x}, z) = 0,$$

where $k_\omega = \omega/c_0$ is the wavenumber. Here, the medium fluctuations are assumed to be small, of order $\varepsilon \ll 1$ (weak scattering regime). To observe non-trivial cumulative stochastic effects on the propagating waves a propagation distance of order

$$L_z \sim \frac{L}{\varepsilon^s} \gg 1$$

is required. The central wavelength is of order one in this problem ($\lambda \sim 1$), that is small compared to the propagation distance ($\lambda \ll L_z$), to place ourselves in a high-frequency regime. The propagation scale parameter s represents how long the propagation distance needs to be to observe the onset of effective random effects on the waves. Assuming

$$\mathbb{E}[\nu(z + z', \mathbf{x})\nu(z', \mathbf{y})] \underset{|z|\to\infty}{\sim} \frac{R_0}{|z|^\gamma} R(\mathbf{x}, \mathbf{y}), \tag{3.2}$$

describing the long-range correlation property for the medium fluctuations, we need to take

$$s = \frac{1}{\mathfrak{H}} < 2 \qquad \text{with} \qquad \mathfrak{H} = 1 - \frac{\gamma}{2} \in (1/2, 1).$$

With this choice, $L/\varepsilon^s \ll L/\varepsilon^2$, where the latter corresponds to the standard scaling to observe non-trivial stochastic effects under fluctuations with short-range correlations. While not being restrictive, in addition to the boundedness of ν, some technical assumptions need to be set on ν to be compatible with a moment technique. Basically, ν is a nonlinear function (with Hermite rank 1) of a Gaussian filed satisfying a relation similar to (3.2). The precise description of these assumptions are omitted here, and we refer to [99] for the complete assumptions. The requirement on the Hermite rank could be relaxed to arbitrary rank, as proposed in [154], with an adaptation of the amplitude ε of the fluctuations. Also, the width of the waveguide d is assumed to be of the order of the central wavelength λ (of order 1), so that only a discrete number of mode is supported by the waveguide. The wavefield $\widehat{p}$ can then be expressed as

$$\widehat{p}(\omega, \mathbf{x}, z) = \widehat{p}_a(\omega, \mathbf{x}, z) + \widehat{p}_e(\omega, \mathbf{x}, z),$$

with

$$\widehat{p}_a(\omega, \mathbf{x}, z) := \sum_{j=1}^{N(\omega)} \frac{\widehat{a}_j(\omega, z)}{\sqrt{\beta_j(\omega)}} e^{i\beta_j(\omega)z}\phi_j(\mathbf{x}) + \sum_{j=1}^{N(\omega)} \frac{\widehat{b}_j(\omega, z)}{\sqrt{\beta_j(\omega)}} e^{-i\beta_j(\omega)z}\phi_j(\mathbf{x}), \tag{3.3}$$

and

$$\widehat{p}_e(\omega, \mathbf{x}, z) := \sum_{j \geq N(\omega)+1} \widehat{p}_j(\omega, z)\phi_j(\mathbf{x}).$$

Here, $\widehat{p}$ is expanded according to the spectral decomposition associated to the transverse Laplacian $-\partial^2_{\mathbf{xx}}$ equipped with Dirichlet boundary conditions on $\partial\mathcal{D}$. Its spectrum is composed of a countable number of positive eigenvalues

$$\lambda_j = \frac{j^2\pi^2}{d^2} \qquad j \geq 1,$$

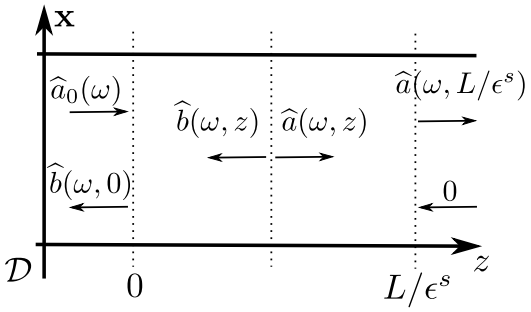

Fig. 3.2: Illustration of the right-going and left-going propagating mode amplitudes $\widehat{a}_j(\omega,z)$ and $\widehat{b}_j(\omega,z)$. The source generates the probing wave $\widehat{a}_0(\omega)$, the reflected wave is $\widehat{b}(\omega,0)$ and the transmitted wave, which is our interest, is $\widehat{a}(\omega,L/\varepsilon^s)$. Note that there is no energy coming from the right-hand-side of the waveguide $z > L/\varepsilon^s$.

with eigenvectors

$$\phi_j(\mathbf{x}) := \sqrt{\frac{2}{d}}\sin\Big(\frac{j\pi\mathbf{x}}{d}\Big) \qquad j \geq 1,$$

providing an orthonormal basis of $L^2(\mathcal{D})$. The family $(\beta_j(\omega))_{j\geq 1}$ is defined as

$$\beta_j(\omega) := \sqrt{k_\omega^2 - \lambda_j} \qquad \text{for } j \in \{1,\dots,N(\omega)\},$$

where $N(\omega)$ is the integer such that $\lambda_{N(\omega)} \leq k_\omega^2 < \lambda_{N(\omega)+1}$, and represents the number of propagating modes. For our planar waveguide model, one has

$$N(\omega) = \Big[\frac{\omega d}{\pi c}\Big],$$

where $[\cdot]$ stands for the integer part. In (3.3), the terms $\widehat{a}_j$ and $\widehat{b}_j$ represent the amplitudes of the right- and left-*propagating modes* respectively, as they corresponds to the oscillatory terms $e^{\pm i\beta_j(\omega)z}$ w.r.t. the variable of the main propagation axis (see Fig. 3.2 for an illustration). Here, there is exactly $2N(\omega)$ propagating modes. The terms $\widehat{p}_j$ in $\widehat{p}_e$ represent the amplitudes of the *evanescent modes* and corresponds to non-oscillatory terms w.r.t. the z-variable. Although the evanescent modes are negligible after propagating over large propagation distances, their influences can be incorporated to the mode-coupling mechanism of the propagating modes $\widehat{a}_j$ and $\widehat{b}_j$ following the strategy of [79]:

$$\frac{d}{dz}\begin{bmatrix}\widehat{a}(\omega,z)\\ \widehat{b}(\omega,z)\end{bmatrix} = \Big[\varepsilon\mathbf{H}(\omega,z) + \varepsilon^2\mathbf{G}(\omega,z)\Big]\begin{bmatrix}\widehat{a}(\omega,z)\\ \widehat{b}(\omega,z)\end{bmatrix}, \tag{3.4}$$

completed with the boundary conditions

$$\widehat{a}_j(\omega,0) = \widehat{a}_{j,0}(\omega) \qquad \text{and} \qquad \widehat{b}_j(\omega,L/\varepsilon^s) = 0. \tag{3.5}$$

The second relation means that no wave is coming from the right-hand side of the random section, and the $\widehat{a}_{j,0}(\omega)$'s are the propagating mode amplitudes generated by the source term. The coupling matrices $\mathbf{H}$ and $\mathbf{G}$ are defined by:

$$\mathbf{H}(\omega,z) := \begin{bmatrix}\mathbf{H}^a(\omega,z) & \overline{\mathbf{H}^b(\omega,z)}\\ \mathbf{H}^b(\omega,z) & \overline{\mathbf{H}^a(\omega,z)}\end{bmatrix} \qquad \text{and} \qquad \mathbf{G}(\omega,z) := \begin{bmatrix}\mathbf{G}^a(\omega,z) & \overline{\mathbf{G}^b(\omega,z)}\\ \mathbf{G}^b(\omega,z) & \overline{\mathbf{G}^a(\omega,z)}\end{bmatrix},$$

with

$$\mathbf{H}^a_{jl}(z) := \frac{ik_\omega^2}{2}C_{jl}(z)e^{i(\beta_l-\beta_j)z}, \qquad \mathbf{H}^b_{jl}(z) := -\frac{ik_\omega^2}{2}C_{jl}(z)e^{i(\beta_l+\beta_j)z}$$

$$\mathbf{G}^a_{jl}(z) := \frac{ik_\omega^4}{4}\sum_{l'\geq N+1}\int_{-\infty}^{\infty} C_{jl'}(z)C_{l'l}(z+u)e^{i\beta_l(z+u)-i\beta_j z-\beta_{l'}|u|}du,$$

$$\mathbf{G}^b_{jl}(z) := -\frac{ik_\omega^4}{4}\sum_{l'\geq N+1}\int_{-\infty}^{\infty} C_{jl'}(z)C_{l'l}(z+u)e^{i\beta_l(z+u)+i\beta_j z-\beta_{l'}|u|}du,$$

and where the coupling coefficient $C_{jl}(z)$ are defined by

$$C_{jl}(z) := \frac{1}{\sqrt{\beta_j \beta_l}} \int_{\mathcal{D}} \nu(z, \mathbf{x}) \phi_j(\mathbf{x}) \phi_l(\mathbf{x}) d\mathbf{x}.$$

The matrix $\mathbf{H}$ describes the coupling between the propagating modes ($\mathbf{H}^a$ describes the coupling between the forward-going modes and backward-going modes themselves, while $\mathbf{H}^b$ describes the coupling between the forward- and backward-going modes). These coupling coefficients involve directly the medium fluctuations ν. Without these fluctuations, there is no mode coupling and the solution to (3.4) is straightforward.

To account for the cumulative stochastic effects over the large propagation distance L/ε^s, the propagating mode amplitudes are rescaled as

$$\widehat{a}^\varepsilon(\omega, z) = \widehat{a}(\omega, z/\varepsilon^s) \qquad \text{and} \qquad \widehat{b}^\varepsilon(\omega, z) = \widehat{b}(\omega, z/\varepsilon^s).$$

The corresponding two-point boundary value problem (3.4) is not convenient to analyze directly. It is more convenient to recast this problem into a initial value problem by mean of a propagator matrix defined as the solution to

$$\frac{d}{dz}\mathbf{P}^\varepsilon(\omega, z) = \Big[\frac{1}{\varepsilon^{s-1}}\mathbf{H}\Big(\omega, \frac{z}{\varepsilon^s}\Big) + \varepsilon^{2-s}\mathbf{G}\Big(\omega, \frac{z}{\varepsilon^s}\Big)\Big]\mathbf{P}^\varepsilon(\omega, z), \qquad \text{with} \qquad \mathbf{P}^\varepsilon(\omega, 0) = Id_{2N(\omega)},$$

so that for all $z \in [0, L]$,

$$\begin{bmatrix}\widehat{a}^\varepsilon(\omega, z)\\ \widehat{b}^\varepsilon(\omega, z)\end{bmatrix} = \mathbf{P}^\varepsilon(\omega, z)\begin{bmatrix}\widehat{a}^\varepsilon(\omega, 0)\\ \widehat{b}^\varepsilon(\omega, 0)\end{bmatrix} \qquad \text{and} \qquad \begin{bmatrix}\widehat{a}^\varepsilon(\omega, L)\\ 0\end{bmatrix} = \mathbf{P}^\varepsilon(\omega, L)\begin{bmatrix}\widehat{a}_0(\omega, 0)\\ \widehat{b}^\varepsilon(\omega, 0)\end{bmatrix},$$

according to (3.5). Due to the form of $\mathbf{H}(\omega, z)$ and $\mathbf{G}(\omega, z)$, the propagator can be expressed as

$$\mathbf{P}^\varepsilon(\omega, z) = \begin{bmatrix}\mathbf{P}^{a,\varepsilon}(\omega, z) & \overline{\mathbf{P}^{b,\varepsilon}(\omega, z)}\\ \mathbf{P}^{b,\varepsilon}(\omega, z) & \overline{\mathbf{P}^{a,\varepsilon}(\omega, z)}\end{bmatrix},$$

where $\mathbf{P}^{a,\varepsilon}$ describes the coupling mechanisms between the right-going modes (resp. left-going modes) with themselves, while $\mathbf{P}^{b,\varepsilon}$ describes the coupling mechanisms between the right-going and left-going modes.

Due to the form of the propagator $\mathbf{P}^\varepsilon$, one can restrict the asymptotic analysis to the one of the two blocks:

$$\mathcal{P}^\varepsilon(\omega, z) = \begin{bmatrix}\mathbf{P}^{a,\varepsilon}(\omega, z)\\ \mathbf{P}^{b,\varepsilon}(\omega, z)\end{bmatrix} \in \mathcal{M}_{N(\omega)}(\mathbb{C}) \times \mathcal{M}_{N(\omega)}(\mathbb{C}),$$

where $\mathcal{M}_{N(\omega)}(\mathbb{C})$ stands for the set of $N(\omega)\times N(\omega)$ matrices with complex coefficients. The asymptotic behavior of the propagator $\mathcal{P}^\varepsilon$ can be described as follows.

Theorem 3.1.1 *For all $z \in [0, L]$, the family $(\mathcal{P}^\varepsilon(\omega, z))_\varepsilon$ converges in law in $\mathcal{M}_N(\mathbb{C}) \times \mathcal{M}_N(\mathbb{C})$ to*

$$\begin{bmatrix}D(\omega, z)\\ \mathbf{0}\end{bmatrix},$$

with

$$D(\omega, z) = diag(e^{i\sigma_{1,\mathfrak{H}}(\omega)W_{\mathfrak{H}}(z)}, \dots, e^{i\sigma_{N,\mathfrak{H}}(\omega)W_{\mathfrak{H}}(z)}),$$

where $W_{\mathfrak{H}}$ is a standard fractional Brownian motion with Hurst index $\mathfrak{H}$,

$$\sigma_{j,\mathfrak{H}}(\omega) = \frac{k_\omega^2}{2\beta_j(\omega)}\sqrt{\frac{R_j}{\mathfrak{H}(2\mathfrak{H}-1)}}, \tag{3.6}$$

and

$$R_j = \iint_{\mathcal{D}\times\mathcal{D}} R(\mathbf{x}, \mathbf{x}')\phi_j^2(\mathbf{x})\phi_j^2(\mathbf{x}')d\mathbf{x}d\mathbf{x}'.$$

The proof of Thm. 3.1.1 is based on a moment technique following the ideas of [15, 66]. Let us clarify the meaning of this result. First, Thm. 3.1.1 implies that the first significant stochastic effects affecting the wave propagation take place for $s = 1/\mathfrak{H} < 2$, which is in contrast with the classical results under short-range correlations with $s = 2$ (see [70, Chap. 20]). The second one concerns the convergence of $\mathbf{P}^{b,\varepsilon}(\omega, z)$ to the null matrix in probability, meaning that the coupling mechanisms between the right- and left-going modes are negligible in the high-frequency limit $\varepsilon \to 0$. In other words, the backscattering is negligible for ε small, and the backscattered amplitudes $\widehat{b}_j^{\varepsilon}(\omega, z)$ (and then the backscattered wavefield) tend to 0. Third, the convergence in distribution of $\mathbf{P}^{a,\varepsilon}(\omega, z)$ to a diagonal matrix means that the coupling mechanisms between two different right-going modes are also negligible in the limit $\varepsilon \to 0$. Finally, the propagating modes are only affected by mode- and frequency-dependent phase modulations, but driven by the same fractional Brownian motion, which does not depend on the frequency ω. This effect of mode-dependent phase modulations driven by a single fractional Brownian motion has already been observed in [15, Thm 1.2] for the random Schrödinger equation with long-range correlations and stated in Thm 2.2.1 of Chap. 2.

A version of Thm. 3.1.1 involving multiple frequencies can be derived following the same strategy, and allows to describe the role of these stochastic effects in the time domain. Considering now a narrowband source term,

$$f^{\varepsilon}(t, \mathbf{x}) = f(\varepsilon^s t) e^{-i\omega_0 t} \Psi(\mathbf{x}),$$

with carrier frequency ω_0 (of order 1) and bandwidth of order ε^s, we have the following result.

Theorem 3.1.2 *For all $j \in \{1, \ldots, N(\omega_0)\}$, let us consider the projection*

$$p_{j,pr}^{\varepsilon}(t, L) = e^{-i\beta_j(\omega_0)(L/\varepsilon^s - L_S)} e^{i\omega_0 t/\varepsilon^s} \big\langle p_{pr}\Big(\frac{t}{\varepsilon^s}, \cdot, \frac{L}{\varepsilon^s}\Big), \phi_j \big\rangle_{L^2(\mathcal{D})}.$$

The family $(p_{1,pr}^{\varepsilon}(\cdot, L), \ldots, p_{N(\omega_0),pr}^{\varepsilon}(\cdot, L))_{\varepsilon}$ converges in law in $\mathcal{C}([-T, T], \mathbb{C}^{N(\omega_0)})$, as $\varepsilon \to 0$, to $(p_{j,pr}^{0}(\cdot, L))_{j \in \{1,\ldots,N(\omega_0)\}}$, where

$$p_{j,pr}^{0}(t, L) = \frac{1}{2} e^{i\sigma_{j,\mathfrak{H}}(\omega_0) W_{\mathfrak{H}}(L)} f(t - \beta_j'(\omega_0) L) \big\langle \phi_j, \Psi \big\rangle_{L^2(\mathcal{D})}.$$

Here, $W_{\mathfrak{H}}$ is a standard fractional Brownian motion with Hurst index $\mathfrak{H} \in (1/2, 1)$, and $\sigma_{j,\mathfrak{H}}(\omega_0)$ is defined by (3.6).

In this result the wavefield is projected over the propagating modes. The reason is that the pulsewidth of the source and the propagation distance are of the same order ($\sim 1/\varepsilon^s$), so that the propagating modes overlap, there is no modal dispersion in this situation. By projecting over the propagating modes, we can compensate the rapid phases $e^{i\beta_j(\omega)L/\varepsilon^s}$ and $e^{-i\omega_0 t/\varepsilon^s}$ (inherent of a high-frequency problem) mode by mode and pass to the limit in ε. Roughly speaking, the transmitted wave can be formally described as

$$p_{tr}\Big(\frac{t}{\varepsilon^s}, \mathbf{x}, \frac{L}{\varepsilon^s}\Big) \underset{\varepsilon \to 0}{\simeq} \frac{e^{-i\omega_0 t/\varepsilon^s}}{2} \sum_{j=1}^{N(\omega_0)} e^{i\sigma_{j,\mathfrak{H}}(\omega_0) W_{\mathfrak{H}}(L)} f(t - \beta_j'(\omega_0) L) e^{i\beta_j(\omega_0)(L/\varepsilon^s - L_S)} \phi_j(\mathbf{x}) \big\langle \phi_j, \Psi \big\rangle_{L^2(\mathcal{D})}.$$

This transmitted wave is therefore a superposition of modes, each of them is centered around its arrival time

$$t_j = \beta_j'(\omega_0) L,$$

$\beta_j'(\omega)$ being the derivative of $\beta_j(\omega)$ w.r.t. ω, but also modulated by a mode-dependent and frequency-dependent random phase. Once again the randomness comes from the same fractional Brownian motion for all the propagating modes.

3.2 Paraxial approximation and fractional Itô-Schrödinger equation

In this section, a full ambient physical space is considered, and two particular asymptotic behaviors are described: the paraxial approximation and the fractional white-noise limit. In contrast with

Chap. 2, where we initially examine the paraxial approximation formally and then proceed with the analysis of the stochastic aspects separately, both of the limits are here obtained under the same limit. Considering both of these aspects under a single limit is much more challenging mathematically than considering two distinct limits.

The first aspect is the paraxial (parabolic) approximation, which is valid when the wave predominantly propagates in a specific direction (here the z-direction) and is sufficiently collimated around it. In the frequency domain, the 3D Helmholtz equation is reduced to 2D Schrödinger equation where the variable along the primary propagation axis takes the role of the evolution variable. This approximation offers a considerable advantage as it transforms a boundary value problem into an evolution problem with lower spatial dimensions. In homogeneous media, deriving the paraxial wave equation is relatively straightforward and involves an asymptotic expansion of the principal symbol of the operator describing the propagation (here the one of the scalar wave equation). However, the situation becomes significantly more complex in heterogeneous media since the interaction with the medium generates some backscattering and a coupling with the evanescent modes. To justify the paraxial approximation under such conditions, one must rely on specific features of the medium, for instance small amplitudes of the fluctuations [24], or oscillatory behaviors [10, 83]. The second limit corresponds to a non-central limit type result arising from the long-range dependencies of the propagation medium. In case of short-range correlations, the random medium fluctuations are then asymptotically statistically equivalent to a white-noise w.r.t. the main propagation axis. The resulting limiting model corresponds to an Itô-Schrödinger equation, as derived in [83], and studied mathematically in detail in [58].

This section depicts the rigorous simultaneous derivation of the paraxial and the (fractional) white-noise approximations in the context of random media with long-range correlations w.r.t. the z-direction. Heuristically, the limiting classical white noise obtained in [83] is replaced by a fractional white noise, leading to a fractional Itô-Schrödinger equation. From the mathematical viewpoint, this is a significantly more difficult problem than the ones addressed in [10, 83]. As already discussed earlier in this manuscript, the martingale techniques used in [10, 83] and standard approximation-diffusion theorems do not apply, and we make use of moment techniques inspired from [15, 66] which are fairly involved analytically. The proof also involves a fine analysis of the backscattering and the coupling between the propagating and evanescent modes. Note as well that the existence theory for the fractional Itô-Schrödinger equation is not trivial, and leads to some additional difficulties in the asymptotic theory.

3.2.1 Paraxial scaling regime

To introduce an appropriate parameter scaling regime under which the paraxial approximation is valid, some assumptions are required on the source term and the random medium fluctuations. Going back to the wave equation (3.1), under a dimensionless setting, the source term is assumed to be of the form

$$F(t,z,\mathbf{x}) := f\Big(\frac{t}{\lambda},\frac{\mathbf{x}}{r_0}\Big)\delta(z-L_S)\mathbf{e}_z,$$

modeling a source located in the plane $z = L_S < 0$, and emitting a pulse in the z-direction with profile f (see Fig. 3.1), central wavelength λ, and transverse width r_0. The wave-speed profile is assumed to be of the form:

$$\frac{1}{c^2(z,\mathbf{x})} := \begin{cases} \dfrac{1}{c_0^2}\left(1+\sigma\nu\Big(\dfrac{z}{l_c},\dfrac{\mathbf{x}}{l_c}\Big)\right) & \text{if} \quad z\in[0,L], \\ \dfrac{1}{c_0^2} & \text{if} \quad z\in(-\infty,0)\cup(L,\infty), \end{cases}$$

for $\mathbf{x}\in\mathbb{R}^2$, and where c_0 stands for the background (constant) velocity. The correlation length of the fluctuations l_c can be seen as their typical scale of variation, and σ characterizes the order of magnitude of these fluctuations. To introduce a high-frequency regime, the central wavelength λ is assumed to be small compared to the propagation distance L_z:

$$\varepsilon^2 := \frac{\lambda}{L_z} \ll 1.$$

Strong interactions between the wave and the medium fluctuations are obtained by assuming

$$r_0 \sim l_c, \qquad \text{and} \qquad \frac{\lambda}{l_c} \sim \varepsilon.$$

We also assume

$$\frac{r_0^2}{\lambda} \sim L_z,$$

so that the Rayleigh length is of order the propagation distance, which is crucial to derive the paraxial approximation. In fact, the Rayleigh length is defined as the distance from the beam waist to the place where its cross-section is doubled, and in homogeneous media it is of order r_0^2/λ. For simplicity in the presentation, we set

$$L_z = L \sim 1, \qquad \lambda = \varepsilon^2, \qquad l_c = \varepsilon, \qquad \text{and} \qquad r_0 = \varepsilon. \tag{3.7}$$

Both the paraxial approximation and the non-central limit type result (fractional white-noise approximation) are obtained by sending ε to 0.

Finally, the strength of the fluctuations is assumed to be small (weak scattering regime)

$$\sigma = \varepsilon^s, \qquad \text{with} \qquad s = 2 - \frac{\gamma}{2}. \tag{3.8}$$

Note that this approach is equivalent to the ones introduced in the previous section and Chap. 2 where the parameter s was related to the propagation distance [15]. The parameter $\gamma \in (0,1)$ still describes the decay rate of the correlation function

$$\mathbb{E}[\nu(z+z',\mathbf{x})\nu(z',\mathbf{y})] \underset{|z|\to\infty}{\sim} \frac{R_0}{|z|^\gamma} R(\mathbf{x}-\mathbf{y}).$$

As for the previous section, while not being restrictive, similar technical assumptions need to be set on ν to be compatible with a moment technique. The precise assumptions are omitted here, and we refer to [95] for their complete descriptions.

3.2.2 Main result and properties

Under the scaling (3.7) and (3.8), the original wave problem (3.1) becomes

$$\Delta p_\varepsilon - \frac{1}{c_0^2}\Big(1 + \varepsilon^s V\Big(\frac{z}{\varepsilon}, \frac{\mathbf{x}}{\varepsilon}\Big)\mathbf{1}_{(0,L)}(z)\Big)\partial_{tt}^2 p_\varepsilon = f\Big(\frac{t}{\varepsilon^2}, \frac{\mathbf{x}}{\varepsilon}\Big)\delta'(z - L_S).$$

The main result of this section concerns the asymptotic description of the pulse front exiting from the random section at $z = L$. It is defined by

$$p_L^\varepsilon(t,\mathbf{x}) = p\Big(\lambda t + \frac{L - L_S}{c_0}, L, r_0\mathbf{x}\Big) = p\Big(\varepsilon^2 t + \frac{L - L_S}{c_0}, L, \varepsilon\mathbf{x}\Big),$$

and it corresponds to the wave observed on a time window of order the pulse width centered around the expected arrival time, and at the transverse scale of the source profile.

Theorem 3.2.1 *The family $(p_L^\varepsilon)_\varepsilon$ converges in law in the space $\mathcal{C}^0((-\infty,+\infty), L^2(\mathbb{R}^2)) \cap L^2((-\infty,+\infty)\times\mathbb{R}^2)$, as $\varepsilon \to 0$, to a limit given by*

$$p_L^0(t,\mathbf{x}) = \frac{1}{2\pi}\int e^{-i\omega t}\Psi_\omega(L,\mathbf{x})d\omega,$$

where Ψ_ω is the unique pathwise solution to the fractional Itô-Schrödinger equation

$$d\Psi_\omega(z,\mathbf{x}) = \frac{i}{2k_\omega}\Delta_{\mathbf{x}}\Psi_\omega(z,\mathbf{x}) + ik_\omega\Psi_\omega(z,\mathbf{x})dW_{\mathfrak{H}}(z,\mathbf{x}) = 0. \tag{3.9}$$

Here, $k_\omega = \omega/c_0$, $W_{\mathfrak{H}}$ is a random mixture of fractional Brownian fields with Hurst index $\mathfrak{H}$ and covariance operator given by

$$\mathbb{E}[W_{\mathfrak{H}}(z_1,\mathbf{x})W_{\mathfrak{H}}(z_2,\mathbf{y})] = \frac{R_0(\mathbf{x}-\mathbf{y})}{2\mathfrak{H}(2\mathfrak{H}-1)}\big(z_1^{2\mathfrak{H}} + z_2^{2\mathfrak{H}} - |z_1 - z_2|^{2\mathfrak{H}}\big),$$

for all $z_1, z_2 \in [0,+\infty)$ and $\mathbf{x},\mathbf{y} \in \mathbb{R}^2$.

The notion of solution for this fractional Itô-Schrödinger equation is made precise in the next section. As for the waveguide, due to a negligible backscattering the energy carried by the pulse is conserved at the end of the random section, that is

$$\|p_L^0\|_{L^2((-\infty,+\infty)\times\mathbb{R}^2)} = \frac{1}{2}\|f\|_{L^2((-\infty,+\infty)\times\mathbb{R}^2)}.$$

Moreover, all the moments

$$\mathbb{E}\Big[\Big\langle \prod_{j_1=1}^{M_1} \Psi_{\omega_{1,j_1}}(z) \prod_{j_2=1}^{M_2} \overline{\Psi_{\omega_{2,j_2}}(z)}, \varphi \Big\rangle_{L^2(\mathbb{R}^{2(M_1+M_2)})}\Big],$$

for all $(M_1, M_2) \in \mathbb{N}^2$, distinct frequencies $(\omega_{i,j_i})_{(i,j_i)\in\{1,2\}\times\{1,\dots,M_i\}}$, and test function $\varphi \in L^2(\mathbb{R}^{2(M_1+M_2)})$, can be explicitly computed through classical Born series (see [120, Sect. 17.2]). These moments are important in imaging applications where they help to quantify the stability of reconstructions with respect to changes in the random medium [19, 20, 39, 86].

3.2.3 Stochastic integral and fractional Itô-Schrödinger equation

The stochastic integral w.r.t. a fractional noise $W_{\mathfrak{H}}$ in the limiting fractional Itô-Schrödinger equation (3.9) is of pathwise type. It is defined here according to the work of Zähle [211] and the approach of [156, 168]. To defined this integral we introduce the Banach space

$$W^\alpha(0, L, B) := \Big\{\psi \in \mathcal{C}^0([0, L], B) \quad \text{such that} \quad \|\psi\|_{\alpha,B} < +\infty\Big\},$$

with

$$\|\phi\|_{\alpha,B} := \sup_{z\in[0,L]} \Big[\|\phi(z)\|_B + \int_0^z \frac{\|\phi(z) - \phi(u)\|_B}{(z-u)^{\alpha+1}} du\Big],$$

and where B is a given Banach space. For $\beta \in (0, 1)$, we denote by $\mathcal{C}^\beta([0, L], B)$ the Banach space of β-Hölder functions on $[0, L]$ with values in B, and equipped with

$$\|\phi\|_{\beta,\mathcal{C},B} := \sup_{z\in[0,L]} \|\phi(z)\|_B + \sup_{0\le v<u\le L} \frac{\|\phi(u) - \phi(v)\|_B}{(u-v)^\beta}.$$

Note that for $\alpha \in (0, 1/2)$, we have

$$\|\phi\|_{\alpha,B} \le \Big(1 + \frac{L^{1-2\alpha}}{1-2\alpha}\Big)\|\phi\|_{1-\alpha,\mathcal{C},B} \quad \text{so that} \quad \mathcal{C}^{1-\alpha}([0, L], B) \subset W^\alpha(0, L, B). \tag{3.10}$$

Now, for $\alpha \in (0, 1)$ and $z \in (0, L)$, we introduce, for a real-valued function f, the so-called Weyl's derivative:

$$D^\alpha_{0+}\phi(z) := \frac{1}{\Gamma(1-\alpha)}\Big[\frac{\phi(z)}{z^\alpha} + \alpha\int_0^z \frac{\phi(z) - \phi(u)}{(z-u)^{\alpha+1}} du\Big],$$
$$D^\alpha_{L^-}\phi(z) := \frac{(-1)^\alpha}{\Gamma(1-\alpha)}\Big[\frac{\phi(z)}{(L-z)^\alpha} + \alpha\int_z^L \frac{\phi(z) - \phi(u)}{(u-z)^{\alpha+1}} du\Big],$$

whenever these quantities are well-defined, and where Γ is the standard Gamma function. Following the idea of [211], the generalized Stieljes integral of a function $\phi \in \mathcal{C}^\nu([0, L], \mathbb{R})$ with respect to $\psi \in \mathcal{C}^\mu([0, L], \mathbb{R})$, with $\nu + \mu > 1$, $\nu > \alpha$, and $\mu > 1 - \alpha$ is defined by

$$\int_0^L \phi d\psi := (-1)^\alpha \int_0^L D^\alpha_{0+}\phi(u) D^{1-\alpha}_{L^-}\psi_{L^-}(u) du, \tag{3.11}$$

where

$$\psi_{L^-}(u) := \psi(u) - \psi(L^-).$$

This definition does not depend on α, and we have

$$\int_0^z \phi d\psi = \int_0^L \phi \mathbf{1}_{(0,z)} d\psi.$$

Moreover, according to [168], this integral can be extended to more general classes of function thanks to the inequality

$$\Big| \int_0^L \phi d\psi \Big| \leq \|\phi\|_{\alpha,1} \Lambda_\alpha(\psi),$$

where

$$\|\phi\|_{\alpha,1} := \int_0^L \Big(\frac{|\phi(u)|}{u^\alpha} + \int_0^u \frac{|\phi(u)-\phi(v)|}{(u-v)^{\alpha+1}} dv \Big) du,$$

and

$$\Lambda_\alpha(\psi) := \frac{1}{\Gamma(1-\alpha)\Gamma(\alpha)} \sup_{0<u<z<L} |D_{z-}^{1-\alpha} \psi_{z^-}(u)|.$$

Consequently, this integral is well-defined as soon as $\phi \in W^\alpha(0,L,\mathbb{R})$ and $\Lambda_\alpha(\psi) < \infty$.

As a result, for a random function $F \in W^\alpha(0,L,L^2(\mathbb{R}^2))$, the stochastic integral with respect to the fractional field $W_{\mathfrak{H}}$,

$$\int_0^z F(u,\mathbf{x}) dW_{\mathfrak{H}}(u,\mathbf{x}),$$

is defined by (3.11) almost everywhere in $\mathbf{x}$ and $\mathbb{P}$-almost surely. In fact, for all $\alpha \in (1-\mathfrak{H}, 1/2)$ and $z \in [0,L]$, we have

$$\Big\| \int_0^z F(u) dW_{\mathfrak{H}}(u) \Big\|_{L^2(\mathbb{R}^2)} \leq C \|F\|_{W^\alpha(0,L,L^2(\mathbb{R}^2))} \sup_{\mathbf{x}\in\mathbb{R}^2} \Lambda_\alpha(W_H(\mathbf{x})),$$

knowing that

$$\mathbb{E}\Big[\sup_{\mathbf{x}\in\mathbb{R}^2} \Lambda_\alpha(W_{\mathfrak{H}}(\mathbf{x})) \Big] < \infty.$$

The fractional Itô-Schrödinger equation. The definition of a solution for the fractional Itô-Schrödinger equation (3.9) is made precise in the definition below, but first let us introduce some additional notations. Let $k \in \mathbb{N}^*$, and $H^k(\mathbb{R}^2)$ be the k-th Sobolev space on $\mathbb{R}^2$. Consider also $W_k^\alpha(0,L) := W^\alpha(0,L,H^k(\mathbb{R}^2))$, equipped with the norm $\|\cdot\|_{\alpha,H^k(\mathbb{R}^2)}$, and the complete metric space

$$W_\infty^\alpha(0,L) := \bigcap_{k\in\mathbb{N}^*} W_k^\alpha(0,L),$$

equipped with

$$d_{\alpha,\infty}(\phi,\psi) := \sum_{k\geq 1} \frac{1}{2^k} \left(1 \wedge \|\phi-\psi\|_{\alpha,H^k(\mathbb{R}^2)} \right).$$

Definition 3.2.1 *Let $\mathfrak{H} \in (1/2,1)$ and $\alpha \in (1-\mathfrak{H}, 1/2)$. We say that $\Psi_\omega \in W_\infty^\alpha(0,L)$ is a pathwise solution of* (3.9) *if, with probability one, for all $(z,\mathbf{x}) \in [0,L]\times\mathbb{R}^2$, we have*

$$\Psi_\omega(z,\mathbf{x}) = \Psi_\omega(0,\mathbf{x}) + \frac{i}{2k_\omega} \int_0^z \Delta_{\mathbf{x}} \Psi_\omega(u,\mathbf{x}) du + ik_\omega \int_0^z \Psi_\omega(u,\mathbf{x}) dW_{\mathfrak{H}}(u,\mathbf{x}).$$

In other words, a solution to (3.9) is a pointwise solution of this equation for almost all realizations. It is worth mentioning that a solution to (3.9) has automatically Hölder regularity

$$\Psi_\omega \in \mathcal{C}_\infty^{\mathfrak{H}-\theta}(0,L) := \bigcap_{k\in\mathbb{N}^*} \mathcal{C}^{\mathfrak{H}-\theta}([0,L],H^k(\mathbb{R}^2)) \quad \text{with} \quad \theta = \mathfrak{H}+\alpha-1.$$

Here, $\mathcal{C}_\infty^{\mathfrak{H}-\theta}(0,L)$ is a complete metric space equipped with

$$d_{\mathfrak{H}-\theta,\mathcal{C},\infty}(\phi,\psi) := \sum_{k\geq 1} \frac{1}{2^k} \left(1 \wedge \|\phi-\psi\|_{\mathfrak{H}-\theta,\mathcal{C},H^k(\mathbb{R}^2)} \right),$$

so that $\mathcal{C}_\infty^{\mathfrak{H}-\theta}(0,L) \subset W_\infty^\alpha(0,L)$ according to (3.10). In the proof of Thm. 3.2.1, $\Psi_\omega(z=0)$ is assumed to belong to all the $H^k(\mathbb{R}^2)$'s in order to apply a fixed point type argument. This is the reason why intersections with all the $H^k(\mathbb{R}^2)$'s are involved in Def. 3.2.1.

Finally, note that the stochastic integral is here the fractional equivalent to the Itô-Stratonovich integral for a standard Brownian motion, and as such satisfies the classical integration by parts formula. This formally yields the conservation relation: for all $z \in [0,L]$,

$$\|\Psi_\omega(z)\|_{L^2(\mathbb{R}^2)} = \|\Psi_\omega(0)\|_{L^2(\mathbb{R}^2)}.$$

3.3 Effective fractional paraxial wave equation

In various contexts such as geophysics, laser beam propagation through the atmosphere, or medical imaging for instance, frequency-dependent attenuations have been observed at rates proportional to

$$|\omega|^\lambda \qquad \lambda \in (0,2), \tag{3.12}$$

for a given angular frequency ω [62,77,90,101,116,130,166,190]. Depending on the field of application, this type of power-law attenuation can be referred to as anomalous diffusion, nonexponential relaxation, inelastic damping, hysteric damping, singular hereditary, or singular memory media [49]. The development of accurate wave propagation models exhibiting power-law attenuations is therefore of great importance for applications in imaging and inverse problems (see [162] for a survey focusing on medical applications and references therein). To capture such power-law decays, several models have been proposed involving fractional derivatives (see [46, 89, 110, 116, 162, 177, 198, 199] for instance). A particular attention has been paid to space-time models as they enable numerical simulations of a wide range of boundary value problems [109] and can be more straightforward to implement and less costly [210] compared to frequency-domain models.

An alternative approach, which has gained more attention recently, involves randomly perturbed propagation media with fractal correlation structures or long-range dependencies (see [84, 85, 191] and [116, Chap. 9]). This section aims at describing a mathematical derivation, from first principles of physics, of a paraxial wave equation exhibiting a power-law attenuation (3.12) with exponent $\lambda \in (1,2]$, in the context of random propagation media with long-range correlations. Both aspects, paraxial approximation and random medium fluctuations with long-range correlations, are again considered under the same limit. The case of mixing random fluctuations is also discussed for comparison. The two previous sections, based on non-central limit type results and corresponding to [153, 154] for 1D propagation media, do not provide any power-law attenuation in frequency. To obtain such a property, we rather consider a central limit theorem scaling within the context of long-range correlations, which presents mathematical challenges. This approach has been explored for 1D propagation media [84,85], but the method used to exhibit a power-law attenuation of the form (3.12) does not seem to apply in a 3D setting. For technical reasons similar to those of Chap. 1, the random fluctuations of the propagation medium are here driven by (1.6). Despite this restrictive assumption, compared to [84,85], the approach we propose can also be applied to more general 3D settings with non-layered fluctuations, at the cost of additional technical difficulties. Nevertheless, more general fluctuation models with long-range correlations should not change the overall results as the asymptotic equation and scattering coefficients depend only on the correlation function of the fluctuation model, and not its precise definition.

As already pointed out, the scaling associated to the central limit theorem can be seen as propagating the non-central limit scaling over longer propagation distances. This latter scaling, which already leads to an effective phase modulation driven by a fractional Brownian motion, results in waves undergoing very fast oscillations over extended propagation distances, and then have to be treated appropriately to still exhibit effective nontrivial effects. In Chap. 1, we look at the energy of the Hamiltonian system (1.13) to exhibit the diffusion effects. For the random Schrödinger equation the Wigner transform is used to study the energy density propagation by analyzing the correlations of the wave function. The quadratic nature of the Wigner transform w.r.t. the wave function naturally cancels out some rapid phases, and provides an effective description of the energy propagation [92,93]. For classical wave propagation problems, a similar approach consists in looking at the wave-front along a proper random characteristic time-frame. The rapid phases still produce some effects by averaging the stochasticity to obtain a deterministic spreading for the wave-front [84, 85].

3.3.1 The random fluctuations

As for Sect. 3.1 and 3.2, the scalar wave model (3.1) is considered, but here with $\mathcal{D} = \mathbb{R}^2$. The main difference w.r.t. the two previous sections lies in the wave-speed profile, which has here the form

$$\frac{1}{c^2(z)} := \frac{1}{c_0^2}\Big(1 + \nu\Big(\frac{z}{l_c}\Big)\mathbf{1}_{(0,L)}(z)\Big), \tag{3.13}$$

representing a randomly layered propagation medium. For this section, the random fluctuations are assumed to be of the form

$$\nu(z) := \Theta(\sigma V(z)).$$

Here, Θ is an odd smooth bounded function with

$$\theta_0' := \Theta'(0) \neq 0 \qquad \text{and} \qquad \sup|\Theta| < 1,$$

and V is the mean-zero stationary Gaussian random process given by (1.6) satisfying

$$\mathbb{E}[V(z+z')V(z')] \underset{|z|\to+\infty}{\sim} \frac{R_0}{|z|^\gamma}. \tag{3.14}$$

The function Θ plays no significant role here. Gaussian random processes being not bounded, this function just guarantees, for a modelization purpose, that $c^2(z)$ is actually always positive (see (3.13)). For σ small enough, the Taylor expansion

$$\Theta(\sigma V(z)) = \sigma V(z)\theta_0' + \mathcal{O}(\sigma^3)$$

($\Theta''(0) = 0$ since Θ is odd) indicates that the medium fluctuations are driven by V.

As in Sect. 1.3.2 of Chap. 1, for the sake of mathematical tractability, a specific form for V is considered. More general fluctuation models have been considered in [153, 154], but the proposed method, based on the rough-path theory, does not seem to apply in the scaling regime described in the next section.

3.3.2 Scaling regime

The scaling regime considered in this section corresponds to the one proposed in [84], and is slightly different from the one of Sect. 3.1 and 3.2. The high-frequency regime is here described by

$$\varepsilon^2 := \frac{\lambda}{L} \ll 1,$$

and both the correlation length and the central wavelength are of the same order

$$l_c \sim \lambda,$$

providing a full interaction between the random fluctuations and the propagating waves. For the paraxial approximation to be valid, we assume that the Rayleigh length is of order the propagation distance,

$$\frac{r_0^2}{\lambda} \sim L.$$

Finally, the strength of the fluctuations is assumed to be small to place ourselves in a weak scattering regime,

$$\sigma \ll 1.$$

To fix the ideas, we set

$$L \sim 1, \qquad \lambda = l_c = \varepsilon^2, \qquad \text{and} \qquad r_0 = \sigma = \varepsilon,$$

where the choice of $\sigma = \varepsilon$ corresponds to the scaling of the central-limit theorem. This choice allows us to derive a nontrivial limit for both short-range and long-range correlations.

Under this scaling the wave equation (3.1) reads now

$$\Delta p_\varepsilon - \frac{1}{c_\varepsilon^2(z)}\partial_{tt}^2 p_\varepsilon = f\Big(\frac{t}{\varepsilon^2}, \frac{\mathbf{x}}{\varepsilon}\Big)\delta(z) \qquad (t, \mathbf{x}, z) \in \mathbb{R}\times\mathbb{R}^2\times\mathbb{R},$$

with

$$\frac{1}{c_\varepsilon^2(z)} = \frac{1}{c_0^2}\Big(1 + \nu_\varepsilon\Big(\frac{z}{\varepsilon^2}\Big)\mathbf{1}_{(0,L)}(z)\Big), \qquad \text{and} \qquad \nu_\varepsilon(z) := \Theta\big(\varepsilon V(z)\big).$$

3.3.3 Main results

The main result of this section is obtained following the strategy of [84,85]. We introduce the random travel time

$$T_\varepsilon(L) := \frac{L}{c_0} + \frac{1}{2c_0}\int_0^L \nu_\varepsilon(z/\varepsilon^2)dz,$$

which corresponds to the expected travel time L/c_0 with a random correction, and the wave-front

$$p^L_{tr,\varepsilon}(s,\mathbf{y}) := p_\varepsilon\big(T_\varepsilon(L) + \varepsilon^2\, s, \varepsilon\,\mathbf{y}, L\big) \qquad (s,\mathbf{y}) \in \mathbb{R}\times\mathbb{R}^2. \tag{3.15}$$

This wave-front corresponds to the wave observed at the end of the random section ($z = L$), on a time window corresponding to the pulse width ε^2, and centered at the random travel time $T_\varepsilon(L)$.

Before stating the main result, we introduce some notations. First, the Fourier convention considered in this section is the following:

$$\hat f(\omega,\kappa) := \iint f(s,\mathbf{y})e^{i\omega(s-\kappa\cdot\mathbf{y})}ds\,d\mathbf{y},$$

and

$$f(s,\mathbf{y}) := \frac{1}{(2\pi)^3}\iint \hat f(\omega,\kappa)e^{-i\omega(s-\kappa\cdot\mathbf{y})}\omega^2 d\omega\,d\kappa,$$

which is convenient to study space-time problems. Second, we introduce

$$\mathcal{S}_0(\mathbb{R}\times\mathbb{R}^2) = \Big\{\psi\in\mathcal{S}(\mathbb{R}\times\mathbb{R}^2): \quad \int\psi(s,\mathbf{y})ds = 0, \quad \forall\mathbf{y}\in\mathbb{R}^2\Big\},$$

where $\mathcal{S}(\mathbb{R}\times\mathbb{R}^2)$ stands for the Schwartz class, and $\mathcal{S}'_{0,s,\mathbf{y}}(\mathbb{R}\times\mathbb{R}^2)$ the set of tempered distributions restricted to $\mathcal{S}_0(\mathbb{R}\times\mathbb{R}^2)$ w.r.t. the variables s and $\mathbf{y}$. This restriction to $\mathcal{S}_0(\mathbb{R}\times\mathbb{R}^2)$ is required for the paraxial wave equation (3.18) to be well-posed. One can remark that the source term f belongs to $\mathcal{S}_0(\mathbb{R}\times\mathbb{R}^2)$ as soon as its Fourier transform does not support the frequency $\omega = 0$. Below, $\mathcal{C}^0_z$ (reps. $\mathcal{C}^1_z$) stands for the set of $\mathcal{C}^0$-functions (resp. $\mathcal{C}^1$-functions) w.r.t. the z-variable.

Theorem 3.3.1 *The family $(p^L_{tr,\varepsilon})_\varepsilon$ converges in probability in $\mathcal{C}(\mathbb{R}\times\mathbb{R}^2)$, as $\varepsilon\to 0$, to*

$$p^L_{tr}(s,\mathbf{y}) = \frac{1}{2}\mathcal{K}(\cdot,\cdot,L) * f(s,\mathbf{y}) \qquad (s,\mathbf{y})\in\mathbb{R}\times\mathbb{R}^2, \tag{3.16}$$

where, in the Fourier domain,

$$\hat{\mathcal{K}}(\omega,\kappa,z) := e^{-\theta_0'^2\omega^2(\Gamma_c(\omega)+i\Gamma_s(\omega))z/(8c_0^2)}e^{-i\omega c_0|\kappa|^2 z/2}, \tag{3.17}$$

with

$$\Gamma_c(\omega) := 2\int_0^\infty R(s)\cos\Big(\frac{2\omega s}{c_0}\Big)ds \qquad \textit{and} \qquad \Gamma_s(\omega) := 2\int_0^\infty R(s)\sin\Big(\frac{2\omega s}{c_0}\Big)ds.$$

Here, R is the correlation function of the medium fluctuations (1.7)*. The convolution kernel $\mathcal{K}$ is the unique solution in $\mathcal{C}^0_z([0,\infty),\mathcal{S}'_{0,s,\mathbf{y}}(\mathbb{R}\times\mathbb{R}^2))\cap\mathcal{C}^1_z((0,\infty),\mathcal{S}'_{0,s,\mathbf{y}}(\mathbb{R}\times\mathbb{R}^2))$ of the paraxial wave equation*

$$\partial^2_{sz}\mathcal{K} - \frac{c_0}{2}\Delta_{\mathbf{y}}\mathcal{K} - \mathcal{I}(\mathcal{K}) = 0, \tag{3.18}$$

with $\mathcal{K}(s,\mathbf{y},z=0) = \delta(s)\delta(\mathbf{y})$, and

$$\mathcal{I}(\phi)(s) := \frac{\theta_0'^2}{8c_0^2}\int_{-\infty}^s R\Big(\frac{c_0(s-\tau)}{2}\Big)\partial^3_{sss}\phi(\tau)d\tau \qquad s\in\mathbb{R}. \tag{3.19}$$

The asymptotic transmitted wave-front p^L_{tr}, at the end of the random section ($z = L$), can be written in term of a convolution where $\mathcal{K}$ represents the pulse deformation. From the explicit formulation of $\mathcal{K}$ in the Fourier domain, the pulse shape is affected in a way which is consistent with the standard ODA theory [70, Chap. 8], even if we are not considering fluctuations with short-range correlations. Typically, according to this theory, the transmitted pulse exhibits a deterministic spreading characterized by a frequency-dependent attenuation and phase modulation. Here, these effects are given

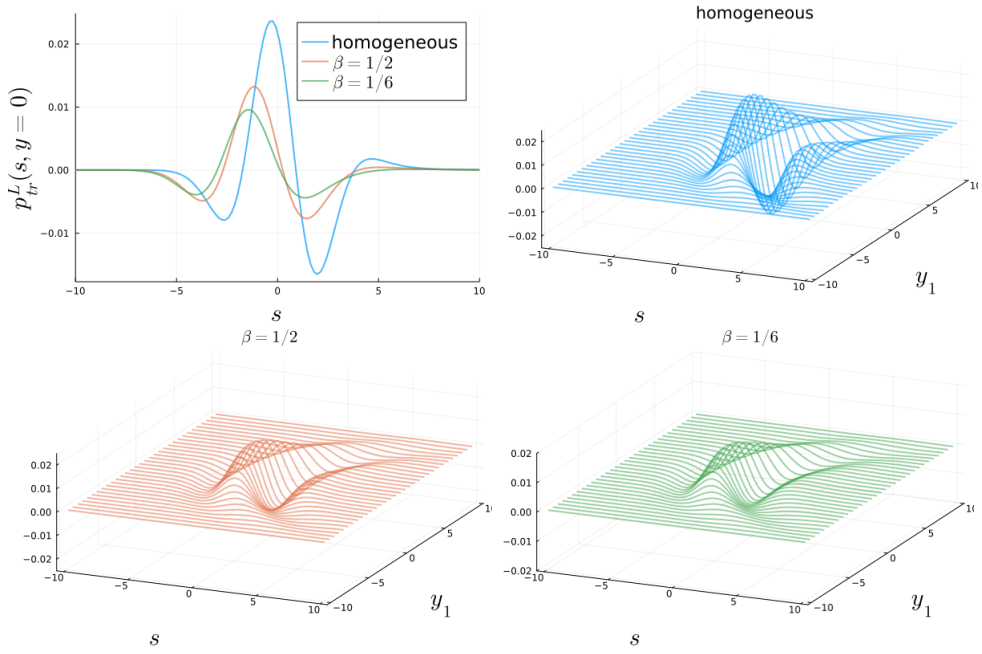

Fig. 3.3: Illustrations of the profile $p^L_{tr}(s, y_1, y_2 = 0)$ in the homogeneous case (blue lines) and for two values of β ($\beta = 1/2$ for the orange curves and $\beta = 1/6$ for the green curves). We take $\alpha = 1/4$, $\mu = 2$, $a(p) = \mathbf{1}_{(-10,10)}(p)$, $L = 5$, $c_0 = \theta_0' = 1$ and a source profile given by $\hat{f}(\omega, \kappa) = 2\omega^2 e^{-\omega^2(1+\kappa^2)}$ centered at $s = 0$ in the time domain for simplicity.

through $\omega^2\Gamma_c(\omega)$ (which is positive thanks to the Bochner theorem) and $\omega^2\Gamma_s(\omega)$ respectively. These two terms are well defined even for slowly decaying correlations due to the oscillatory functions. We refer to Fig. 3.3 for illustrations regarding the influence of the kernel $\mathcal{K}$ on the pulse spreading.

The standard ODA theory also provides a random time-shift driven by a standard Brownian motion, meaning that the transmitted pulse exhibits a random arrival time at $z = L$ of order the pulse width. In the context of long-range correlations the situation is more delicate. The aforementioned random time-shift is already compensated in Thm. 3.3.1 by considering the random travel time $T_\varepsilon(L)$ in (3.15). Due to the asymptotic behavior of $T_\varepsilon(L)$, which is described in the following result, this time-shift allows to remove pathological behaviors when studying the asymptotic of the transmitted wave front.

Proposition 3.3.1 *Let us defined*

$$W_\varepsilon(L) := \frac{1}{\sigma_\varepsilon}\Big(T_\varepsilon(L) - \frac{L}{c_0}\Big),$$

where

$$\sigma_\varepsilon := \begin{cases} \varepsilon^{1+\gamma} & \text{if} \quad \gamma \in (0,1), \\ \varepsilon^2 |\ln(\varepsilon)|^{1/2} & \text{if} \quad \gamma = 1, \\ \varepsilon^2 & \text{if} \quad \gamma > 1. \end{cases}$$

The family $(W_\varepsilon(L))_\varepsilon$ converges in law to a limit $W_0(L)$, as $\varepsilon \to 0$, where:

- *for $\gamma \in (0,1)$, W_0 is a fractional Brownian motion with Hurst index*

$$\mathfrak{H} = 1 - \frac{\gamma}{2} \in (1/2, 1),$$

and

$$\mathbb{E}[W_0(L)^2] = L^{2\mathfrak{H}} \frac{\theta_0'^2 R_0}{\mathfrak{H}(2\mathfrak{H}-1)};$$

- *for $\gamma \geq 1$, W_0 is a Brownian motion such that*

$$\mathbb{E}[W_0(L)^2] = L\,\theta_0'^2\Gamma_0, \qquad \textit{with} \qquad \Gamma_0 := \begin{cases} \dfrac{2a(0)}{\mu\,\beta} & \textit{if} \quad \gamma = 1, \\ \\ \Gamma_c(0) & \textit{if} \quad \gamma > 1. \end{cases}$$

For rapidly decaying correlations ($\gamma > 1$), $T_\varepsilon(L)$ can be approximated by a Gaussian variable with mean L/c_0 and a standard deviation of order the pulse width, which is consistent with the standard ODA theory. In the case of long-range correlations, $T_\varepsilon(L)$ can also be approximated by a Gaussian variable but with a standard deviation very large w.r.t. the pulse width. This is the reason why we compensate this term in (3.15), as it leads to blowing up terms in the derivation of the pulse spreading.

Regarding the backscattered signal at $z = 0$, it can be shown that

$$p_{bk,\varepsilon}(s, \mathbf{y}) := p_\varepsilon\big(\varepsilon^2 s, \varepsilon\mathbf{y}, 0\big)$$

converges in probability to 0, in $\mathcal{C}(\mathbb{R} \times \mathbb{R}^2)$, as $\varepsilon \to 0$. This is consistent with [70, Chap. 9], in which the authors show that the backscatter wave is made of a *small* amplitude incoherent signal that can be described through a random field.

In case of long-range correlations, the operator $\mathcal{I}$ can be approximated by a Weyl fractional derivative whose order depends directly on the decay rate γ of the correlation function R at infinity. The Weyl fractional derivative is given for $\gamma \in (0, 1)$ by

$$D^\gamma \phi(s) := \frac{\gamma}{\Gamma(1-\gamma)} \int_{-\infty}^{s} \frac{\phi(s) - \phi(\tau)}{(s-\tau)^{1+\gamma}} d\tau \qquad s \in \mathbb{R},$$

whenever this quantity is well-defined, and Γ stands for the Gamma function. For instance, ϕ can be a bounded γ'-Hölder function with $\gamma < \gamma'$. However, for $\mathcal{C}^1$-functions with fast enough decay at $-\infty$, the Weyl derivative can be rewritten as

$$D^\gamma \phi(s) = \frac{1}{\Gamma(1-\gamma)} \int_{-\infty}^{s} \frac{\phi'(\tau)}{(s-\tau)^{\gamma}} d\tau.$$

To define higher order derivatives, one can just set

$$D^{j+\gamma} \phi(s) := D^\gamma \phi^{(j)}(s) = \frac{1}{\Gamma(1-\gamma)} \int_{-\infty}^{s} \frac{\phi^{(j+1)}(\tau)}{(s-\tau)^{\gamma}} d\tau \qquad j \in \mathbb{N},$$

assuming ϕ smooth enough, with enough decay at $-\infty$ of its derivatives $\phi^{(j)}$. These latter requirements hold true for the kernel $\mathcal{K}$ as soon as $z > 0$ thanks to the damping term $\omega^2\Gamma_c(\omega)$ in (3.17). Therefore, (3.14) and (3.19) suggests that the integro-differential operator $\mathcal{I}$ in (3.18) can be approximated as follows,

$$\mathcal{I}(\mathcal{K}) \propto D_s^{2+\gamma}\mathcal{K}.$$

Below, we emphasis that the fractional derivative $D^{2+\gamma}$ acts on the s-variable with the notation $D_s^{2+\gamma}$. This observation can be derived by considering the scaled correlation function

$$\sigma(l_0) R(z/l_0),$$

where l_0 will be sent to 0, and

$$\sigma(l_0) := \begin{cases} \dfrac{1}{l_0^\gamma} & \text{if} \quad \gamma \in (0,1), \\ \\ \dfrac{1}{l_0|\ln(l_0)|} & \text{if} \quad \gamma = 1, \\ \\ \dfrac{1}{l_0} & \text{if} \quad \gamma > 1. \end{cases}$$

In other words, the correlation length l_0 is assumed to be small compared to the pulse duration, and we can defined the transmitted wave-front p^L_{tr,l_0} from (3.16) accordingly.

Theorem 3.3.2 *The family $(p^L_{tr,l_0})_{l_0}$ converges in $\mathcal{C}(\mathbb{R}\times\mathbb{R}^2)$, as $l_0\to 0$, to*

$$p^L_{tr,0}(s,\mathbf{y}) := \frac{1}{2}\mathcal{K}_0(\cdot,\cdot,L) * \Psi(s,\mathbf{y}) \qquad (s,\mathbf{y})\in\mathbb{R}\times\mathbb{R}^2.$$

Here, $\mathcal{K}_0$ is defined in the Fourier domain by

$$\hat{\mathcal{K}}_0(\omega,\kappa,z) := \begin{cases} e^{-\theta_0'^2\omega^2\Gamma_0 z/(8c_0^2)}e^{-i\omega c_0|\kappa|^2 z/2} & \text{if} \quad \gamma\geq 1, \\ \\ e^{-\theta_0'^2 R_0|\omega|^{1+\gamma}(\Gamma_{c,0}(\omega)+i\Gamma_{s,0}(\omega))z/(8c_0^2)}e^{-i\omega c_0|\kappa|^2 z/2} & \text{if} \quad \gamma\in(0,1), \end{cases} \tag{3.20}$$

with

$$\Gamma_{c,0}(\omega) = \Gamma(1-\gamma)\cos\Big(\frac{(1-\gamma)\pi}{2}\Big)\Big(\frac{2}{c_0}\Big)^{\gamma-1},$$
$$\Gamma_{s,0}(\omega) = \Gamma(1-\gamma)\sin\Big(\frac{(1-\gamma)\pi}{2}\Big)\Big(\frac{2}{c_0}\Big)^{\gamma-1}\mathrm{sign}(\omega),$$

and

$$\Gamma_0 := \begin{cases} \dfrac{2a(0)}{\mu\,\beta} & \text{if} \quad \gamma=1, \\ \\ \Gamma_c(0) & \text{if} \quad \gamma>1. \end{cases}$$

Moreover, $\mathcal{K}_0$ is the unique solution in $\mathcal{C}^0_z([0,\infty),\mathcal{S}'_{0,s,\mathbf{y}}(\mathbb{R}\times\mathbb{R}^2))\cap\mathcal{C}^1_z((0,\infty),\mathcal{S}'_{0,s,\mathbf{y}}(\mathbb{R}\times\mathbb{R}^2))$ of the paraxial wave equation

$$\partial^2_{sz}\mathcal{K}_0 - \frac{c_0}{2}\Delta_{\mathbf{y}}\mathcal{K}_0 - \mathcal{I}_0(\mathcal{K}_0) = 0,$$

with $\mathcal{K}_0(s,\mathbf{y},z=0)=\delta(s)\delta(\mathbf{y})$, and

$$\mathcal{I}_0(\phi) := \begin{cases} \dfrac{\theta_0'^2 R_0}{8c_0^2}\partial^3_{sss}\phi & \text{if} \quad \gamma\geq 1, \\ \\ \dfrac{\theta_0'^2 R_0\Gamma(1-\gamma)}{2^{3-\gamma}c_0^{1+\gamma}}D_s^{2+\gamma}\phi & \text{if} \quad \gamma\in(0,1). \end{cases}$$

The difference between the case $\gamma\geq 1$ and $\gamma\in(0,1)$ can easily be highlighted from this result. In the former case, $\mathcal{I}_0$ is a classical third order differential operator, while for $\gamma\in(0,1)$, it is a fractional derivative of order $2+\gamma\in(2,3)$. Moreover, even if the case $\gamma=1$ corresponds to slowly decaying correlations, the kernel $\mathcal{K}_0$ behaves as for short-range correlations $\gamma>1$. The case $\gamma=1$ plays somehow the role of a continuity point w.r.t. the order of derivation in $\mathcal{I}_0$. For long-range correlations, one can observe in (3.20) the frequency-dependent attenuation given by the power law

$$|\omega|^{1+\gamma} \qquad \gamma\in(0,1],$$

with exponent depending directly on the decay rate of the correlation function of the medium fluctuations (3.14).

3.4 Perspectives

Wave propagation in randomly perturbed media with long-range correlations exhibits interesting multiscale phenomena that differs from the standard ODA theory. While being mathematically challenging, the main perspective in this direction concerns the derivation of effective diffusion effects with random fluctuations involving the lateral variable. Although the context of a waveguide does not bring much more difficulty compared to the last section of this chapter, extending this type of result in the context of Sect. 3.2 appears to be a challenging problem. A second aspect that needs to be investigated, as in Chap. 1 and 2, concerns the restriction over the noise model. For instance, in

the context of Sect. 3.3, we are not able to capture power-law attenuations with exponent between 0 and 1. Such a case can be captured under short-range correlations with the additional anti-persistence assumption [84],

$$\int_{-\infty}^{\infty} R(z)dz = 0,$$

but our noise model (1.6) is not compatible with this assumption.

A deeper analysis of the fractional Itô-Schrödinger equation could be of interest for practical uses. In fact, due to the nature of the stochastic integral, it is not straightforward to provide a simple formulation for basic quantities such as the coherent wave (the expectation of the solution of the fractional Itô-Schrödinger equation). Even if our approach provides an explicit expression for all the order moments, the resulting formulas are quite complex. This is in contrast with the standard Itô-Schrödinger equation involving a classical Itô-Stratonovich integral, and the resulting martingale property, for which the coherent wave can easily be evaluated. As a perspective, our fractional Itô-Schrödinger equation could be investigated under the so-called scintillation or spot dancing regimes [58,86]. These asymptotics could lead to simplified expression of the resulting moments and quantities of interest.

Chapter 4

Radiative transfer with nonintegrable singular scattering kernels

Radiative transfer models have been used for more than a century to describe wave energy propagation through complex/random media [48, 124], as well as neutron transport [142, 143, 192], heat transfer [207], and are still active research subjects in astrophysics, geophysics, and optical tomography for instance [150, 167, 175, 176].

This chapter discusses interesting effects and numerical difficulties for radiative transfer models involving a singular scattering kernel:

$$\begin{cases} \partial_t u + \widehat{\mathbf{k}} \cdot \nabla_{\mathbf{x}} u = \mathcal{Q} u \\ u(t=0, \mathbf{x}, \widehat{\mathbf{k}}) = u_0(\mathbf{x}, \widehat{\mathbf{k}}) \end{cases} \qquad (t, \mathbf{x}, \widehat{\mathbf{k}}) \in (0, \infty) \times \mathbb{R}^d \times \mathbb{S}^{d-1}, \tag{4.1}$$

where $\mathbb{S}^{d-1}$ denotes the unit sphere in $\mathbb{R}^d$, and u is the wave energy density in the context of wave propagation or the particle distribution function in the context of neutronics. The scattering operator $\mathcal{Q}$ has the standard form

$$(\mathcal{Q}u)(\widehat{\mathbf{k}}) = \int_{\mathbb{S}^{d-1}} \Phi(|\widehat{\mathbf{p}} - \widehat{\mathbf{k}}|)(u(\widehat{\mathbf{p}}) - u(\widehat{\mathbf{k}}))\sigma(d\widehat{\mathbf{p}}),$$

where $\sigma(d\widehat{\mathbf{p}})$ stands for the surface measure on $\mathbb{S}^{d-1}$. Here, the scattering kernel Φ is assumed to be of the form

$$\Phi(|\widehat{\mathbf{p}} - \widehat{\mathbf{k}}|) := \frac{a(|\widehat{\mathbf{p}} - \widehat{\mathbf{k}}|)}{|\widehat{\mathbf{p}} - \widehat{\mathbf{k}}|^{d-1+\alpha}} = F(\widehat{\mathbf{k}} \cdot \widehat{\mathbf{p}}),$$

with

$$F(s) := \frac{a\big(\sqrt{2(1-s)}\big)}{(2(1-s))^{(d-1+\alpha)/2}}, \qquad s \in [-1, 1), \qquad \alpha \in (0, 2),$$

and a is a nonnegative function. The difficulty in this situation resides in the vanishing of the mean free time t_0 associated with $\mathcal{Q}$:

$$\frac{1}{t_0} = \int_{\mathbb{S}^{d-1}} \Phi(|\widehat{\mathbf{k}} - \widehat{\mathbf{p}}|)\sigma(d\widehat{\mathbf{p}}) = \infty. \tag{4.2}$$

In the context of gas dynamics and the Boltzmann equation, a singular collision operator refers to the so-called non cut-off case [3, 206], where the particle interactions have long-range properties. Such a scenario also arises in the context of highly peaked-forward light scattering in biological tissues, in turbulent atmosphere, or more generally in the context of wave propagation in random media with long-range correlations.

Here are some examples for $d = 3$. When the momentum variable is restricted to the unit sphere, radiative transfer equations (RTEs) can be derived from high-frequency wave propagation in random

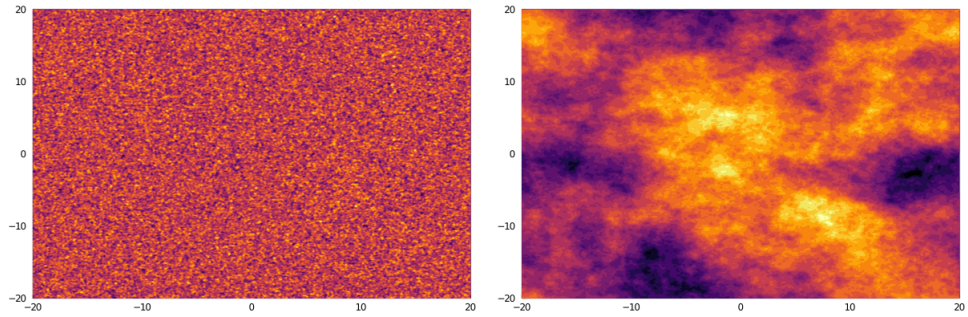

Fig. 4.1: Realizations of Gaussian random fields (for $d = 2$) with correlation function (4.3). The left picture represents a field with short-range correlations, while the right picture depicts a field with long-range correlations with $\alpha = 0.999$.

media to describe the energy density propagation [12, 45, 180]. In such a context, the velocity field $c(\mathbf{x})$ has the form

$$c^2(\mathbf{x}) = c_0^2\Big(1 + \sqrt{\varepsilon}\, V\Big(\frac{\mathbf{x}}{\varepsilon}\Big)\Big) \qquad \mathbf{x} \in \mathbb{R}^3,$$

where V is a mean-zero random field modeling fluctuations around the background velocity c_0. A singular scattering kernel can then be obtained by considering a correlation function of the form

$$\mathbb{E}[V(\mathbf{x})V(\mathbf{y})] = R(\mathbf{x}-\mathbf{y}) = \int \frac{a(|\mathbf{p}|)}{|\mathbf{p}|^{2+\alpha}} e^{i\mathbf{p}\cdot(\mathbf{x}-\mathbf{y})} d\mathbf{p}. \tag{4.3}$$

However, such a formula holds only for $\alpha < 1$. The Fourier transform of R being singular at $\mathbf{p} = 0$ (unbounded), the correlation function R cannot be integrable, and more precisely we have $R(\mathbf{x}) \sim 1/|\mathbf{x}|^{1-\alpha}$. This situation corresponds to a random media with long-range correlations where a realization is provided in Fig. 4.1. Because of the long-range correlations one can observe significantly larger statistical patterns than for short-range correlations. In the context of neutronics and light scattering by biological tissues, the following Gegenbauer scattering kernel ρ_G and Henyey-Greenstein (HG) kernel ρ_{HG} are commonly used in the peaked-forward regime [114, 123, 178]:

$$F_G(s) := \frac{\alpha\, g\, (1 + g^2 - 2g\, s)^{-1-\alpha/2}}{2\pi((1-g)^{-\alpha} - (1+g)^{-\alpha})}, \qquad F_{HG}(s) := \frac{1}{4\pi}\frac{1-g^2}{(1+g^2-2g\, s)^{3/2}}. \tag{4.4}$$

The parameter $g \in (-1, 1)$ is called the anisotropy factor. The case $g = 0$ corresponds to isotropic energy transfer over the unit sphere, $g < 0$ to dominant transfer in the backward direction, and $g > 0$ to forward energy transfer. The peaked forward regime is obtained in the limit $g \to 1$, for which

$$\frac{1}{(1-g)^\alpha} F_G(\widehat{\mathbf{k}}\cdot\widehat{\mathbf{p}}) \underset{g\to 1}{\sim} \frac{\alpha}{2\pi(2 - 2\widehat{\mathbf{k}}\cdot\widehat{\mathbf{p}})^{1+\alpha/2}} = \frac{\alpha}{2\pi|\widehat{\mathbf{k}} - \widehat{\mathbf{p}}|^{2+\alpha}}. \tag{4.5}$$

A typical realization of the corresponding random field in 2D, as $g \to 1$, is depicted in Fig. 4.1. Another example is provided by the so-called Kolmogorov power spectrum for standard atmospheric turbulence:

$$\Phi(|\mathbf{k}|) \propto \frac{a(|\mathbf{k}|)}{|\mathbf{k}|^{11/3}},$$

for $|\mathbf{k}|$ in the inertial range of turbulence, which corresponds to the case $\alpha = 5/3$.

In this chapter, the particular role played by the singularity of the scattering operator $\mathcal{Q}$ is discussed at both the theoretical and numerical levels. The first part of this chapter presents regularization effects in all variables produced by such a singular kernel, and the diffusion limit of the RTE. The second part presents Monte-Carlo (MC) methods allowing to handle efficiently the singularity of the scattering operator.

This chapter covers the results of [8, 9, 13, 15] of the bibliography list on page 6.

4.1 Regularizing effects

In the spirit of [3,40,141] for the Boltzmann equation, our main motivation was to derive hypoelliptic type estimates that characterize the transfer of regularity from the momentum variable $\widehat{\mathbf{k}}$ to the spatial variable $\mathbf{x}$ for solutions of (4.1). Similar problems are considered in the Euclidean case where $\mathbf{k} \in \mathbb{R}^d$ [4,40,92,141] using various approaches. These results have been extended to RTEs where the momentum is confined to the unit sphere. In the case of the Boltzmann equation, the non-linearity in the collision operator makes the problem much harder than in the present linear situation [5,6,102,103], but the non-integrability of the scattering kernel leads to comparable phenomena. The operator $\mathcal{L}$ roughly acts as a fractional Laplace-Beltrami operator on the unit sphere. A standard energy estimate then yields some Sobolev regularity in $\widehat{\mathbf{k}}$, and the main question is to figure how this regularity is propagated to the spatial variable $\mathbf{x}$. Bootstrapping the estimates, the solution to (4.1) turns to be $\mathcal{C}^\infty$ in all its variables for any time $t > 0$, which is equivalent to the hypoellipticity of the operator $\partial_t + \widehat{\mathbf{k}} \cdot \nabla_{\mathbf{x}} - \mathcal{Q}$. Compared to the Euclidean case, where $\mathbf{k} \in \mathbb{R}^d$, the fact that $\widehat{\mathbf{k}} \in \mathbb{S}^{d-1}$ brings serious additional technical difficulties. To prove proper hypoelliptic estimates we follow the approach of [40] and build the estimates by regularization of the momentum variable using averaging lemmas on the sphere. These latter lemmas were established in [41–44] in various configurations, and needed to be extended to the case where the scattering operator in the transport equation involves fractional derivatives on the unit sphere. The hypoelliptic estimate we use to prove the global regularity for (4.1) is the following.

Theorem 4.1.1 *Assume $g, h \in L^2(\mathbb{R} \times \mathbb{R}^d \times \mathbb{S}^{d-1})$, and let $u \in L^2(\mathbb{R} \times \mathbb{R}^d \times \mathbb{S}^{d-1})$ satisfies the transport equation*

$$\partial_t u + \widehat{\mathbf{k}} \cdot \nabla_{\mathbf{x}} u = (-\Delta_{\mathbb{S}^{d-1}})^\beta h + g \tag{4.6}$$

in the distribution sense, where $\Delta_{\mathbb{S}^{d-1}}$ is the Laplace-Beltrami operator on $\mathbb{S}^{d-1}$, and $\beta \geq 0$. For some $\theta > 0$, suppose in addition that

$$(-\Delta_{\mathbb{S}^{d-1}})^{\theta/2} u \in L^2(\mathbb{R} \times \mathbb{R}^d \times \mathbb{S}^{d-1}).$$

Then, for

$$\Upsilon := \frac{\theta}{2(1+2\beta)+\theta},$$

we have $\partial_{t,\mathbf{x}}^\Upsilon u \in L^2(\mathbb{R} \times \mathbb{R}^d \times \mathbb{S}^{d-1})$ with the estimate

$$\|\partial_{t,\mathbf{x}}^\Upsilon u\|_{L^2} \leq C \left(\|(-\Delta_{\mathbb{S}^{d-1}})^{\theta/2} u\|_{L^2} + \|u\|_{L^2} + \|g\|_{L^2} + \|h\|_{L^2} \right),$$

for some constant $C > 0$, and where the L^2 norm holds on all the variables.

The above fractional derivatives are defined in the Fourier domain using the following convention:

$$\hat{f}(\xi) = \mathcal{F} f(\xi) = \int e^{-i\mathbf{x}\cdot\xi} f(\mathbf{x}) d\mathbf{x}, \qquad \mathcal{F}^{-1} f(\mathbf{x}) = \frac{1}{(2\pi)^d} \int e^{i\mathbf{x}\cdot\xi} \hat{f}(\xi) d\xi,$$

and introduce the fractional derivative as,

$$\partial_{\mathbf{x}_j}^\Upsilon f(\mathbf{x}) = \mathcal{F}^{-1}[(i\xi_j)^\Upsilon \hat{f}(\xi)](\mathbf{x}) \qquad \text{for } \Upsilon \in (0,1),$$

with a similar definition for the fractional derivative involving the time variable and both variables. We denote by $\partial_{t,\mathbf{x}}^\Upsilon f$ any of the fractional derivatives w.r.t. t and $\mathbf{x}_j$, and $\partial_{t,\mathbf{x}}^\Upsilon f = \partial_{t,\mathbf{x}}^{\Upsilon - [\Upsilon]} \partial_{t,\mathbf{x}}^{[\Upsilon]} f$ when $\Upsilon \geq 1$, where $[\Upsilon]$ is the integer part of Υ.

From this result, replacing formally $(-\Delta_{\mathbb{S}^{d-1}})^\beta h$ in (4.6) by $\mathcal{Q}u$, and using bootstrap arguments, we obtain that u has derivatives of any order in all variables. The regularity result is the following.

Theorem 4.1.2 *The operator $\partial_t + \widehat{\mathbf{k}} \cdot \nabla_{\mathbf{x}} - \mathcal{Q}$ is hypoelliptic. Namely, for any $u_0 \in L^2(\mathbb{R}^d \times \mathbb{S}^{d-1})$, (4.1) admits a unique classical solution u that satisfies*

$$u \in \mathcal{C}^\infty((0,\infty) \times \mathbb{R}^d \times \mathbb{S}^{d-1}).$$

4.2 Diffusion limit

The diffusion limit described in this section is obtained through a probabilistic interpretation of the solution to (4.1). This probabilistic representation is also the basis of the numerical Monte-Carlo method proposed in the following section. According to [75, Thm. 7.2.1 pp. 302], after a proper extension of the operator $\mathcal{Q}$, there exists a Markov process K on $\mathbb{S}^{d-1}$ with infinitesimal generator $\mathcal{Q}$. Setting

$$D := (X, K), \qquad \text{with} \qquad X_t := X_0 - \int_0^t K(s)ds \qquad t \geq 0,$$

defines a Markov process with infinitesimal generator

$$\mathcal{L}f(\mathbf{x}, \widehat{\mathbf{k}}) = -\widehat{\mathbf{k}} \cdot \nabla_{\mathbf{x}} f(\mathbf{x}, \widehat{\mathbf{k}}) + \mathcal{Q}f(\mathbf{x}, \widehat{\mathbf{k}}),$$

from which we can write

$$u(t, \mathbf{x}, \widehat{\mathbf{k}}) = \mathbb{E}_{\mathbf{x}, \widehat{\mathbf{k}}}\big[u_0(D(t))\big] := \mathbb{E}\big[u_0(D(t)) \,|\, D(0) = (\mathbf{x}, \widehat{\mathbf{k}})\big].$$

The diffusion regime takes place in the presence of strong scattering effects, which can be represented using the following changes of variables:

$$t \to \frac{t}{\varepsilon^2} \qquad \text{and} \qquad \mathbf{x} \to \frac{\mathbf{x}}{\varepsilon},$$

and considering

$$u^\varepsilon(t, \mathbf{x}, \widehat{\mathbf{k}}) = u\Big(\frac{t}{\varepsilon^2}, \frac{\mathbf{x}}{\varepsilon}, \widehat{\mathbf{k}}\Big),$$

with $u^\varepsilon(t = 0, \mathbf{x}, \mathbf{k}) = u_0(\mathbf{x}, \mathbf{k})$. This scaling corresponds to a long-time and space scaling providing at the macroscopic scale strong scattering effects. The transport equation (4.1) then becomes

$$\varepsilon^2 \partial_t u^\varepsilon + \varepsilon\, \widehat{\mathbf{k}} \cdot \nabla_{\mathbf{x}} u^\varepsilon = \mathcal{Q}u^\varepsilon, \tag{4.7}$$

and the associated probabilistic representation is obtained by considering the rescaled Markov process

$$D^\varepsilon(t) := \Big(X^\varepsilon(0) - \varepsilon \int_0^{t/\varepsilon^2} K(s)ds, K(t/\varepsilon^2)\Big),$$

with generator

$$\mathcal{L}_\varepsilon f = -\frac{1}{\varepsilon}\widehat{\mathbf{k}} \cdot \nabla_{\mathbf{x}} f + \frac{1}{\varepsilon^2}\mathcal{Q}f.$$

The solution to (4.7) then reads

$$u^\varepsilon(t, \mathbf{x}, \widehat{\mathbf{k}}) = \mathbb{E}_{\mathbf{x}, \widehat{\mathbf{k}}}[u_0(D^\varepsilon(t))],$$

and its asymptotic behavior in ε is given by the following result.

Theorem 4.2.1 *Suppose there exists $\eta > 0$ such that $a \geq \eta$ almost everywhere, and let*

$$Y^\varepsilon_{\mathbf{y}}(t) = \mathbf{y} - \varepsilon \int_0^{t/\varepsilon^2} K(s)ds.$$

Then, the process $Y^\varepsilon_{\mathbf{y}}$ converges in law in $\mathcal{C}^0([0, \infty), \mathbb{R}^d)$, as $\varepsilon \to 0$, to a diffusion process $Y_{\mathbf{y}}$, starting at $\mathbf{y}$, with generator

$$\mathcal{L}_0 = \nabla_{\mathbf{x}} \cdot A \nabla_{\mathbf{x}}.$$

The positive-definite diffusion matrix A is given by

$$A_{jl} = \frac{1}{\mathfrak{C}} \int_{\mathbb{S}^{d-1}} \tilde{\sigma}(d\widehat{\mathbf{k}}) \hat{k}_j \hat{k}_l \qquad \text{with} \qquad \mathfrak{C} = \sigma(\mathbb{S}^{d-2}) \int_{-1}^{1} F(s)(1 - s^2)^{(d-3)/2}(1 - s)ds.$$

Above, $\tilde{\sigma}$ is the uniform measure on $\mathbb{S}^{d-1}$ (i.e. $\tilde{\sigma} = \sigma/\sigma(\mathbb{S}^{d-1})$). Moreover, for any $u_0 \in L^2(\mathbb{R}^d \times \mathbb{S}^{d-1})$ and $t > 0$, $u^\varepsilon(t)$ converges weakly in $L^2(\mathbb{R}^d \times \mathbb{S}^{d-1})$, as $\varepsilon \to 0$, to the unique solution to

$$\partial_t \tilde{u} = \nabla_{\mathbf{x}} \cdot \big(A \nabla_{\mathbf{x}} \tilde{u}\big), \qquad \text{with} \qquad \tilde{u}(t=0,\mathbf{x}) = \int_{\mathbb{S}^{d-1}} u_0(\mathbf{x},\mathbf{p}) d\tilde{\sigma}(\mathbf{p}),$$

and where the function $\tilde{u}$ reads

$$\tilde{u}(t,\mathbf{x}) = \mathbb{E}[\tilde{u}(t=0, Y_{\mathbf{x}}(t))].$$

The main ingredient of the proof is a spectral gap estimate showing that the Markov process $Y^\varepsilon_{\mathbf{y}}$ is ergodic, and allows the use of standard approximation-diffusion theorems to obtain the convergence. The hypothesis that a is strictly positive is crucial to obtain this spectral gap. Moreover, the constant $\mathfrak{C}$ is non-zero and finite, and so does A, despite the long-range correlations and the singular behavior of F.

4.3 A Monte-Carlo methods for radiative transfer with singular kernels in 2D propagation media

MC methods have been used for a long time to solve numerically (4.1) (see [140,192]). These methods have several advantages compared to classical finite element or finite volume methods. They can handle the high-dimensionality in a simple manner, since no mesh is required and the quantities of interest only need be discretized at a detector where measurements take place. They are very flexible in terms of geometry, translate boundary conditions onto the underlying stochastic process, and are easily applicable even when the coefficients in the equation depend on the variables $(\mathbf{x}, \widehat{\mathbf{k}})$. MC methods are also very easy to implement and can be parallelized in a straightforward manner, which is a strong feature with today's technology. Note that discretization-based methods would have to handle carefully the singularity of the cross-section. Without singular scattering operators, the standard MC methods rely on the mean free time between two scattering events. However, as shown by (4.2), when considering a singular scattering operator this mean free time is zero. This section illustrates how to overcome efficiently this difficulty.

With a singular scattering operator $\mathcal{Q}$, the underlying Markov process K of the MC method no longer relies on a Poisson process to describe its jump times as in the case of a nonnull mean free time. In our context, K corresponds to a general jump process with infinite jump intensity on $\mathbb{S}^1$. The simulation of such Lévy processes in the context of transport equations seems much less studied than its compound Poisson process counterpart. We focus in this section on the two-dimensional case with momentum on the circle $\mathbb{S}^1$, and will address the three-dimensional case in the next section. Note that the choice of $\mathbb{S}^1$ is arbitrary, any circle of given radius would be handle similarly.

The key for efficient MC methods resides in an appropriate simulation method of the process K representing the scattering mechanism w.r.t. the momentum variable. To this end, we adapt a method of the probabilistic literature developed by Asmussen-Rosiński [9], and Cohen-Rosiński [53], that we refer to as the ACR method. The first ingredient is to introduce a cut-off in the scattering operator to remove the singularity. The resulting operator is then the one of a compound Poisson process with finite (but large) intensity. The main issue with this cut-off approach is that a small value of the cut-off parameter is required for good accuracy, leading to a high intensity and therefore to many scattering events increasing the computational time. This issue is fixed by the second ingredient of this method, which consists in adding a correction term describing asymptotically the behavior of the operator around the singularity. This term models frequent jumps of small amplitude, while the regularized generator describes more rare jumps with larger amplitudes. In the work of Asmussen-Rosiński, and Cohen-Rosiński, the correction takes the form of a Brownian motion on the real line, while in the present context it corresponds to a Brownian motion on the circle (the unit sphere in the 3D case).

For comparison, and to illustrate the efficiency of the ACR method for the simulation of RTEs, an alternative MC method that does not involve a regularization of the generator is also introduced. This alternative method is based on the so-called Alpha-Stable processes, and is referred to as the AS method.

4.3.1 The ACR method

To introduce the ACR method, the operator $\mathcal{Q}$ needs to be appropriately parametrized. The natural choice on $\mathbb{S}^1$ are the polar coordinates and we introduce the surjective map

$$P : \phi \in \mathbb{R} \longmapsto (\cos(\phi), \sin(\phi)) \in \mathbb{S}^1.$$

Setting $\widehat{\mathbf{k}} = (\cos(\theta), \sin(\theta))$ and $\widehat{\mathbf{p}} = (\cos(\theta'), \sin(\theta'))$, so that $\widehat{\mathbf{k}} \cdot \widehat{\mathbf{p}} = \cos(\theta' - \theta)$, the scattering kernel $\mathcal{Q}$ can be recast as

$$\begin{aligned}
\mathcal{Q}(f)(k) &= \frac{1}{2^{(1+\alpha)/2}} \int_{-\pi}^{\pi} \frac{a(\theta' - \theta)(\tilde{f}(\theta') - \tilde{f}(\theta))}{(1 - \cos(\theta' - \theta))^{(1+\alpha)/2}} d\theta' \\
&= \frac{1}{2^{(1+\alpha)/2}} \int_{-\pi}^{\pi} \frac{a(\theta')(\tilde{f}(\theta' + \theta) - \tilde{f}(\theta))}{(1 - \cos(\theta'))^{(1+\alpha)/2}} d\theta' \\
&= \tilde{\mathcal{Q}}(\tilde{f})(\theta), \qquad \theta \in [-\pi, \pi],
\end{aligned}$$

where $\tilde{f} = f \circ P$ is a 2π-periodic function. Note that the 2π-periodic function a is symmetric with respect to 0 and is nonnegative. The operator $\tilde{\mathcal{Q}}$ can be seen as the generator of a Lévy process on $\mathbb{R}$ starting from 0, that we denote by $(\Theta(t))_{t \geq 0}$. According to our parametrization,

$$K = P(\Theta + \theta)$$

in law, when $K(0) = \widehat{\mathbf{k}}$. For $\varepsilon \in (0, 1)$, the ACR method consists in splitting $\tilde{\mathcal{Q}}$ into

$$\begin{aligned}
\tilde{\mathcal{Q}}(g)(\theta) &= \mathcal{Q}^{\varepsilon}_{<}(g)(\theta) + \mathcal{Q}^{\varepsilon}_{>}(g)(\theta) \\
&:= \frac{1}{2^{(1+\alpha)/2}} \int_{I_\varepsilon^C} \frac{a(\theta')(g(\theta' + \theta) - g(\theta))}{(1 - \cos(\theta'))^{(1+\alpha)/2}} d\theta' + \frac{1}{2^{(1+\alpha)/2}} \int_{I_\varepsilon} \frac{a(\theta')(g(\theta' + \theta) - g(\theta))}{(1 - \cos(\theta'))^{(1+\alpha)/2}} d\theta'
\end{aligned}$$

where I_ε is defined by

$$I_\varepsilon := \{\theta' \in [-\pi, \pi], \quad |\tan(\theta'/4)| > \varepsilon/4\},$$

and I_ε^C its complementary in $[-\pi, \pi]$. Because of the regularization, the second part of the generator, namely $\mathcal{Q}^{\varepsilon}_{>}(g)$, is now the generator of a classical compound Poisson process θ_ε with jump intensity

$$\mu_\varepsilon = \frac{\Pi^0_\varepsilon}{2^{(1+\alpha)/2}}, \qquad \text{where} \qquad \Pi^0_\varepsilon = \int_{I_\varepsilon} \frac{a(\theta) d\theta}{(1 - \cos(\theta))^{(1+\alpha)/2}},$$

and jump distribution

$$\Pi_\varepsilon(d\theta) = \frac{\mathbf{1}_{I_\varepsilon}(\theta) a(\theta)}{\Pi^0_\varepsilon (1 - \cos(\theta))^{(1+\alpha)/2}} d\theta.$$

The expected number of jumps for the compound Poisson process in any time interval $[0, T]$ is given by $\mu_\varepsilon T$, but the term μ_ε blows up as $\varepsilon \to 0$,

$$\mu_\varepsilon \propto \frac{1}{\alpha \varepsilon^\alpha}.$$

In other words the process jumps more and more as ε becomes small, this rate blows up even more rapidly when α gets close to 2, and hence increases the simulation cost. An efficient simulation technique for the jump distribution is therefore required. Good performances to approximately simulate numerically the jump distribution is achieved using the stochastic collocation method [104].

The first term of the generator $Q^{\varepsilon}_{<}$ models frequent jumps of small amplitude and can be asymptotically reduced to the generator of a Brownian motion on the circle. The following lemma describes the relation between $\mathcal{Q}^{\varepsilon}_{<}$ and the Laplace operator.

Lemma 4.3.1 *Suppose that $a \in C^2([-\pi,\pi])$ and that g is a smooth 2π-periodic bounded function with bounded derivatives. Then, for any $\phi \in [-\pi,\pi]$,*

$$\mathcal{Q}^\varepsilon_<(g)(\phi) = \frac{\sigma_\varepsilon}{2}\frac{\partial^2 g(\phi)}{\partial \phi^2} + \mathcal{R}_\varepsilon[g](\phi),$$

where

$$\sigma_\varepsilon = \frac{2a(0)\varepsilon^{2-\alpha}}{2-\alpha} \qquad \text{and} \qquad \|\mathcal{R}_\varepsilon[g]\|_\infty \leq \frac{\varepsilon^{4-\alpha}}{4-\alpha}\|a\|_{C^2([-\pi,\pi])}\|g\|_{C^4([-\pi,\pi])}.$$

The leading term in $\mathcal{Q}^\varepsilon_<$ is the generator of $\phi_\varepsilon = (\sigma_\varepsilon W_t \mod 2\pi)_t$, where W is a Brownian motion. Brownian trajectories can easily be generated, but note that σ_ε is proportional to $\varepsilon^{2-\alpha}/(2-\alpha)$, which becomes larger as α increases. We therefore expect the inclusion of the Brownian term in the simulation to be critical in order to obtain good accuracy and computational cost.

Error analysis

The main idea of the ACR method is that the Lévy process K on $\mathbb{S}^1$, starting at $\widehat{\mathbf{k}}$ with generator $\mathcal{Q}$, is approximated by the process

$$K^\varepsilon = \big(\cos(\phi_\varepsilon + \theta_\varepsilon + \theta), \sin(\phi_\varepsilon + \theta_\varepsilon + \theta)\big),$$

which is the one simulated numerically in practice. Here θ_ε accounts for the regularized compound Poisson process and ϕ_ε for the Brownian correction. Note that these two processes are independent. Introducing

$$X^\varepsilon_{\mathbf{x}}(t) = \mathbf{x} - \int_0^t K^\varepsilon(s)ds,$$

the function

$$u_\varepsilon(t,\mathbf{x},\widehat{\mathbf{k}}) = \mathbb{E}[u_0(X^\varepsilon_{\mathbf{x}}(t), K^\varepsilon(t)) \,|\, K^\varepsilon(0) = \widehat{\mathbf{k}}] \tag{4.8}$$

is then the solution of the following transport equation, with the parametrization $\widehat{\mathbf{k}} = (\cos(\theta), \sin(\theta))$:

$$\partial_t u_\varepsilon + \widehat{\mathbf{k}}\cdot\nabla_{\mathbf{x}} u_\varepsilon = \mathcal{Q}^\varepsilon_>(u_\varepsilon) + \frac{D_\varepsilon}{2}\partial^2_\theta u_\varepsilon, \qquad u_\varepsilon(t=0) = u_0.$$

The following proposition quantifies the approximation error, in term of the cut-off parameter, when using this model to approximate the original RTE.

Proposition 4.3.1 *Suppose that $a \in C^2([-\pi,\pi])$. Then, for all $t \in (0,T)$,*

$$\|u_\varepsilon(t,\cdot,\cdot) - u(t,\cdot,\cdot)\|_{L^2(\mathbb{R}^2\times\mathbb{S}^1)} \leq \frac{\varepsilon^{4-\alpha}}{4-\alpha}\|a\|_{C^2([-\pi,\pi])}\int_0^t \|u(s)\|_{L^2(\mathbb{R}^2, C^4(\mathbb{S}^1))}ds.$$

Recall that u satisfies the regularity requirement thanks to the hypoelliptic property of the RTE.

4.3.2 The AS method

This section introduces an alternative method to compare against the ACR method. The main idea is to exactly simulate the process K, without using the small jumps - larger jumps approximation of the generator. The method is applicable provided an additional assumption on the function a. In this section $a(\theta)$ is assumed to admit a global minimizer at $\theta = 0$, or equivalently $A(s) = a(\theta)$ (for $s = \widehat{\mathbf{k}}\cdot\widehat{\mathbf{p}} = \cos(\theta)$) admits a global minimizer at $s = 1$. This assumption allows us to decompose $\mathcal{Q}$ in terms of two infinitesimal generators

$$\begin{aligned}\mathcal{Q}(f)(\widehat{\mathbf{k}}) &= \frac{A(1)}{2^{(1+\alpha)/2}}\int_{\mathbb{S}^1}\frac{f(\widehat{\mathbf{p}}) - f(\widehat{\mathbf{k}})}{(1-\cos(\widehat{\mathbf{k}}\cdot\widehat{\mathbf{p}}))^{(1+\alpha)/2}}\sigma(d\widehat{\mathbf{p}}) \\ &\quad + \frac{1}{2^{(1+\alpha)/2}}\int_{\mathbb{S}^1}\frac{A(\widehat{\mathbf{k}}\cdot\widehat{\mathbf{p}}) - A(1)}{(1-\cos(\widehat{\mathbf{k}}\cdot\widehat{\mathbf{p}}))^{(1+\alpha)/2}}\big(f(\widehat{\mathbf{p}}) - f(\widehat{\mathbf{k}})\big)\sigma(d\widehat{\mathbf{p}}) \\ &=: \mathcal{Q}^1(f)(\widehat{\mathbf{k}}) + \mathcal{Q}^2(f)(\widehat{\mathbf{k}}).\end{aligned}$$

The second term $\mathcal{Q}^2$ is the generator of a compound Poisson process on $\mathbb{S}^1$ with a finite jump intensity, which does not pose any computational issue since now the average length of the jumps is large compared to those generated by $\mathcal{Q}^\varepsilon_>$. The main difficulty is to simulate numerically random trajectories for a Lévy process K^1 with self-adjoint generator $\mathcal{Q}^1$. Such trajectories are simulated numerically through piecewise constant trajectories on a fine time grid, and each transitions are simulated using the transition density function

$$p(h, \widehat{\mathbf{k}}, \widehat{\mathbf{q}}) = \mathbb{P}\big(K^1(h) = \widehat{\mathbf{k}} \,\big|\, K^1(0) = \widehat{\mathbf{q}}\big),$$

where h corresponds to the time stepsize. This function can be derived explicitly by solving the forward Kolmogorov equation

$$\partial_t p(\widehat{\mathbf{k}}) = \mathcal{Q}^1(p)(\widehat{\mathbf{k}}), \qquad \text{with} \qquad p(t=0, \widehat{\mathbf{k}}, \widehat{\mathbf{q}}) = \delta(\widehat{\mathbf{k}} - \widehat{\mathbf{q}}),$$

for $\widehat{\mathbf{k}}, \widehat{\mathbf{q}} \in \mathbb{S}^1$, and where δ is the Dirac measure. With the parametrization $\widehat{\mathbf{k}} \cdot \widehat{\mathbf{q}} = \cos(\theta)$, the operator $\mathcal{Q}$ can be diagonalized using Fourier series, and we obtain the following exact expression for p (written as a function of θ),

$$p(t, \theta) = \frac{1}{2\pi} + \frac{1}{\pi} \sum_{\ell=1}^{\infty} e^{t\lambda_\ell} \cos(\ell\theta),$$

where (with $a_0 = a(0) = A(1)$)

$$\lambda_\ell = \frac{a_0 \pi^{\frac{1}{2}} \Gamma(-\frac{\alpha}{2})}{2^\alpha \Gamma(\frac{1+\alpha}{2})} \left(\frac{\Gamma(\ell + \frac{1+\alpha}{2})}{\Gamma(\ell + \frac{1-\alpha}{2})} - \frac{\Gamma(\frac{1+\alpha}{2})}{\Gamma(\frac{1-\alpha}{2})} \right),$$

according to [182] with a slight adjustment of the constant prefactors, and Γ the usual Gamma function. It does not seem possible to directly simulate the increments using p. To address this issue, we should use an approximation of it that enables fast simulations. Once we have this approximation, we can once again apply the stochastic collocation method [104] to provide accurate simulations to p. The operator $\mathcal{Q}^1$ should not be far from a fractional Laplace-Beltrami operator on $\mathbb{S}^1$. Therefore, we introduce

$$p_0(h, \theta) := \frac{1}{2\pi} + \frac{1}{\pi} \sum_{\ell=1}^{\infty} e^{-hD_\alpha \ell^\alpha} \cos(\ell\theta)$$

as a rough approximation to $p(h, \cdot)$, which corresponds to the distribution to $(hD_\alpha)^{1/\alpha} X \mod 2\pi$, where X stands for a random variable with an α-stable distribution, which has characteristic function

$$\mathbb{E}[e^{ivX}] = e^{-|v|^\alpha}.$$

Following the strategy of [208], the α-stable distribution can be easily exactly simulated numerically from the uniform distribution over $(0, 1)$.

It is worth mentioning that the density p_0 is already an excellent approximation of p, as shown in Fig. 4.2. For both cases illustrated in this figure, the L^2 relative error is about 0.3%. Even though these small errors translate into small errors in the simulation of the RTE, it is not possible to obtain an arbitrary precision by using p_0 instead of p. For arbitrary accuracy, a random variable drawn according to p_0 needs to be corrected to be seen as distributed according to p. This can be achieved with the use of the efficient stochastic collocation method [104].

4.3.3 Numerical Illustrations

To perform relevant numerical simulations, we need first to define a typical time scale. When the scattering kernel is integrable this time scale is given by the mean free time (4.2). In our non-integrable case, this mean free time is zero and we need a different quantity. A natural one is the inverse of $-\lambda_1$, that is the inverse of the first non zero eigenvalue of $-\mathcal{Q}$. When $t \gg t_S := (-\lambda_1)^{-1}$, the distribution of the angles is almost uniform over $\mathbb{S}^1$. Fig. 4.3 represents the characteristic time t_S as a function of α for $a \equiv a_0 = 0.1$.

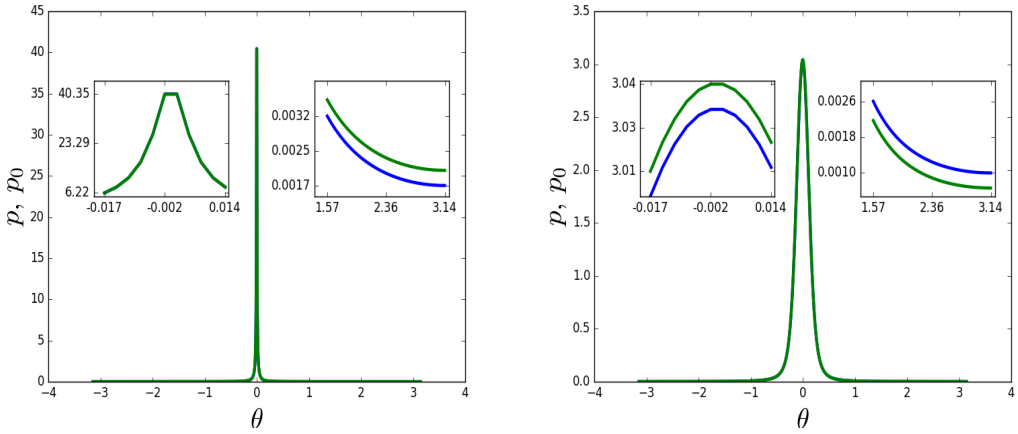

Fig. 4.2: Comparison between p (blue) and p_0 (green), $a_0 = 0.1$ and $h = 0.03$, for $\alpha = 0.8$ (left) and $\alpha = 1.6$ (right).

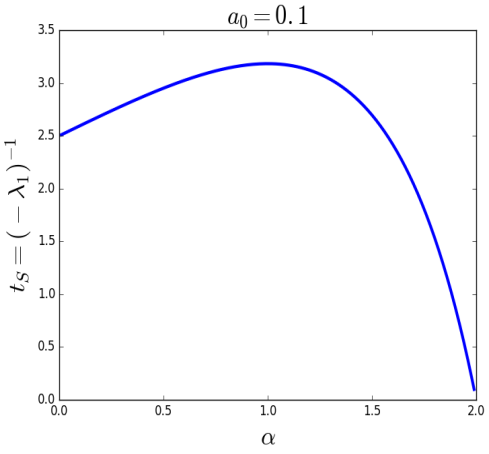

Fig. 4.3: Characteristic time t_S as a function of α for $a(s) = a_0 = 0.1$.

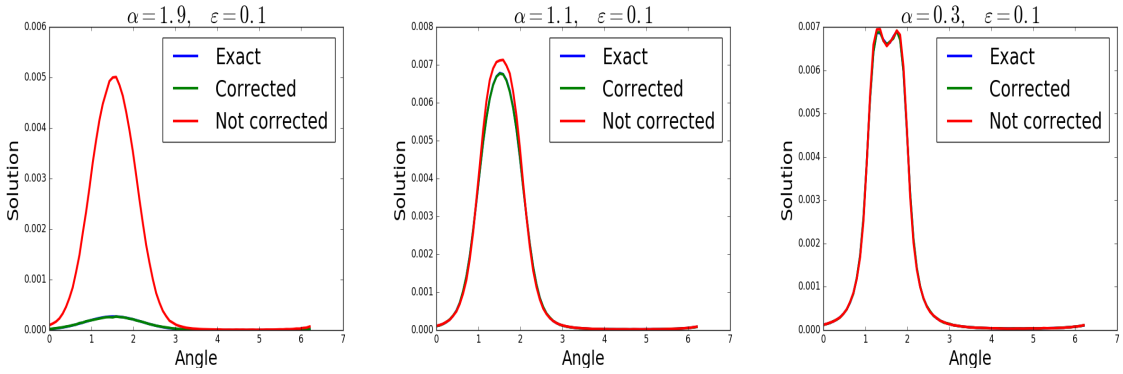

Fig. 4.4: Comparison between the reference solution and the numerical solutions including or not the Brownian correction. The non corrected solution is completely off when $\alpha = 1.9$, while there is a good accuracy when the Brownian part is included. Here, $h = 0.03$ for the time stepsize, $\varepsilon = a_0 = 0.1$, $t = 3$, $N_B = 80$, $z_1 = 2.7$, $z_2 = 3$, and 10^7 trajectories have been used for the MC method.

Impact of the Brownian correction in the ACR method

In view of Lem. 4.3.1 this correction is expected to play a crucial role for large α. To highlight the role of this correction, we compare the numerical simulations against a reference solution. In our context no explicit analytical formula for the solution of the RTE is available, so that we only rely on a semi-analytical expression corresponding to

$$J_i(t) = \int_{z_1}^{z_2} dx_1 \int_{\mathbb{R}} dx_2 \int_{\theta_i}^{\theta_{i+1}} d\theta \, u(t, x_1, x_2, \theta)$$

with $\mathbf{x} = (x_1, x_2)$, and $\widehat{\mathbf{k}} = (\cos(\theta), \sin(\theta))$. Here, u is the solution to the RTE with a particular initial condition

$$u_0(\mathbf{x}, \theta) = \frac{1}{\sqrt{2\pi c^2}} e^{-\frac{|\mathbf{x}|^2}{2c^2}} \frac{1}{2\pi} (1 + \cos(\theta)),$$

with $c = 0.1$ for the numerical evaluation. The time is here fixed at $t = 3$, which is roughly the characteristic time t_S depicted in Fig. 4.3. When $\alpha = 1.9$, the observation time is about $3t_S$. The solution u is integrated over several bins $[\theta_i, \theta_{i+1}]$, $i = 1, \ldots, N_B$, $\theta_{i+1} = \theta_i + \Delta\theta$. In Fig. 4.4, we represent the reference solution $(J_i(t))_{i=1,\ldots,N_B}$ and the numerical solution to the RTE $u_{\varepsilon,h}$, including or not the Brownian correction. When $\alpha = 1.9$ the solution is completely off when the correction is not included, while the relative error is about 3% when it is included. When $\alpha = 1.1$, the relative errors are 6% without the Brownian correction, and 0.3% with it, and 1.4% and 0.4% respectively for $\alpha = 0.3$. In all cases, this shows that the Brownian correction is crucial in order to obtain a good accuracy in the simulations.

Comparison ACR/AS methods

The ACR and AS methods are compared to each other in terms of accuracy versus computational cost for $\alpha = 0.7, 1.3, 1.8$. For the evaluation of the accuracy, the outcomes of both methods are compared to our reference solution $(J_i(t))_{i=1,\ldots,N_B}$ with $N_B = 20$. All the other parameters remain as before. The errors are averaged over 20 simulations of the MC methods to obtain more stable estimates. The results are depicted in Fig. 4.5. The cost is expressed in units of 0.17s, which is the computational time to achieve an error of about 10% for a code written in the Julia language, and ran in parallel on a 32 cores Intel Xeon E5-2697A at 2.60GHz.

In the case $\alpha = 0.7$, the cost to achieve an error of 0.2% is about 10 times higher for the AS method than for the ACR method. This difference is reduced for lower accuracies. Similar observations hold for $\alpha = 1.3$ and $\alpha = 1.8$, with the gap shrinking as α increases. This can be explained on the one hand by the fact that the ACR method is more sensitive to the parameter α than the AS method. In fact, there are more and more scattering events as α grows, and on the other hand the jumps are smaller

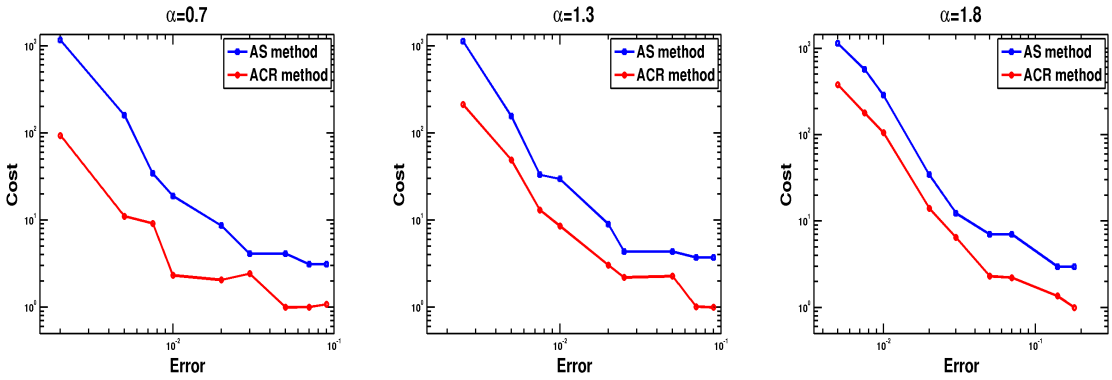

Fig. 4.5: Comparison of the AS and ACR methods in terms of cost versus accuracy for $\alpha = 0.7, 1.3, 1.8$. The ACR method is consistently more efficient.

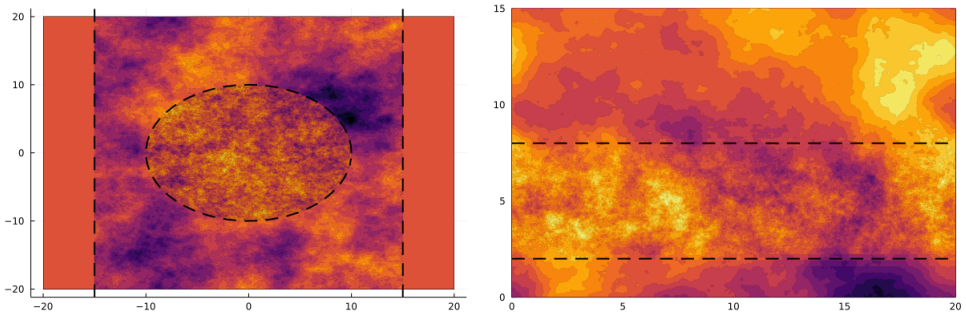

Fig. 4.6: Realizations of Gaussian random fields. In the left picture, we have $\lambda = \mathbf{1}_{\{|x_1|<15\}}$, and $\alpha = 0.1 \cdot \mathbf{1}_{\{|x|\leq 10\}} + 1 \cdot \mathbf{1}_{\{10<|x|\}}$. In the right picture, we have $\lambda = 1_{\{x_2\in(0,20)\}}$ and $\alpha(x_2) = 5/3 \cdot \mathbf{1}_{\{x_2\leq 2\}} + 0.5 \cdot \mathbf{1}_{\{2<x_2\leq 8\}} + 1.9 \cdot \mathbf{1}_{\{8<x_2\}}$.

for large α, which reduces the error when evaluating the integral for the position variable $X(t)$ in the AS method. Nevertheless, the cost of a 0.5% error when $\alpha = 1.8$ is more than twice higher for the AS method, and the cost significantly increases when going from an accuracy of about 10% to about 0.1%.

4.4 A Monte-Carlo method for 3D radiative transfer equations with multifractional singular kernels

The radiative transfer model (4.1) can be extended to more general situations by letting the properties of the scattering operator depends on the position $\mathbf{x}$:

$$\Phi(\mathbf{x}, |\widehat{\mathbf{p}} - \widehat{\mathbf{k}}|) := \frac{\lambda(\mathbf{x}) a(|\widehat{\mathbf{p}} - \widehat{\mathbf{k}}|)}{|\widehat{\mathbf{p}} - \widehat{\mathbf{k}}|^{2+\alpha(\mathbf{x})}} = \frac{\lambda(\mathbf{x})}{2^{1+\alpha(\mathbf{x})/2}} \rho(\mathbf{x}, \widehat{\mathbf{k}} \cdot \widehat{\mathbf{p}}),$$

with

$$\rho(\mathbf{x}, s) := \frac{a\big(\sqrt{2(1-s)}\big)}{(1-s)^{1+\alpha(\mathbf{x})/2}} \qquad s \in [-1, 1). \tag{4.9}$$

Above, $\alpha : \mathbb{R}^3 \longrightarrow (0, 2)$ accounts for variations of scattering properties across the ambient space, and $\lambda \geq 0$ is a function modeling the support of the scattering region. Regions where $\lambda(\mathbf{x}) = 0$ are homogeneous and u undergoes a free transport. In Fig. 4.6, we provide examples of 2D random fields for which α and λ are not constant. In these two pictures, we highlight the roles of λ and α: λ characterizes scattering regions, and α defines the correlation structure. In the inner circle of

the left picture we have $\alpha \equiv 0.1$, which tends to create shorter correlation patterns than outside the circle where $\alpha \equiv 1$. In the right picture, we have a three-layer model for α in which the inner band exhibits smaller statistical patterns than the outer ones. This type of model is used for modeling non-Kolmogorov atmospheric turbulences.

From a numerical perspective, the 3D context outline in this section is more involved compared to the 2D setting, where the small-jumps part can simply be approximated by a Brownian motion mod 2π. Here, the singularity is approximated using a Laplace-Beltrami operator (with respect to the momentum variable) on the unit sphere $\mathbb{S}^2$, so that simulating paths of a jump-diffusion process over the unit sphere is necessary to handle the *small-jumps* part. Remember that disregarding small jumps altogether in order to use standard MC methods results in substantial errors, and mitigating these errors comes with a notable increase in computational cost.

4.4.1 Approximation and probabilistic representation

In order to adapt the ACR method, we introduce the following small region over which the singularity of the kernel ρ (in (4.9)) is not integrable:

$$S^\varepsilon_< = S^\varepsilon_<(\widehat{\mathbf{k}}) := \{\widehat{\mathbf{p}} \in \mathbb{S}^2 : \quad 1 - \widehat{\mathbf{p}} \cdot \widehat{\mathbf{k}} < \varepsilon\} \qquad \text{for } \varepsilon \in (0,1). \tag{4.10}$$

The ACR method is based on decomposing the scattering operator $\mathcal{Q}$ into two parts:

$$\begin{aligned} \mathcal{L}Q(\mathbf{x},\widehat{\mathbf{k}}) &= +\mathcal{Q}^\varepsilon_< f(\mathbf{x},\widehat{\mathbf{k}}) + \mathcal{Q}^\varepsilon_> f(\mathbf{x},\widehat{\mathbf{k}}) \\ &:= \frac{\lambda(\mathbf{x})}{2^{1+\alpha(\mathbf{x})/2}} \left(\int_{S^\varepsilon_<} + \int_{S^\varepsilon_>} \right) \rho(\mathbf{x}, \widehat{\mathbf{p}} \cdot \widehat{\mathbf{k}}) \big(f(\mathbf{x},\widehat{\mathbf{p}}) - f(\mathbf{x},\widehat{\mathbf{k}}) \big) \sigma(d\widehat{\mathbf{p}}), \end{aligned}$$

where $S^\varepsilon_> = (S^\varepsilon_<)^c$ is the complementary set of the region (4.10) over the unit sphere. The term $\mathcal{Q}^\varepsilon_>$ of the scattering operator, with no singularity, is the infinitesimal generator of a standard jump Markov process with *large-jumps*. Regarding $\mathcal{Q}^\varepsilon_<$, with the singularity, the following result justifies the approximation of this operator by a Laplace-Beltrami operator $\Delta_{\mathbb{S}^2}$ over the unit sphere $\mathbb{S}^2$. In what follows, we use the notations $r'_\varepsilon = \sqrt{1-(1-\varepsilon)^2}/(2-\varepsilon)$ and $0 \le \alpha_m \le \alpha(\mathbf{x}) \le \alpha_M < 2$.

Proposition 4.4.1 *Let u be the solution to* (4.1) *with kernel* (4.9)*, and u_ε be the solution of*

$$\begin{cases} \partial_t u_\varepsilon + \widehat{\mathbf{k}} \cdot \nabla_{\mathbf{x}} u_\varepsilon = \sigma^2_\varepsilon(\mathbf{x}) \Delta_{\mathbb{S}^2} u_\varepsilon + \dfrac{\lambda(\mathbf{x})}{2^{1+\alpha(\mathbf{x})/2}} \displaystyle\int_{S^\varepsilon_>} \rho(\mathbf{x}, \widehat{\mathbf{p}} \cdot \widehat{\mathbf{k}}) (u_\varepsilon(\widehat{\mathbf{p}}) - u_\varepsilon(\widehat{\mathbf{k}})) \sigma(d\widehat{\mathbf{p}}), \\ \qquad u_\varepsilon(0,\mathbf{x},\widehat{\mathbf{k}}) = u_0(\mathbf{x},\widehat{\mathbf{k}}), \end{cases} \tag{4.11}$$

for $(t,\mathbf{x},\widehat{\mathbf{k}}) \in (0,\infty) \times \mathbb{R}^3 \times \mathbb{S}^2$, where

$$\sigma^2_\varepsilon(\mathbf{x}) := \frac{2^{1-\alpha(\mathbf{x})} a(0) \pi \lambda(\mathbf{x})}{2-\alpha(\mathbf{x})} {r'_\varepsilon}^{2-\alpha(\mathbf{x})}. \tag{4.12}$$

Assuming $a'(0) = 0$, for any $T > 0$, we have

$$\sup_{t \in [0,T]} \|u(t,\cdot,\cdot) - u_\varepsilon(t,\cdot,\cdot)\|_{L^2(\mathbb{R}^3 \times \mathbb{S}^2)} \le \varepsilon^{2-(\alpha_M/2)} \sqrt{2T}\, E(u), \tag{4.13}$$

where $E(u)$ is a constant depending on the 2nd- and 4th-order derivatives of u.

As we know from Sect. 4.1, when λ and α are constants, u is infinitely differentiable in all variables for any square integrable initial conditions. However, when λ and α are infinitely differentiable with bounded derivatives at all orders (from above and below), this result remains valid so u is still assumed to be smooth.

Based on the approximation result (4.13), we then devise a MC method for (4.11) instead of (4.1). The advantage in using (4.11) lies in that the angular diffusion term $\sigma^2_\varepsilon(\mathbf{x})\Delta_{\mathbb{S}^2}$ is the generator of a Markov process that can be easily simulated. Indeed, for W a standard 3D Brownian motion on $\mathbb{R}^3$, and $\times$ being the cross product in $\mathbb{R}^3$, it is shown in [205] that the process B solving the SDE

$$dB = B \times dW - B dt, \qquad B(0) \in \mathbb{S}^2,$$

has infinitesimal generator $\frac{1}{2}\Delta_{\mathbb{S}^2}$, and corresponds to a Brownian motion over $\mathbb{S}^2$. A simple adaptation gives the desired diffusion coefficient. Note also that $\sigma_\varepsilon(\mathbf{x})$ increases as $\alpha(\mathbf{x})$ gets close to 2, and diffusion on the sphere eventually becomes the dominant dynamics.

In this section the MC method is built by interpreting (4.11) as the forward Kolmogorov equation of an appropriate Markov process, and as a consequence focusing for simplicity on the *forward* MC method (see [140] for terminology). The Markov process we consider for this approach is defined by

$$D_\varepsilon(t) := \sum_{n\geq 0} \mathbf{1}_{[T_n, T_{n+1})}(t)\psi_n^{Z_n}(t-T_n) \qquad t \geq 0, \tag{4.14}$$

where for $z = (\mathbf{x}, \widehat{\mathbf{k}})$:

1. The flow $\psi_n^z = (X_n^{\mathbf{x}}, K_n^{\widehat{\mathbf{k}}})$ is the unique strong solution to the SDE

$$\left\{ \begin{array}{rcl} dX_n^{\mathbf{x}}(t) & = & K_n^{\widehat{\mathbf{k}}}(t)\, dt \\ dK_n^{\widehat{\mathbf{k}}}(t) & = & \sqrt{2}\,\sigma_\varepsilon(X_n^{\mathbf{x}}(t))\, K_n^{\widehat{\mathbf{k}}}(t) \times dW_n(t) - 2\,\sigma_\varepsilon^2(X_n^{\mathbf{x}}(t))\, K_n^{\widehat{\mathbf{k}}}(t)\, dt, \end{array} \right. \tag{4.15}$$

   where $\psi_n^z(0) = z$, $(W_n)_n$ is a sequence of independent standard Brownian motions on $\mathbb{R}^3$, and σ_ε is defined by (4.12).

2. The jump times $(T_n)_n$ are distributed according to

$$\mathbb{P}\big(T_{n+1} - T_n > t \,|\, D_\varepsilon(T_n) = z,\, (\psi_n^z(s))_{s\in[0,t]}\big) = \exp\Big(-\int_0^t \Lambda_\varepsilon(\psi_n^z(s))ds\Big) \qquad n \geq 0,$$

   with $T_0 = 0$, and for ρ given by (4.9),

$$\Lambda_\varepsilon(z) := \frac{\lambda(\mathbf{x})}{2^{1+\alpha(\mathbf{x})/2}} \int_{S^\varepsilon_>} \rho(\mathbf{x}, \widehat{\mathbf{p}}\cdot\widehat{\mathbf{k}})\sigma(d\widehat{\mathbf{p}}).$$

3. The jumps $(Z_n)_n$ describe a Markov chain with transition probability

$$\mathbb{P}(Z_{n+1} \in d\mathbf{y} \otimes \sigma(d\widehat{\mathbf{p}}) \,|Z_n, T_{n+1} - T_n) = \Pi_\varepsilon(z_{n+1},\, dz),$$

   where $z_{n+1} := \psi_n^{Z_n}(T_{n+1} - T_n)$, and

$$\Pi_\varepsilon(z, dz) := \pi_\varepsilon(z, \widehat{\mathbf{p}})\sigma(d\widehat{\mathbf{p}})\delta_{\mathbf{x}}(d\mathbf{y}),$$

   with probability density function

$$\pi_\varepsilon(z, \widehat{\mathbf{p}}) := \frac{\rho(\mathbf{x}, \widehat{\mathbf{p}}\cdot\widehat{\mathbf{k}})}{\int_{S^\varepsilon_>} \rho(\mathbf{x}, \widehat{\mathbf{p}}'\cdot\widehat{\mathbf{k}})d\sigma(\widehat{\mathbf{p}}')} \mathbf{1}_{S^\varepsilon_>}(\widehat{\mathbf{p}}).$$

   The above Dirac mass $\delta_{\mathbf{x}}(d\mathbf{y}) := \delta(\mathbf{x}-\mathbf{y})d\mathbf{y}$ translates the fact that the jumps only hold w.r.t. the $\widehat{\mathbf{k}}$-variable.

From this construction we have the following probabilistic representation for the solution to (4.11).

Proposition 4.4.2 *The Markov process D_ε defined in* (4.14) *has for infinitesimal generator*

$$\mathcal{A}_\varepsilon g(z) := \widehat{\mathbf{k}}\cdot\nabla_{\mathbf{x}} g(z) + \sigma_\varepsilon^2(\mathbf{x})\Delta_{\mathbb{S}^2} g(z) + \Lambda_\varepsilon(z)\int_{\mathbb{S}^2} \pi_\varepsilon(z, \widehat{\mathbf{p}})\big(g(\mathbf{x}, \widehat{\mathbf{p}}) - g(\mathbf{x}, \widehat{\mathbf{k}})\big)\sigma(d\widehat{\mathbf{p}}),$$

and we have

$$\mathbb{P}_{\mu_0}(D_\varepsilon(t) \in d\mathbf{x}\otimes\sigma(d\widehat{\mathbf{k}})) = \frac{1}{\bar{u}_0} u_\varepsilon(t, \mathbf{x}, \widehat{\mathbf{k}})\, d\mathbf{x}\, \sigma(d\widehat{\mathbf{k}}), \tag{4.16}$$

where

$$\mu_0(d\mathbf{x}, d\widehat{\mathbf{k}}) := \mathbb{P}(D_\varepsilon(0) \in d\mathbf{x}\otimes\sigma(d\widehat{\mathbf{k}})) = \frac{u_0(\mathbf{x}, \widehat{\mathbf{k}})}{\bar{u}_0}\, d\mathbf{x}\, \sigma(d\widehat{\mathbf{k}}), \qquad \textit{with} \qquad \bar{u}_0 := \int_{\mathbb{R}^3\times\mathbb{S}^2} u_0(\mathbf{x}, \widehat{\mathbf{k}})\, d\mathbf{x}\, \sigma(d\widehat{\mathbf{k}}).$$

The terminology *forward*, for this MC method, comes from the fact that the particles are emitted at random points at time $t = 0$, through μ_0 and the initial condition u_0, and propagate toward the observation positions $z = (\mathbf{x}, \widehat{\mathbf{k}})$. This approach is used when we want to simulate the propagation over the entire space, or at least over regions large compared to the support of the initial condition. For the 2D case of Sect. 4.3, the probabilistic representation (4.8) corresponds to the *backward* MC method, where the particles are emitted at the observation point $z = (\mathbf{x}, \widehat{\mathbf{k}})$ and are evaluated at time t through the initial condition u_0 of the RTE. This approach is convenient when the initial condition has a support larger than the region over which we want to evaluate the solution of the RTE.

Let us illustrate two aspects of the representation (4.16). In order to obtain an estimation of $u_\varepsilon(t, \mathbf{x}, \widehat{\mathbf{k}})$ at point $z = (\mathbf{x}, \widehat{\mathbf{k}})$, we evaluate the probability

$$\frac{\bar{u}_0}{|\mathbf{B}(z,r)|}\,\mathbb{P}_{\mu_0}\big(D_\varepsilon(t) \in \mathbf{B}(z,r)\big) \simeq u_\varepsilon(t, \mathbf{x}, \widehat{\mathbf{k}}),$$

where $\mathbf{B}(z,r) \subset \mathbb{R}^3 \times \mathbb{S}^2$ stands for the ball centered at $z = (\mathbf{x}, \widehat{\mathbf{k}})$ with radius $r \ll 1$. If we are only interested in the energy density at point $\mathbf{x}$ for instance, we estimate

$$\frac{\bar{u}_0}{|B(\mathbf{x},r)|}\,\mathbb{P}_{\mu_0}\big(D_\varepsilon(t) \in B(\mathbf{x},r) \times \mathbb{S}^2\big) = \frac{\bar{u}_0}{|B(\mathbf{x},r)|}\mathbb{P}_{\mu_0}\big(D_{1,\varepsilon}(t) \in B(\mathbf{x},r)\big) \simeq \int_{\mathbb{S}^2} u_\varepsilon(t, \mathbf{x}, \widehat{\mathbf{k}})\sigma(d\widehat{\mathbf{k}}),$$

where $B(\mathbf{x},r) \subset \mathbb{R}^3$ stands for the ball centered at $\mathbf{x}$ with radius $r \ll 1$, and $D_{1,\varepsilon}$ is the $\mathbf{x}$-component of D_ε.

4.4.2 The Monte-Carlo method

Based on the previous probabilistic representation (4.16), solving (4.11) requires the generation of random paths of the stochastic process D_ε. For any measurable bounded function f, the convergence of the estimator

$$\mu_N(t,f) := \frac{1}{N}\sum_{j=1}^{N} f(D_\varepsilon^j(t)) \underset{N\to\infty}{\longrightarrow} \int f(\mathbf{x}, \widehat{\mathbf{k}}) u_\varepsilon(t, \mathbf{x}, \widehat{\mathbf{k}})\, d\mathbf{x}\, \sigma(d\widehat{\mathbf{k}}) \qquad \mathbb{P}_{\mu_0} - \text{almost surely},$$

is guaranteed by the strong law of large numbers. Above $(D_\varepsilon^j)_j$ is a sample of D_ε. The process D_ε being inhomogeneous, i.e. Λ_ε and Π_ε both depend on $z = (\mathbf{x}, \widehat{\mathbf{k}})$, we make use of the so-called *thinning* method, also referred to as the *fictitious shocks* method [140], to simulate the jump part. It is based on a acceptation/rejection step and consists in simulating at first more jumps (or shocks) than necessary. In a second step, some of the jumps are rejected according to an appropriate probability distribution in order to recover the original dynamics.

The diffusion part between two jumps satisfies the linear SDE (4.15), and can be simulated using the following Euler-Maruyama type scheme

$$(S_{n,m}) : \left\{ \begin{array}{rcl} X_{n,m+1} & = & X_{n,m} + h_{n,m}\,\hat{K}_{n,m} \\ K_{n,m+1} & = & \hat{K}_{n,m} - 2h_{n,m}\,\sigma_\varepsilon^2(X_{n,m})\,\hat{K}_{n,m} + \sqrt{2h_{n,m}}\,\sigma_\varepsilon(X_{n,m})\,\hat{K}_{n,m} \times W_{n,m} \\ \hat{K}_{n,m+1} & = & \frac{K_{n,m+1}}{|K_{n,m+1}|}, \end{array} \right.$$

where the $(W_{n,m})_{m,n}$ are i.i.d. mean-zero Gaussian random vectors with identity covariance matrix, and $h_{n,m}$ some appropriate stepsizes.

The theoretical justification of our MC method is supported by the following convergence result.

Theorem 4.4.1 *Consider*

$$\mu_{N,h,\varepsilon}(t,f) = \frac{1}{N}\sum_{j=1}^{N} f(D_{h,\varepsilon}^j(t)), \qquad \textit{and} \qquad \mu(t,f) = \int f(\mathbf{x}, \widehat{\mathbf{k}}) u(t, \mathbf{x}, \widehat{\mathbf{k}})\, d\mathbf{x}\, \sigma(d\widehat{\mathbf{k}}),$$

where $(D_{h,\varepsilon}^j)_j$ is a sample of the numerical approximation to D_ε. For any $T > 0$, $\eta > 0$ and any smooth bounded function f on $\mathbb{R}^3 \times \mathbb{S}^2$, we have

$$\limsup_{N\to\infty} \mathbb{P}\Big(|\mu_{N,h,\varepsilon}(T,f) - \mu(T,f)| > \frac{\eta\Sigma_{h,\varepsilon}}{\sqrt{N}} + \varepsilon^{2-(\alpha_M/2)}F_0 + hF_1\Big) \le \operatorname{erfc}(\eta/\sqrt{2}), \tag{4.17}$$

where

$$\Sigma_{h,\varepsilon} = \sqrt{Var\big(f(D_{h,\varepsilon}(T))\big)} \leq \sup|f|,$$

and F_0 and F_1 are explicit constants independent of ε and the stepsize h.

In (4.17), there is three terms that quantify the approximation error of our estimator $\mu_{N,h,\varepsilon}(t,f)$: one of order $\varepsilon^{2-(\alpha_M/2)}$ due to the approximation of u by u_ε (the smaller the α_M, i.e. the less singular the kernel is, the smaller the error), one of order h due to the numerical approximation of the diffusion over the unit sphere, and one due to the MC approximation with the standard $1/\sqrt{N}$ convergence rate. Note that the discretization error of the diffusion process is only of order h and not of order the standard $\sqrt{h}$. The reason is that we are only interested in the convergence of MC estimators, allowing us to consider this discretization error in the weak sense [200]. Note that a weak second-order Runge-Kutta method can be considered to provide an error in h^2 instead of h for the Euler scheme [59], and a modifications of the SDE (4.15) can also be considered to provide weak higher-order schemes [1].

4.4.3 Numerical illustrations

We first illustrate the role of the correction and the role of α. We also present two situations, related to optical tomography and propagation through a non-Kolmogorov turbulent atmosphere, where α is no longer a constant. Furthermore, the stepsize h is chosen proportionally to the shortest mean free time,

$$\bar{\Lambda}_\varepsilon^{-1} := \frac{\alpha_m \varepsilon^{\alpha_M/2}}{2\pi \sup\lambda \sup a},$$

and small enough so that the approximation error w.r.t. ε in dominant. N is also chosen large enough for the MC error to be small compared to the approximation error in ε. The numerical simulations below are performed using the Julia programming language (v1.6.5) on a NVIDIA Quadro RTX 6000 GPU driven by a 24 Intel Xeon Sliver 2.20GHz CPUs station.

Role of the correction

To highlight the role of the correction provided by the diffusion on the unit sphere, the MC simulations, with and without the correction, are compared to a semi-analytic reference solution in the same spirit as in Sect. 4.3.

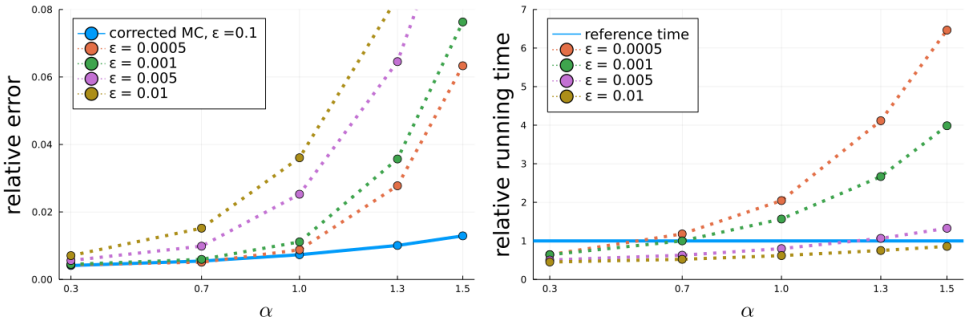

Fig. 4.7: Illustration of the relative error and running time of the MC method with and without a diffusive correction. The reference time in the right picture is the one of the corrected method with $\varepsilon = 0.1$. The observation time $T = 3t_S$ (t_S computed for $\alpha = 1$) and $N = 6 \times 10^8$.

In Fig. 4.7, we represent the relative error for various sizes of the cutoff ε. The left picture illustrates the evolution of the relative error for various ε. The blue curve corresponds to the corrected MC method with $\varepsilon = 0.1$ (with still a fairly large stepsize $h = 0.5/\bar{\Lambda}_\varepsilon$) providing at most a relative error slightly larger than 1%. The other curves correspond to the noncorrected MC method for several values of ε. The corrected MC method consistently yields a better accuracy compared to the noncorrected versions, and even in weakly singular cases where α is less than one. A very small value of ε (orange and green curves) is necessary to match the accuracy of the corrected method. The right

picture illustrates the evolution of the relative running time of the noncorrected method w.r.t. the corrected one. For values of α less than 0.7 (weakly singular kernels), corrected and noncorrected methods have similar computational times for comparable accuracy, while in the case of singular kernels, with $\alpha \geq 1$, the noncorrected method yields a much larger cost and a much lower accuracy.

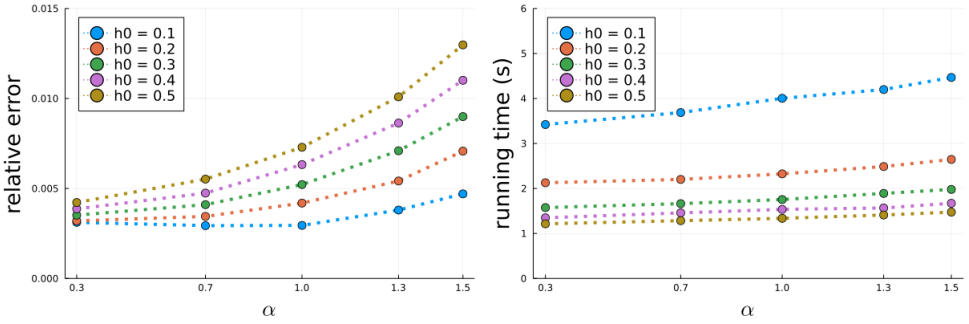

Fig. 4.8: Illustration of the relative error and running time of the corrected MC method.

In Fig. 4.8, we illustrate the precision and running time sensitivity of the (corrected) MC method w.r.t. the stepsize $h = h_0/\bar{\Lambda}_\varepsilon$. As expected, we obtain a better precision for smaller stepsizes but at the price of a longer running time. These effects are amplified as α increases due to the increasing strength of the diffusion correction. In what follows, we select $h_0 = 0.3$ since this value yields a relative error less than 1% for a wide range of α's while not changing significantly the running time.

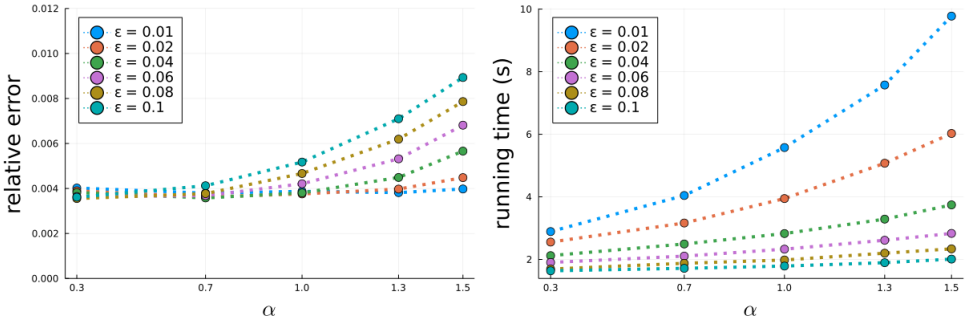

Fig. 4.9: Illustration of the relative error and running time of the corrected MC method.

In Fig. 4.9, we depict the precision and running time sensitivity w.r.t. the cutoff parameter ε, and observe the same phenomena as in the case of the stepsize h. With our choice of h, the parameter ε defines not only the accuracy of the diffusion correction, but also the average number of jumps, and as a consequence the running time increases as ε decreases as in the case of the noncorrected MC method.

The role of α

In this section, we highlight the effects of the kernel singularity on the energy density. We consider here a constant α's, with $a \equiv 0.002$. Our setting is depicted in Fig. 4.10. The spatial variable $\mathbf{x}$ is decomposed into a main propagation axis x_3 and a transverse plane $\mathbf{x}_\perp$, i.e. $\mathbf{x} = (\mathbf{x}_\perp, x_3) \in \mathbb{R}^2 \times \mathbb{R}$. The same notation holds for the direction variable $\widehat{\mathbf{k}} = (\widehat{\mathbf{k}}_\perp, \hat{k}_3) \in \mathbb{S}^2$. We choose an initial condition for the RTE of the form

$$u_0(\mathbf{x}, \widehat{\mathbf{k}}) = \delta(\mathbf{x})\delta(\widehat{\mathbf{k}} - \widehat{\mathbf{k}}_0), \qquad \text{with} \qquad \widehat{\mathbf{k}}_0 = (0, 0, 1),$$

modeling a source located at $\mathbf{x} = 0$, embedded in the random medium, and emitting in the forward x_3-direction. We set a function λ of the form $\lambda(\mathbf{x}) = \mathbf{1}_{(-5,40)}(x_3)$, that defines a scattering layer between $x_3 = -5$ and $x_3 = 40$. In such a configuration, both transmitted and reflected quantities at

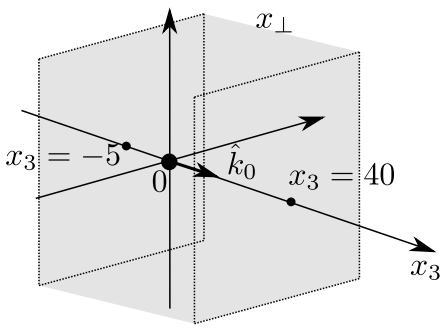

Fig. 4.10: Illustration of the numerical setting.

$x_3 = 40$ and $x_3 = -5$ are of interest. With our particular choice of $\widehat{\mathbf{k}}_0$, what is observed at $x_3 = -5$ is purely due to backscattering.

The observables, that are estimated by the MC method, are the following: the (time-integrated) transverse reflected and transmitted energy respectively defined by

$$F_{tr}^T(\mathbf{x}_\perp) := \int_0^T dt \int_{\mathbb{S}^2} \sigma(d\widehat{\mathbf{k}})\, u(t, \mathbf{x}_\perp, x_3 = 40, \widehat{\mathbf{k}})$$

and

$$F_{ref}^T(\mathbf{x}_\perp) := \int_0^T dt \int_{\mathbb{S}^2} \sigma(d\widehat{\mathbf{k}})\, u(t, \mathbf{x}_\perp, x_3 = -5, \widehat{\mathbf{k}}),$$

and the reflected and transmitted time evolution of the integrated energy exiting the slab by

$$\mathcal{F}_{tr}(t) := \int_{\mathbb{R}^2} d\mathbf{x}_\perp \int_{\mathbb{S}^2} \sigma(d\widehat{\mathbf{k}})\, u(t, \mathbf{x}_\perp, x_3 = 40, \widehat{\mathbf{k}})$$

and

$$\mathcal{F}_{ref}(t) := \int_{\mathbb{R}^2} d\mathbf{x}_\perp \int_{\mathbb{S}^2} \sigma(d\widehat{\mathbf{k}})\, u(t, \mathbf{x}_\perp, x_3 = -5, \widehat{\mathbf{k}}).$$

In what follows, the MC estimations of the observables are obtained using $N = 1 \times 10^9$ particles and a diffusion stepsize $h = 0.3/\bar{\Lambda}_\varepsilon$. We set $\varepsilon = 0.01$ for the transmitted quantities, and $\varepsilon = 0.1$ for the reflected ones. In the transmission case, and when ε is too large, the mean free time for the jumps is large as well and it is possible that particles escape the slab without undergoing any jumps, leading to inaccurate results. The choice $\varepsilon = 0.01$ provides good results to simulate transmitted quantities. Nonetheless, a larger value of ε still provides a good accuracy for the reflected quantities since the particles exiting the slab at $x_3 = -5$ have necessarily undergone some number of jumps and diffusion steps.

The running times for the time-integrated transmitted ($\varepsilon = 0.01$) and reflected ($\varepsilon = 0.1$) signals for different values of α are the following:

running time (s)	$\alpha = 0.3$	$\alpha = 0.7$	$\alpha = 0.1$	$\alpha = 1.3$	$\alpha = 1.5$
$\varepsilon = 0.01$	9.38	15.21	24.54	42.74	65.39
$\varepsilon = 0.1$	3.61	3.72	4.12	4.92	6.01

All these running time measurements account also for the transfer of the resulting arrays from the device (GPU) to the host, and correspond to the cost for the MC method to reach the expected accuracy for fixed ε's and α's. We clearly observe significantly larger running times for smaller values of ε and large values of α as expected. This is due to the increase in scattering events and diffusion steps as the mean free time decreases.

Comparision with the Henyey-Greenstein scattering kernel

According to the definition of the so-called Henyey-Greenstein scattering kernel (4.4) together with the asymptotic (4.5), our MC method should be a candidate to simulate numerically RTE with such

a scattering kernel in the highly peaked forward regime. In this section, we compare the solution to the RTE with the Henyey-Greenstein scattering kernel, for an anisotropy factor g close to one, with the solution to (4.11) with a singular kernel derived from (4.5), that is by setting $a \equiv (1-g)/(2\pi)$ and $\alpha = 1$ in (4.9). Note that the value of the constant a changes with g, and as a consequence $\bar{\Lambda}_\varepsilon$, h, and σ_ε vary accordingly. To illustrate this approximation, we still consider the setting depicted in Fig. 4.10 and the various observables introduced in the previous sections, but now at time $T = 300$. We observe in Fig. 4.11 the very good agreement between the two solutions. The reflected signal

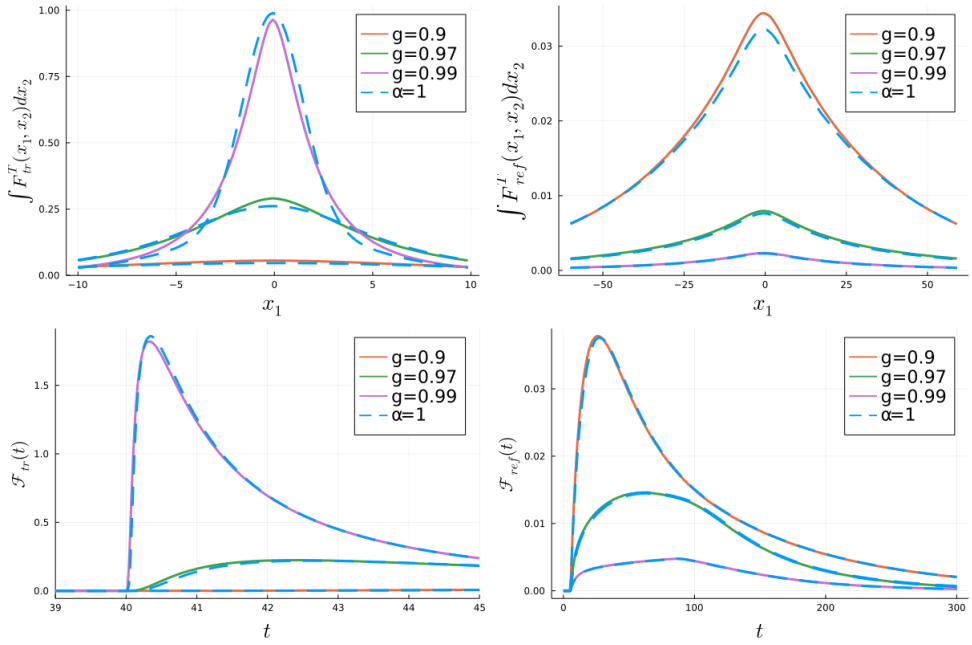

Fig. 4.11: Comparison of the observables obtained using the Henyey-Greenstein scattering kernel and our singular kernel with $\alpha = 1$, $T = 300$, $\varepsilon = 0.01$ for the transmitted observables (left panels), and $\varepsilon = 0.1$ for the reflected ones (right panels).

is well captured by our method despite fairly large values of ε and h. Also, let us mention that the computational cost is decreasing as the anisotropic parameter g is getting close to 1, as the overall jump intensity decreases in this case in the highly peaked regime $g \to 1$.

The RTE with a Henyey-Greenstein scattering kernel is simulated through a standard MC method. Compared to our method, its computational costs to simulate the transmitted and reflected observables are the following:

running time (s)	$g = 0.97$	$g = 0.98$	$g = 0.99$
HG kernel	8.3	7.6	6.0
singular kernel, $\varepsilon = 0.01$	13.9	6.7	2.0
singular kernel, $\varepsilon = 0.1$	2.5	1.5	0.7

According to this table, under our MC method, and for the reflected observables, lower computational times are observed for the three considered values of g compared to a standard MC method for the Henyey-Greenstein scattering kernel. Our MC method provides therefore an efficient tool to simulate numerically a RTE with such a scattering kernel. For transmitted observables, g needs to be quite close to one to provide a significant advantage to our method.

Now, we illustrate the influence of a varying α characterizing the strength of the singularity. We consider two situations, one inspired from optical tomography, and the second one from wave propagation through atmospheric turbulence.

A two-stage model with a sphere

We keep the setting depicted in Fig. 4.10, and add a defect with a different value of α. This defect is modeled by ball of radius 3 centered at the origin, with α sets to α_1 within the ball, and to 1 in

the exterior of the ball. See Fig. 4.12 for an illustration. This situation models a biological tissue in which statistical properties are changing and define a region of interest for imaging.

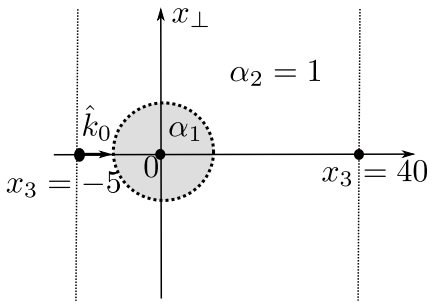

Fig. 4.12: Illustration of the setting with $\lambda = \mathbf{1}_{\{x_3 \in (-5,40)\}}$ and $\alpha(\mathbf{x}) = \alpha_1 \mathbf{1}_{\{\mathbf{x} \in B\}} + 1 \cdot \mathbf{1}_{\{\mathbf{x} \notin B\}}$ where B is a ball centered at 0 with radius 3. The source is here located at $(0, 0, -5)$.

We illustrate in Fig. 4.13 the impact of the defect on the observables introduced above. The impact is stronger on transmitted observables and quite significant, giving then the possibility to identify the defect inside the scattering medium. Reflected quantities tend to be less sensitive to the presence of the defect since a fraction of the signal is backscattered before reaching it.

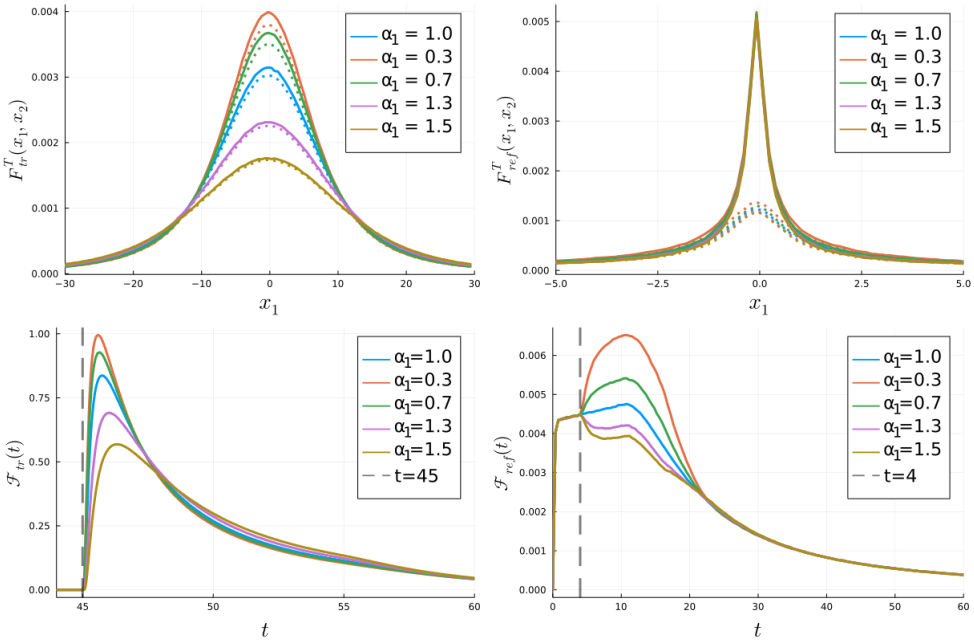

Fig. 4.13: Illustration of the transmitted (left-hand-side) and reflected (right-hand-side) observables with $T = 300$, and $\varepsilon = 0.01$. For the two top pictures we set $x_2 = 0$ (solid lines), and $x_2 = 1.5$ for the top-left and $x_2 = 0.5$ for top-right picture (dotted lines).

Non-Kolmogorov turbulences

We consider one more time the setting depicted in Fig. 4.10, with the difference that $\lambda = \mathbf{1}_{\{x_3 \in (0,20)\}}$ and that α takes three different large values depending on the altitude parametrized by x_3, see Fig. 4.14,

$$\alpha(x_3) = 5/3 \cdot \mathbf{1}_{\{x_3 \leq 2\}} + 4/3 \cdot \mathbf{1}_{\{2 < x_3 \leq 8\}} + 1.9 \cdot \mathbf{1}_{\{8 < x_3\}}.$$

The value 5/3 corresponds to a standard Kolmogorov turbulence model, while other values are associated with non-Kolmogorov turbulence models [31, 195, 212]. In these models, it is considered that

for altitudes higher than 8km, the atmospheric turbulence yields larger statistical patterns (which can be modeled through singular scattering kernels) than around the ground (0-2km). Hence, we set $\alpha = 1.9$ for altitudes greater than 8km. The function a is no longer constant in these models, and for our illustrations we chose

$$a(r) = 0.002 \cdot \exp(-r^2/(2 \times 0.8^2)).$$

In Fig. 4.15, one can notice that non-Kolmogorov turbulence yields quite different signals compared to Kolmogorov turbulence, in particular for reflected quantities. As we can see, the higher the α, the more diffuse is the signal which then enhances reflected signals. This explains the increased reflections in the non-Kolmogorov case.

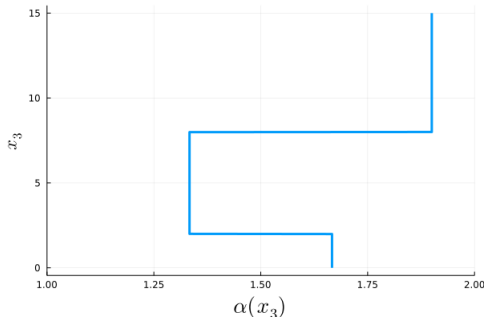

Fig. 4.14: Illustration of a three stages α-profile for a non-Kolmogorov phase function.

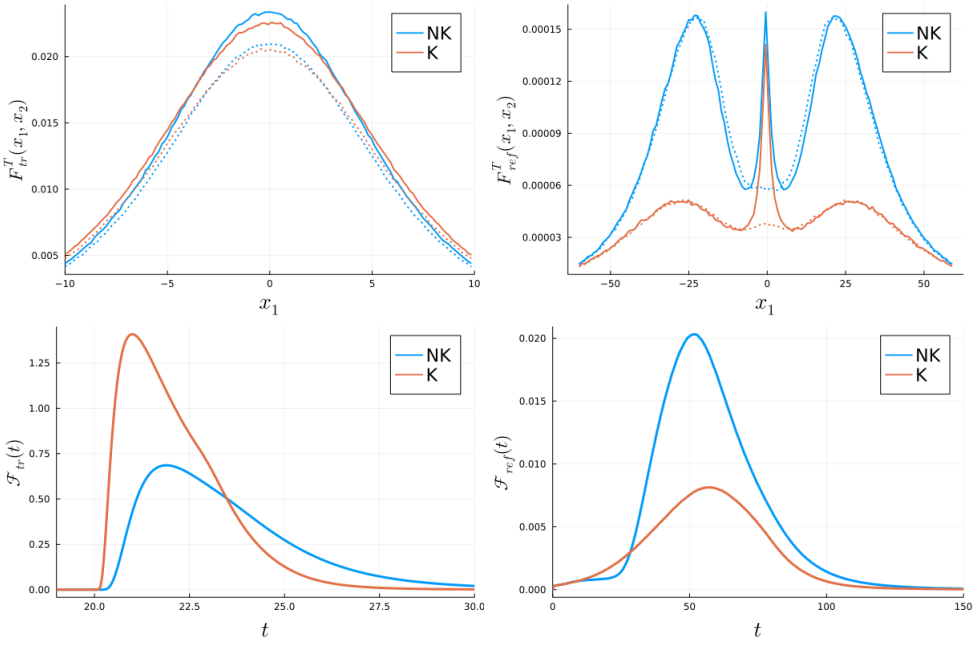

Fig. 4.15: Illustration of the transmitted (left-hand-side) and reflected (right-hand-side) observables with $T = 300$, and $\varepsilon = 0.01$. For the top two pictures we illustrate $x_2 = 0$ (solid lines) and $x_2 = 2$ for the top-left and $x_2 = 5$ for top-right picture (dot lines).

4.5 Perspectives

The original motivation for studying radiative transfer models with a spatially dependent scattering kernel (4.9) is driven by the resolution of some inverse problems. These include source or reflector

localization in turbulent atmosphere, as well as the estimation of the map α, which has applications in medical imaging or turbulence atmosphere. Inversion techniques for transport equations often rely on the singularities of the solution u of the RTE (see [20, 21]). However, the smoothness of u in the context of a singular scattering kernel suggests that the inversion could be more challenging compared to the situation of an integrable scattering kernel.

Although MC methods provide a relatively good accuracy at low cost, are easy to implement, and highly parallelizable, achieving higher accuracy often come at a significant increase in the computational time. Some variance reduction techniques might then be necessary to lower this cost. They generally amount to bias the particle trajectories toward regions of higher importance, and often result in important gains in terms of efficiency [142, 192].

Nowadays machine learning techniques are increasingly used to enhance the performance of numerical schemes and tackle inverse problems. Another perspective is therefore to evaluate the potential of machine learning techniques in simulating numerically RTEs, enabling variance reduction techniques, and solving radiative transfer based inverse problems.

Chapter 5

Boundary effects and weak localization in radiative transfer

This chapter describes the results obtained in Adel Messaoudi's Ph.D. thesis [158] under the supervision of Régis Cottereau (Laboratory of Mechanics and Acoustics in Marseille) and myself. The pictures presented in this chapter are all borrowed from this Ph.D. thesis. The two first sections of this chapter correspond to [16, 18] in the publication list on page 6.

Radiative transfer models are usually derived for wave problems defined on the entire space $\mathbb{R}^3$ under the weak scattering regime [12, 45, 180]. For instance, the scalar wave equation,

$$\partial_{tt}^2 p_\varepsilon(t,\mathbf{x}) - c^2\Big(\frac{\mathbf{x}}{\varepsilon}\Big)\Delta_{\mathbf{x}} p_\varepsilon(t,\mathbf{x}) = 0 \qquad (t,\mathbf{x}) \in (0,\infty)\times\Omega, \tag{5.1}$$

with $\Omega = \mathbb{R}^3$,

$$c^2\Big(\frac{\mathbf{x}}{\varepsilon}\Big) := c_0^2\Big(1+\sqrt{\varepsilon}V\Big(\frac{\mathbf{x}}{\varepsilon}\Big)\Big), \tag{5.2}$$

and equipped with appropriate initial conditions at $t = 0$, can be recast as the following first-order hyperbolic system:

$$\varepsilon\partial_t \mathbf{u}_\varepsilon + \mathcal{A}_\varepsilon \mathbf{u}_\varepsilon = 0, \qquad \text{where} \qquad \mathcal{A}_\varepsilon := -\begin{pmatrix} 0 & c^2(\mathbf{x}/\varepsilon) \\ \varepsilon^2\Delta_{\mathbf{x}} & 0 \end{pmatrix},$$

and

$$\mathbf{u}_\varepsilon(t,\mathbf{x}) := \begin{pmatrix} p_\varepsilon(t,\mathbf{x}) \\ \varepsilon\, c^{-2}(\mathbf{x}/\varepsilon)\partial_t p_\varepsilon(t,\mathbf{x}) \end{pmatrix} \qquad (t,\mathbf{x}) \in [0,\infty)\times\Omega.$$

The random field V in (5.2) accounts for variations of the wave-speed profile, and is assumed to exhibit some mixing properties. The energy carried by $\mathbf{u}_\varepsilon$ can be described using the Wigner transform,

$$W_\varepsilon(t,\mathbf{x},\mathbf{k}) := W[\mathbf{u}_\varepsilon,\mathbf{u}_\varepsilon](t,\mathbf{x},\mathbf{k}) = \int e^{i\mathbf{k}\cdot\mathbf{y}}\mathbf{u}_\varepsilon(\mathbf{x}-\varepsilon\mathbf{y}/2)\otimes\mathbf{u}_\varepsilon(\mathbf{x}+\varepsilon\mathbf{y}/2)\frac{d\mathbf{y}}{(2\pi)^3}.$$

The asymptotic behavior of this energy density is given by

$$W_0(t,\mathbf{x},\mathbf{k}) = \lim_{\varepsilon\to 0} W_\varepsilon(t,\mathbf{x},\mathbf{k}) = a(t,\mathbf{x},\mathbf{k})\mathbf{B}(\mathbf{k}) + a(t,\mathbf{x},-\mathbf{k})\mathbf{B}^T(\mathbf{k}), \tag{5.3}$$

where

$$\mathbf{B}(\mathbf{k}) := \frac{1}{2}\begin{pmatrix} 1/|\mathbf{k}|^2 & i/(c_0|\mathbf{k}|) \\ -i/(c_0|\mathbf{k}|) & 1/c_0^2 \end{pmatrix}, \tag{5.4}$$

and $\mathbf{B}^T(\mathbf{k})$ stands for its transposition. Here, $\mathbf{B}$ corresponds, in the Fourier domain, to an eigenvector of a dispersion matrix associated to $\mathcal{A}_\varepsilon$ with c_0^2 instead of $c^2(\mathbf{x}/\varepsilon)$. The amplitude $a(t,\mathbf{x},\mathbf{k})$ satisfies the following radiative transfer equation (RTE):

$$\partial_t a(t,\mathbf{x},\mathbf{k}) + c_0\widehat{\mathbf{k}}\cdot\nabla_{\mathbf{x}} a(t,\mathbf{x},\mathbf{k}) = -\Sigma(\mathbf{k})a(t,\mathbf{x},\mathbf{k}) + \int \sigma(\mathbf{k},\mathbf{q})a(t,\mathbf{x},\mathbf{q})\delta(c_0(|\mathbf{q}|-|\mathbf{k}|))d\mathbf{q}, \tag{5.5}$$

with $\widehat{\mathbf{k}} := \mathbf{k}/|\mathbf{k}|$, initial conditions of the form

$$a(t=0,\mathbf{x},\mathbf{k}) = \mathbb{A}(\mathbf{k})\delta(\mathbf{x}-\mathbf{x}_0), \tag{5.6}$$

and scattering kernel and attenuation respectively given by

$$\sigma(\mathbf{k},\mathbf{q}) := \frac{\pi c_0^2|\mathbf{k}|^2}{2(2\pi)^3}\widehat{R}(\mathbf{k}-\mathbf{q}), \qquad \text{and} \qquad \Sigma(\mathbf{k}) := \int \sigma(\mathbf{k},\mathbf{q})\delta(c_0(|\mathbf{q}|-|\mathbf{k}|))d\mathbf{q}. \tag{5.7}$$

Here, $\widehat{R}$ stands for the power spectral density of the random fluctuations V. It is worth mentioning that the limiting equation is deterministic while the original wave problem is of stochastic nature. Due to the high-frequency regime under consideration, averaging phenomena occur resulting in a deterministic model for the energy propagation.

Despite being a significant challenge for engineering applications, radiative transfer models involving boundaries have received less attention [2,22,150,161,181]. The main configuration studied in the literature corresponds to a half-space ($\Omega = \mathbb{R}^2 \times \mathbb{R}^*_-$), where radiative transfer models remain valid. With either Dirichlet or Neumann boundary conditions on $\partial\Omega = \{x_n = 0\}$, the resulting boundary condition for the Wigner transform is a geometric optic type reflection condition:

$$W(t,\mathbf{x}_\perp, x_n=0, \mathbf{k}_\perp, k_n) = W(t,\mathbf{x}_\perp, x_n=0, \mathbf{k}_\perp, -k_n). \tag{5.8}$$

In this chapter the spatial variable $\mathbf{x}$ is split into two components, $\mathbf{x} = (\mathbf{x}_\perp, x_n)$. Here, the x_n-variable represents the coordinate along the unit normal vector to the plane $\mathbb{R}^2 \times \{0\}$, while $\mathbf{x}_\perp$ denotes its transverse coordinate. Similarly, the wavevector is decomposed as $\mathbf{k} = (\mathbf{k}_\perp, k_n)$. Therefore, the relation (5.8) corresponds to a reflection condition w.r.t. the x_n-variable.

In what follows three propagation domains are discussed: the half-space, the slab, and the rectangle, all considered with Neumann boundary conditions for simplicity. For each case, the energy density propagation is described using RTEs, similar to (5.5), with reflection conditions (5.8) along each boundaries. Additionally, we present interference effects resulting from the presence of these boundaries. These effects can take place along the boundaries or within the propagation domain. Our approach is based on a method of images, which allows to extend the propagation domain over the full physical space $\mathbb{R}^3$ and conveniently represents these interference effects using the standard Wigner transform.

5.1 Boundary effects for a half-space

For the half-space $\Omega = \mathbb{R}^2 \times \mathbb{R}^*_-$, the wave equation (5.1) is equipped with Neumann boundary conditions,

$$\partial_{x_n} p_\varepsilon(t,\mathbf{x}_\perp, x_n=0) = 0 \qquad (t,\mathbf{x}_\perp) \in (0,\infty)\times\mathbb{R}^2,$$

and initial conditions of the form

$$p_\varepsilon(t=0,\mathbf{x}) = \frac{1}{\varepsilon^{3/2}}A\Big(\frac{\mathbf{x}-\mathbf{x}_0}{\varepsilon}\Big) \qquad \text{and} \qquad \partial_t p_\varepsilon(t=0,\mathbf{x}) = \frac{1}{\varepsilon^{3/2}}B\Big(\frac{\mathbf{x}-\mathbf{x}_0}{\varepsilon}\Big), \tag{5.9}$$

where $\mathbf{x}_0$ represents the source location in Ω. Here, the scaling in ε allows a nontrivial limit for the Wigner transform. The functions A and B are assumed to be even w.r.t the x_n-variable to provide convenient symmetry properties, and compactly supported so that the supports of the initial conditions do not cross the interface $\{x_n = 0\}$. In this chapter, we only consider the situation of initial conditions supported at a distance of order 1 from the boundaries. Situations where the source in close to the border (e.g. $x_{0,n} \to \varepsilon x_{0,n}$ for instance) and Dirichlet boundary conditions are addressed in [158].

5.1.1 The method of images

The basic principle of the method of images is to replace the wave propagation problem posed on a half-space with two new ones posed on the full-space:

$$\partial_{tt}^2 p_\varepsilon^\pm(t,\mathbf{x}) - c_{\sharp,\varepsilon}^2(\mathbf{x})\Delta_{\mathbf{x}} p_\varepsilon^\pm(t,\mathbf{x}) = 0 \qquad (t,\mathbf{x}) \in (0,\infty)\times\mathbb{R}^3,$$

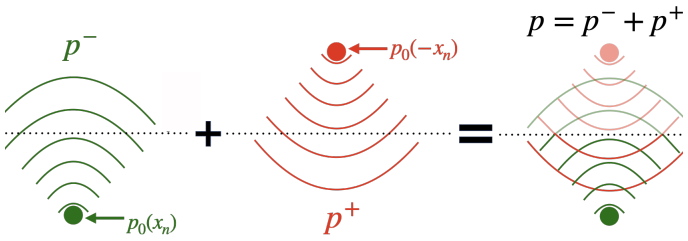

Fig. 5.1: Illustration of the method of images for the half-space bounded above by the dashed line representing $\{x_n = 0\}$. p^- represents an up-going wave propagating in a full-space from the original source location (in green). p^+ represents the down-going wave propagating from a fictitious source location resulting from the method of images (in red). The rightmost picture illustrates the original wave p propagating in the half-space, from the original source location, as a superposition of p^+ and p^-.

with symmetric initial conditions,

$$p_\varepsilon^-(t=0,\mathbf{x}) = \frac{1}{\varepsilon^{3/2}} A\Big(\frac{\mathbf{x}_\perp - \mathbf{x}_{0,\perp}}{\varepsilon}, \frac{x_n - x_{0,n}}{\varepsilon}\Big), \qquad p_\varepsilon^+(t=0,\mathbf{x}) = \frac{1}{\varepsilon^{3/2}} A\Big(\frac{\mathbf{x}_\perp - \mathbf{x}_{0,\perp}}{\varepsilon}, \frac{x_n + x_{0,n}}{\varepsilon}\Big),$$

and

$$\partial_t p_\varepsilon^-(t=0,\mathbf{x}) = \frac{1}{\varepsilon^{3/2}} B\Big(\frac{\mathbf{x}_\perp - \mathbf{x}_{0,\perp}}{\varepsilon}, \frac{x_n - x_{0,n}}{\varepsilon}\Big), \qquad \partial_t p_\varepsilon^+(t=0,\mathbf{x}) = \frac{1}{\varepsilon^{3/2}} B\Big(\frac{\mathbf{x}_\perp - \mathbf{x}_{0,\perp}}{\varepsilon}, \frac{x_n + x_{0,n}}{\varepsilon}\Big).$$

The extended wave-speed profile reads

$$c_{\sharp,\varepsilon}(\mathbf{x}) := c\Big(\frac{\mathbf{x}_\perp}{\varepsilon}, \frac{x_n}{\varepsilon}\Big)\mathbf{1}_{\mathbb{R}_-}(x_n) + c\Big(\frac{\mathbf{x}_\perp}{\varepsilon}, -\frac{x_n}{\varepsilon}\Big)\mathbf{1}_{\mathbb{R}_+^*}(x_n) \qquad \mathbf{x} \in \mathbb{R}^3.$$

The solution p_ε^- is referred to as the up-going wave, and p_ε^+ to as the down-going wave. Note that $c_{\sharp,\varepsilon}$ is an even function w.r.t. the x_n-variable so that

$$p_\varepsilon^+(t, \mathbf{x}_\perp, x_n) = p_\varepsilon^-(t, \mathbf{x}_\perp, -x_n), \tag{5.10}$$

for all $(t, \mathbf{x}_\perp, x_n) \in [0,\infty) \times \mathbb{R}^2 \times \mathbb{R}$. Finally, the extended wave problem is obtained by considering $p_\varepsilon^\sharp$ defined as

$$p_\varepsilon^\sharp(t,\mathbf{x}) := p_\varepsilon^-(t,\mathbf{x}) + p_\varepsilon^+(t,\mathbf{x}) \qquad (t,\mathbf{x}) \in \mathbb{R}_+ \times \mathbb{R}^3.$$

The symmetry relation (5.10) leads to the boundary conditions $\partial_{x_n} p_\varepsilon^\sharp(t, \mathbf{x}_\perp, x_n = 0) = 0$, so that, restricted to the half-space, the extended wavefield $p_\varepsilon^\sharp$ corresponds to the original one p_ε:

$$p_\varepsilon^\sharp(t,\mathbf{x}) = p_\varepsilon(t,\mathbf{x}),$$

for any $(t,\mathbf{x}) \in [0,\infty) \times \Omega$.

The wave equations associated to the up- and down-going waves can be recast as first order hyperbolic systems:

$$\varepsilon \partial_t \mathbf{u}_\varepsilon^j + \mathcal{A}_\varepsilon \mathbf{u}_\varepsilon^j = 0, \qquad \text{where} \qquad \mathcal{A}_\varepsilon := -\begin{pmatrix} 0 & c_{\sharp,\varepsilon}^2(\mathbf{x}) \\ \varepsilon^2\Delta & 0 \end{pmatrix},$$

with

$$\mathbf{u}_\varepsilon^j(t,\mathbf{x}) := \begin{pmatrix} p_\varepsilon^j(t,\mathbf{x}) \\ \varepsilon\, c_{\sharp,\varepsilon}^{-2}(\mathbf{x}) \partial_t p_\varepsilon^j(t,\mathbf{x}) \end{pmatrix} \qquad (t,\mathbf{x}) \in [0,\infty) \times \mathbb{R}^3,$$

for $j \in \{-,+\}$. A similar system can be obtained for $p_\varepsilon^\sharp$ by setting

$$\mathbf{u}_\varepsilon^\sharp := \mathbf{u}_\varepsilon^- + \mathbf{u}_\varepsilon^+.$$

The energy density carried by $\mathbf{u}_\varepsilon^\sharp$ is described through its Wigner transform

$$W_\varepsilon^\sharp := W[\mathbf{u}_\varepsilon^\sharp, \mathbf{u}_\varepsilon^\sharp],$$

and the energy density associated to the original problem is assumed to be given by the restriction of $W_\varepsilon^\sharp$ over the original half-space.

Note that $c_{\sharp,\varepsilon}^2$ can be written as (5.2), where the fluctuations around the background wave speed c_0 are of the form

$$V_\sharp\Big(\mathbf{x}, \frac{\mathbf{x}}{\varepsilon}\Big) = V_\sharp(\mathbf{x}, \mathbf{y})_{|\mathbf{y}=\frac{\mathbf{x}}{\varepsilon}} := V(\mathbf{y}_\perp, y_n)\mathbf{1}_{\mathbb{R}_-}(x_n) + V(\mathbf{y}_\perp, -y_n)\mathbf{1}_{\mathbb{R}_+^*}(x_n)\,{}_{|\mathbf{y}=\frac{\mathbf{x}}{\varepsilon}}.$$

For any fixed slow component $\mathbf{x}$, the power spectral density of $V_\sharp(\mathbf{x}, \cdot)$, w.r.t. the fast component $\mathbf{y}$, reads

$$\mathbb{E}\big[\widehat{\nu_\sharp}(\mathbf{x}, \mathbf{p})\widehat{\nu_\sharp}(\mathbf{x}, \mathbf{q})\big] = (2\pi)^3\delta(\mathbf{p}+\mathbf{q})\widehat{R}(\mathbf{p}), \tag{5.11}$$

where $\widehat{V_\sharp}(\mathbf{x}, \mathbf{p})$ stands for the Fourier transform of $V_\sharp(\mathbf{x}, \cdot)$ w.r.t. the $\mathbf{y}$-variable. Due to the symmetries, the resulting power spectral density does not depend on the slow component $\mathbf{x}$, and the method of images plays no role in the limiting RTE.

5.1.2 Radiative transfer model and boundary effects

The Wigner transform for $\mathbf{u}_\varepsilon^\sharp$ can be expanded as

$$\begin{aligned} W_\varepsilon^\sharp(t, \mathbf{x}, \mathbf{k}) = W[\mathbf{u}_\varepsilon^\sharp, \mathbf{u}_\varepsilon^\sharp](t, \mathbf{x}, \mathbf{k}) = W_\varepsilon^s(t, \mathbf{x}, \mathbf{k}) + W_\varepsilon^s(t, \mathbf{x}_\perp, -x_n, \mathbf{k}_\perp, -k_n) \\ + W_\varepsilon^c(t, \mathbf{x}, \mathbf{k}) + W_\varepsilon^c(t, \mathbf{x}_\perp, -x_n, \mathbf{k}_\perp, -k_n), \end{aligned}$$

where, using the symmetry relation (5.10),

$$W_\varepsilon^s := W[\mathbf{u}_\varepsilon^-, \mathbf{u}_\varepsilon^-] \qquad \text{and} \qquad W_\varepsilon^c := W[\mathbf{u}_\varepsilon^-, \mathbf{u}_\varepsilon^+].$$

The term W_ε^s is referred to as *self-Wigner transform*, and W_ε^c to as *cross-Wigner transform*.

To describe the energy density carried by $\mathbf{u}_\varepsilon^\sharp$, it is necessary to analyze the asymptotic behavior of both the self-Wigner transform and cross-Wigner transform. Thanks to the method of images the asymptotic behavior of the self-Wigner transform remains as for the full space (5.3). However, when considering the cross-Wigner transform, the same asymptotic analysis to that of the self-Wigner transform can be applied. This strategy results as well in a standard (linear) RTE, but this time with null initial conditions,

$$\lim_{\varepsilon\to 0} W_\varepsilon^c(t=0) = 0,$$

as the supports of the initial conditions of $\mathbf{u}_\varepsilon^-$ and $\mathbf{u}_\varepsilon^+$ are disjoint. Therefore, the contribution of the cross-Wigner transform is here negligible:

$$\lim_{\varepsilon\to 0} W_\varepsilon^c(t) = 0,$$

for any time $t > 0$. As a result, the energy density carried by $\mathbf{u}_\varepsilon^\sharp$ is given by

$$\begin{aligned} W^{tot}(t, \mathbf{x}, \mathbf{k}) &:= \lim_{\varepsilon\to 0} W_\varepsilon^\sharp(t, \mathbf{x}, \mathbf{k}) = W_0(t, \mathbf{x}, \mathbf{k}) + W_0(t, \mathbf{x}_\perp, -x_n, \mathbf{k}_\perp, -k_n) \\ &= \big(a(t, \mathbf{x}, \mathbf{k}) + a(t, \mathbf{x}_\perp, -x_n, \mathbf{k}_\perp, -k_n)\big)\mathbf{B}(\mathbf{k}) \\ &+ \big(a(t, \mathbf{x}, -\mathbf{k}) + a(t, \mathbf{x}_\perp, -x_n, -\mathbf{k}_\perp, k_n)\big)\mathbf{B}^T(\mathbf{k}), \end{aligned}$$

where the amplitude a satisfies the RTE (5.5) defined over the full-space $\mathbb{R}^3$, and $\mathbf{B}$ is given by (5.4). The resulting asymptotic energy density W^{tot} satisfies the reflection condition (5.8), and describes the energy propagation over the entire propagation domain. To capture interference effects we need to be a bit more careful.

The idea behind the interference phenomena is the following. Considering two mean-zero random variables X and Y with variance s^2, one can draw an analogy between the variance $\mathbb{E}[(X+Y)^2]$ and

the total energy density of the extended wave field $p_\varepsilon^\sharp$, which is the superposition of p_ε^- and p_ε^+. By expanding the square and the expectation, we obtain:

$$\mathbb{E}[(X+Y)^2] = E[X^2] + \mathbb{E}[Y^2] + 2\mathbb{E}[XY] = 2s^2(1+\cos(\phi)),$$

with $\phi \in [0, 2\pi)$. Therefore, the manifestation of the amplification phenomenon depends on the correlation between the two random variables. More precisely, for two independent random variables, no phenomenon is observed; for two perfectly positively correlated variables, the mean square of $X+Y$ is doubled. To observe some correlations between p_ε^- and p_ε^+, it should necessarily be at the interface $\{x_n = 0\}$, where the two waves are crossing. These correlations can be captured by the cross-Wigner transform that can be rewrite as

$$W_\varepsilon^c(t, \mathbf{x}, \mathbf{k}) = \frac{2}{\varepsilon(2\pi)} \iint e^{-2ik_n y_n/\varepsilon} e^{2ip_n x_n/\varepsilon} W_\varepsilon^s(t, \mathbf{x}_\perp, y_n, \mathbf{k}_\perp, p_n) dp_n dy_n. \tag{5.12}$$

The presence of the highly oscillatory terms $e^{-2ik_n/\varepsilon}$ and $e^{2ip_n x_n/\varepsilon}$ suggests to focus our attention at the vicinity of the interface $\{x_n = 0\}$ (within one wavelength), leading to the two changes of variables:

$$\mathbf{x} \to \mathbf{x}_\varepsilon := (\mathbf{x}_\perp, \varepsilon\tilde{x}_n/2) \qquad \text{and} \qquad \mathbf{k} \to \mathbf{k}_\varepsilon := (\mathbf{k}_\perp, \varepsilon\tilde{k}_n/2).$$

This first change of variable allows to focus near the boundary $\{x_n = 0\}$, and the second one corresponds to directions approximately parallel to this plane.

As a result, the asymptotic (nontrivial) contribution of W_ε^c is given by

$$\lim_{\varepsilon\to 0} \varepsilon W_\varepsilon^c(t, \mathbf{x}_\varepsilon, \mathbf{k}_\varepsilon) = \frac{2}{(2\pi)} \int e^{-i\tilde{k}_n y_n} e^{ip_n\tilde{x}_n} W_0(t, \mathbf{x}_\perp, y_n, \mathbf{k}_\perp, p_n) dp_n dy_n,$$

with W_0 defined by (5.3). This yields the total energy at the vicinity of the boundary $\{x_n = 0\}$:

$$E_{boundary}(t, \mathbf{x}_\perp, \tilde{x}_n) = 2 \int a(t, \mathbf{x}_\perp, x_n = 0, \mathbf{k})(1 + \cos(k_n\tilde{x}_n))\mathbf{D}(\mathbf{k}) d\mathbf{k},$$

with

$$\mathbf{D}(\mathbf{k}) := \begin{pmatrix} 1/|\mathbf{k}|^2 & 0 \\ 0 & 1/c_0^2 \end{pmatrix}. \tag{5.13}$$

Finally, for $\tilde{x}_n = 0$, that is exactly at the boundary, we have the relation:

$$E_{boundary}(t, \mathbf{x}_\perp, \tilde{x}_n = 0) = 2 \int W^{tot}(t, \mathbf{x}_\perp, x_n = 0) d\mathbf{k},$$

corresponding to a doubling of the energy described at the macroscopic level.

To conclude this section, it's important to note that the underlying idea to exhibit interference effects involves the analyze of two waves propagating in opposite directions along the mediator plane of the line joining the two sources. In the case of the half-space, the two waves cross at the boundary. In the remaining of this chapter, this idea is behind all the interference effects we describe.

5.2 Weak localization phenomena for a slab

In this section, a slab is defined as a domain contained in between two parallel planes:

$$\Omega = \mathbb{R}^2 \times (0, H).$$

The wave equation (5.1) is equipped with two Neumann boundary conditions,

$$\partial_{x_n} p(t, \mathbf{x}_\perp, x_n = 0) = \partial_{x_n} p(t, \mathbf{x}_\perp, x_n = H) = 0, \qquad (t, \mathbf{x}_\perp) \in (0, \infty) \times \mathbb{R}^2.$$

The initial conditions (5.9) are again assumed to be compactly supported within Ω to do not cross the boundaries, and even w.r.t the x_n-variable to provide convenient symmetry properties.

As described below, the situation in a slab slightly differs from that in a half-space. Although similar interference effects can be observed at the boundaries of the slab, additional interferences occur

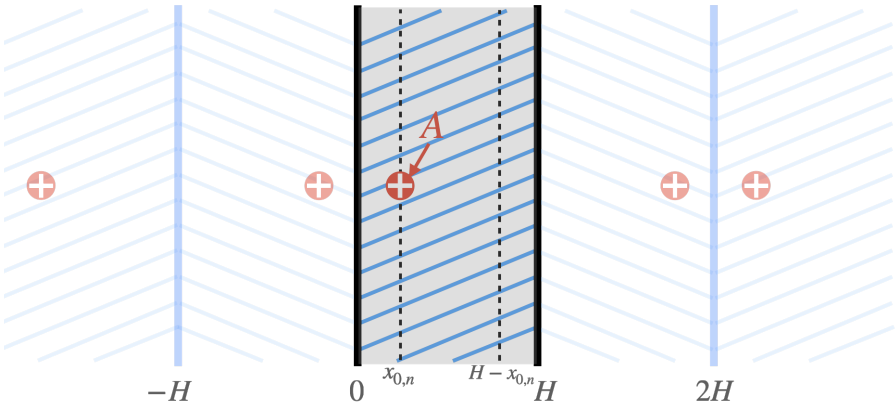

Fig. 5.2: Illustration of the method of images for the slab. The red crosses correspond to the source locations. Each wave propagates in a periodic full-space. Interference effects are observed within one wavelength of the boundaries (thick black lines), as well as along the dashed lines within the slab.

between waves emitted in opposite directions and crossing each other within the slab after bouncing back and forth between the boundaries. We refer to these additional interference effects as *weak localization phenomena* in the sense of [47, 76]. Although this term is often associated with enhance backscattering produced by heterogeneous propagation media, this terminology is here associated to reflection produced by the boundaries of the propagation medium.

The methodology used to analyze this situation relies again on the method of images, but it is now combined with an appropriate periodization of the source and wave-speed profile.

5.2.1 The method of images

The main idea is here to replace the wave problem posed on the slab, with given initial conditions, by a family of problems set over the full-space (see Fig. 5.2). To this end, we introduce the following wave problem over the full-space:

$$\partial_{tt}^2 q_\varepsilon(t,\mathbf{x}) - c_{\sharp,\varepsilon}^2(\mathbf{x})\Delta_{\mathbf{x}} q_\varepsilon(t,\mathbf{x}) = 0 \qquad (t,\mathbf{x}) \in (0,\infty)\times\mathbb{R}^3,$$

with initial conditions (5.9), and wave-speed profile

$$c_{\sharp,\varepsilon}(\mathbf{x}) = \sum_{j\in\mathbb{Z}} c\Big(\frac{\mathbf{x}_\perp}{\varepsilon}, \frac{x_n - 2jH}{\varepsilon}\Big) 1_{[0,H)}(x_n - 2jH) + c\Big(\frac{\mathbf{x}_\perp}{\varepsilon}, \frac{-x_n + 2jH}{\varepsilon}\Big) 1_{[-H,0]}(x_n - 2jH) \qquad \mathbf{x}\in\mathbb{R}^3.$$

The extended wavefield over the full-space is then given by

$$p_\varepsilon^\sharp(t,\mathbf{x}) := \sum_{j\in\mathbb{Z}} q_\varepsilon(t,\mathbf{x}_\perp, x_n - 2jH) + q_\varepsilon(t,\mathbf{x}_\perp, -(x_n - 2jH)) \qquad (t,\mathbf{x})\in[0,\infty)\times\mathbb{R}^3, \tag{5.14}$$

and through symmetry relations corresponds to the original wavefield on the slab:

$$p_\varepsilon^\sharp(t,\mathbf{x}) = p_\varepsilon(t,\mathbf{x}),$$

for all $(t,\mathbf{x})\in[0,\infty)\times\Omega$.

A first order hyperbolic system can be associated to $p_\varepsilon^\sharp$ and q_ε by considering

$$\mathbf{u}_\varepsilon(t,\mathbf{x}) := \begin{pmatrix} q_\varepsilon(t,\mathbf{x}) \\ \varepsilon\, c_{\sharp,\varepsilon}^{-2}(\mathbf{x})\partial_t q_\varepsilon(t,\mathbf{x}) \end{pmatrix} \qquad \text{and} \qquad \mathbf{u}_\varepsilon^\sharp(t,\mathbf{x}) := \begin{pmatrix} p_\varepsilon^\sharp(t,\mathbf{x}) \\ \varepsilon\, c_{\sharp,\varepsilon}^{-2}(\mathbf{x})\partial_t p_\varepsilon^\sharp(t,\mathbf{x}) \end{pmatrix},$$

for $(t,\mathbf{x})\in[0,\infty)\times\mathbb{R}^3$. According to (5.14) both wavefield are related as follows,

$$\mathbf{u}_\varepsilon^\sharp(t,\mathbf{x}) = \sum_{j\in\mathbb{Z}} \mathbf{u}_\varepsilon(t,\mathbf{x}_\perp, x_n - 2jH) + \mathbf{u}_\varepsilon(t,\mathbf{x}, -x_n + 2jH) \qquad (t,\mathbf{x})\in[0,\infty)\times\mathbb{R}^3.$$

5.2.2 The self- and cross-Wigner transforms

The energy density carried by $p_\varepsilon^\sharp$, represented by the Wigner transform of $\mathbf{u}_\varepsilon^\sharp$, can be expanded as

$$W_\varepsilon^\sharp := W[\mathbf{u}_\varepsilon^\sharp, \mathbf{u}_\varepsilon^\sharp] = W_\varepsilon^{1,\sharp} + W_\varepsilon^{2,\sharp} + W_\varepsilon^{3,\sharp},$$

with

$$\begin{aligned}
W_\varepsilon^{1,\sharp}(t,\mathbf{x},\mathbf{k}) &:= \sum_{j\in\mathbb{Z}} W_\varepsilon(t,\mathbf{x}_\perp, x_n - 2jH, \mathbf{k}) + W_\varepsilon(t,\mathbf{x}_\perp, -x_n + 2jH, \mathbf{k}_\perp, -k_n),\\
W_\varepsilon^{2,\sharp}(t,\mathbf{x},\mathbf{k}) &:= \sum_{j,\ell\in\mathbb{Z}} V_\varepsilon^{j\ell}(t,\mathbf{x},\mathbf{k}) + V_\varepsilon^{j\ell}(t,\mathbf{x}_\perp, -x_n, \mathbf{k}_\perp, -k_n),\\
W_\varepsilon^{3,\sharp}(t,\mathbf{x},\mathbf{k}) &:= \sum_{\substack{j,l\in\mathbb{Z}\\ \ell\neq j}} W_\varepsilon^{j\ell}(t,\mathbf{x},\mathbf{k}) + W_\varepsilon^{j\ell}(t,\mathbf{x}_\perp, -x_n, \mathbf{k}_\perp, -k_n),
\end{aligned}$$

where

$$W_\varepsilon := W[\mathbf{u}_\varepsilon, \mathbf{u}_\varepsilon],$$

refers to as the self-Wigner transform, and

$$\begin{aligned}
V_\varepsilon^{j\ell}(t,\mathbf{x},\mathbf{k}) := \int_{\mathbb{R}^3} e^{i\mathbf{k}\cdot\mathbf{y}} &\mathbf{u}_\varepsilon\Big(t,\mathbf{x}_\perp - \frac{\varepsilon\mathbf{y}_\perp}{2}, x_n - \frac{\varepsilon y_n}{2} - 2jH\Big)\\
&\otimes \mathbf{u}_\varepsilon\Big(t,\mathbf{x}_\perp + \frac{\varepsilon\mathbf{y}_\perp}{2}, -x_n - \frac{\varepsilon y_n}{2} + 2\ell H\Big)\Big)\frac{d\mathbf{y}}{(2\pi)^3}\\
W_\varepsilon^{j\ell}(t,\mathbf{x},\mathbf{k}) := \int_{\mathbb{R}^3} e^{i\mathbf{k}\cdot\mathbf{y}} &\mathbf{u}_\varepsilon\Big(t,\mathbf{x}_\perp - \frac{\varepsilon\mathbf{y}_\perp}{2}, x_n - \frac{\varepsilon y_n}{2} - 2jH\Big)\\
&\otimes \mathbf{u}_\varepsilon\Big(t,\mathbf{x}_\perp + \frac{\varepsilon\mathbf{y}_\perp}{2}, x_n + \frac{\varepsilon y_n}{2} - 2\ell H\Big)\frac{d\mathbf{y}}{(2\pi)^3},
\end{aligned}$$

which both refer to as cross-Wigner transforms.

The cross-Wigner transform $V_\varepsilon^{j\ell}$ corresponds to waves whose initial conditions are located around $(\mathbf{x}_{0,\perp}, 2jH + x_{0,n})$ and $(\mathbf{x}_{0,\perp}, 2\ell H - x_{0,n})$ respectively. The mediator plane of the line joining these two sources, and along which interference effects take place, is $\{x_n = (j+\ell)H\}$. When restricted to the slab, $V_\varepsilon^{j\ell}$ provides nontrivial effects at the boundaries of the slab: $\{x_n = 0\}$ for $\ell = -j$, and $\{x_n = H\}$ for $\ell = 1 - j$.

Regarding the cross-Wigner transform $W_\varepsilon^{j\ell}$, it corresponds to waves whose initial conditions are located around either $(\mathbf{x}_{0,\perp}, 2jH + x_{0,n})$ and $(\mathbf{x}_{0,\perp}, 2\ell H + x_{0,n})$ in a first case, or around $(\mathbf{x}_{0,\perp}, -2jH - x_{0,n})$ and $(\mathbf{x}_{0,\perp}, -2\ell H - x_{0,n})$ in a second case. The mediator plane of the line joining these two sources, and along which interference effects take place, is $\{x_n = \pm x_{0,n} \pm (j+\ell)H\}$. When restricted to the slab, $W_\varepsilon^{j\ell}$ provides nontrivial effects along $\{x_n = x_{0,n}\}$ for $\ell = -j$ in the first case, and $\{x_n = H - x_{0,n}\}$ for $\ell = -1 - j$ in the second case. In contrast to $V_\varepsilon^{j\ell}$, the terms $W_\varepsilon^{j\ell}$ describe interference effects affecting only the coherent part of the energy. The reason for this difference, w.r.t. $V_\varepsilon^{j\ell}$, arise from the fact that when the two waves associated to $W_\varepsilon^{j\ell}$ intersect, they have experienced different random propagation media, while for $V_\varepsilon^{j\ell}$ they travel through the same medium by symmetry.

5.2.3 Boundary effects and weak localization phenomena

As for the half-space, without specific precaution, both cross-Wigner transforms $V_\varepsilon^{j\ell}$ and $W_\varepsilon^{j\ell}$ go to 0 as $\varepsilon \to 0$. In fact, the limits of $V_\varepsilon^{j\ell}$ and $W_\varepsilon^{j\ell}$ can be both described as solutions to standard (linear) transport equations with null initial conditions. As a result, the total energy density propagating over

the whole slab is only given by the contribution of $W_\varepsilon^{1,\sharp}$, which is associated to self-Wigner transforms:

$$\begin{aligned}W^{tot}(t,\mathbf{x},\mathbf{k}) := \lim_{\varepsilon\to 0} W_\varepsilon^\sharp(t,\mathbf{x},\mathbf{k}) &= \lim_{\varepsilon\to 0} W_\varepsilon^{1,\sharp}(t,\mathbf{x},\mathbf{k})\\ &= \sum_{j\in\mathbb{Z}} W_0(t,\mathbf{x}_\perp, x_n - 2jH,\mathbf{k}) + W_0(t,\mathbf{x}_\perp,-x_n+2jH,\mathbf{k}_\perp,-k_n)\\ &= \sum_{j\in\mathbb{Z}} (a(t,\mathbf{x}_\perp,x_n-2jH,\mathbf{k}) + a(t,(\mathbf{x}_\perp,-x_n+2jH,\mathbf{k}_\perp,-k_n))\mathbf{B}(\mathbf{k})\\ &+ \sum_{j\in\mathbb{Z}} (a(t,\mathbf{x}_\perp,x_n-2jH,-\mathbf{k}) + a(t,\mathbf{x}_\perp,-x_n+2jH,-\mathbf{k}_\perp,k_n))\mathbf{B}^T(\mathbf{k}),\end{aligned}$$

according to (5.3). From this formulation, W^{tot} satisfies the reflexion condition (5.10) at both $x_n = 0$ and $x_n = H$. The sum in j accounts for the periodic behavior of the energy density within the slab.

Regarding the interference effects within one wavelength of the boundary $\{x_n = 0\}$, and using a representation similar to (5.12), we have now

$$\begin{aligned}E_{\{x_n=0\}}(t,\mathbf{x}_\perp,\tilde{x}_n) &:= \int \lim_{\varepsilon\to 0} W_\varepsilon^\sharp(t,\varepsilon\tilde{x}_n/2,\mathbf{k})d\mathbf{k}\\ &= \int \lim_{\varepsilon\to 0} W_\varepsilon^{1,\sharp}(t,\varepsilon\tilde{x}_n/2,\mathbf{k})d\mathbf{k}\\ &+ \frac{1}{2}\sum_{j\in\mathbb{Z}} \int \lim_{\varepsilon\to 0} \varepsilon V_\varepsilon^{j,\ell=-j}(t,\mathbf{x}_\perp,\varepsilon\tilde{x}_n/2,\mathbf{k}_\perp,\varepsilon\tilde{k}_n/2))\\ &\qquad + \lim_{\varepsilon\to 0} \varepsilon V_\varepsilon^{j,\ell=-j}(t,\mathbf{x}_\perp,-\varepsilon\tilde{x}_n/2,\mathbf{k}_\perp,-\varepsilon\tilde{k}_n/2)d\mathbf{k}_\perp d\tilde{k}_n,\end{aligned}$$

yielding after some algebra to

$$E_{\{x_n=0\}}(t,\mathbf{x}_\perp,\tilde{x}_n) = 2\sum_{j\in\mathbb{Z}} \int a(t,\mathbf{x}_\perp,2jH,\mathbf{k})(1+\cos(k_n\tilde{x}_n))\mathbf{D}(\mathbf{k})d\mathbf{k},$$

where $\mathbf{D}$ is given by (5.13). At exactly the boundary, we obtain again a doubling of the total energy,

$$E_{\{x_n=0\}}(t,\mathbf{x}_\perp,\tilde{x}_n=0) = 2\int W^{tot}(t,\mathbf{x}_\perp,x_n=0)d\mathbf{k}.$$

The same type of result holds at the boundary $\{x_n = H\}$,

$$\begin{aligned}E_{\{x_n=H\}}(t,\mathbf{x}_\perp,\tilde{x}_n) &= \int \lim_{\varepsilon\to 0} W_\varepsilon^\sharp(t,H+\varepsilon\tilde{x}_n/2,\mathbf{k})d\mathbf{k}\\ &= 2\sum_{j\in\mathbb{Z}} \int a(t,\mathbf{x}_\perp,(2j+1)H,\mathbf{k})(1+\cos(k_n\tilde{x}_n))\mathbf{D}(\mathbf{k})d\mathbf{k}.\end{aligned}$$

yielding also a doubling of the total energy

$$E_{\{x_n=H\}}(t,\mathbf{x}_\perp,\tilde{x}_n=0) = 2\int W^{tot}(t,\mathbf{x}_\perp,x_n=H)d\mathbf{k}.$$

Regarding, the interference effects along the plane $\{x_n = x_{0,n}\}$, we have this time

$$\begin{aligned}E_{\{x_n=x_{0,n}\}}(t,\mathbf{x}_\perp,\tilde{x}_n) &:= \int \lim_{\varepsilon\to 0} W_\varepsilon^\sharp(t,\mathbf{x}_\perp,x_{0,n}+\varepsilon\tilde{x}_n/2,\mathbf{k})d\mathbf{k}\\ &= \int \lim_{\varepsilon\to 0} W_\varepsilon^{1,\sharp}(t,\mathbf{x}_\perp,x_{0,n}+\varepsilon\tilde{x}_n/2,\mathbf{k})d\mathbf{k}\\ &+ \frac{1}{2}\sum_{j\in\mathbb{Z}^*} \iint \lim_{\varepsilon\to 0} W_\varepsilon^{j,\ell=-j}(t,\mathbf{x}_\perp,x_{0,n}+\varepsilon\tilde{x}_n/2,\mathbf{k}_\perp,\varepsilon\tilde{k}_n/2)d\mathbf{k}_\perp d\tilde{k}_n.\end{aligned}$$

After some algebra, the total energy reads

$$
\begin{aligned}
E_{\{x_n=x_{0,n}\}}(t,\mathbf{x}_\perp,\tilde{x}_n) = &\int W^{tot}(t,\mathbf{x}_\perp,x_n=x_{0,n})d\mathbf{k} \\
&+2\sum_{j\in\mathbb{Z}^*}\int \cos(k_n\tilde{x}_n)e^{-\Sigma(\mathbf{k})t}\mathbb{A}(\mathbf{k})\delta(\mathbf{x}_\perp-\mathbf{x}_{0,\perp}-c_0t\widehat{\mathbf{k}}_\perp) \\
&\qquad\qquad \times\delta(2jH-c_0t\widehat{\mathbf{k}}_n)\mathbf{D}(\mathbf{k})d\mathbf{k} \\
&+2\sum_{j\in\mathbb{Z}^*}\int \sin(k_n\tilde{x}_n)e^{-\Sigma(\mathbf{k})t}\mathbb{A}(\mathbf{k})\delta(\mathbf{x}_\perp-\mathbf{x}_{0,\perp}-c_0t\widehat{\mathbf{k}}_\perp) \\
&\qquad\qquad \times\delta(2jH-c_0t\widehat{\mathbf{k}}_n)\widetilde{\mathbf{D}}(\mathbf{k})d\mathbf{k},
\end{aligned}
$$

with

$$
\widetilde{\mathbf{D}}(\mathbf{k}) := \frac{1}{c_0|\mathbf{k}|}\begin{pmatrix}0 & 1\\ -1 & 0\end{pmatrix},
$$

$\mathbf{D}$ given by (5.13), $\mathbb{A}$ by (5.6), and $\Sigma(\mathbf{k})$ by (5.7). In this formulation, the Dirac masses $\delta(2jH-c_0t\widehat{\mathbf{k}}_n)$ account for the periodic onset of the interferences, which occurs at each time $2jH/c_0$ for $j\geq 1$. Also, each contribution is damped at rate $\Sigma(\mathbf{k})$ (no multiple scattering) and freely transport along the plane $\{x_n=x_{0,n}\}$. These additional contributions are associated to the coherent part carried by the amplitude a, satisfying the RTE (5.5), along the plan $\{x_n=x_{0,n}\}$.

The same type of result holds for the plane $\{x_n=H-x_{0,n}\}$, where the total energy reads

$$
\begin{aligned}
E_{\{x_n=H-x_{0,n}\}}(t,\mathbf{x}_\perp,\tilde{x}_n) = &\int W^{tot}(t,\mathbf{x}_\perp,x_n=H-x_{0,n})d\mathbf{k} \\
&+2\sum_{j\in\mathbb{Z}}\int \cos(k_n\tilde{x}_n)e^{-\Sigma(\mathbf{k})t}\mathbb{A}(\mathbf{k})\delta(\mathbf{x}_\perp-\mathbf{x}_{0,\perp}-c_0t\widehat{\mathbf{k}}_\perp) \\
&\qquad\qquad \times\delta((2j+1)H-c_0t\widehat{\mathbf{k}}_n)\mathbf{D}(\mathbf{k})d\mathbf{k} \\
&+2\sum_{j\in\mathbb{Z}}\int \sin(k_n\tilde{x}_n)e^{-\Sigma(\mathbf{k})t}\mathbb{A}(\mathbf{k})\delta(\mathbf{x}_\perp-\mathbf{x}_{0,\perp}-c_0t\widehat{\mathbf{k}}_\perp) \\
&\qquad\qquad \times\delta((2j+1)H-c_0t\widehat{\mathbf{k}}_n)\widetilde{\mathbf{D}}(\mathbf{k})d\mathbf{k}.
\end{aligned}
$$

5.3 The case of a rectangle

The interference effects we observe for a rectangular domain $[0,H_1]\times[0,H_2]$ share similarities with those observed in the half-space and the slab. Nevertheless, due to the bounded nature of the propagation domain, there are additional interference locations. In this section, we follow the same strategy, but do not provide any mathematical details on the interference effects as their descriptions are quite technical. Instead, we provide formal descriptions supported by some illustrations. A detailed treatment of this situation can be found in [158].

The method of images The method of images follows here a similar strategy to that used for the slab. The solution to the wave equation on the rectangle is extended over the full space $\mathbb{R}^3$, but in contrast to the slab, both coordinates are bounded and necessitate a periodic extension. The solution to the extended wave equation can be expressed as a superposition of waves whose initial conditions are located in a symmetric and periodic manner in order to enforce Neumann boundary conditions. We refer to Fig. 5.3 for an illustration. As a result, the extended solution reduces to the original wave problem when restricted to the rectangle.

Self- and cross-Wigner transform The analysis of the energy propagation is conducted using the Wigner transform of the extended solution. This Wigner transform can be expanded over two types of Wigner transform: the self- and cross-Wigner transform. As with the slab, the self-Wigner

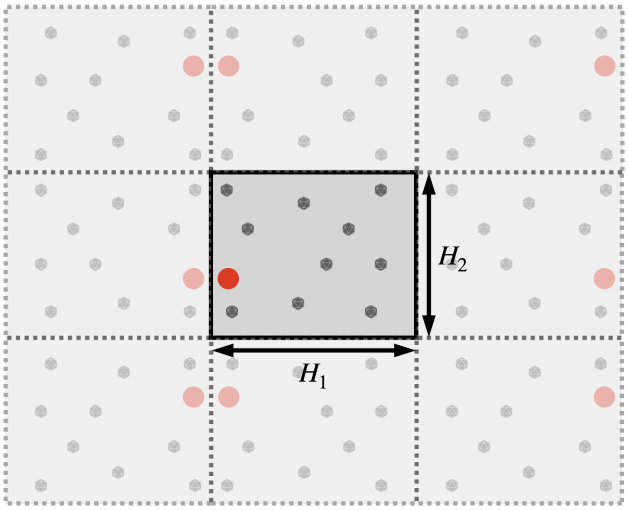

Fig. 5.3: Illustration of the method of images for the rectangle $[0, H_1] \times [0, H_2]$. Each wave propagates from a different initial location (in red).

transforms account for energy propagation all over the rectangle, and can be described in terms of the standard RTE (5.5) over the full space:

$$\int W^{tot}(t, \mathbf{x}, \mathbf{k}) d\mathbf{k} = \sum_{j_1, j_2 \in \mathbb{Z}^2} \sum_{\alpha_1, \alpha_2 \in \{+,-\}} \int a(t, \alpha_1(x_1 - 2j_1 H_1), \alpha_2(x_2 - 2j_2 H_2), \mathbf{k}) \mathbf{D}(\mathbf{k}) d\mathbf{k},$$

where a satisfies (5.5) in $\mathbb{R}^2$ instead of $\mathbb{R}^3$, $\mathbf{D}$ is given by (5.13). Here, W^{tot} satisfies reflexion conditions similar to (5.10) along each boundaries. The infinite sums in j_1 and j_2 account for the periodic behavior of the energy propagation when restricted to the rectangle w.r.t. both variables.

The cross-Wigner transforms capture interference effects over the propagation domain. As observed for the half-space and the slab, these effects occur along the mediator line of the line connecting the two source locations.

Interference effects along the boundaries As in the context of a half-space or a slab, constructive interference effects can be observed within one wavelength of each boundaries, resulting in a doubling of the total energy when looking exactly at the borders. In this case the whole energy is affected, not only its coherent part. We refer to Fig. 5.4 for an illustration.

Interference effects along lines parallel to the boundaries Similar to the slab, interference effects occur within one wavelength along lines parallel to the boundaries, passing through the source location and three other symmetric points. In this context, the two interacting waves have not experienced the same propagation medium, so that only the coherent part of the energy is affected. We refer to Fig. 5.5 for an illustration.

Due to the bounded nature of the propagation domain, additional symmetries between two source locations become possible.

Interference effects along lines passing though the corners The periodic extension of the rectangle in both coordinates allows to draw mediator lines, w.r.t. the lines connecting the source locations, that are now oblique when crossing the rectangle. As illustrated in Fig. 5.6, pairs of sources are able to produce interference effects along oblique lines passing through symmetric points, here the corners of the rectangle. In this context, the two interacting waves have travel through the same propagation medium, resulting in interferences that affect the whole energy, not only its coherent part. In contrast with the interference lines parallel to the boundaries, here, a given line supports interference effects only once over time. Despite the periodic nature of these effects, as they pass through the same corner, the lines supporting the interference effects rotate as the source locations producing these interferences are getting apart from each other.

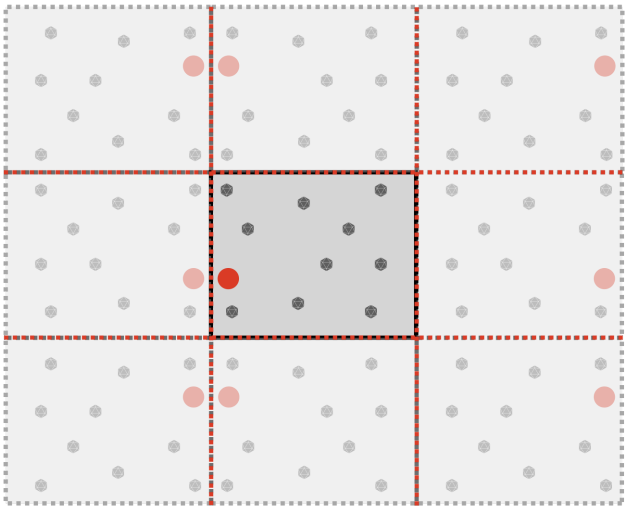

Fig. 5.4: Illustration of the interference effects localized within one wavelength of the four boundaries (red dashed lines).

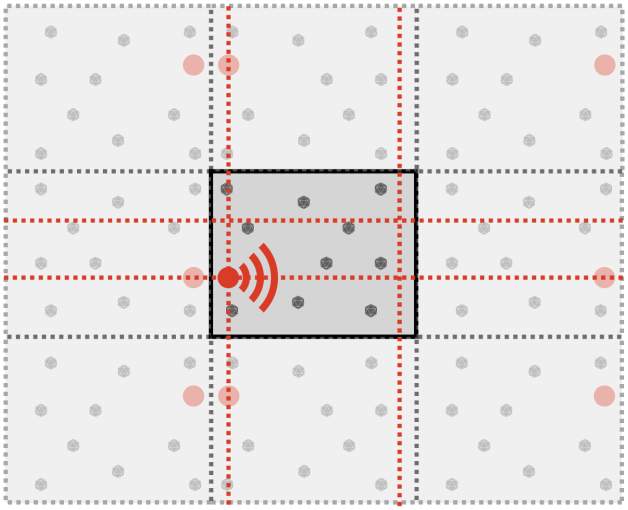

Fig. 5.5: Illustration of the interference effects within one wavelength of the vertical lines $\{x_1 = x_{0,1}\}$ and $\{x_1 = H_1 - x_{0,1}\}$, as well as the horizontal lines $\{x_2 = x_{0,2}\}$ and $\{x_2 = H_2 - x_{0,2}\}$ (the red dashed lines).

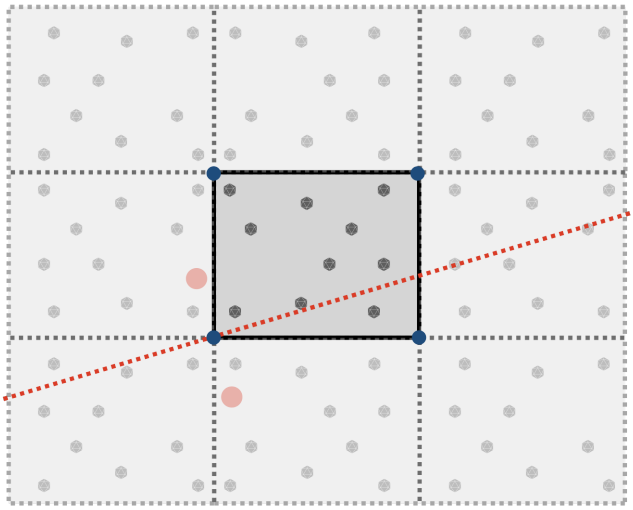

Fig. 5.6: Illustration of an interference effect within one wavelength of the line passing through the lower left corner (red dashed lines).

Interference effects along lines passing though the source location and symmetric points Twelve additional symmetric points can be identified, all located along the boundaries and inside the rectangle (including the original source location). We refer to Fig. 5.7 for an illustration. As for the corners, and for the same reasons, oblique lines of interference are passing periodically through these points. However, a given line supports interference effects only once over time. Nonetheless, in this context, the two interacting waves have not experienced the same propagation medium, resulting in interference affecting only the coherent part of the energy.

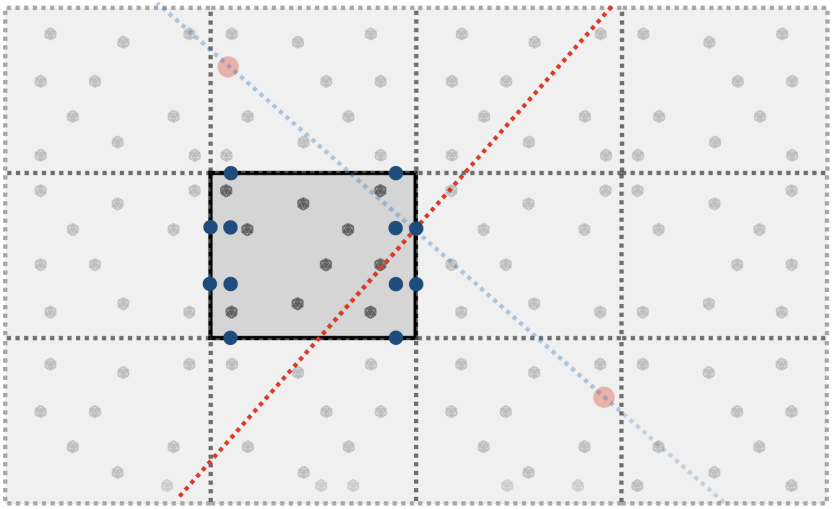

Fig. 5.7: Illustration of an interference effect within one wavelength of the line passing through one of the twelve points (here $(H_1, H_2 - x_{0,2})$). The points are $\mathbf{x}_0$ (the source location), and from the bottom to the top, $(x_{0,1}, 0)$, $(H_1 - x_{0,1}, 0)$, $(0, x_{0,2})$, $(H_1 - x_{0,1}, x_{0,2})$, $(H_1, x_{0,2})$, $(0, H_2 - x_{0,2})$, $(x_{0,1}, H_2 - x_{0,2})$, $(H_1 - x_{0,1}, H_2 - x_{0,2})$, $(H_1, H_2 - x_{0,2})$, $(x_{0,1}, H_2)$, $(H_1 - x_{0,1}, H_2)$.

5.4 Perspectives

The understanding of the weak localization phenomena in the context of RTEs is a major challenge in nondestructive testing of concrete structures. These phenomena, driven by interference effects, offer the opportunity to extract valuable information from the enhancement intensity about the internal

structure and material properties. Numerical test should be performed to compare our theory with the work of [47, 76] conducted in homogeneous media. In particular, in heterogeneous media, the weak localization effects are exponentially damped, much like the total energy traveling over the whole domain. Therefore, quantifying the duration over which weak localization phenomena can be effectively leveraged in measurements before becoming negligible would be an interesting pursuit.

For engineering applications, the boundaries of the propagation medium play an important role. An interesting problem is to provide a precise description, in the context of elastic waves, of the surface modes (Rayleigh and Love) and their interplay with bulk modes. This relation could be incorporated into radiative transfer models, for applications in geophysics and nondestructive testing, and investigate how surface modes are related to the weak localization effects presented in this chapter.

Chapter 6

Wave scattering by rough surfaces

Two aspects are discussed in this chapter. The first situation corresponds to waves propagating along a waveguide with rough-boundaries, and the second to waves that impinge upon a rough surface.

Acoustic wave propagation in waveguides has been studied for a long time due to its wide range of applications. One of its most important application is submarine detection, such as mines or archaeological artifacts detection. Additionally, it finds applications in underwater communication and the study of the ocean's structure or biology. Underwater acoustic waveguides are used to model propagation media such as a continental shelves. These environments are characterized by indexes of refraction that are both spatially and time dependent. Despite this complexity, the sound speed in water, approximately 1500m/s, remains sufficiently large with respect to the motions of water masses to consider this propagation medium as time independent. However, even small inhomogeneities in water conditions, such as the heave or rough ocean bottoms, can induce significant effects over large propagation distances.

When waves impinge upon a rough surface, they undergo scattering events due to the irregularities in the surface profile. These scattering events result in changes of the wave's direction, amplitude, and phase. Consequently, the study of wave scattering phenomena by rough surfaces involves unraveling the intricate details of these interactions to predict and analyze the behavior of waves in practical scenarios. In applications such as radar systems, electromagnetic wave scattering theory from rough surfaces is crucial to account for the effects of the roughness of the land or the sea surface. A similar theoretical framework can be applied in optics. For acoustic waves, one can refer to applications in ocean acoustic tomography or thermometry, where the sea bed and sea surface roughness play a critical role, but also in non-destructive testing using ultrasonic waves.

This chapter describes both of these scenarios. First, we discuss the situation where a wave propagates along a random surface in context of a waveguide. Then, we discuss the classical situation where a wave impinges upon a rough surface, producing reflected and transmitted components. This chapter covers the results obtained in [7, 19] of the publication list on page 6.

6.1 A Pekeris waveguide model with a rough surface and bottom topography

Mathematical studies regarding acoustic wave propagation in randomly perturbed waveguides have been carried out in many papers [70, 82, 91] under the assumption of rigid waveguide boundaries and random perturbations of its index of refraction. This section focuses on a two-dimensional acoustic waveguide model with a Pekeris profile, a randomly perturbed free surface, and uneven bottom topography (see Fig. 6.1). Our approach is built on a conformal transformation providing a smooth change of coordinates and allowing the use of the modal decomposition of the unperturbed waveguide (Fig. 6.1 left picture). In this context, a propagating wavefield can be decomposed over three kinds of mode: the propagating modes, which propagate over long distances along the waveguide; the evanescent modes, whose amplitudes decrease exponentially with the propagation distance along the waveguide; and the radiating modes, representing modes that can penetrate beneath the ocean floor.

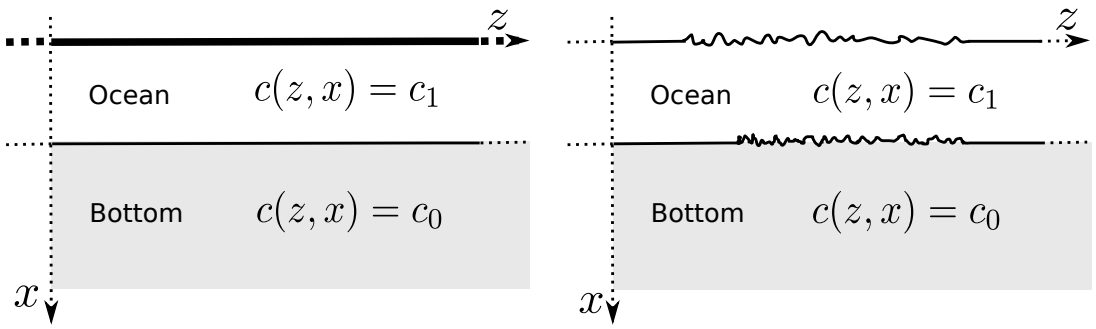

Fig. 6.1: Illustration of two semi-infinite waveguides with a Pekeris profile. The left picture depicts an unperturbed waveguide, while the right picture illustrates a perturbed waveguide with a free surface and an uneven bottom topography. In both cases, the bulk properties of the waveguides are homogeneous with a propagation speed c_1 in the oceanic section of the waveguide, and c_0 in the bottom part of the waveguide.

Using an asymptotic analysis, corresponding to a high-frequency regime, the impact of the randomly perturbed waveguide geometry on the mode coupling can be described in term of a diffusion model.

These mechanisms result in an effective attenuation of the mode amplitudes. It turns out that the surface and bottom fluctuations mainly affect the propagating-mode amplitudes in a similar manner. However, for the majority of the propagating modes, the attenuation mechanism is mainly due to the coupling between the propagating mode themselves. In contrast, for the highest propagating modes, the attenuation mechanism is mainly due to the coupling with the radiating modes, and it is significantly stronger than for the lower propagating modes.

6.1.1 Waveguide model

A two-dimensional linear acoustic wave model is considered:

$$\Delta - \frac{1}{c_\varepsilon^2(z,x)}\partial_{tt}^2 p = \nabla \cdot F \qquad (t,z,x) \in \mathbb{R}\times\mathbb{R}\times(0,\infty), \tag{6.1}$$

with $\Delta = \partial_{xx}^2 + \partial_{zz}^2$. Here, the coordinate z represents the propagation axis along the waveguide, and the coordinate x represents the transverse section of the waveguide (see Fig. 6.1). Let $d > 0$ be the average ocean depth. The velocity field is given, for $z \in \mathbb{R}$, by

$$c_\varepsilon(z,x) = \begin{cases} c_1 & \text{if} \quad V_s^\varepsilon(z) < x < d + V_b^\varepsilon(z), \\ c_0 & \text{if} \quad x > d + V_b^\varepsilon(z), \end{cases} \tag{6.2}$$

with $c_0 > c_1$, and where V_s^ε and V_b^ε model respectively the free surface and the bottom topography (see Fig. 6.2 for an illustration). In our context, the free surface models the heave produced by the wind speed, and the uneven bottom topography models a sandy seabed with variations induced by water currents [126]. The forcing term F is defined as:

$$\mathbf{F}(t,z,x) = f(t)\Psi(x)\delta(z - L_S)\mathbf{e}_z,$$

where $\mathbf{e}_z$ stands for the unit vector pointing in the z-direction. This term models a source located in the plane $z = L_S$, emitting a signal $f(t)$ in the z-direction with transverse profile Ψ supported in $(0,d)$. Furthermore, due to the continuity of the pressure field at the free surface $x = V_s^\varepsilon(z)$, which is tantamount to neglect the surface tension, the wave equation (6.1) is complemented by the following boundary conditions:

$$p(t,z,V_s^\varepsilon(z)) = p_{surface} \qquad (t,z) \in \mathbb{R}\times\mathbb{R},$$

where $p_{surface}$ represents the atmospheric pressure. However, one can assume without loss of generality that:

$$p_{surface} = 0,$$

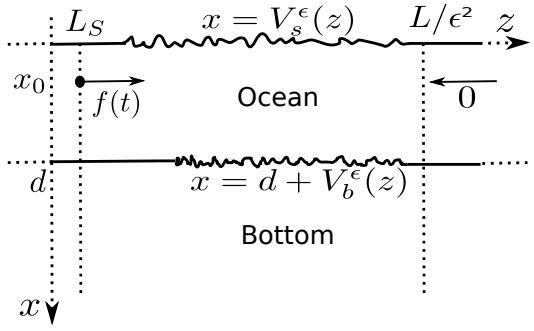

Fig. 6.2: Illustration of the waveguide model. In this figure d represents the mean ocean depth, and the random fluctuations are given by the graphs of V_s^ε at the free surface, and $d+V_b^\varepsilon$ at the bottom of the waveguide model. We illustrate the source term $\mathbf{F}$ emitting a wave $f(t)$ in the z-direction. L/ε^2 characterizes the size of the section in which the random fluctuations occur. The right arrow (with a 0) pointing to the left at $z = L/\varepsilon^2$ indicates that no wave is coming from the right at the end of the random section.

which leads to Dirichlet boundary conditions at the free surface, and corresponding to a pressure-release condition. The central wavelength λ of the source term is assumed to be of order one, and we consider a propagation distance given by L/ε^2 to place ourselves in a high-frequency regime.

Waveguide models with a Pekeris profile (6.2) have been extensively studied for half a century [174], and has been widely used to model an ocean with a constant propagation speed profile (like in Figure 6.1). Such conditions can be found during the winter in Earth's mid latitudes and in water shallower than about 30 meters [138]. This profile is convenient for mathematical treatments, but it underestimates the real complexity of the medium. Nevertheless, the analysis carried out in this paper can be extended to more general propagation speed profiles. This model can also be used for electromagnetic waveguides, such as dielectric slabs or optical fibers with randomly perturbed boundaries [145, 149].

In (6.2), the perturbations of the waveguide geometry V_s^ε and V_b^ε are defined by

$$V_s^\varepsilon(z) = \varepsilon V_s(z) f_s(\varepsilon^2 z) \qquad \text{and} \qquad V_b^\varepsilon(z) = \varepsilon V_b(z) f_b(\varepsilon^2 z).$$

Here, V_s and V_b are assumed to be two independent mean-zero stationary bounded stochastic processes. The two functions f_s and f_b, which specify the locations of the waveguide fluctuations, are assumed to be smooth with their supports included within the interval $(0, L)$. Note that the scaling $\varepsilon \ll 1$, in front of V_s and V_b, corresponds to small fluctuations of the waveguide geometry, and place ourselves in the weak scattering regime. In fact, wind speeds at approximately 5m/s result in a standard deviation of the surface roughness at about 0.1m. A similar order of magnitude applies to the roughness of sandy bottoms (see [126, Chapter 2] and [137]). Therefore, we have to wait for long propagation distances (of order $1/\varepsilon^2$) to observe significant cumulative stochastic effects on the pressure wave. Let us note that the two random processes V_s and V_b are assumed to be independent. This assumption is justified because the surface and bottom standard deviations are small compared to the ocean depth, and then the bottom topography does not induce any ripples on the free surface. Power spectral densities for V_s and V_b can be found in the literature [126, Section 2.4 and Section 2.9]

$$I_s(u) := \int R_s(z) e^{iuz} dz = \frac{C_s}{|u|^{\alpha_s}} e^{-C_s'/|u|^{\mu_s}} \quad \text{and} \quad I_b(u) := \int R_b(z) e^{iuz} dz = \frac{C_b}{4\pi(u^2+1)^{\alpha_b/2}}, \quad (6.3)$$

with $C_s, C_s', C_b > 0$, and

$$R_s(z) := \mathbb{E}[V_s(z+z_0)V_s(z_0)] \qquad \text{and} \qquad R_b(z) := \mathbb{E}[V_b(z+z_0)V_b(z_0)].$$

For instance, the cases $\alpha_s = 4$, $\alpha_s = 6$, and $\mu_s = 2$, I_s is referred to as the Pierson-Neumann spectra, and for $\alpha_s = 5$ and $\mu_s = 4$ to as the Pierson-Moscovitz spectra. Consequently, the trajectories of V_s^ε

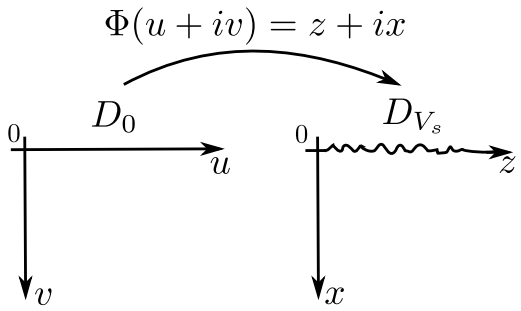

Fig. 6.3: Schematic representation of the change of coordinates from the unperturbed domain D_0 onto the perturbed domain D_{V_s}.

and V_b^ε are at least $\mathcal{C}^2$ with bounded derivatives, and therefore the surface fluctuations (the graph of V_s^ε) produce no breaking wave.

To develop the asymptotic analysis, the random fluctuations V_s and V_b are assumed to be ϕ-mixing processes: considering the σ-algebras

$$\mathcal{F}_{0,z} := \sigma(V_s(u), V_b(u), \quad 0 \le u \le z) \qquad \text{and} \qquad \mathcal{F}_{z,\infty} := \sigma(V_s(u), V_b(u), \quad z \le u),$$

we have

$$\sup_{\substack{z\ge 0 \\ A\in\mathcal{F}_{z+u,\infty} \\ B\in\mathcal{F}_{0,z}}} \big|\mathbb{P}(A|B) - \mathbb{P}(A)\big| \le \phi(u) \qquad \text{with} \qquad \phi \in L^1(\mathbb{R}) \cap L^2(\mathbb{R}).$$

This mixing property describes, through the function ϕ, the loss of the statistical dependency between the past and the future of a random trajectories.

6.1.2 The conformal mapping

To investigate the asymptotic behavior of the acoustic pressure wave within the perturbed waveguide domain, we use a change of coordinates through a conformal transformation [179] from

$$D_0 = \{u+iv \in \mathbb{C} : \quad u > 0\} \qquad \text{onto} \qquad D_{V_s} = \{z+ix \in \mathbb{C} : \quad x > V_s^\varepsilon(z)\}.$$

This change of coordinates allows us to study the pressure wave $p(t,z,x)$ in a waveguide domain with a flat surface (see Fig. 6.3). In other words, one can focus our attention on $p_0(t,u,v)$ defined by

$$p_0(t,u,v) = p(t, z(u,v), x(u,v)),$$

which represents the pressure wave $p(t,z,x)$ solution to (6.1) in a waveguide domain with a flat surface. Here, $z(u,v) + ix(u,v) = \Phi(u+iv)$ stands for the change of coordinates from D_0 onto D_{V_s}. In the new set of coordinates, the acoustic pressure wave p_0 satisfies Dirichlet boundary conditions at the flat surface of the waveguide,

$$p_0(t,u,v=0) = 0 \qquad (t,u) \in \mathbb{R}\times\mathbb{R}.$$

The original pressure wave $p(t,z,x)$ can be obtained from $p_0(t,u,v)$ by inverting the change of coordinates,

$$p(t,z,x) = p_0(t, Re(\Phi^{-1}(z+ix)), Im(\Phi^{-1}(z+ix))).$$

The main effect of this change of coordinates is to transfer the random fluctuations of the free surface to random fluctuations into the interior and at the bottom of the waveguide (see Fig. 6.4).

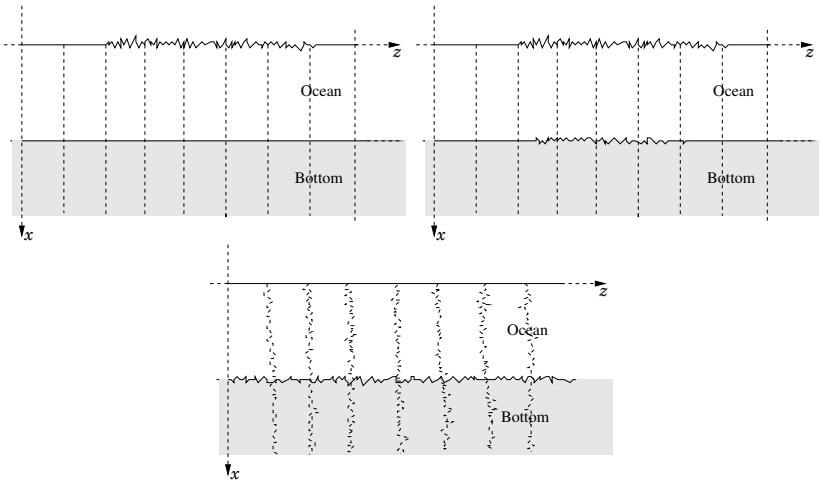

Fig. 6.4: Illustration of the conformal transformation applied to a waveguide with a free surface and uneven bottom topography. The two top figures depict waveguides with a free surface. In these figures the vertical dashed lines represent unperturbed medium parameters. In the top-left picture, the bottom is unperturbed, that is $V_b^\varepsilon \equiv 0$, while in the top-right picture, the bottom of the waveguide is perturbed. The bottom picture illustrates the waveguide after the conformal transformation. In this figure, the perturbed vertical dashed lines mean perturbed medium parameters. Moreover, if the bottom was already perturbed before the conformal transformation, it is now also perturbed by the waveguide transformation.

In the time-Fourier domain p_0 can be decomposed over a basis of modes,

$$\widehat{p}_0(\omega,u,v) = \underbrace{\sum_{j=1}^{N(\omega)} \widehat{p}_j(\omega,u)\phi_j(\omega,v)}_{\text{propagating modes}} + \underbrace{\int_0^{k_\omega^2} \widehat{p}_\gamma(\omega,u)\phi_\gamma(\omega,v)d\gamma}_{\text{radiating modes}} + \underbrace{\int_{-\infty}^{0} \widehat{p}_\gamma(\omega,u)\phi_\gamma(\omega,v)d\gamma}_{\text{evanescent modes}}, \tag{6.4}$$

corresponding to the spectral decomposition of the (unperturbed) Pekeris operator defined by

$$R_\omega = \frac{d^2}{dv^2} + k_\omega^2 n^2(v) \qquad \text{with} \qquad n(v) = \begin{cases} n_1 = c_0/c_1 > 1 & \text{if} \quad v \in (0,d), \\ 1 & \text{if} \quad v \geq d, \end{cases}$$

where $k_\omega = \omega/c_0$. The $(\phi_j)_{j\in\{1,\dots,N(\omega)\}}$ and $(\phi_\gamma)_{\gamma\in(-\infty,k^2(\omega))}$ are the (eigen)elements of the spectral measure associated to R_ω, corresponding respectively to its discrete spectrum and continuous spectrum. The coefficients $\widehat{p}_j$ and $\widehat{p}_\gamma$ represent the amplitudes associated to each mode (propagating, radiative and evanescent modes).

The waveguide fluctuations result in a coupling between all these modes. In (6.4), the only modes that can propagate over long distances along the waveguide are the propagating modes. All the other modes play only a secondary role in the analysis.

6.1.3 Main result

Neglecting the backscattering effects, an asymptotic analysis can be applied based on a approximation-diffusion theorem. The effective mode-coupling mechanism can be described in term of a diffusion process, so that the expected pressure field of $\widehat{p}_0(\omega,u,v)$, at the end of the perturbed section $u = L/\varepsilon^2$, can be approximated for $\varepsilon \ll 1$ by

$$\mathbb{E}\Big[\widehat{p}_0\Big(\omega, u=\frac{L}{\varepsilon}, v\Big)\Big] \simeq \sum_{j=1}^{N(\omega)} \frac{\widehat{a}_{j,0}(\omega)}{\sqrt{\beta_j(\omega)}} e^{-\mathcal{T}_j(\omega,L)+i\mathcal{P}_j(\omega,L)} e^{i\beta_j(\omega)L/\varepsilon^2} \phi_j(\omega,v).$$

Here, the $\beta_j(\omega)$'s correspond to modal wavenumbers as introduced in Sect. 3.1, and the $\widehat{a}_{j,0}(\omega)$'s represent the initial amplitudes of the propagating modes generated by the source term and entering

the random section. It turns out that the coherent transmitted wavefield at $u = L/\varepsilon^2$ is composed of a superposition of propagating modes, where each mode is affected by an effective frequency-dependent attenuation and phase modulation through respectively $\mathcal{T}_j(\omega, L)$ and $\mathcal{P}_j(\omega, L)$. In particular, the attenuation coefficients are of the form

$$\mathcal{T}_j(\omega, L) = C_j^s(\omega) \int_0^L f_s^2(z)dz + C_j^b(\omega) \int_0^L f_b^2(z)dz,$$

with $C_j^s(\omega), C_j^b(\omega) > 0$, accounting for the modal cumulative net scattering effects of the perturbed waveguide geometry.

Due to the exponential decay of the evanescent mode amplitudes w.r.t the propagation distance, these modes do not play a direct role in the transmitted wavefield. Nonetheless, they induce an indirect influence on the propagating modes through a mode-dependent phase modulation encoded in $\mathcal{P}_j(\omega, L)$. The radiating modes do not play any direct significant role neither. Through the asymptotic analysis and the continuous nature of the associated spectrum, it can be shown that these modes are not affected by the perturbations of the propagation medium. Their contributions are therefore of the form

$$\int_0^{k_\omega^2} \frac{\widehat{a}_{\gamma,0}(\omega)}{\gamma^{1/4}} e^{i\sqrt{\gamma}L/\varepsilon^2} \phi_\gamma(\omega, v)d\gamma,$$

involving a rapid phase term which cancels out the integral in the limit $\varepsilon \to 0$. Nevertheless, they also play an indirect role in the attenuation coefficient $\mathcal{T}_j(\omega, L)$ as described in the following result.

Theorem 6.1.1 *In the limit of a large number of propagating modes $k_\omega \gg 1$, knowing that $N(\omega) = [k_\omega d\theta/(c_1\pi)]$, we have for $\alpha \in \{s, b\}$:*

- *for $j \ll N(\omega)^{1/2}$,*
$$C_j^\alpha(\omega) \underset{k_\omega \gg 1}{\sim} K_{1,\alpha} k_\omega^{3/2} \frac{j^2}{N(\omega)^2} \int_0^\infty \sqrt{u} I_\alpha(u)du;$$
- *for $j \sim N(\omega)^{1/2}$,*
$$C_j^\alpha(\omega) \underset{k_\omega \gg 1}{\sim} K_{2,\alpha} k_\omega^{3/2} \frac{j^2}{N(\omega)^2} \int_0^\infty \sqrt{u} I_\alpha\Big(u - \frac{j^2\pi\theta}{2N(\omega)d}\Big)du;$$
- *for $N(\omega)^{1/2} \ll j \lesssim \nu N(\omega)$, with $\nu \in (0, 1)$,*
$$C_j^\alpha(\omega) \underset{k_\omega \gg 1}{\sim} K_{3,\alpha} k_\omega^2 \frac{j^3}{N(\omega)^3} \int_0^\infty I_\alpha(u)du;$$
- *for $j \sim N(\omega)$,*
$$K_{4,\alpha} k_\omega^{5/2} \leq C_j^\alpha(\omega) \leq K_{5,\alpha} k_\omega^{5/2};$$

where all the $K_{j,\alpha}$ are positive constants, the I_α's are given by (6.3)*, and $\theta = \sqrt{1 - 1/n_1^2}$.*

This result provides the order of magnitude of the mode-dependent and frequency-dependent attenuation $\mathcal{T}_j(\omega, L)$, which is responsible for the effective attenuation of the forward propagating-mode amplitudes. Let us make two remarks. First, the surface and bottom fluctuations affect the mode amplitudes mainly in a similar manner. Secondly, higher-order modes experience more significant attenuation as they interact more intensely with the random boundaries, leading to increased scattering. In fact, the higher the mode is the more it bounces on the random boundaries, and then the more it is scattered. While low-order modes have their attenuations mainly produced by the coupling between the propagating modes, high-order modes ($j \sim N(\omega)$) experience stronger attenuations due their coupling with the radiating modes. The reason is that only the highest order modes can efficiently couple with the radiating modes, resulting in a stronger attenuation as the radiating modes allow strong losses in the bottom of the waveguide [91]. This kind of result has also been reported in [7] for waveguides with a bounded cross-section, which do not support radiative modes and, therefore, does not exhibit these additional affects.

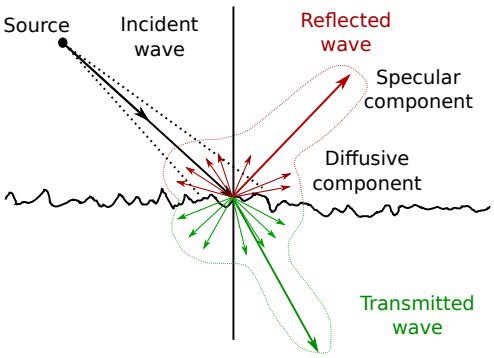

Fig. 6.5: Illustration of the basic physical setup: A source illuminates a rough surface producing reflected (in red) and transmitted waves (in green). Both waves exhibit a specular and diffusive components. The diffusive component, the speckle, corresponds to scattering of the incident wave by the rough interface.

6.2 Reflection and transmission problems of high-frequency waves through a randomly perturbed interface: generalized Snell's laws

Despite the huge importance of this problem and the wide range of applications, there exists a limited number of rigorous results characterizing the wavefield, whether it is transmitted through or reflected from a rough interface [7, 16, 94, 163]. Many works in the physical literature consider a random interface problem in a perturbative situation, where the effects of small interface variations yield relatively small corrections in the transmitted and reflected wavefields. In this section, the interface fluctuations are modeled trough a random field, enabling us to describe the transmitted and reflected fields, even though they are modified to leading order. It is worth mentioning that the problem of reflection from or transmission through a rough interface requires specialized techniques that differ from those associated with bulk propagation, that is the approximation-diffusion approach [70]. The basic configuration we consider here is illustrated in Fig. 6.5: a beam like wavefield (under the paraxial scaling) illuminates a rough surface with constant medium parameters, that are different above and below the interface.

The incident wave is typically decomposed into a reflected wave and a transmitted wave. These wavefields are further decomposed into two main components: the specular component and the speckle, also called incoherent or diffuse component, which results from scattering. Two central questions are then:

i How does the fluctuations of the interface modify the specular components?

ii How can we characterize the speckle components of the wavefields, and what parameters influence their relative magnitudes and spatial supports?

It turns out that the central scaling ratio that distinguishes various canonical scattering situations is the correlation length (or characteristic scale) of interface variations relative to the beam width. This is particularly relevant in the critical scaling scenario considered here, where the amplitude of the interface fluctuations is of the order of the wavelength. In particular, if the interface fluctuations occur on the scale of the probing cone width, the reflected and transmitted specular cones exhibit random arrival time properties. However, their main wave energies remain confined within the specular cones as the interface fluctuations does not induce strong coupling in between modes with different lateral wave vectors (traveling in relative oblique direction). On the other hand, when the interface fluctuations occur on a smaller scale relative to the width of the probing cone, such a coupling takes place. This generates homogenized specular reflected and transmitted cones with frequency-depend attenuations related the interface elevation statistics. The missing energy from these effective specular cones have been converted into wide speckle cones that carry a total energy of order one. The radius

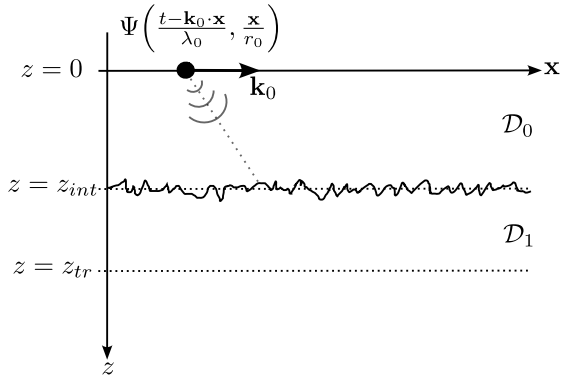

Fig. 6.6: Illustration of the physical setup. The plan $z = 0$ contains the source location, while the rough interface between $\mathcal{D}_0$ and $\mathcal{D}_1$ occurs around $z = z_{int}$. The reflected wave is observed at $z = 0$, and the transmitted wave is observed at $z = z_{tr}$.

of these large cones are characterized by the ratio of the wavelength with the correlation length of the interface variations. In our situation, the roughness of the interface is not strong enough to generate the enhanced backscattering effects [121]. The scattering operator we obtain is similar to the one obtained in [183] under the Born (single scattering) approximation, and involves the statistics of the interface relative elevation.

There is a large literature addressing the important interface scattering problem. Most of the literature deals with physically motivated expansions, such as perturbative approaches or Kirchhoff-type approximations, which impose stringent conditions on the applicable scaling regimes [25, 57, 189]. Additionally, integral equation formulations are commonly employed, especially in characterizing near-field scattering [148, 187]. Sophisticated numerical methods have been developed [56, 184] to understand wave scattering from complicated geometries. Here, we provide statistical representations of such geometries and related scattering effects, as well as a statistical description of the speckles in term of a Gaussian random fields.

6.2.1 The physical model

The wave equation In this section, a three-dimensional linear wave propagation modeled is considered through the scalar wave equation:

$$\Delta u - \frac{1}{c^2(\mathbf{x}, z)}\partial_{tt}^2 u = \nabla \cdot F(t, \mathbf{x}, z) \qquad (t, \mathbf{x}, z) \in \mathbb{R} \times \mathbb{R}^2 \times \mathbb{R}, \tag{6.5}$$

equipped with null initial conditions

$$u(t = 0, \mathbf{x}, z) = \partial_t u(t = 0, \mathbf{x}, z) = 0 \qquad (\mathbf{x}, z) \in \mathbb{R}^2 \times \mathbb{R},$$

and continuity conditions at the interface that are specified below. The coordinate z represents the main propagation axis while $\mathbf{x}$ represents the transverse directions, F corresponds to the source term, and the Laplacian operator $\Delta = \Delta_\perp + \partial_{zz}^2$ acts on all spatial variables $\mathbf{x}$ and z. The propagation medium consists of two homogeneous subdomains separated by a randomly perturbed interface around $z = z_{int}$:

$$\mathcal{D}^0 := \{(\mathbf{x}, z) \in \mathbb{R}^2 \times \mathbb{R} \quad \text{s.t.} \quad z < z_{int} + \sigma V(\mathbf{x}/l_c)\} \tag{6.6}$$

and

$$\mathcal{D}^1 := \{(\mathbf{x}, z) \in \mathbb{R}^2 \times \mathbb{R} \quad \text{s.t.} \quad z > z_{int} + \sigma V(\mathbf{x}/l_c)\}. \tag{6.7}$$

We refer to Fig. 6.6 for an illustration of the physical setup. The term V corresponds to a mean-zero random field with second order derivatives (for technical reasons), modeling the interface variations and characterizing its roughness. Away from the interface the velocity field is given by:

$$c(\mathbf{x}, z) := \begin{cases} c_0 & \text{if} \quad (\mathbf{x}, z) \in \mathcal{D}^0, \\ c_1 & \text{if} \quad (\mathbf{x}, z) \in \mathcal{D}^1. \end{cases}$$

The forcing term

$$F(t,\mathbf{x},z) := \Psi\Big(\frac{t-\mathbf{k}_0\cdot\mathbf{x}}{\lambda},\frac{\mathbf{x}}{r_0}\Big)\delta(z)\mathbf{e}_z,$$

where $\mathbf{e}_z$ denotes the unit vector pointing in the z-direction, models a source located in the plane $z=0$ and emitting a quasi plan wave Ψ in the spatial direction $(\mathbf{k}_0,(c_0^{-2}-|\mathbf{k}_0|^2)^{1/2})$ towards the random interface (requiring $|\mathbf{k}_0|<c_0^{-1}$). In a dimensionless situation, λ represents the wavelength and r_0 the spatial beam width of the source term.

The above wave equation (6.5) only requires the two following continuity relations across the randomly perturbed interface:

$$u(z=z_{int}(\mathbf{x})^+)=u(z=z_{int}(\mathbf{x})^-) \qquad \text{and} \qquad \partial_z u(z=z_{int}(\mathbf{x})^+)=\partial_z u(z=z_{int}(\mathbf{x})^-),$$

where

$$z_{int}(\mathbf{x}) := z_{int}+\sigma V(\mathbf{x}/l_c).$$

Finally, no wave is assumed to come from above the source location nor below the interface. The only waves present in the system are generated by the source term.

The parameter scaling Here, the distance from the source to the interface is denoted by z_{int}, and the distance from the source to the plane where the transmitted wave is recorded by z_{tr}. Both of these distances are assumed to be of order $L\sim 1$ (the reference scale). The dimensionless parameter

$$\varepsilon := \frac{\lambda}{L} \ll 1,$$

is assumed to be small to provide a high-frequency regime. Moreover, a paraxial (or parabolic) scaling is considered by enforcing

$$\frac{r_0^2}{\lambda}\sim L,$$

which corresponds to a Rayleigh length of order the typical propagation distance. As already mentioned in this manuscript, in the homogeneous case, the Rayleigh length $L_R=\pi r_0^2/\lambda$ corresponds to the distance from the beam waist to the place where the area of its cross-section is doubled. The interface fluctuations are here *critically scaled* in the sense that the magnitude of the interface fluctuations and the central wavelength are of the same order,

$$\sigma\sim\lambda.$$

Finally, l_c denotes the correlation length of the interface fluctuations, which ranges from the central wavelength to the beam width:

$$\lambda\lesssim l_c\lesssim r_0.$$

Note that if $r_0\ll l_c$ the situation is trivial and corresponds essentially to a planar interface. The ratio λ/l_c characterizes how rough the surface is for the incident wave, and the cone radius for the reflected and transmitted speckle components. For simplicity, we set

$$L=L_R\sim 1, \qquad \lambda=\varepsilon, \qquad r_0=\sqrt{\varepsilon}, \qquad \sigma=\varepsilon, \qquad \text{and} \qquad l_c=\varepsilon^\gamma, \tag{6.8}$$

with

$$\gamma\in[1/2,1].$$

In the forthcoming presentation, a distinction is made between $\gamma=1/2$ (that is $l_c\sim r_0$) and $1/2<\gamma\leq 1$ (corresponding to $\lambda\lesssim l_c\ll r_0$). These two scenarios result in fundamentally different behaviors for the reflected and transmitted signals. While the former induces only random specular components (without speckle), the latter, due to fast interface oscillations compared to the beam radius ($l_c\ll r_0$), induces homogenization effects for the specularly reflected and the transmitted wave components. In this case, random speckles over cones larger than the ones covered by the specular and transmitted components are observed.

Random fluctuations In (6.6) and (6.7), the random fluctuations of the interface delimiting the two subspaces are defined by a mean-zero stationary random field V. These random fluctuations are assumed to satisfy *mixing* properties describing the loss of statistical dependency for V over the interface. In our 2D context, the *mixing* property is defined as follow. We introduce

$$\alpha(r) := \sup_{\substack{S,S'\subset\mathbb{R}^2 \\ d(S,S')>r}} \sup_{\substack{A\in\sigma(V(\mathbf{x}),\,\mathbf{x}\in S) \\ B\in\sigma(V(\mathbf{x}),\,\mathbf{x}\in S')}} |\mathbb{P}(A\cap B)-\mathbb{P}(A)\mathbb{P}(B)|,$$

where

$$d(S,S') = \inf_{\substack{s\in S \\ s'\in S'}} |s-s'|$$

is the distance between two nonempty subsets S and S', and $\sigma(V(\mathbf{x}),\,\mathbf{x}\in S)$ is the σ-field generated by the family $V_{|S} := (V(\mathbf{x}))_{\mathbf{x}\in S}$. Roughly speaking, the value $\alpha(r)$ quantifies the degree of statistical dependency for the random field V over pair of regions at distance at least r. The α-mixing property consists in assuming

$$\alpha(r)\to 0 \qquad \text{as} \qquad r\to\infty,$$

giving a vanishing of the statistical dependency between $V_{|S}$ and $V_{|S'}$ as the distance between S and S' tends to infinity.

6.2.2 Refection and transmission for an unperturbed interface

In the context of an unperturbed (flat) interface, the asymptotic specular reflected wave is given by

$$\begin{aligned} U^{ref}(s,\mathbf{y}) &:= \lim_{\varepsilon\to 0} u^\varepsilon\big(t^\varepsilon_{obs,ref}(\mathbf{y})+\varepsilon s, \mathbf{x}_{obs,ref}+\sqrt{\varepsilon}\,\mathbf{y}, z=0\big) \\ &= \frac{\mathcal{R}}{2(2\pi)^3}\int e^{-i\omega(s-\mathbf{y}\cdot\mathbf{q})}\hat{\mathcal{U}}_0(\omega,\mathbf{q},2z_{int})\hat{\Psi}(\omega,\mathbf{q})\omega^2 d\omega d\mathbf{q}. \end{aligned} \tag{6.9}$$

Here, u^ε corresponds to the scaled solution of (6.5) according to (6.8). Therefore, U^{ref} corresponds to the asymptotic wave front observed at position $\mathbf{x}_{obs,ref}+\sqrt{\varepsilon}\,\mathbf{y}$ (depending on the source frame $\sqrt{\varepsilon}\,\mathbf{y}$) and time $t^\varepsilon_{obs,ref}(\mathbf{y})+\varepsilon s$ (depending of the pulse duration εs), where

$$t^\varepsilon_{obs,ref}(\mathbf{y}) := t_{obs,ref}+\sqrt{\varepsilon}\,\mathbf{k}_0\cdot\mathbf{y}, \qquad \text{with} \qquad t_{obs,ref} := \frac{2z_{int}}{c_0^2\lambda_0},$$

and

$$\mathbf{x}_{obs,ref} := \frac{2\mathbf{k}_0 z_{int}}{\lambda_0}.$$

Here, λ_0 is defined by

$$\lambda_0 = \frac{\sqrt{1-c_0^2|\mathbf{k}_0|^2}}{c_0}.$$

The travel time is influenced here by the offset $\mathbf{y}$ as the beam width $\sqrt{\varepsilon}$ is large compared to the pulse duration ε, and that the wave front travels obliquely relative to the vertical direction. Note that $\mathbf{x}_{obs,ref}$ is twice the lateral position

$$\mathbf{x}_{int} := \frac{\mathbf{k}_0 z_{int}}{\lambda_0}, \tag{6.10}$$

where the incident pulse hits the interface. Therefore, the standard reflexion relation reads

$$\theta_{inc} = \theta^0_{ref} := \arctan\Big(\frac{|\mathbf{k}_0|}{\lambda_0}\Big), \tag{6.11}$$

where the incident and reflected angles are equal. We refer to Fig. 6.7 for an illustration of the geometrical properties of the reflection.

Regarding the reflected wave profile, the reflection coefficient $\mathcal{R}$ is given by

$$\mathcal{R} := \frac{\lambda_0-\lambda_1}{\lambda_0+\lambda_1},$$

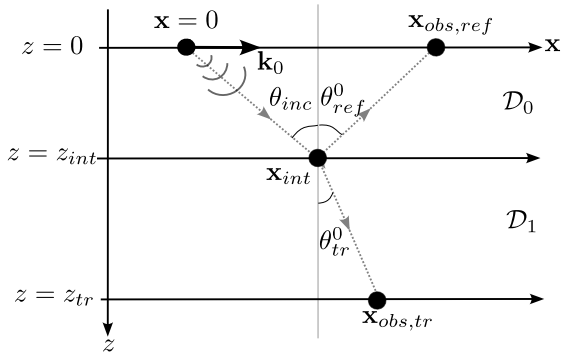

Fig. 6.7: Illustration of the reflection and transmission in the context of a flat interface at $z = z_{int}$. The source is located at $\mathbf{x} = 0$ in the plan $z = 0$, and the emitted wave hits the interface at $\mathbf{x} = \mathbf{x}_{int}$, in the plan $z = z_{int}$, with an incident angle θ_{inc}. The reflected wave, with angle θ^0_{ref}, is observed in the plan $z = 0$ at $\mathbf{x} = \mathbf{x}_{obs,ref}$, while the transmitted wave, with angle θ^0_{tr}, is observed in the plan $z = z_{tr}$ at $\mathbf{x} = \mathbf{x}_{obs,tr}$.

where λ_1 is defined as λ_0 by just replacing c_0 by c_1, and

$$\hat{\mathcal{U}}_0(\omega, \mathbf{q}, z) := e^{-i\omega z c_0 \mathbf{q}^T A_0 \mathbf{q}}, \tag{6.12}$$

where A_0 is defined by

$$A_0 := \frac{1}{2(1 - c_0^2|\mathbf{k}_0|^2)^{3/2}} \begin{pmatrix} 1 - c_0^2\mathbf{k}_{0,2}^2 & c_0^2\mathbf{k}_{0,1}\mathbf{k}_{0,2} \\ c_0^2\mathbf{k}_{0,1}\mathbf{k}_{0,2} & 1 - c_0^2\mathbf{k}_{0,1}^2 \end{pmatrix} = \frac{1}{2c_0^3\lambda_0^3}\big(\mathbf{I}_2 - c_0^2\,\mathbf{k}_0^\perp(\mathbf{k}_0^\perp)^T\big). \tag{6.13}$$

The term $\hat{\mathcal{U}}_0$ leads to the following homogeneous semi-group

$$\check{\mathcal{U}}_0(\omega, \mathbf{y}, z) := \frac{\omega^2}{(2\pi)^2} \int e^{i\omega \mathbf{y}\cdot\mathbf{q}} e^{-i\omega z c_0 \mathbf{q}^T A_0 \mathbf{q}} d\mathbf{q}, \tag{6.14}$$

satisfying the Schrödinger type equation

$$i\partial_z \check{\mathcal{U}}_0(\omega, \mathbf{y}, z) + \frac{1}{k_{0,\omega}} \nabla_{\mathbf{y}} \cdot \Big(A_0 \nabla_{\mathbf{y}} \check{\mathcal{U}}_0\Big)(\omega, \mathbf{y}, z) = 0 \qquad z > 0, \tag{6.15}$$

where

$$\check{\mathcal{U}}_0(\omega, \mathbf{y}, z = 0) = \delta(\mathbf{y}), \qquad \text{and} \qquad k_{0,\omega} = \omega/c_0,$$

which is characteristic of the paraxial approximation. Due to the initial lateral direction $\mathbf{k}_0$, we do not have the standard Schrödinger equation with a Laplacian term. Nevertheless, the standard Laplacian can be recovered by sending this direction to zero. Under this paraxial wave model, the limit (6.9) corresponds to the travel of the emitted pulse from the source location to the interface, and back from the interface to the source location (yielding the $z = 2z_{int}$).

The transmitted specular wave is given by

$$\begin{aligned} U^{tr}(s, \mathbf{y}) &:= \lim_{\varepsilon \to 0} u^\varepsilon \big(t^\varepsilon_{obs,tr}(\mathbf{y}) + \varepsilon s, \mathbf{x}_{obs,tr} + \sqrt{\varepsilon}\mathbf{y}, z = z_{tr}\big) \\ &= \frac{\mathcal{T}}{2(2\pi)^3} \sqrt{\frac{\lambda_0}{\lambda_1}} \int e^{-i\omega(s - \mathbf{y}\cdot\mathbf{q})} \hat{\mathcal{U}}_1(\omega, \mathbf{q}, z_{tr} - z_{int}) \hat{\mathcal{U}}_0(\omega, \mathbf{q}, z_{int}) \hat{\Psi}(\omega, \mathbf{q}) \omega^2 d\omega d\mathbf{q}, \end{aligned} \tag{6.16}$$

with this time

$$\mathbf{x}_{obs,tr} := \mathbf{x}_{int} + \mathbf{x}_{tr} := \mathbf{x}_{int} + \frac{\mathbf{k}_0(z_{tr} - z_{int})}{\lambda_1},$$

where $\mathbf{x}_{int}$ is given by (6.10), and

$$t^\varepsilon_{obs,tr}(\mathbf{y}) := t_{obs,tr} + \sqrt{\varepsilon}\mathbf{y}, \qquad \text{with} \qquad t_{obs,tr} := \frac{z_{int}}{c_0^2\lambda_0} + \frac{z_{tr} - z_{int}}{c_1^2\lambda_1}.$$

Here, U^{tr} corresponds to the wave front observed in the frame of the source term at position $\mathbf{x}_{obs,tr}$, and time $t^{\varepsilon}_{obs,tr}(\mathbf{y})$. The time $t_{obs,tr}$, for the pulse to reach the plan $z = z_{tr}$, is the sum of the time to reach the interface and the time to go from the interface to the plan $z = z_{tr}$. The lateral position $\mathbf{x}_{obs,tr}$, where the pulse hits the plan $z = z_{tr}$, corresponds to a sum of vectors. The first vector represents the lateral position where the pulse hits the interface, and the second one the additional lateral displacement once the pulse goes through the interface and reaches the plan $z = z_{tr}$. We refer to Fig. 6.7 for an illustration for the geometrical properties of transmission. From this formulation, one has the usual Snell's law:

$$\frac{\sin(\theta_{inc})}{c_0} = \frac{\sin(\theta^0_{tr})}{c_1},$$

with θ_{inc} defined by (6.11), and

$$\theta^0_{tr} := \arctan\Big(\frac{|\mathbf{k}_0|}{\lambda_1}\Big).$$

Regarding the transmitted pulse profile, the transmission coefficient is defined by

$$\mathcal{T} := \frac{2\sqrt{\lambda_0\lambda_1}}{\lambda_0 + \lambda_1},$$

so that the conservation relation $\mathcal{R}^2 + \mathcal{T}^2 = 1$ holds, and $\hat{\mathcal{U}}_0$ is defined by (6.12). The term $\hat{\mathcal{U}}_1$ is defined in the same way as $\hat{\mathcal{U}}_0$:

$$\hat{\mathcal{U}}_1(\omega, \mathbf{q}, z) := e^{-i\omega z c_1 \mathbf{q}^T A_1 \mathbf{q}}, \tag{6.17}$$

where A_1 is defined as A_0 (6.13) by just changing c_0 by c_1. The term $\check{\mathcal{U}}_1$, defined as (6.14) with c_1 and A_1 instead of c_0 and A_0, satisfies a corresponding paraxial wave equation (6.15). Therefore, the formulation (6.16) corresponds to the travel of the emitted pulse from the source location to the interface, and from the interface to the plane $z = z_{tr}$ under the paraxial approximation. The factor $\mathcal{T}$ accounts for the transmission at the interface.

6.2.3 Random specular components for $l_c \sim r_0$ ($\gamma = 1/2$)

From now on, the interface is randomly perturbed. In case of a correlation length of order the beam radius, the asymptotic reflected pulse front, as defined in (6.9), is given by the following result.

Proposition 6.2.1 *The family $(U^{\varepsilon,ref})_\varepsilon$ converges in law in $L^2(\mathbb{R}\times\mathbb{R}^2)$, as $\varepsilon \to 0$, to*

$$U^{ref}(s,\mathbf{y}) := \frac{\mathcal{R}}{2(2\pi)^5} \iiiint e^{-i\omega(s-2\lambda_0\mathcal{V}(\mathbf{y}')-\mathbf{q}\cdot\mathbf{y})} e^{i\omega(\mathbf{q}'-\mathbf{q})\cdot\mathbf{y}'} \times \hat{\mathcal{U}}_0(\omega,\mathbf{q},z_{int})\hat{\mathcal{U}}_0(\omega,\mathbf{q}',z_{int})\hat{\Psi}(\omega,\mathbf{q}')\omega^4 d\omega d\mathbf{y}' d\mathbf{q}' d\mathbf{q},$$

where $\mathcal{V}$ is a random field with the same law as V.

The reflected wave front consists in a superposition of contribution observed at point $\mathbf{y}$. Each of these contributions results in waves emitted with initial lateral direction $\mathbf{q}'$, propagating according to $\hat{\mathcal{U}}_0(\mathbf{q}')$, and scattered into direction $\mathbf{q}$ at point $\mathbf{y}'$ before propagating back according to $\hat{\mathcal{U}}_0(\mathbf{q})$ (see Fig. 6.8 for an illustration). Note that a random time correction $2\lambda_0\mathcal{V}(\mathbf{y}')$ is observed for contributions scattered at point $\mathbf{y}'$. In U^{ref}, for a given frequency ω, the scattering operator corresponds to

$$K_{ref}(\omega,\mathbf{q}',\mathbf{q}) := \int e^{i\omega(\mathbf{q}'-\mathbf{q})\cdot\mathbf{y}'} e^{2i\omega\lambda_0\mathcal{V}(\mathbf{y}')} d\mathbf{y}'. \tag{6.18}$$

A similar result holds for the transmitted wave front.

Proposition 6.2.2 *The family $(U^{\varepsilon,tr})_\varepsilon$ converges in law in $L^2(\mathbb{R}\times\mathbb{R}^2)$, as $\varepsilon \to 0$, to*

$$U^{tr}(s,\mathbf{y}) := \frac{\mathcal{T}}{2(2\pi)^5}\sqrt{\frac{\lambda_0}{\lambda_1}} \iiiint e^{-i\omega(s-(\lambda_0-\lambda_1)\mathcal{V}(\mathbf{y}')-\mathbf{q}\cdot\mathbf{y})} e^{i\omega(\mathbf{q}'-\mathbf{q})\cdot\mathbf{y}'} \times \hat{\mathcal{U}}_1(\omega,\mathbf{q},z_{tr}-z_{int})\hat{\mathcal{U}}_0(\omega,\mathbf{q}',z_{int})\hat{\Psi}(\omega,\mathbf{q}')\omega^4 d\omega d\mathbf{y}' d\mathbf{q}' d\mathbf{q},$$

where $\mathcal{V}$ is a random field with the same distribution as V.

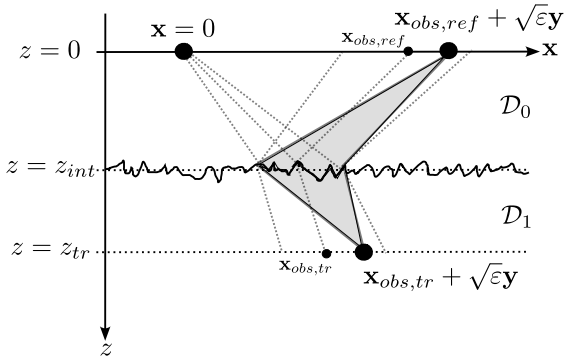

Fig. 6.8: Illustration of the contributions to the reflected and transmitted waves observed at points $\mathbf{x}_{obs,ref} + \sqrt{\varepsilon}\mathbf{y}$ and $\mathbf{x}_{obs,tr} + \sqrt{\varepsilon}\mathbf{y}$ respectively. The dashed light grey lines represent the specular cones.

The transmitted wave front U^{tr} consists as well in a superposition of diffracted contributions observed at point $\mathbf{y}$. Each of these contribution results in waves emitted with initial lateral direction $\mathbf{q}'$, propagating according to $\hat{\mathcal{U}}_0$, scattered into direction $\mathbf{q}$ at point $\mathbf{y}'$ when going through the interface, and then propagates according to $\hat{\mathcal{U}}_1$ until it reaches $z = z_{tr}$ (see Figure 6.8 for an illustration). For the transmitted wave, the scattering operator reads

$$K_{tr}(\omega, \mathbf{q}', \mathbf{q}) := \int e^{i\omega(\mathbf{q}'-\mathbf{q})\cdot\mathbf{y}'} e^{i\omega(\lambda_0-\lambda_1)\mathcal{V}(\mathbf{y}')} d\mathbf{y}'. \tag{6.19}$$

6.2.4 Effective specular components for $l_c \ll r_0$ ($\gamma > 1/2$)

The case $\gamma > 1/2$ corresponds to a correlation length smaller than the beam width. The incident wave is therefore strongly scattered and homogenization phenomena take place, as well as incoherent wave fluctuations. In this context the asymptotic behavior of the reflected wave front (6.9) is given by the following result.

Proposition 6.2.3 *The family $(U^{\varepsilon,ref})_\varepsilon$ converges in probability, as $\varepsilon \to 0$, in $\mathcal{S}'(\mathbb{R}\times\mathbb{R}^2)$, the set of tempered distributions, to the deterministic pulse profile*

$$U^{ref}(s, \mathbf{y}) = \frac{\mathcal{R}}{2(2\pi)^3} \iiint e^{-i\omega(s-\mathbf{q}\cdot\mathbf{y})} \hat{\mathcal{U}}_0(\omega, \mathbf{q}, 2z_{int}) \phi_V(2\omega\lambda_0) \hat{\Psi}(\omega, \mathbf{q}) \omega^2 d\omega d\mathbf{q}.$$

Here,

$$\phi_V(u) = \mathbb{E}\big[e^{iuV(0)}\big] \tag{6.20}$$

is the characteristic function of $V(0)$, and $\hat{\mathcal{U}}_0$ is defined by (6.12).

In this result, for simplicity, the wave front does not have any dependence at the scale of the correlation length as the asymptotic profile would not depend on it. Let us make two remarks. First, the impact of the interface fluctuations on the specular reflected wave can be described as the reflection problem with a flat interface where the homogenized scattering property are captured through a convolved initial pulse profile:

$$\frac{1}{2}\Phi *_s \Psi(s, \mathbf{y}),$$

where $*_s$ is the convolution operator acting on the s-variable, and

$$\Phi(s) := \frac{1}{2\pi} \int e^{-i\omega s} \phi_V(2\omega\lambda_0) d\omega$$

corresponds to a scaled version of the probability density function of $V(0)$. Second, compared to the case $\gamma = 1/2$, the scattering operator (6.18) is now homogenized,

$$\mathbb{E}[K_{ref}(\omega, \mathbf{q}', \mathbf{q})] = \int e^{i\omega(\mathbf{q}'-\mathbf{q})\cdot\mathbf{y}'} \mathbb{E}\Big[e^{2i\omega\lambda_0\mathcal{V}(\mathbf{y}')}\Big] d\mathbf{y}' = \delta(\omega(\mathbf{q}'-\mathbf{q}))\phi_V(2\omega\lambda_0).$$

This homogenized version of the scattering operator acts as for a flat surface, it does not modify the incident direction $\mathbf{q}'$, and the effective contributions of the interface fluctuations produce only a low-pass filter in frequency through the characteristic function ϕ_V.

The same strategy applies for the transmitted wave front, and we have the following result.

Proposition 6.2.4 *The family $(U^{\varepsilon,tr})_\varepsilon$ converges in probability, as $\varepsilon \to 0$, in $\mathcal{S}'(\mathbb{R}\times\mathbb{R}^2)$ to the deterministic pulse profile:*

$$U^{tr}(s,\mathbf{y}) = \frac{\mathcal{T}}{2(2\pi)^5}\sqrt{\frac{\lambda_0}{\lambda_1}}\iiiint e^{-i\omega(s-\mathbf{q}\cdot y)}\hat{\mathcal{U}}_1(\omega,\mathbf{q},z_{tr}-z_{int})\hat{\mathcal{U}}_0(\omega,\mathbf{q},z_{int}) \\ \times \phi_V((\lambda_0-\lambda_1)\omega)\hat{\Psi}(\omega,\mathbf{q})\omega^2 d\omega d\mathbf{x}' d\mathbf{q},$$

where ϕ_V is defined by (6.20)*, the $\hat{\mathcal{U}}_j$'s by* (6.12) *and* (6.17)*.*

The profile U^{tr} is similar to the one obtained for a flat surface (6.16), but again with a convolved initial condition accounting for the homogenization effects. The scattering operator (6.19) becomes here

$$\mathbb{E}[K_{tr}(\omega,\mathbf{q}',\mathbf{q})] = \int e^{i\omega(\mathbf{q}'-\mathbf{q})\cdot\mathbf{y}'}\mathbb{E}\Big[e^{i\omega(\lambda_0-\lambda_1)\mathcal{V}(\mathbf{y}')}\Big]d\mathbf{y}' = \delta(\omega(\mathbf{q}'-\mathbf{q}))\phi_V((\lambda_0-\lambda_1)\omega).$$

6.2.5 Incoherent wave fluctuations and generalized Snell's laws for $l_c \ll r_0$ $(\gamma > 1/2)$

We now aim at describing the incoherent wave fluctuations, resulting from diffraction, which account for the missing energy carried by the homogenized specular components.

The reflected speckle profile refers to the following reflected wavefield

$$S^{\varepsilon,ref}(\bar{s},\bar{\mathbf{y}},\mathbf{y},\widetilde{s},\widetilde{\mathbf{y}}) := \varepsilon^{-2(\gamma-1/2)}u^{\varepsilon,ref}(t^\varepsilon_{obs,ref}(\bar{s},\bar{\mathbf{y}},\mathbf{y},\widetilde{\mathbf{y}}) + \varepsilon\widetilde{s},\mathbf{x}^\varepsilon_{obs,ref}(\bar{\mathbf{y}},\mathbf{y}) + \varepsilon^\gamma\widetilde{\mathbf{y}},z=0),$$

observed at position

$$\mathbf{x}^\varepsilon_{obs,ref}(\bar{\mathbf{y}},\mathbf{y}) := \mathbf{x}_{obs,ref} + \varepsilon^{1-\gamma}\bar{\mathbf{y}} + \sqrt{\varepsilon}\,\mathbf{y}, \tag{6.21}$$

and time

$$t^\varepsilon_{obs,ref}(\bar{s},\bar{\mathbf{y}},\mathbf{y},\widetilde{\mathbf{y}}) := t_{obs,ref} + \varepsilon^{1-\gamma}\mathbf{k}_0\cdot\bar{\mathbf{y}} + \sqrt{\varepsilon}\,\mathbf{k}_0\cdot\mathbf{y} + \varepsilon^\gamma\mathbf{k}_0\cdot\widetilde{\mathbf{y}} + \varepsilon^{2(1-\gamma)}\bar{s}. \tag{6.22}$$

Here, the observation point and time exhibit extra terms in $\varepsilon^{1-\gamma}$ and $\varepsilon^{2(1-\gamma)}$ corresponding to the roughness parameter λ/l_c. These terms account for neighborhood and time windows larger than the ones of the specular components (see Fig. 6.9 for an illustration). They can even be of order one if $\lambda \sim l_c$ (that is $\gamma = 1$). The order of magnitude of the speckle can be understood as spreading a beam width of order r_0 over a two dimensional spatial window of order $r_0^2/l_c \sim \lambda/l_c$. Therefore, it is indeed expected to observe a speckle with amplitude of order

$$\Big(\frac{r_0}{r_0^2/l_c}\Big)^2 \sim \Big(\frac{l_c}{r_0}\Big)^2 \sim \varepsilon^{2(\gamma-1/2)}.$$

The following result describes the asymptotic behavior of the two-point statistics of the speckle profile:

$$\mathcal{C}^{\varepsilon,ref}(\bar{s},\bar{\mathbf{y}},\mathbf{y},\widetilde{s}_1,\widetilde{\mathbf{y}}_1,\widetilde{s}_2,\widetilde{\mathbf{y}}_2) := S^{\varepsilon,ref}(\bar{s},\bar{\mathbf{y}},\mathbf{y},\widetilde{s}_1,\widetilde{\mathbf{y}}_1)S^{\varepsilon,ref}(\bar{s},\bar{\mathbf{y}},\mathbf{y},\widetilde{s}_2,\widetilde{\mathbf{y}}_2). \tag{6.23}$$

Proposition 6.2.5 *We have*

$$\lim_{\varepsilon\to 0}\mathcal{C}^{\varepsilon,ref}(\bar{s},\bar{\mathbf{y}},\mathbf{y},\widetilde{s}_1,\widetilde{\mathbf{y}}_1,\widetilde{s}_2,\widetilde{\mathbf{y}}_2) = \mathbf{C}^{ref}(\bar{s},\bar{\mathbf{y}},\widetilde{s}_1-\widetilde{s}_2,\widetilde{\mathbf{y}}_1-\widetilde{\mathbf{y}}_2),$$

in probability in $\mathcal{S}'(\mathbb{R}\times\mathbb{R}^2\times\mathbb{R}^2\times\mathbb{R}\times\mathbb{R}^2\times\mathbb{R}\times\mathbb{R}^2)$, where

$$\mathbf{C}^{ref}(\bar{s},\bar{\mathbf{y}},\widetilde{s},\widetilde{\mathbf{y}}) := \frac{\mathcal{R}^2}{4(2\pi)^3}\iint e^{-i\omega(\widetilde{s}-\mathbf{p}\cdot\widetilde{\mathbf{y}})}\mathcal{A}(2\lambda_0,\omega,\mathbf{p})|\hat{\Psi}|_2^2(\omega) \\ \times \delta(\bar{s}-s^{ref}_{\mathbf{p}})\delta(\bar{\mathbf{y}}-\mathbf{y}^{ref}_{\mathbf{p}})\omega^4 d\omega d\mathbf{p}, \tag{6.24}$$

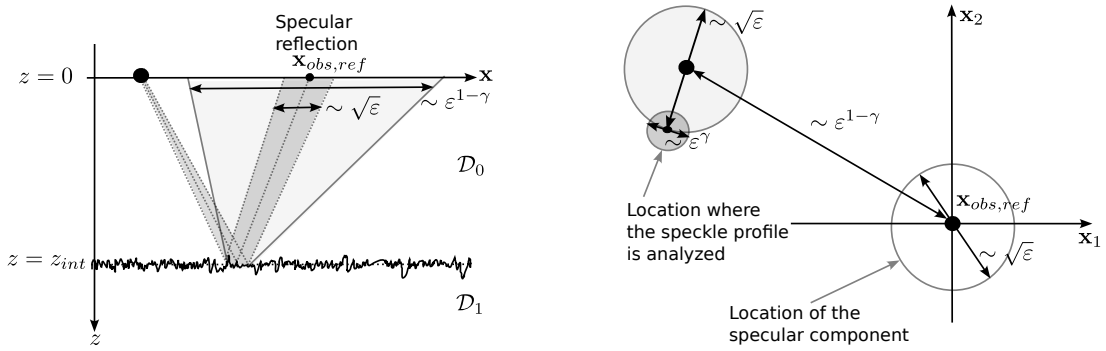

Fig. 6.9: The left picture illustrates the zone where the reflected speckle profile can be observed (in light grey) compared to the specular reflected component (in grey). The right picture illustrates the spatial window over which the speckle profile is analyzed.

with

$$\mathcal{A}(v,\omega,\mathbf{p}) := \int \mathbb{E}\big[e^{iv(V(\mathbf{y}')-V(0))}\big] e^{-i\omega \mathbf{p}\cdot\mathbf{y}'} d\mathbf{y}', \tag{6.25}$$

and

$$|\hat{\Psi}|_2^2(\omega) := \frac{1}{(2\pi)^2} \int |\hat{\Psi}(\omega,\mathbf{q})|^2 d\mathbf{q}. \tag{6.26}$$

We also have,

$$\mathbf{y}_{\mathbf{p}}^{ref} := 2z_{int} c_0 A_0 \mathbf{p} \qquad \textit{and} \qquad s_{\mathbf{p}}^{ref} := \mathbf{p}\cdot\mathbf{y}_{\mathbf{p}}^{ref}/2 = z_{int} c_0 \mathbf{p}^T A_0 \mathbf{p} \geq 0.$$

The asymptotic correlation function exhibits stationarity w.r.t. the variables in $\widetilde{s}, \widetilde{\mathbf{y}}$ (evolving respectively at the scale of the pulse width and correlation length), but does not depend on the variable $\mathbf{y}$ (corresponding to variations at the beam width scale). This means that the two-point statistics in $\widetilde{s}$ and $\widetilde{\mathbf{y}}$ are identical over regions of order the beam width. In a similar manner, the intensity carried by the speckle profile satisfies

$$\lim_{\varepsilon\to 0} \left|S^{\varepsilon,ref}(\bar{s},\bar{\mathbf{y}},\mathbf{y},\widetilde{s},\widetilde{\mathbf{y}})\right|^2 = \mathbf{C}^{ref}(\bar{s},\bar{\mathbf{y}},0,0),$$

which does not depend on the variable $\mathbf{y}$ and the small scale fluctuations in $\widetilde{s}$ and $\widetilde{\mathbf{y}}$. The intensity is therefore uniform over these scales.

Regarding the self-averaging property of the correlation function, the speckle profile is here correlated around a given $(\bar{s},\bar{\mathbf{y}},\mathbf{y})$. Hence, looking at the second order moment of the correlation function in $\mathcal{S}'$ corresponds to look at the fourth order moment of the speckle, but with two elements around some $(\bar{s}_1,\bar{\mathbf{y}}_1,\mathbf{y}_1)$ and two others around some $(\bar{s}_2,\bar{\mathbf{y}}_2,\mathbf{y}_2)$. These two observation points being far apart from each other (in time and space) the correlated speckles around each of these points become statistically independent:

$$\mathbb{E}[\mathcal{C}^{\varepsilon,ref}(\bar{s}_1,\bar{\mathbf{y}}_1,\mathbf{y}_1)\mathcal{C}^{\varepsilon,ref}(\bar{s}_2,\bar{\mathbf{y}}_2,\mathbf{y}_2)] \simeq \mathbb{E}[\mathcal{C}^{\varepsilon,ref}(\bar{s}_1,\bar{\mathbf{y}}_1,\mathbf{y}_1)]\mathbb{E}[\mathcal{C}^{\varepsilon,ref}(\bar{s}_2,\bar{\mathbf{y}}_2,\mathbf{y}_2)].$$

The term $\mathcal{A}(\cdot,\omega,\mathbf{p})$ corresponds to the distribution of the scattered directions $\mathbf{p}$ produced by the random interface. These directions $\mathbf{p}$ are related to variations at the scale of the correlation length through the characteristic function of the relative elevation $V(\mathbf{y}') - V(0)$. This effective scattering operator has already been formally derived in [183] to describe the mean intensity of the diffusive reflected wavefield under the Born approximation. From the Dirac masses in (6.24), the resulting speckle can be observed, for a given direction $\mathbf{p}$, at position $\mathbf{y}_{\mathbf{p}}^{ref}$ and time $s_{\mathbf{p}}^{ref} := \mathbf{p}\cdot\mathbf{y}_{\mathbf{p}}^{ref}/2$. Both of these quantities depend on the distance z_{int} from the source term to the interface location, and therefore influence the cone size of the reflected speckle and the time window to observe its evolution.

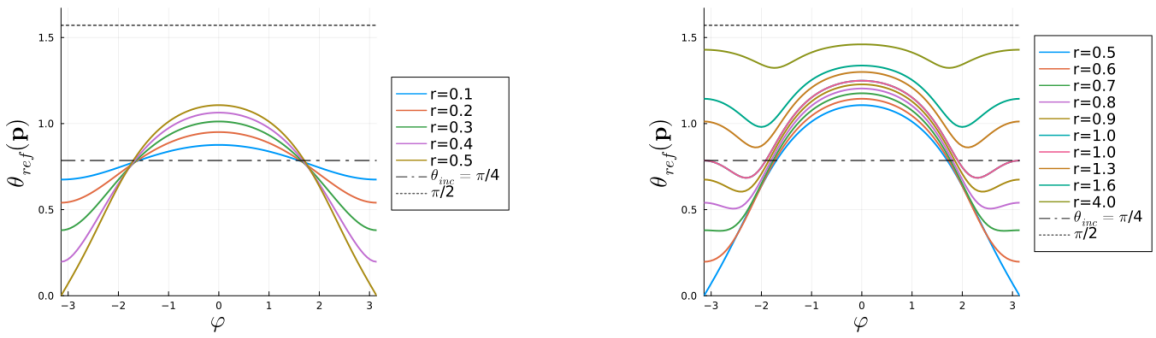

Fig. 6.10: Illustration of the incident angle θ^0_{inc} (dash-dot line) and the reflected angle $\theta_{ref}(\mathbf{p}) \in (0, \pi/2)$ for $\gamma = 1$ and $\mathbf{p} = \beta_1 \mathbf{k}_0 + \beta_2 \mathbf{k}_0^{\perp}$, with $(\beta_1, \beta_2) = r\,(\cos(\varphi), \sin(\varphi))$.

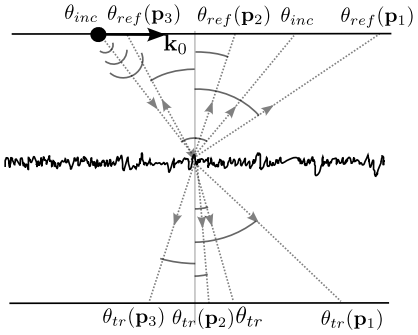

Fig. 6.11: Illustration of the generalized Snell's laws of refraction and transmission.

Generalized Snell's law of refraction From the observation point $\mathbf{y}^{ref}_{\mathbf{p}}$, the standard reflection relation between the incident and reflected angle (6.11) can be generalized as follows. For a given frequency ω and nonnull slowness vector $\mathbf{k}_0$, $(\theta_{inc} > 0)$, we have

$$\frac{\tan(\theta_{ref}(\mathbf{p}))}{\tan(\theta_{inc})} = \frac{|\mathbf{x}_{int} + \varepsilon^{1-\gamma}\mathbf{y}^{ref}_{\mathbf{p}}|}{|\mathbf{x}_{int}|} = \sqrt{\Big(1 + \xi_\varepsilon \frac{\mathbf{p}\cdot\mathbf{k}_0}{\cos^2(\theta_{inc})}\Big)^2 + \xi_\varepsilon^2 (\mathbf{p}\cdot\mathbf{k}_0^{\perp})^2}, \qquad \xi_\varepsilon := \varepsilon^{1-\gamma}\frac{c_0^2}{\sin^2(\theta_{inc})}$$

for $\mathbf{p}$ distributed according to the scattering operator $\mathcal{A}(2\lambda_0, \omega, \cdot)$. The case $\gamma \in (1/2, 1)$ yields the perturbation formula

$$\theta_{ref}(\mathbf{p}) = \theta_{inc} + \xi_\varepsilon \tan(\theta_{inc})\mathbf{p}\cdot\mathbf{k}_0 + \mathcal{O}(\varepsilon^{2(1-\gamma)}|\mathbf{p}|^2).$$

We refer to Fig. 6.10 for an illustration of $\theta_{ref}(\mathbf{p})$ when $\gamma = 1$ (that is $\lambda \sim l_c$). From these illustrations, one can remark that the cone produced by the reflected speckle can be fairly large, depending on the norms of the scattered directions $\mathbf{p}$. For null slowness vector $\mathbf{k}_0$ $(\theta_{inc} = 0)$, the refraction formula is simply given by $\tan(\theta_{ref}(\mathbf{p})) = \varepsilon^{1-\gamma} c_0 |\mathbf{p}|$, that is

$$\theta_{ref}(\mathbf{p}) = \arctan(\varepsilon^{1-\gamma} c_0 |\mathbf{p}|).$$

In a similar manner, the transmitted speckle profile is given by

$$S^{\varepsilon,tr}(\bar{s}, \bar{\mathbf{y}}, \mathbf{y}, \widetilde{s}, \widetilde{\mathbf{y}}) := \varepsilon^{-2(\gamma-1/2)} u^{\varepsilon,tr}(t^{\varepsilon}_{obs,tr}(\bar{s}, \bar{\mathbf{y}}, \mathbf{y}, \widetilde{\mathbf{y}}) + \varepsilon\widetilde{s}, \mathbf{x}^{\varepsilon}_{obs,tr}(\bar{\mathbf{y}}, \mathbf{y}) + \varepsilon^{\gamma}\widetilde{\mathbf{y}}, z = z_{tr}),$$

where

$$\mathbf{x}^{\varepsilon}_{obs,tr}(\mathbf{y}, \bar{\mathbf{y}}) := \mathbf{x}_{obs,tr} + \varepsilon^{1-\gamma}\bar{\mathbf{y}} + \sqrt{\varepsilon}\,\mathbf{y},$$

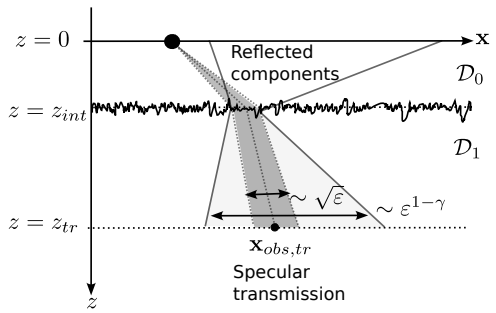

Fig. 6.12: Illustration to the zone where the transmitted speckle profile can be observed (in light grey) compared to the specular reflection component (in grey).

and

$$t^{\varepsilon}_{obs,tr}(\bar{s},\bar{\mathbf{y}},\mathbf{y},\widetilde{\mathbf{y}}) := t_{obs,tr} + \varepsilon^{1-\gamma}\mathbf{k}_0\cdot\bar{\mathbf{y}} + \sqrt{\varepsilon}\,\mathbf{k}_0\cdot\mathbf{y} + \varepsilon^{\gamma}\mathbf{k}_0\cdot\widetilde{\mathbf{y}} + \varepsilon^{2(1-\gamma)}\bar{s}.$$

The corresponding correlation function is defined as:

$$\mathcal{C}^{\varepsilon,tr}(\bar{s},\bar{\mathbf{y}},\mathbf{y},\widetilde{s}_1,\widetilde{\mathbf{y}}_1,\widetilde{s}_2,\widetilde{\mathbf{y}}_2) := S^{\varepsilon,tr}(\bar{s},\bar{\mathbf{y}},\mathbf{y},\widetilde{s}_1,\widetilde{\mathbf{y}}_1)S^{\varepsilon,tr}(\bar{s},\bar{\mathbf{y}},\mathbf{y},\widetilde{s}_2,\widetilde{\mathbf{y}}_2),$$

where its asymptotic behavior is given by the following result.

Proposition 6.2.6 *We have*

$$\lim_{\varepsilon\to 0}\mathcal{C}^{\varepsilon,tr}(\bar{s},\bar{\mathbf{y}},\mathbf{y},\widetilde{s}_1,\widetilde{\mathbf{y}}_1,\widetilde{s}_2,\widetilde{\mathbf{y}}_2) = \mathbf{C}^{tr}(\bar{s},\bar{\mathbf{y}},\widetilde{s}_1-\widetilde{s}_2,\widetilde{\mathbf{y}}_1-\widetilde{\mathbf{y}}_2),$$

in probability in $\mathcal{S}'(\mathbb{R}\times\mathbb{R}^2\times\mathbb{R}^2\times\mathbb{R}\times\mathbb{R}^2\times\mathbb{R}\times\mathbb{R}^2)$*, where*

$$\mathbf{C}^{tr}(\bar{s},\bar{\mathbf{y}},\mathbf{y},\widetilde{s},\widetilde{\mathbf{y}}) := \frac{\mathcal{T}^2\lambda_0}{4\lambda_1(2\pi)^3}\iint e^{-i\omega(\widetilde{s}-\mathbf{p}\cdot\widetilde{\mathbf{y}})}\mathcal{A}(\lambda_0-\lambda_1,\omega,\mathbf{p})|\hat{\Psi}|^2_2(\omega)\delta(\bar{s}-s^{tr}_{\mathbf{p}})\delta(\bar{\mathbf{y}}-\mathbf{y}^{tr}_{\mathbf{p}})\omega^4 d\omega d\mathbf{p}.$$

with $\mathcal{A}$ *defined by* (6.25)*,* $|\hat{\Psi}|^2_2$ *by* (6.26)*, and*

$$\mathbf{y}^{tr}_{\mathbf{p}} := 2(z_{tr}-z_{int})c_1A_1\mathbf{p} \geq 0, \qquad \textit{and} \qquad s^{tr}_{\mathbf{p}} := \mathbf{p}\cdot\mathbf{y}^{tr}_{\mathbf{p}}/2 = (z_{tr}-z_{int})c_1\mathbf{p}^TA_1\mathbf{p}.$$

Accordingly, the mean intensity carried by the speckle profile is given by

$$\lim_{\varepsilon\to 0}\left|S^{\varepsilon,tr}(\bar{s},\bar{\mathbf{y}},\mathbf{y},\widetilde{s},\widetilde{\mathbf{y}})\right|^2 = \mathbf{C}^{tr}(\bar{s},\bar{\mathbf{y}},0,0),$$

in probability, which does not depend on the variable $\mathbf{y}$ and the small scale fluctuations in $\widetilde{s}$ and $\widetilde{\mathbf{y}}$. The intensity is therefore again uniform over these scales.

Generalized Snell's law of transmission From $\mathbf{y}^{tr}_{\mathbf{p}}$, we obtain the following relation between the transmission angle and the specular transmission angle θ^0_{tr}:

$$\begin{aligned}\frac{\tan(\theta_{tr}(\mathbf{p}))}{\tan(\theta^0_{tr})} &= \frac{|\mathbf{x}_{obs,tr}-\mathbf{x}_{int}+\varepsilon^{1-\gamma}\mathbf{y}^{tr}_{\mathbf{p}}|}{|\mathbf{x}_{obs,tr}-\mathbf{x}_{int}|}\\ &= \sqrt{\Big(1+\xi_\varepsilon\frac{\mathbf{p}\cdot\mathbf{k}_0}{\cos^2(\theta_{tr})}\Big)^2+\xi^2_\varepsilon(\mathbf{p}\cdot\mathbf{k}^\perp_0)^2}, \qquad \xi_\varepsilon := \varepsilon^{1-\gamma}\frac{c_0^2}{\sin^2(\theta_{inc})},\end{aligned}$$

for $\mathbf{p}$ distributed according to the scattering operator $\mathcal{A}(\lambda_0-\lambda_1,\omega,\cdot)$. From this relation, the standard Snell's relation of transmission can be generalized as follow:

$$\frac{\sin(\theta_{tr}(\mathbf{p}))}{c_1} = \frac{\sin(\theta_{inc})}{c_0}\sqrt{\frac{\Xi}{1+\sin^2(\theta^0_{tr})\Big(\Xi-1\Big)}}, \qquad \Xi := \Big(1+\xi_\varepsilon\frac{\mathbf{p}\cdot\mathbf{k}_0}{\cos^2(\theta_{tr})}\Big)^2+\xi^2_\varepsilon(\mathbf{p}\cdot\mathbf{k}^\perp_0)^2,$$

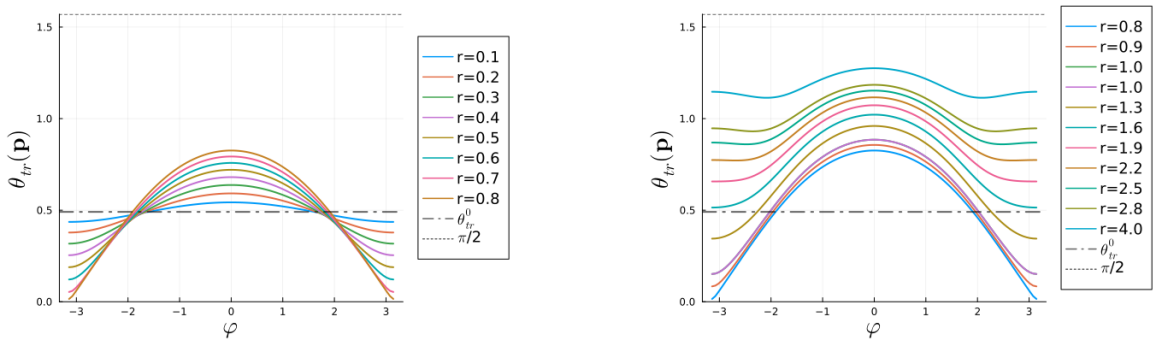

Fig. 6.13: Illustration of the specular transmission angle θ^0_{tr} (dash-dot line) and the transmission angle $\theta_{ref}(\mathbf{p}) \in (0, \pi/2)$ for $\gamma = 1$, $c_0 = 1.5$, $c_1 = 1$, and $\mathbf{p} = \beta_1 \mathbf{k}_0 + \beta_2 \mathbf{k}_0^\perp$ with $(\beta_1, \beta_2) = r(\cos(\varphi), \sin(\varphi))$.

leading for $\gamma \in (1/2, 1)$ to the perturbed relation

$$\frac{\sin(\theta_{tr}(\mathbf{p}))}{c_1} = \frac{\sin(\theta_{inc})}{c_0}\Big(1 + \xi_\varepsilon \frac{\mathbf{p}\cdot\mathbf{k}_0}{\cos^2(\theta^0_{tr})} + \mathcal{O}(\varepsilon^{2(1-\gamma)}|\mathbf{p}|^2)\Big),$$

providing the approximation

$$\theta_{tr}(\mathbf{p}) = \theta^0_{tr} + \xi_\varepsilon \frac{\tan(\theta_{tr})}{\cos^2(\theta_{tr})}\mathbf{p}\cdot\mathbf{k}_0 + \mathcal{O}(\varepsilon^{2(1-\gamma)}|\mathbf{p}|^2).$$

We refer to Fig. 6.13 for an illustration of $\theta_{tr}(\mathbf{p})$ when $\gamma = 1$, that is in the context of a rough interface $\lambda \sim l_c$. From these illustrations, one can again remark that the cone produced by the transmitted speckle can also be fairly large, depending on the norms of the scattered directions $\mathbf{p}$. Finally, for a null slowness vector $\mathbf{k}_0 = 0$ ($\theta_{inc} = 0$), the transmission angle satisfies $\tan(\theta_{tr}(\mathbf{p})) = \varepsilon^{1-\gamma} c_1 |\mathbf{p}|$, so that

$$\theta_{tr}(\mathbf{p}) = \arctan(\varepsilon^{1-\gamma} c_1 |\mathbf{p}|).$$

6.2.6 Gaussian statistics of the speckle patterns for $l_c \ll r_0$ ($\gamma > 1/2$)

We conclude this section with a direct statistical description of the speckles themselves in the Fourier domain at the scale of the pulse width and correlation length. For the reflected speckle, we consider

$$\hat{S}^{\varepsilon,ref}(\bar{s}, \bar{\mathbf{y}}, \mathbf{y}, \omega, \mathbf{p}) := \varepsilon^{-2(\gamma-1/2)} \iint e^{i\omega(\widetilde{s}-\mathbf{p}\cdot\widetilde{\mathbf{y}})} u^{\varepsilon,ref}\big(t^\varepsilon_{obs,ref}(\bar{s}, \bar{\mathbf{y}}, \mathbf{y}, \widetilde{\mathbf{y}}) + \varepsilon\widetilde{s}, \mathbf{x}^\varepsilon_{obs,ref}(\bar{\mathbf{y}}, \mathbf{y}) + \varepsilon^\gamma \widetilde{\mathbf{y}}\big) d\widetilde{s} d\widetilde{\mathbf{y}},$$

where $\mathbf{x}^\varepsilon_{obs,ref}$ and $t^\varepsilon_{obs,ref}$ are respectively given by (6.21) and (6.22). To regularize the Dirac masses in (6.24) around $\mathbf{y}^{ref}_{\mathbf{p}}$ and $s^{ref}_{\mathbf{p}}$, we introduce

$$\hat{\mathcal{S}}^{\varepsilon,ref}_{\mathbf{y}}(\bar{s}, \bar{\mathbf{y}}, \omega, \mathbf{p}) := \hat{S}^{\varepsilon,ref}(\bar{s}, \bar{\mathbf{y}}, \mathbf{y}, \omega, \mathbf{p}) \frac{1}{\varepsilon^{3(\gamma-1/2)}} \varphi^{1/2}\Big(2\frac{\bar{s} - s^{ref}_{\mathbf{p}}}{\varepsilon^{2(\gamma-1/2)}}, 2\frac{\bar{\mathbf{y}} - \mathbf{y}^{ref}_{\mathbf{p}}}{\varepsilon^{2(\gamma-1/2)}}\Big), \tag{6.27}$$

where we have added the square root of a symmetric mollifier, that acts as a windowing around $\bar{s} = s^{ref}_{\mathbf{p}}$ and $\bar{\mathbf{y}} = \mathbf{y}^{ref}_{\mathbf{p}}$. Recalling that $\bar{s}$ and $\bar{\mathbf{y}}$ scale at respectively $\varepsilon^{2(1-\gamma)}$ and $\varepsilon^{1-\gamma}$, the resulting window scales at the pulse width ε and correlation length ε^γ respectively. The asymptotic behavior of the speckle is the following.

Theorem 6.2.1 *For $n \geq 1$ and any fixed $\mathbf{y}_1, \ldots, \mathbf{y}_n, \in \mathbb{R}^2$, the family $(\hat{\mathcal{S}}^{\varepsilon,ref}_{\mathbf{y}_1}, \ldots, \hat{\mathcal{S}}^{\varepsilon,ref}_{\mathbf{y}_n})_\varepsilon$ converges in law, as $\varepsilon \to 0$, in $\mathcal{S}'_n$ (which is n times the Cartesian product of $\mathcal{S}'(\mathbb{R}\times\mathbb{R}^2\times\mathbb{R}\times\mathbb{R}^2, \mathbb{C})$) to a limit $(\hat{\mathcal{S}}^{ref}_1, \ldots, \hat{\mathcal{S}}^{ref}_n)$ made of n independent copies of a complex valued mean-zero Gaussian random field*

$\hat{\mathcal{S}}^{ref}$ *(independent of the* $\mathbf{y}_j$*'s) with covariance functions of the form*

$$\mathbb{E}[\hat{\mathcal{S}}^{ref}(\phi)\hat{\mathcal{S}}^{ref}(\psi)] = \int\cdots\int \hat{\mathcal{K}}_{ref}(\bar{s}_1,\bar{s}_2,\bar{\mathbf{y}}_1,\bar{\mathbf{y}}_2,\omega_1,-\omega_2,\mathbf{p}_1,\mathbf{p}_2) \times \overline{\phi(\bar{s}_1,\bar{\mathbf{y}}_1,\omega_1,\mathbf{p}_1)\psi(\bar{s}_2,\bar{\mathbf{y}}_2,\omega_2,\mathbf{p}_2)}d\bar{s}_1d\bar{s}_2d\bar{\mathbf{y}}_1d\bar{\mathbf{y}}_2d\omega_1d\omega_2d\mathbf{p}_1d\mathbf{p}_2, \tag{6.28}$$

$$\mathbb{E}[\hat{\mathcal{S}}^{ref}(\phi)\overline{\hat{\mathcal{S}}^{ref}(\psi)}] = \int\cdots\int \hat{\mathcal{K}}_{ref}(\bar{s}_1,\bar{s}_2,\bar{\mathbf{y}}_1,\bar{\mathbf{y}}_2,\omega_1,\omega_2,\mathbf{p}_1,\mathbf{p}_2) \times \overline{\phi(\bar{s}_1,\bar{\mathbf{y}}_1,\omega_1,\mathbf{p}_1)}\psi(\bar{s}_2,\bar{\mathbf{y}}_2,\omega_2,\mathbf{p}_2)d\bar{s}_1d\bar{s}_2d\bar{\mathbf{y}}_1d\bar{\mathbf{y}}_2d\omega_1d\omega_2d\mathbf{p}_1d\mathbf{p}_2, \tag{6.29}$$

for any $\phi,\psi\in\mathcal{S}(\mathbb{R}\times\mathbb{R}^2\times\mathbb{R}\times\mathbb{R}^2,\mathbb{C})$*, where the kernel* $\hat{\mathcal{K}}_{ref}$ *is given by*

$$\hat{\mathcal{K}}_{ref}(\bar{s}_1,\bar{s}_2,\bar{\mathbf{y}}_1,\bar{\mathbf{y}}_2,\omega_1,\omega_2,\mathbf{p}_1,\mathbf{p}_2) = \frac{(2\pi)^3\mathcal{R}^2}{4}\mathcal{A}(2\lambda_0,\omega_1,\mathbf{p}_1)|\hat{\Psi}|_2^2(\omega_1)\hat{\varphi}(\omega_1,\mathbf{p}_1)\delta(\omega_1-\omega_2) \times \delta(\mathbf{p}_1-\mathbf{p}_2)\delta(\bar{s}_1-s^{ref}_{\mathbf{p}_1})\delta(\bar{s}_2-\bar{s}_1)\delta(\bar{\mathbf{y}}_1-\mathbf{y}^{ref}_{\mathbf{p}_1})\delta(\bar{\mathbf{y}}_2-\bar{\mathbf{y}}_1). \tag{6.30}$$

In contrast to the correlation function (6.23), exhibiting a self-averaging property, the asymptotic behavior of the speckle (6.27) is described through a Gaussian random field w.r.t. the scattered direction $\mathbf{p}$. The term $\delta(\mathbf{p}_1-\mathbf{p}_2)$ in (6.30) translates that two distinct directions produce independent components. This is of course expected as these two components will be observed at locations far apart from each other. The $\mathbf{p}$-variable being also related to fluctuations at the scale of the correlation length, the resulting Gaussian field is then described at this scale around the given time $s^{ref}_{\mathbf{p}}$ and location $\mathbf{y}^{ref}_{\mathbf{p}}$.

A similar result can be obtained for the transmitted speckle in the Fourier domain,

$$\hat{S}^{\varepsilon,tr}(\bar{s},\bar{\mathbf{y}},\mathbf{y},\omega,\mathbf{p}) := \varepsilon^{-2(\gamma-1/2)}\iint e^{i\omega(\widetilde{s}-\mathbf{p}\cdot\widetilde{\mathbf{y}})}u^{\varepsilon,tr}\big(t^{\varepsilon}_{obs,tr}(\bar{s},\bar{\mathbf{y}},\mathbf{y},\widetilde{\mathbf{y}})+\varepsilon\widetilde{s},\mathbf{x}^{\varepsilon}_{obs,tr}(\bar{\mathbf{y}},\mathbf{y})+\varepsilon^{\gamma}\widetilde{\mathbf{y}}\big)d\widetilde{s}d\widetilde{\mathbf{y}},$$

after introducing a window around $\mathbf{y}^{tr}_{\mathbf{p}}$ and $s^{tr}_{\mathbf{p}}$,

$$\hat{\mathcal{S}}^{\varepsilon,tr}_{\mathbf{y}}(\bar{s},\bar{\mathbf{y}},\omega,\mathbf{p}) := \hat{S}^{\varepsilon,tr}(\bar{s},\bar{\mathbf{y}},\mathbf{y},\omega,\mathbf{p})\frac{1}{\varepsilon^{3(\gamma-1/2)}}\varphi^{1/2}\Big(2\frac{\bar{s}-s^{tr}_{\mathbf{p}}}{\varepsilon^{2(\gamma-1/2)}},2\frac{\bar{\mathbf{y}}-\mathbf{y}^{tr}_{\mathbf{p}}}{\varepsilon^{2(\gamma-1/2)}}\Big).$$

Theorem 6.2.2 *For* $n\geq 1$ *and any fixed* $\mathbf{y}_1,\ldots,\mathbf{y}_n\in\mathbb{R}^2$*, the family* $(\hat{\mathcal{S}}^{\varepsilon,tr}_{\mathbf{y}_1},\ldots,\hat{\mathcal{S}}^{\varepsilon,tr}_{\mathbf{y}_n})_\varepsilon$ *converges in law, as* $\varepsilon\to 0$*, in* $\mathcal{S}'_n$ *to* $(\hat{\mathcal{S}}^{tr}_1,\ldots,\hat{\mathcal{S}}^{tr}_n)_\varepsilon$*, made of* n *independent copies of a complex mean-zero Gaussian random field* $\hat{\mathcal{S}}^{ref}$ *with covariance functions similar to* (6.28) *and* (6.29)*, but with kernel*

$$\hat{\mathcal{K}}_{tr}(\bar{s}_1,\bar{s}_2,\bar{\mathbf{y}}_1,\bar{\mathbf{y}}_2,\omega_1,\omega_2,\mathbf{p}_1,\mathbf{p}_2) = \frac{(2\pi)^3\mathcal{T}^2\lambda_0}{4\lambda_1}\mathcal{A}(\lambda_0-\lambda_1,\omega_1,\mathbf{p}_1)|\hat{\Psi}|_2^2(\omega_1)\hat{\varphi}(\omega_1,\mathbf{p}_1)\delta(\omega_1-\omega_2) \times \delta(\mathbf{p}_1-\mathbf{p}_2)\delta(\bar{s}_1-s_{\mathbf{p}_1})\delta(\bar{s}_2-s_{\mathbf{p}_1})\delta(\bar{\mathbf{y}}_1-\mathbf{y}_{\mathbf{p}_1})\delta(\bar{\mathbf{y}}_2-\mathbf{y}_{\mathbf{p}_1}).$$

6.3 Perspectives

In the second part of this chapter, the statistical properties of the reflected and transmitted wavefields are described in the case of a moderately rough interface (the central wavelength and the magnitude of the interface fluctuations are of the same order $\lambda\sim\sigma$). In this regime, effective specular and diffusive (speckle) components are observed, but no enhance backscattering effects. To observe such effects, it would be necessary for the rough surface to produce significant multiple scattering, which is achieved when $\lambda\ll\sigma$.

This novel framework precisely characterizes the statistics of the diffusive scattered waves from rough interfaces, both in transmission and reflection, in term of a Gaussian random field. This characterization can be used in remote sensing type imaging problems including: estimating the parameters of the rough (random) interface, and imaging objects hidden behind the interface by computing the empirical spectrum of the reflected speckle [88, 127]. The analysis can also be extended to Synthetic Aperture Radar (SAR) probing scenarios where the source cone is moving, typical mounted on an aircraft. In general imaging contexts one can exploit the memory effect, which means that the speckle pattern illuminating a hidden object is not completely changed, but rather shifted by a specific amount when the incoming angle of the source is shifted.

Chapter 7

Digressions in mathematical biology: Stochastic and deterministic models for the secondary metastatic emission process

The emergence of a metastatic phenotype is governed by a number of key mutations that was translated into mathematical models by [107,160], resulting in the derivation of a metastatic risk score. In an early work, [136] established a link between the primary tumor size at surgery and the risk of recurrence from a large cohort of breast cancer patients. In addition to such phenotypic characteristics, specific genetic signatures of the primary tumor have been identified as associated with increased risk of metastasis [204]. Nevertheless, these risk prediction models are static; they do not aim to represent the time evolution of the disease. In contrast, dynamic models offer the ability to predict how a system evolves over time, making it easier to incorporate data obtained at various observation points. To account for the relationship between the metastatic process and the primary tumor, a dynamic description of primary tumor growth is integrated into metastatic models. The simplest dynamic model for tumor growth is the exponential model, which describes growth under no restriction such as in vitro settings. However, in many cases of interest, especially in vivo scenarios, sigmoid (S-shaped) models with an initial exponential phase followed by a deceleration provide more suitable descriptions of growth dynamics. The Gompertz model is a classical example that has been commonly used, as well as power growth models that have been used for the description of clinical [111] and preclinical tumor growth data [32].

A stochastic dynamic model for metastasis was proposed by [28]. Their approach characterizes the emission times of metastases as random events through a non-homogeneous Poisson process with an emission rate increasing according to the primary tumor size. The Poisson law allows for an interpretation of the emission process as being memoryless, and provide fairly explicit mathematical formulations. A variant of this model successfully described data on bone lesions in the case of a metastatic breast cancer [108]. Dynamic models for metastasis can also be used to infer parts of the process that cannot be directly observed experimentally or clinically. For instance, [122] introduced a PDE model to describe the size distribution of metastatic colonies. Using clinical information concerning visible metastatic colonies, they successfully characterized the micrometastatic state of a patient with hepatocellular carcinoma. Later, this size-structured model was integrated into mixed-effects models, providing prediction of the size evolution of metastases in animal models without [113] and with [33] surgical removal of the primary tumor. Both approaches incorporate secondary metastatic emission into the model, that is the ability for metastasis to spread further. Indirect evidence of secondary metastatic emission has been provided through cancer network models [50,164, 165] and the identification of self-seeding mechanisms [55,186].

In most of the models mentioned above, metastases do not have the ability to emit metastases themselves. However, it is easy to think of situations where this property would make a difference in the model. For instance, consider a scenario in which a single metastasis is emitted before the primary

tumor surgery[1]. If this metastasis cannot generate further metastases, its successful removal cures the patient. However, the second surgery might fail if the metastasis is able to seed additional metastasis as well. Of course, there are other mechanisms potentially leading to treatment failure (e.g. local recurrence, surgery impossible,...), but for simplicity they are not discussed here. This section presents the relationship between the Iwata PDE model, which accounts for secondary metastatic emission, and a stochastic model based on a cascade of Poisson processes. Under this stochastic framework, the cascade effect accounts for secondary metastatic emissions, and we illustrate how this stochastic approach can be used to assess metastatic risk post-surgery.

7.1 A simple probabilistic framework for metastatic risk

Forecasting the likelihood of metastatic disease at the time of the primary tumor's diagnosis is of major clinical importance since it is strongly linked to survival expectancy. One possibility to construct such a predictive model is by using large databases to correlate information regarding the presence of metastases and the primary tumor's characteristics at the time of diagnosis or surgery. As an illustration, [159] proposed a relationship between the primary tumor size at surgery and the probability of metastasis based on clinical data on breast cancer:

$$\mathbb{P}(\text{no metastases}) = \exp(-c\, d^z),$$

where d is the largest diameter of the primary tumor at surgery, and c and z are parameters inferred from the data. Such a probability formula can be derived through the use of a nonhomogeneous Poisson process with an intensity function depending on a power growth model for the primary tumor.

Power growth. The growth diameter d of the largest primary tumor is the solution of the ordinary differential equation $d'(t) = a_{\mathrm{PG}}\, d(t)^\alpha$. Here, a_{PG} corresponds to the growth speed and α allows to describe different growth shapes: exponential growth ($\alpha = 1$), linear growth ($\alpha = 0$), and a range of sigmoid growth patterns in between ($0 < \alpha < 1$).

Power law of emission. The emission intensity λ of the Poisson process depends on the current size of the primary tumor through a power law, $\lambda(t) = b\, d(t)^\beta$. In this context, b can be understand as the metastatic aggressiveness of the primary tumor. In [122], the parameter β is linked to the type of primary tumor vascularization: $\beta = 3$ (dimension of space) for a uniform vascularization, and $\beta = 2$ (dimension of a surface)[2] for a surficial vascularization.

The stochastic nature of the metastatic emission process can also be described using various probability distributions, allowing to drop the memorylessness property. Nevertheless, the Poisson model offers the advantage of not necessitating extra statistical parameters, while ensuring a high level of analytical tractability and ease of numerical implementation.

7.2 Mathematical formalism and results

7.2.1 Size-structured model

To describe the micrometastatic state of cancer patients, [122] developed a *size-structured model* that describes the time evolution of a density function $\rho(t, x)$ representing the size distribution of metastatic colonies. Before describing this model, we need to introduce some notations.

The relationship between the size of the primary tumor X_p and its emission intensity λ_p is here given by a size-dependent emission law γ_p,

$$\lambda_p(t) := \gamma_p(X_p(t)).$$

[1] After a surgery the emission intensity is set to zero.

[2] The interpretation of β depends on the unit of the primary tumor measure. A surficial vascularization would correspond to $\beta = 2$ if the size is measured in diameter, but to $\beta = 2/3$ (the fractal dimension of a surface in space) if the size is measured in volume.

The evolution of X_p is given by a Gompertz law:

$$X_p' = g(X_p), \qquad \text{with} \qquad X_p(0) = x_0,$$

with a set of clinical parameters summarized in Table 7.1. These parameters were estimated by [122] from clinical data on a hepatocellular carcinoma with multiple liver metastases. In a similar manner,

Model	Parameter	Symbol	Value	Unit
Growth (Gompertz law)	Initial size	x_0	1	cells
$g(x) := a_{\text{Gomp}}\, x \log(x_p^\infty / x)$	Growth rate	a_{Gomp}	0.00286	days^{-1}
	Maximum size	x_p^∞	$7.3 \cdot 10^{10}$	cells
Emission (power law)	Rate constant	b	$5.3 \cdot 10^{-8}$	$\text{days}^{-1}\ \text{cells}^{-\beta}$
$\gamma_p(x) = b\, x^\beta$	Emission power	β	0.663	–

Table 7.1: Growth and emission laws derived by [122] from clinical data of a hepatocellular carcinoma with multiple liver metastases.

the size of a metastasis is given by X_m, which is the solution to

$$X_m'(t) = g(X_m(t)), \qquad \text{with} \qquad X_m(0) = x_m^0,$$

and corresponding secondary emission intensity by

$$\lambda_m(t) := \gamma_m(X_m(t)).$$

The metastatic density function ρ of the Iwata model solves the following PDE:

$$\begin{cases} \partial_t \rho(x,t) + \partial_x[g(x)\rho(x,t)] = 0, & (x,t) \in (x_m^0, x_m^\infty) \times (0, +\infty), \\ g(x_m^0)\rho(x_m^0,t) = \gamma_p(X_p(t)) + \displaystyle\int_{x_m^0}^{x_m^\infty} \gamma_m(x)\rho(x,t)dx, & t \in (0, +\infty), \\ \rho(x,0) = 0, & x \in [x_m^0, x_m^\infty], \end{cases} \tag{7.1}$$

where x_m^0 corresponds to the size of a newly emitted metastasis and x_m^∞ corresponds to the theoretical maximum size of the metastases. The well-posedness for this model has been established under general conditions by [27].

Various *model observable* (MO) associated to this model can be defined: for a given function f, a MO is defined by

$$\text{MO}_f(t) := \int_{x_m^0}^{x_m^\infty} f(x)\rho(x,t)dx.$$

Here are some examples.

- $f = \mathbf{1}$ corresponds to the number of metastases:

$$\text{MO}_{\mathbf{1}}(t) := \int_{x_m^0}^{x_m^\infty} 1 \cdot \rho(x,t)dx$$

- Similarly, the number of macrometastases is obtained with

$$f_{\text{macro}}(x) := \begin{cases} 1 & \text{if} \quad x \geq c \\ 0 & \text{if} \quad x < c \end{cases},$$

and the number of micrometastases with

$$f_{\text{micro}}(x) := \begin{cases} 0 & \text{if} \quad x \geq c \\ 1 & \text{if} \quad x < c \end{cases},$$

where c stands for the detectability threshold (depending on the imaging modality).

- The total metastatic mass M is obtained with the identity function $f_{\mathrm{Id}}(x) = x$ for all x:

$$\mathrm{MO}_{f_{\mathrm{Id}}}(t) := \int_{x_m^0}^{x_m^\infty} x\rho(x,t)dx.$$

The PDE model (7.1) is not convenient when it comes to evaluate MO numerically. Fortunately, all the MO can be characterized as being the solutions of a Volterra convolution equation [112].

Theorem 7.2.1 *For any $f \in L^\infty([x_m^0, x_m^\infty])$, MO_f is the unique solution of the following renewal equation,*

$$\mathrm{MO}_f(t) = \int_0^t \lambda_p(s) f(X_m(t-s))ds + \int_0^t \lambda_m(s)\mathrm{MO}_f(t-s)ds. \tag{7.2}$$

This representation is the basis of an efficient numerical resolution algorithm [112] that can be used for parameter estimation [113].

7.2.2 Probabilistic framework for secondary metastatic emission

We now introduce the stochastic counter part of the Iwata model. This stochastic model is based on a cascade of independent Poisson processes (PPs), and define recursively the emission times with respect to a generational hierarchy.

- The emission times $(T^{(j)})_{j\geq 1}$ at which the first generation of metastases occur, those emanating from the primary tumor, are modeled as the jump times of a PP $(N^{(1)})_{t\geq 0}$ with intensity λ_p.

The emission times for the next generations of metastases are defined recursively.

- Let $k \geq 2$ and $n_1, \ldots, n_{k-1} \geq 1$. The j-th emission time for the k-th generation of metastasis and filiation $n_1, \ldots, n_{k-1}$ is defined by

$$T^{(n_1,\ldots,n_{k-1},j)} := T^{(n_1,\ldots,n_{k-1})} + \tilde{T}^{(n_1,\ldots,n_{k-1},j)}.$$

  This corresponds to the time it takes for the offspring, with filiation $n_1, \ldots, n_{k-1}$, to give birth to its j-th offspring. Here, $(\tilde{T}^{(n_1,\ldots,n_{k-1},j)})_{j\geq 1}$ are the jump times of a PP $(N_t^{(n_1,\ldots,n_{k-1})})_{t\geq 0}$ with intensity λ_m.

For instance, $T^{(2,3,4)}$ corresponds to the emission time of the 4^{th} offspring produced by the 3^{rd} offspring of the 2^{nd} offspring of the primary tumor. Also, we assume that

$$\left\{(N_t^{(n_1,\ldots,n_k)})_{t\geq 0}, \quad k \geq 1, \quad n_1, \ldots, n_k \geq 1\right\}$$

forms a family of independent PPs. In other words, we assume that the primary tumors and all the metastases emit independently from each other.

From this construction, a *stochastic model observable* (SMO) for the k-th generation can be expressed by

$$\mathrm{SMO}_f^{(k)}(t) := \sum_{n_1,\ldots,n_k \geq 1} \mathbf{1}_{(T^{(n_1,\ldots,n_k)} \leq t)} f\big(X_m\big(t - T^{(n_1,\ldots,n_k)}\big)\big),$$

for $f \in L^\infty([x_m^0, x_m^\infty])$. Therefore, a global SMO with secondary emission can be defined by

$$\mathrm{SMO}_f(t) := \sum_{k=1}^{\infty} \mathrm{SMO}_f^{(k)}(t). \tag{7.3}$$

A global SMO accounts for the contribution of $\mathrm{SMO}_f^{(k)}$ over all the generations. The following result establish the connection between the SMO and MO.

Proposition 7.2.1 *Let $f \in L^\infty([x_m^0, x_m^\infty])$. The SMO (7.3) is well defined in the sense that*

$$\mathbb{P}\big(0 \leq \mathrm{SMO}_f(t) < +\infty \quad \forall t \geq 0\big) = 1,$$

and $\mathbb{E}[\mathrm{SMO}_f(t)]$ is finite for any time $t \geq 0$. Moreover, we have for any $t \geq 0$

$$\mathrm{MO}_f(t) = \mathbb{E}[\mathrm{SMO}_f(t)].$$

Let us remark that all the SMO can be seen as integrals w.r.t. a random measure:

$$\mathrm{SMO}_f(t) = \int f(x)\mathcal{M}_t(dx),$$

for any $t \geq 0$, with

$$\mathcal{M}_t := \sum_{k\geq 1} \sum_{n_1,\ldots,n_k \geq 1} \delta_{X_m(t-T^{(n_1,\ldots,n_k)})}.$$

From this representation, we can establish the connection between the stochastic model and structure size model (Iwata model).

Theorem 7.2.2 (Link to the structured population model) *For all $t \geq 0$, the measure*

$$\mu_t := \mathbb{E}[\mathcal{M}_t]$$

is σ-finite, absolutely continuous with respect to the Lebesgue measure, and its Radon-Nikodyn density is given by $\rho(\cdot, t)$,

$$\frac{d\mu_t}{dx} = \rho(\cdot, t),$$

where ρ is the solution to (7.1).

From Prop. 7.2.1, one can remark that all the SMO can be seen as a probabilistic representation of the corresponding MO. This remark is of interest to design rough confidence/prediction intervals from inferred parameters. In this respect, the following result concerns the variability of the SMO with respect to its mean MO.

Proposition 7.2.2 *Let $f \in L^\infty([x_m^0, x_m^\infty])$. The variance of the SMO,*

$$v_f(t) := \mathrm{var}[\mathrm{SMO}_f(t)]$$

is finite for any $t \geq 0$, and satisfies a renewal equation,

$$v_f(t) = \int_0^t \lambda_p(s)(f(X_m(t-s)) + e_{m,f}(t-s))^2 + \int_0^t \lambda_m(s) v_f(t-s), \tag{7.4}$$

Here,

$$e_{m,f}(t) := \mathbb{E}[\mathrm{SMO}_{m,f}(t)],$$

where $\mathrm{SMO}_{m,f}$ is defined as (7.3)*, but for a different cascade of PPs, which has only λ_m for intensity (for both the first and subsequent generations).*

The renewal equation (7.4) allows the use of an efficient numerical resolution algorithm [112] to compute the variance of SMO_f and not rely on a Monte-Carlo approach.

7.3 Numerical illustrations

Let us illustrate this approach with the parameters of Table 7.1, and the observables that were used in [122] to parametrize their model, that is the number of metastases exceeding given thresholds c (i.e. f_{macro} with different thresholds). The corresponding numerical simulations are given in Fig. 7.1. In this illustration one can observe the prediction of the size-structured model (blue line). Some paths of the PP cascade model are also displayed to illustrate the variability inherent of a stochastic model. Note that these paths evolves mainly between the two red dashed lines accounting for the variance of the model.

In this context, the stochastic framework is a valuable tool to assess the impact of secondary metastatic emission following the surgery of the primary tumor, and evaluate the risk of a metastatic disease through a Monte-Carlo approach. To represent the impact of a surgery at time t_{surgery}, the emission intensity $\lambda_p(t)$ of the primary tumor is set to zero for $t \geq t_{\mathrm{surgery}}$. Using the clinical parameters of Table 7.1, we assume that the primary tumor is surgically removed 500 days after its inception, where it has reached a tumor mass of 180 g, and evaluate the number of metastases

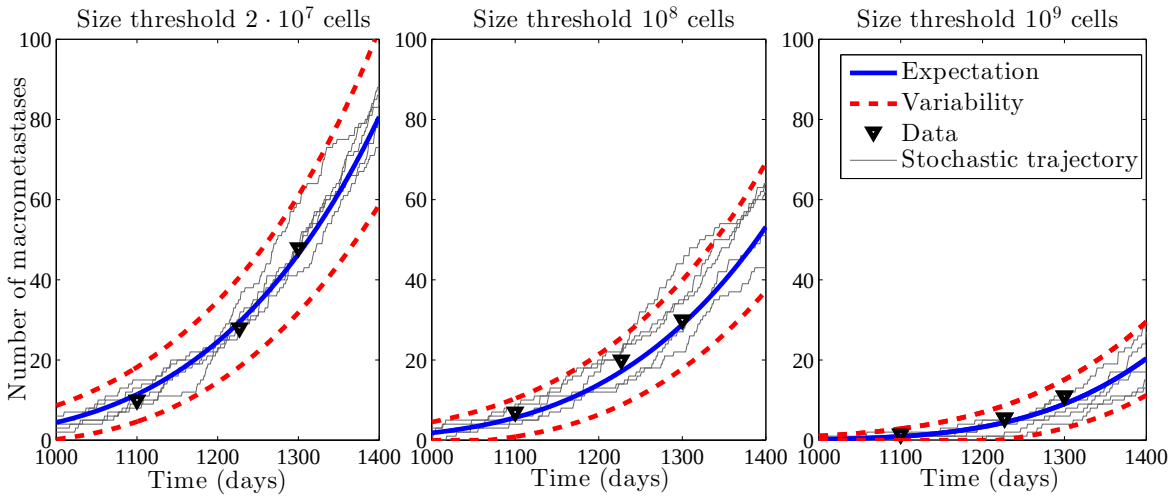

Fig. 7.1: Comparison of the size-structured model fit and stochastic variability of the PP cascade model. Expectation (blue solid line) corresponds to the size-structured model prediction used to fit the clinical data from [122] (computed via Eq. (7.2)). Random trajectories of the PP cascade model are displayed through thin grey lines, and the red dashed lines corresponds to $\mathbb{E}[N_{\text{macro},t}] \pm 2 \cdot \sqrt{\text{var}[N_{\text{macro},t}]}$ (with $\text{var}[N_{\text{macro},t}]$ computed via Eq. (7.4)). As in [122], we count time from inception of the first primary tumor cell, which was back-calculated from primary tumor data assuming a Gompertzian growth model (hence the first CT scan with metastatic disease is approximately 3 years post-inception).

another 500 days later (Fig. 7.2). We consider both a model with secondary metastatic emission and a model without secondary emission (where metastases cannot emit themselves new metastasis). Knowing that every secondary emission is preceded by at least one primary emission, the probability of a metastatic disease is the same for both models. However, the model with secondary emission predicts a significantly higher number of metastases in average ($\mathbb{E}[N_t] = 4.7$ with secondary emission vs. $\mathbb{E}[N_t] = 1.2$ without). Not surprisingly, the model with secondary metastatic emission is more pessimistic than without secondary emission.

7.4 Perspectives

This approach combining a deterministic and a stochastic model could benefit from further developments for individualized risk predictions, and be included as a factor (among others) in comprehensive decision frameworks based on modern machine learning methods. Other (individual) factors play a key role in the context of cancer and metastatic diseases. For instance, circulating biomarkers, such as circulating tumor cells or circulating tumor DNA, can be a useful source of information. Once validated, a mathematical model can serve as a powerful tool for informed treatment decisions by integrating case-specific information into a consistent quantitative framework.

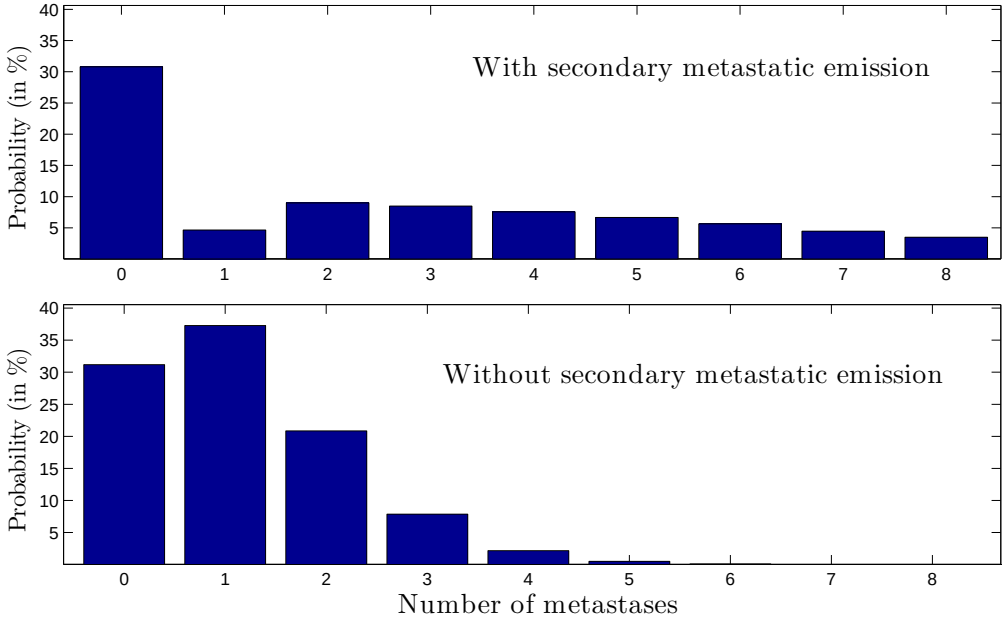

Fig. 7.2: Probability of a metastatic disease after surgery with (top panel) or without (bottom panel) secondary metastatic emission (each based on 10.000 simulations). The primary tumor is assumed to be surgically removed 500 days after its inception. The number of metastases is evaluated another 500 days later.

Bibliography

[1] A. Abdulle, D. Cohen, G. Vilmart, and K. C. Zygalakis, *High weak order methods for stochastic differential equations based on modified equations*, SIAM J. Sci. Comput. **34** (2012), A1800 – A1823.

[2] J.-L. Akian, *Space-time semiclassical measures for three-dimensional elastodynamics: boundary conditions for the hyperbolic set*, Asymptot. Anal. **78** (2012), 37–83.

[3] R. Alexandre, *A review of Boltzmann equation with singular kernels*, Kinet. Relat. Models **2** (2009), 551–646.

[4] ———, *Fractional order kinetic equations and hypoellipticity*, Anal. Appl. **10** (2012), 237–247.

[5] R. Alexandre, Y. Morimoto, S. Ukai, C.-J. Xu, and T. Yang, *Global existence and full regularity of the Boltzmann equation without angular cutoff*, Comm. Math. Phys. **304** (2011), 513–581.

[6] R. Alexandre and C. Villani, *On the Boltzmann equation for long-range interactions*, Comm. Pure Appl. Math. **55** (2002), 30–70.

[7] R Alonso, L. Borcea, and J. Garnier, *Wave propagation in waveguides with random boundaries*, Commun. Math. Sci. **11** (2012), 233–267.

[8] V. I. Arnold, *Mathematical methods of classical mechanics*, Springer, 1989.

[9] S. Asmussen and J. Rosiński, *Approximations of small jumps of lévy processes with a view towards simulation*, J. Appl. Probab. **38** (2001), 482–493.

[10] F. Bailly, J. F. Clouet, and J. P. Fouque, *Parabolic and gaussian white noise approximation for wave propagation in random media*, SIAM J. Appl. Math. **56** (1996), 1445–1470.

[11] G. Bal, *On the self-averaging of wave energy in random media*, SIAM Multiscale model. simul. **2** (2004), 398–420.

[12] ———, *Kinetics of scalar wave fields in random media*, Wave Motion (2005), 132–157.

[13] G. Bal and Y. Gu, *Limiting models for equations with large random potential; a review*, Comm. Math. Sci. **13** (2013), 729–748.

[14] G. Bal, T. Komorowski, and L. Ryzhik, *Kinetic limits for waves in a random medium*, Kinet. Relat. Models **3** (2010), 529–644.

[15] ———, *Asymptotics of the phase of the solutions of the random Schrödinger equation*, Arch. Rat. Mech. Anal. **100** (2011), 613–664.

[16] G. Bal, G. C. Papanicolaou, and L. Ryzhik, *Diffusive energy scattering from weakly random surfaces*, J. Math. Phys. **40** (1999), 4813–4827.

[17] ———, *Radiative transport limit for the random Schrödinger equation*, Nonlinearity **15** (2002), 513–529.

[18] _____, *Self-averaging in time reversal for the parabolic wave equation*, Stoch. Dyn. **2** (2002), 507–532.

[19] G. Bal and O. Pinaud, *Dynamics of wave scintillation in random media*, Commun. Part. Diff. Eq. **35** (2010), 1176–1235.

[20] _____, *Imaging using transport models for wave-wave correlations*, Math. Mod. Meth. App. Sci. **21** (2011), 1071–1093.

[21] G. Bal and K. Ren, *Transport-based imaging in random media*, SIAM J. Appl. Math. **68** (2008), 1738–1762.

[22] G. Bal and L. Ryzhik, *Wave transport for a scalar model of the love waves*, Wave Motion **36** (2002), 49–66.

[23] _____, *Time splitting for wave equations in random media*, M2AN Math. Model. Numer. Anal. **38** (2004), 961–988.

[24] A. Bamberger, B. Engquist, L. Halpern, and P. Joly, *Parabolic wave equation approximations in heterogeneous media*, SIAM J. Appl. Math. **48** (1988), 99–128.

[25] J.P. Banon, Ø. S. Hetland, and I. Simonsen, *Physics of polarized light scattering from weakly rough dielectric surfaces: Yoneda and brewster scattering phenomena*, Phys. Rev. A **99** (2019), 023834.

[26] W. Bao, S. Jin, and P. A. Markowich, *On time-splitting spectral approximations for the Schrödinger equation in the semiclassical regime*, J. Comp. Phys. **175** (2002), 487–524.

[27] D. Barbolosi, B. Benabdallah, F. Hubert, and F. Verga, *Mathematical and numerical analysis for a model of growing metastatic tumors*, Math. Biosci **218** (2009), 1–14.

[28] R. Bartoszyński, L. Edler, L. Hanin, A. Kopp-Schneider, L. Pavlova, A. Tsodikov, A. Zorin, and A. Yakovlev, *Modeling cancer detection: tumor size as a source of information on unobservable stages of carcinogenesis*, Math. Biosci. **171** (2001), 113–142.

[29] F. G. Bass and I. M. Fuks, *Wave scattering from statistically rough surfaces*, International series in natural philosophy, Elsevier, 2013.

[30] A. Basson and D. Gérard-Varet, *Wall laws for fluid flows at a boundary with random roughness*, Commun. Pure Appl. Math. **61** (2008), 941–987.

[31] M. S. Belen'kii, S. J. Karis, C. L. Osmon, J.M. Brown II, and R. Q. Fugate, *Experimental evidence of the effects of non-kolmogorov turbulence and anisotropy of turbulence*, Proc. SPIE 3749, 18th Congress of the International Commission for Optics (1999).

[32] S. Benzekry, C. Lamont, A. Beheshti, A. Tracz, J.M.L Ebos, L. Hlatky, and P. Hahnfeldt, *Classical Mathematical Models for Description and Prediction of Experimental Tumor Growth*, PLOS Comput. Biol. **10** (2014), e1003800.

[33] S. Benzekry, A. Tracz, M. Mastri, R. Corbelli, D. Barbolosi, and J.M.L. Ebos, *Modeling spontaneous metastasis following surgery: an in vivo-in silico approach*, Cancer Res. **76** (2015).

[34] P. Blomgren, G. C. Papanicolaou, , and H. Zhao, *Super-resolution in time-reversal acoustics*, J. Acoust. Soc. Am. **111** (2002), 230–248.

[35] L. Borcea and J. Garnier, *A ghost imaging modality in a random waveguide*, Inverse Probl. **34** (2018), 124007.

[36] L. Borcea, J. Garnier, and K. Sølna, *Wave propagation and imaging in moving random media*, SIAM Multiscale Model. Simul. **17** (2019), 31–67.

[37] L. Borcea, J. Garnier, and C. Tsogka, *A quantitative study of source imaging in random waveguides*, Commun. Math. Sci. **13** (2015), 749–776.

[38] L. Borcea, I. Issa, and C. Tsogka, *Source localization in random acoustic waveguides*, SIAM Multiscale Model. Simul. **5** (2010), 1981–2022.

[39] L. Borcea, G. C. Papanicolaou, and C Tsogka, *Interferometric array imaging in clutter*, Inverse Probl. **21** (2005), 1419–1460.

[40] F. Bouchut, *Hypoelliptic regularity in kinetic equations*, J. Math. Pures Appl. **81** (2002), 1135–1159.

[41] N. Bournaveas and S. Gutiérrez, *On the regularity of averages over spheres for kinetic transport equations in hyperbolic Sobolev spaces*, Rev. Mat. Iberoam. **23** (2007), 481–512.

[42] ———, *Averages over spheres for kinetic transport equations with velocity derivatives in the right-hand side*, SIAM J. Math. Anal. **40** (2008), 653–674.

[43] N. Bournaveas and B. Perthame, *Averages over spheres for kinetic transport equations; hyperbolic Sobolev spaces and Strichartz inequalities*, J. Math. Pures Appl. (9) **80** (2001), 517–534.

[44] N. Bournaveas and H. Wang, *Velocity averaging lemmas in hyperbolic Sobolev spaces for the kinetic transport equation with velocity field on the sphere*, **16** (2009), 131–142.

[45] M. Butz, *Kinetic limit for wave propagation in a continuous, weakly random medium*, Ph.D. thesis, Technische Universität München, 2015.

[46] M Caputo, J. M Carcione, and F Cavallini, *Wave simulation in biologic media based on the kelvin-voigt fractional-derivative stress-strain relation*, Ultrasound in Medicine & Biology **37** (2011), 996–1004.

[47] S. Catheline, T. Gallot, P. Roux, G. Ribay, and J. De Rosny, *Coherent backscattering enhancement in cavities: The simple-shape cavity revisited*, Wave Motion **48** (2011), 214–222.

[48] S. Chandrasekhar, *Radiative transfer*, Dover Publications, New York, 1960.

[49] G. Chen and C. Qiuming, *Fractal density modeling of crustal heterogeneity from the ktb deep hole*, J. Geophys. Res. Solid Earth **122** (2017), 1919–1933.

[50] L. L. Chen, N. Blumm, N. A. Christakis, A. L. Barabasi, and T. S. Deisboeck, *Cancer metastasis networks and the prediction of progression patterns*, Br. J. Cancer **101** (2009), 749–758.

[51] T. Chen, T. Komorovski, and L. Ryzhik, *The weak coupling limit for the random Schrödinger equation: The average wave function*, Arch. Rational Mech. Anal. **227** (2018), 387–422.

[52] J. F. Claerbout, *Imaging the earth's interior*, Blackwell Science, Palo Alto, CA, 1985.

[53] S. Cohen and J. Rosiński, *Gaussian approximation of multivariate lévy processes with applications to simulation of tempered stable processes*, Bernoulli **13** (2007), 195–210.

[54] M. D Collins and W. L Siegmann, *Parabolic equation techniques for seismology, seismo-acoustics, and arctic acoustics*, Journal of Theoretical and Computational Acoustics **29** (2021), 2130003.

[55] E. Comen, L. Norton, and J. Massague, *Clinical implications of cancer self-seeding*, Nat. Rev. Clin. Oncol. **8** (2011), 369–377.

[56] H. Contopanagos, B. Dembart, M. Epton, J. J. Ottusch, V. Rokhlin, J.L. Visher, and S.M. Wandzura, *Well-conditioned boundary integral equations for three-dimensional electromagnetic scattering*, IEEE Trans. Antennas Propag. **50** (2002), 1824–1830.

[57] M. Darmon, V. Dorval, and F. Baqué, *Acoustic scattering models from rough surfaces: a brief review and recent advances*, Appl. Sci. **10** (2020), 8305.

[58] D. A. Dawson and G. C. Papanicolaou, *A random wave process*, Appl. Math. Optim. **12** (1984), 97–114.

[59] K. Debrabant and A. Rößer, *Families of efficient second order runge–kutta methods for the weak approximation of itô stochastic differential equations*, Appl. Numer. Math. **59** (2009), 582–594.

[60] S. Dolan, C. Bean, and B Riollet, *The broad-band fractal nature of heterogeneity in the upper crust from petrophysical logs*, Geophys. J. Int. **132** (1998), 489–507.

[61] L. B. Dozier, *A numerical treatment of rough surface scattering for the parabolic wave equation*, J. Acoust. Soc. Am. **75** (1984), 1415–1432.

[62] F.A. Duck, *Physical properties of tissue*, Academic Press, London, 1996.

[63] A. I. Dyachenko, E. A. Kuznetsov, M. D. Spector, and V. E. Zakharov, *Analytical description of the free surface dynamics of an ideal fluid (canonical formalism and conformal mapping)*, Phys. Lett. A **221** (1996), 73–79.

[64] L. Erdös, M Salmhofer, and H.-T. Yau, *Quantum diffusion of the random Schrödinger evolution in the scaling limit ii. the recollision diagrams*, Comm. Math. Phys. **271** (2007), 1–53.

[65] _____, *Quantum diffusion of the random Schrödinger evolution in the scaling limit i. the non-recollision diagrams*, Acta Math. **200** (2008), 211–277.

[66] L. Erdös and H.-T. Yau, *Linear boltzmann equation as the weak coupling limit of the random Schrödinger equation*, Commun. Pure Appl. Math. **53** (2000), 667–735.

[67] A. Fannjiang and T. Komorowski, *Fractional brownian motions in a limit of turbulent transport*, Ann. Appl. Probab. **10** (2000), 1100–1120.

[68] A. C. Fannjiang and K. Sølna, *Scaling limits for beam wave propagation in atmospheric turbulence*, Stoch. Dyn. **4** (2004), 135–151.

[69] _____, *Propagation and time-reversal of wave beams in atmospheric turbulence*, SIAM Multiscale Model. Simul. **3** (2005), 522–558.

[70] J.-P. Fouque, J. Garnier, G. C. Papanicolaou, and K. Sø lna, *Wave propagation and time reversal in randomly layered media*, Stochastic Modelling and Applied Probability, vol. 56, Springer, New York, 2007.

[71] M.I. Freidlin and M. Weber, *Random perturbations of nonlinear oscillators*, Ann. Probab. **26** (1998), 925–967.

[72] M.I. Freidlin and A.D Wentzell, *Diffusion processes on graphs and the averaging principle*, Ann. Probab. **21** (1993), 2215–2245.

[73] _____, *Random perturbations of hamiltonian systems*, Mem. Amer. Math. Soc. **109** (1994), viii+82.

[74] P. K. Friz and M. Hairer, *A course on rough paths: with an introduction to regularity structures*, Universitext, Springer Cham, 2014.

[75] M. Fukushima, *Dirichlet forms and Markov processes*, North-Holland Mathematical Library, vol. 23, North-Holland Publishing Co., Amsterdam-New York; Kodansha, Ltd., Tokyo, 1980.

[76] T. Gallot, S. Catheline, and P. Roux, *Coherent backscattering enhancement in cavities. highlights of the role of symmetry*, J. Acoust. Soc. Am. **129** (2011), 1963–1971.

[77] A. E. Gargett, *The scaling of turbulence in the presence of stable stratification*, J. Geophys. Res. **93** (1988), 5021–5036.

[78] J. Garnier, *Multi-scaled diffusion-approximation. Applications to wave propagation in random media*, ESAIM Probab. Statist. **1** (1997), 183–206.

[79] _____, *The role of evanescent modes in randomly perturbed single-mode waveguides*, Discrete Cont. Dyn.-B **8** (2007), 455–472.

[80] _____, *Ghost imaging in the random paraxial regime*, Inverse Problems and Imaging **10** (2016), 409–432.

[81] J. Garnier, J. C. Munoz Grajales, and A. Nachbin, *Effective behavior of solitary waves over random topography*, SIAM Multiscale Model. Simul. **6** (2007), 995–1025.

[82] J. Garnier and K. Sølna, *Effective transport equations and enhanced backscattering in random waveguides*, SIAM J. Appl. Math **68** (2008), 1574–1599.

[83] _____, *Coupled paraxial wave equations in random media in the white-noise regime*, Ann. Appl. Probab. **19** (2009), 318–346.

[84] _____, *Pulse propagation in random media with long-range correlation*, SIAM Multiscale Model. Simul. **7** (2009), 1302–1324.

[85] _____, *Effective fractional acoustic wave equations in random multiscale media*, J. Acoust. Soc. Am. **127** (2010), 67–72.

[86] _____, *Scintillation in the white-noise paraxial regime*, Commun. Part. Diff. Eq. **39** (2014), 626–650.

[87] _____, *Focusing waves through a randomly scattering medium in the white-noise paraxial regime*, SIAM J. Appl. Math. **77** (2017), 500–519.

[88] _____, *Imaging through a scattering medium by speckle intensity correlations*, Inverse Probl. **34** (2018), 094003.

[89] S Gelinsky, S. A Shapiro, and T Müller, *Dynamic poroelasticity of thinly layered structure*, Int. J. Solids Structures **35** (1998), 4739–4751.

[90] A. Gomez, A. Callejas, G. Rus, and N. Saffari, *Experimental evidence of shear waves in fractional viscoelastic rheological models*, Sci Rep **12** (2022), 7448.

[91] C. Gomez, *Wave propagation in shallow-water acoustic random waveguides*, Commun. Math. Sci. **9** (2011), 81–125.

[92] _____, *Radiative transport limit for the random Schrödinger equation with long-range correlations*, J. Math. Pures Appl. **98** (2012), 295–327.

[93] _____, *Wave decoherence for the random Schrödinger equation with long-range correlations*, Commun. Math. Phys. **320** (2013), 37–71.

[94] _____, *Wave propagation in underwater acoustic waveguides with rough boundaries*, Commun. Math. Sci. **13** (2015), 2005–2052.

[95] C. Gomez and O. Pinaud, *Fractional white-noise limit and paraxial approximation for waves in random media*, Arch. Rational Mech. Anal. **226** (2017), 1061–1138.

[96] _____, *Monte carlo methods for radiative transfer with singular kernels*, SIAM J. Sci. Comput. **40** (2018), A1714–A1741.

[97] C. Gomez, O. Pinaud, and L. Ryzhik, *Hypoelliptic estimates in radiative transfer*, Commun. Part. Diff. Eq. **41** (2015), 150–184.

[98] _____, *Radiative transfer with long-range interactions: regularity and asymptotics*, SIAM Multiscale Model. Simul. **15** (2017), 1048–1072.

[99] C. Gomez and K. Sølna, *Wave propagation in random waveguide with long-range correlations*, Commun. Math. Sci. **16** (2018), 1557–1596.

[100] A. A. Gonoskov and I. A. Gonoskov, *Suppression of reflection from the grid boundary in solving the time-dependent Schrödinger equation by split-step technique with fast fourier transform*, ArXiv Physics e-prints (2006).

[101] S. A. Goss, R.L. Johnston, and F. Dunn, *Comprehensive compilation of empirical ultrasonic properties of mammalian tissues*, J. Acoust. Soc. Am. **64** (1978), 423–457.

[102] P. T. Gressman and R. M. Strain, *Global classical solutions of the Boltzmann equation with long-range interactions*, Proc. Natl. Acad. Sci. **107** (2010), 5744–5749.

[103] _____, *Global classical solutions of the Boltzmann equation without angular cut-off*, J. Amer. Math. Soc. **24** (2011), 771–847.

[104] L. A. Grzelak, J. Witteveen, M. Suarez-Taboada, and C. W. Oosterlee, *The stochastic collocation monte carlo sampler: Highly efficient sampling from "expensive" distributions*, Quant. Finance **19** (2019).

[105] Y. Gu and T. Komorovski, *Gaussian fluctuations from random schrödinger equation*, Commun. Partial. Differ. Equ. **46** (2021), 201–232.

[106] Y. Gu, T. Komorovski, and L. Ryzhik, *The Schrödinger equation with spatial white noise: The average wave function*, J. Differ. Equ. **274** (2018), 2113–2138.

[107] H. Haeno and F. Michor, *The evolution of tumor metastases during clonal expansion*, J. Theor. Biol. **263** (2010), 30–44.

[108] L. Hanin, J. Rose, and M. Zaider, *A stochastic model for the sizes of detectable metastases*, J. Theor. Biol. **243** (2006), 407–417.

[109] A Hanyga, *Multidimensional solutions of time-fractional diffusion-wave equations*, Proc. R. Soc. Lond. A. **458** (2002), 933–957.

[110] A Hanyga and V. E Rok, *Wave propagation in micro-heterogeneous porous media: A model based on an integro-differential wave equation*, J. Acoust. Soc. Am. **107** (2000), 2965–2972.

[111] D. Hart, E. Shochat, and Z. Agur, *The growth law of primary breast cancer as inferred from mammography screening trials data*, Br. J. Cancer **78** (1998), 382–7.

[112] N. Hartung, *Efficient resolution of metastatic tumour growth models by reformulation into integral equations*, Discret. Contin. Dyn. S. B **20** (2015), 445–467.

[113] N. Hartung, S. Mollard, D. Barbolosi, A. Benabdallah, G. Chapuisat, G. Henry, S. Giacometti, A. Iliadis, J. Ciccolini, C. Faivre, and F. Hubert, *Mathematical modeling of tumor growth and metastatic spreading: validation in tumor-bearing mice*, Cancer Res. **74** (2014), 6397–6407.

[114] L. G. Henyey and J. Greenstein, *Diffuse radiation in the galaxy*, Astrophys. J. (1941), 70–83.

[115] T. Ho, L. Landau, and A. Wilkins, *On the weak coupling limit for a fermi gas in a random potential*, Rev. Math. Phys. **5** (1993), 209–298.

[116] S. Holm, *Waves with power-law attenuation*, Springer Cham, 2019.

[117] S. Holm and R. Sinkus, *A unifying fractional wave equation for compressional and shear wave*, J. Acoust. Soc. Am. **127** (2010), 542–548.

[118] H. Hurst, *Long-term storage capacity of reservoirs*, Trans. Am. Soc. Civ. Eng. **116** (1951), 770–808.

[119] _____, *Methods of using long-term storage in reservoirs*, P I CIVIL ENG-CIV EN **Part I** (1955), 519–577.

[120] A. Ishimaru, *Wave propagation and scattering in random media*, vol. 2, Academic Press, London, 1978.

[121] _____, *Wave propagation and scattering in random media and rough surfaces*, Proceedings of the IEEE **79** (1991), 1359–1366.

[122] K. Iwata, K. Kawasaki, and N. Shigesada, *A dynamical model for the growth and size distribution of multiple metastatic tumors*, J. Theor. Biol. **203** (2000), 177–186.

[123] S. L. Jacques, *Optical properties of biological tissues: A review*, Phys. Med. Biol. **58** (2013), R37–61.

[124] J. H. Jeans, *Stars, gaseous, radiative transfer of energy*, Mon. Notices Royal Astron. Soc. **78** (1917), 28–36.

[125] S. Jin, P. Markowich, and C. Sparber, *Mathematical and computational methods for semiclassical Schrödinger equations*, Acta Numer. **20** (2011), 121–209.

[126] B. Katsnelson, V. Petnikov, and J. Lynch, *Fundamentals of shallow water acoustics*, Springer, New York, 2012.

[127] O. Katz, P. Heidmann, M. Fink, and S. Gigan, *Non-invasive single-shot imaging through scattering layers and around corners via speckle correlations*, Nature Photon **8** (2014), 784–790.

[128] R. Z. Khasminskii, *A limit theorem for solutions of differential equations with random right hand side*, Theory Probab. Appl. **11** (1966), 390–406.

[129] _____, *On stochastic processes defined by differential equations with a small parameter*, Theory Probab. Appl. **11** (1966), 211–228.

[130] M. Kiss, T. Varghese, and T. Hall, *Viscoelastic characterization of in vitro canine tissue*, Phys. Med. Biol. **49** (2004), 4207–4218.

[131] T. Komorowski and E. Nieznaj, *On the asymptotic behavior of solutions of the heat equation with a random, long-range correlated potential*, Potential Anal. **33** (2009), 175–197.

[132] T. Komorowski, A. Novikov, and L. Ryzhik, *Evolution of particle separation in slowly decorrelating velocity fields*, Commun Math Sci **10** (2012), 767 – 786.

[133] _____, *Homogenization driven by a fractional brownian motion: the shear layer case*, SIAM Multiscale Model. Simul. **12** (2014), 440–457.

[134] T. Komorowski and L. Ryzhik, *On asymptotics of a tracer advected in a locally self-similar correlated flow*, Asymptot. Anal. **53** (2007), 159–187.

[135] _____, *Passive tracer in a slowly decorrelating random flow with a large mean*, Nonlinearity **20** (2007), 1215–1239.

[136] S. Koscielny, M. , Tubiana, M.G. Lê, J. Valleron, H. Mouriesse, G. Contesso, and D. Sarrazin, *Breast cancer: relationship between the size of the primary tumour and the probability of metastatic dissemination*, Br. J. Cancer **49** (1984), 709–715.

[137] W. A. Kuperman and F. Ingenito, *Attenuation of the coherent component of sound propagating in shallow water with rough boundaries*, J. Acoust. Soc. Am. **61** (1977), 1178–1187.

[138] W. A. Kuperman and J. F. Lynch, *Shallow-water acoustics*, Phys. Today **57** (2004), 55–61.

[139] H. J. Kushner, *Approximation and weak convergence methods for random processes, with applications to stochastic systems theory*, MIT Press Series in Signal Processing, Optimization, and Control, 6, MIT Press, Cambridge, MA, 1984.

[140] B. Lapeyre, E. Pardoux, and R. Sentis, *Introduction to monte-carlo methods for transport and diffusion equations*, Oxford University Press, 2003.

[141] N. Lerner, Y. Morimoto, and K. Pravda-Starov, *Hypoelliptic estimates for a linear model of the Boltzmann equation without angular cutoff*, Commun. Part. Diff. Eq. **37** (2012), 234–284.

[142] H. Louvin, E. Dumonteil, T. Lelièvre, M. Rousset, and C. M. Diop, *Adaptive multilevel splitting for monte carlo particle transport*, EPJ Nuclear Sci. Technol. **3** (2017).

[143] I. Lux and L. Koblinger, *Monte carlo particle transport methods : neutron and photon calculations*, CRC Press, 1991.

[144] T. Lyons, *Differential equations driven by rough signals*, Rev. Mat. Iberoam. **14** (1998), 215–310.

[145] R. Magnanini and F. Santosa, *Wave propagation in a 2-d optical waveguide*, SIAM J. Appl. Math **61** (2000), 1237–1252.

[146] B. Mandelbrot, *Une classe de processus stochastiques homothetiques a soi; application a loi climatologique de h.e. hurst*, Comptes Rendus Acad. Sci. Paris **240**, 3274–3277.

[147] B. Mandelbrot and J. Wallis, *Noah, joseph and operational hydrology*, Water Resour. Res. **4** (1968), 909–918.

[148] A.A. Maradudin, T. Michel, A. R. McGurn, and E.R. Méndez, *Enhanced backscattering of light from a random grating*, Ann. Phys. **203** (1990), 255–307.

[149] D. Marcuse, *Theory of dielectric optical waveguides*, Academic press, New York, 1991.

[150] L. Margerin, A. Bajaras, and M. Campillo, *A scalar radiative transfer model including the coupling between surface and body waves*, Geophys. J. Int. **219** (2019), 1092–1108.

[151] J. M. Martin and S. M Flatté, *Intensity images and statistics from numerical simulation of the wave propagation in 3-d random media*, Appl. Optim. **247** (1988), 2111–2126.

[152] R. Marty, *Asymptotic behavior of differential equations driven by periodic and random processes with slowly decaying correlations*, ESAIM Probab. Stat. **9** (2005), 165–184.

[153] R. Marty and K. Sølna, *Acoustic waves in long range random media*, SIAM J. Appl. Math. **69** (2009), 1065–1083.

[154] ———, *A general framework for waves in random media with long-range correlations*, Ann. Appl. Probab. **21** (2011), 115–139.

[155] ———, *Asymptotic behavior of oscillatory fractional processes*, Séminaire de Probabilités XLIV (C. Donati-Martin, A. Lejay, and A. Rouault, eds.), Springer Berlin Heidelberg, Berlin, Heidelberg, 2012, pp. 247–269.

[156] B. Maslowsky and D. Nualart, *Evolution equation driven by a fractional brownian motion*, J. Funct. Anal. **202** (2003), 277–305.

[157] R. I. McLachlan, G. Quispel, and Reinout W., *Splitting methods*, Acta Numer. **11** (2002), 341–434.

[158] A. Messaoudi, *Radiative transfer models for acoustic waves in a randomly fluctuating medium with boundaries : boundary effects and weak localization*, Ph.D. thesis, Aix Marseille University, 2023.

[159] J.S. Michaelson, M. Silverstein, J. Wyatt, G. Weber, R. Moore, E. Halpern, D.B. Kopans, and K. Hughes, *Predicting the survival of patients with breast carcinoma using tumor size*, Cancer **95** (2002), 713–723.

[160] F. Michor, M.A. Nowak, and Y. Iwasa, *Stochastic dynamics of metastasis formation*, J. Theor. Biol. **240** (2006), 521–530.

[161] L. Miller, *Refraction of high-frequency waves density by sharp interfaces and semiclassical measures at the boundary*, J. Math. Pures Appl. **79** (2000), 227–269.

[162] S. P. Näsholm and S. Holm, *On a fractional zener elastic wave equation*, fcaa **16** (2013), 26–50.

[163] J. Nevard and J.B. Keller, *Homogenization of rough boundaries and interfaces*, SIAM J. Appl. Math. **57** (1997), 1660–1686.

[164] P. K. Newton, J. Mason, K. Bethel, L. Bazhenova, J. Nieva, L. Norton, and P. Kuhn, *Spreaders and sponges define metastasis in lung cancer: a Markov chain Monte Carlo mathematical model*, Cancer Res. **73** (2013), 2760–2769.

[165] P. K. Newton, J. Mason, K. Bethel, L. A. Bazhenova, J. Nieva, and P. Kuhn, *A stochastic Markov chain model to describe lung cancer growth and metastasis*, PLoS ONE **7** (2012), e34637.

[166] S. Nicolle, M. Lounis, R. Willinger, and J. F. Palierne, *Shear linear behavior of brain tissue over a large frequency range*, Biorheology **42** (2005), 209–223.

[167] U. M. Noebauer and S. A. Sim, *Monte carlo radiative transfer*, Living rev. comput. astrophys. **5** (2019), 1.

[168] D. Nualart and A. Răşcanu, *Differential equations driven by fractional brownian motion*, Collect. Math. **53** (2002), 55–81.

[169] J. A. Ogilvy, *Theory of wave scattering from random rough surfaces*, CRC Press, 1991.

[170] K. Pantel, R. J. Cote, and O. Fodstad, *Detection and Clinical Importance of Micrometastatic Disease*, J. Natl. Cancer Inst. **91** (1999), 1113–1124.

[171] G. C. Papanicolaou and W. Kohler, *Asymptotic theory of mixing stochastic ordinary differential equations*, Comm. Pure Appl. Math **27** (1974), 641–668.

[172] G. C. Papanicolaou and K. Sølna, *Wavelet based estimation of local kolmogorov turbulence*, Long-range dependence: theory and applications (P. Doukhan, G. Oppenmeim, and M. S. Taqqu, eds.), Birkhauser, 2002, pp. 473–507.

[173] G. C. Papanicolaou, D. Stroock, and S. R. S. Varadhan, *Martingale approach to some limit theorem*, Statistical Mechanics, Dynamical Systems and the Duke Turbulence Conference (D. Ruelle, ed.), Duke Univ. Math. Ser., 1977, pp. 1–120.

[174] C. I. Pekeris, *Theory of propagation of explosive sound in shallow water*, Propagation of Sound in the Ocean, Geological Society of America, 1948.

[175] S. Powell, B. T. Cox, and S. R. Arridge, *A pseudospectral method for solution of the radiative transport equation*, J. Comput. Phys. **384** (2019), 376–382.

[176] J. Przybilla and M. Korn, *Monte carlo simulation of radiative energy transfer in continuous elastic random media - three-component envelopes and numerical validation*, Geophys. J. Int. (2008), 566–576.

[177] D Ren, X Shen, C Li, and X Cao, *The fractional kelvin-voigt model for rayleigh surface waves in viscoelastic fgm infinite half space*, Mechanics Research Communications **87** (2018), 53–58.

[178] L. Reynolds and N. McCormick, *Approximate two-parameter phase function for light scattering*, J. Opt. Soc. Am. **70** (1980), 1206–1212.

[179] W. Rudin, *Real and complex analysis*, McGraw-Hill, New York, 1987.

[180] L. Ryzhik, G. C. Papanicolaou, and J. B. Keller, *Transport equations for elastic and other waves in random media*, Wave motion **24** (1996), 327–370.

[181] ———, *Transport equations for waves in a half-space*, Commun. Partial. Differ. Equ. **22** (1997), 1869–1910.

[182] S. G. Samko, A. A. Kilbas, and O. I. Marichev, *Fractional integrals and derivatives*, Gordon and Breach, 1993.

[183] A. Santenac and J. Daillant, *Statistical aspects of wave scattering at rough surface*, X-ray and Neutron Reflectivity, Lecture Notes in Physics (J. Daillant and A. Gibaud, eds.), vol. 770, Springer, Berlin, Heidelberg, 2009, pp. 59–84.

[184] F. Sayas, O. Bruno, and V. Dominguez, *Convergence analysis of a high-order nystrom integral-equation method for surface scattering problems*, Numer. Math. **124** (2013), 603–645.

[185] A. Schuster, *Radiation through a foggy atmosphere*, Astrophys. J. **21**, 1–22.

[186] J.G. Scott, D. Basanta, A.R. Anderson, and P. Gerlee, *A mathematical model of tumour self-seeding reveals secondary metastatic deposits as drivers of primary tumour growth*, J. R. Soc. Interface **10** (2013), 20130011.

[187] F Shi, M.J.S. Lowe, and R.V. Craster, Diffusely scattered and transmitted elastic waves by random rough solid-solid interfaces using an elastodynamic kirchhoff approximation **95** (2017), 214305.

[188] C. Sidi and F. Dalaudier, *Turbulence in the stratified atmosphere: recent theoretical developments and experimental results*, Adv. in Space Res. **10** (1990), 25–36.

[189] I. Simonsen, D. Vandembroucq, and S. Roux, *Wave scattering from self-affine surfaces*, Phys. Rev. E **61** (2000), 5914–5917.

[190] R. Sinkus, K. Siegmann, T. Xydeas, M. Tanter, C. Claussen, and M. Fink, *Mr elastography of breast lesions: Understanding the solid/liquid duality can improve the specificity of contrast-enhanced mr mammography*, Magn. Reson. Med. **58** (2007), 1135–1144.

[191] K. Sølna, *Acoustic pulse spreading in a random fractal*, SIAM J. Appl. Math. **63** (2003), 1764–1788.

[192] J. Spanier and E. M. Gelbard, *Monte carlo principles and neutron transport problems*, Dover Publications, New York, 2008.

[193] H. Spohn, *Derivation of the transport equation for electrons moving through random impurities*, Jour. Stat. Phys. **17** (1977), 385–412.

[194] G. Strang, *On the construction and comparison of difference schemes*, SIAM J. Numer. Anal. **5** (1968), 506–517.

[195] B. E. Stribling, B. M. Welsh, and M. C. Roggemann, *Optical propagation in non-kolmogorov atmospheric turbulence*, Proc. SPIE 2471, Atmospheric Propagation and Remote Sensing IV (1995).

[196] J. W. Strohbehn, *Laser beam propagation in the atmosphere*, Springer, Berlin, 1978.

[197] D. W. Stroock and S. R. S. Varadhan, *Multidimensional diffusion processes*, Springer, Berlin, 1979.

[198] N. V Sushilov and R. S. C Cobbold, *Frequency domain wave equation and its time-domain solutions in attenuating media*, J. Acoust. Soc. Am. **115** (2003), 1431–1435.

[199] T. L Szabo, *Time domain wave equations for lossy media obeying a frequency power law*, J. Acoust. Soc. Am. **96** (1994), 491–500.

[200] D. Talay and L. Tubaro, *Expansion of the global error for numerical schemes solving stochastic differential equations*, Stoch. Anal. Appl. **8** (1991), 94–120.

[201] F. D Tappert, *The parabolic approximation method in wave propagation and underwater acoustics*, Lecture Notes in Phys., Spinger, Berlin **70** (1977), 224–287.

[202] M. S. Taqqu, *Weak convergence to fractional brownian motion and to the rosenblatt process*, Z. Wahrscheinlichkeitstheorie und Verw. Gebiete **31** (1975), 287–302.

[203] ———, *Law of the iterated logarithm for sums of non-linear functions of gaussian variables that exhibit a long range dependence*, Z. Wahrscheinlichkeitstheorie und Verw. Gebiete **40** (1977), 203–238.

[204] M. J. van de Vijver, Y. D. He, L. J. van't Veer, H. Dai, A. A. M. Hart, D. W. Voskuil, G. J. Schreiber, J. L. Peterse, C. Roberts, M. J. Marton, M. Parrish, D. Atsma, A. Witteveen, A. Glas, L. Delahaye, T. van der Velde, H. Bartelink, S. Rodenhuis, E. T. Rutgers, S. H. Friend, and R. Bernards, *A gene-expression signature as a predictor of survival in breast cancer*, N. Engl. J. Med. **347** (2002), 1999–2009.

[205] M. van den Berg and J.T. Lewis, *Brownian motion on hypersurface*, Bull. London Math. Soc. **17** (1985), 144–150.

[206] C. Villani, *A review of mathematical topics in collisional kinetic theory*, Handbook of mathematical fluid dynamics, Vol. I, North-Holland, Amsterdam, 2002, pp. 71–305.

[207] R. Viskanta and M. P. Mengüc, *Radiation heat transfer in combustion systems*, Prog. Energy Combust. Sci. **13** (1987), 97–160.

[208] R. Weron, *On the chambers-mallows-stuck method for simulating skewed stable random variables*, Stat. Probab. Lett. **28** (1996), 165 – 171.

[209] WHO, *Cancer fact sheet*, 2015, http://www.who.int/mediacentre/factsheets/fs297/en/ (accessed 14 Jan 2016).

[210] M. Wismer and R. Ludwig, *An explicit numerical time domain formulation to simulate pulsed pressure waves in viscous fluids exhibiting arbitrary frequency power law attenuation*, IEEE Trans. Ultrason. Ferro- electr. Freq. Control **42** (1995), 1040–1049.

[211] M. Zähle, *Integration with respect to fractal functions and stochastic calculus. i*, Probab. Theory Relat. Fields **111** (1998), 333–374.

[212] A. Zilberman, E. Golbraikh, N. S. Kopeika, A. Virtser, I. Kupershmidt, and Y. Shtemler, *Lidar study of aerosol turbulence characteristics in the troposphere: Kolmogorov and non-kolmogorov turbulence*, Atmos. Res. (2008), 66–77.